Trinity College Dublin
Coláiste na Tríonóide, Baile Átha Cliath
The University of Dublin

School of Physics

Developing a Next Generation Readout System for Microwave Kinetic Inductance Detectors

Eoin Baldwin

October 19, 2022

A thesis submitted in partial fulfilment
of the requirements for the degree of
Doctor of Philosophy

"Measure what is measurable, and make measurable what is not so."

Galileo

To my parents, grandparents, brother, sister, and Edel

Declaration

I hereby declare that this project is entirely my own work and that it has not been submitted as an exercise for a degree at this or any other university.

I have read and I understand the plagiarism provisions in the General Regulations of the University Calendar for the current year, found at `http://www.tcd.ie/calendar`.

I have also completed the Online Tutorial on avoiding plagiarism 'Ready Steady Write', located at `http://tcd-ie.libguides.com/plagiarism/ready-steady-write`.

Signed: _____ Date: _____

Abstract

Microwave Kinetic Inductance Detectors (MKIDs) are photon detectors based on superconducting resonators, capable of detecting single photons with inherent energy resolution and μs time resolution, while also allowing arrays of tens of thousands of MKIDs to be read out on a single feedline using frequency domain multiplexing (FDM). MKIDs are a promising technology for a range of applications, including astronomy, particle physics, and THz imaging. We are developing MKIDs for optical to near infrared astronomy. This thesis covers work done at Trinity College Dublin and the Dublin Institute for Advanced Studies developing MKIDs optical to near infrared astronomy, as well as the readout electronics needed to perform this FDM.

This thesis gives an outline of the background information needed to understand MKIDs, and also gives an outline of their applications. It details the work done developing a laboratory setup for measuring MKIDs, and also developing code for performing frequency sweep measurements. Code is presented for fitting the data generated to equations from the literature, to obtain the quality factors and resonant frequencies of the MKIDs. The results of this are shown. Following this the work done developing a single pixel readout system based on a Re-configurable Open Access Computer Hardware (ROACH) board is detailed. This setup was used to measure and analyse photon pulses in the MKIDs' phase and I/Q data. The results gathered by this setup are presented. An analysis was performed into some potential future systems for reading out large arrays of MKIDs, ultimately selecting the Xilinx ZCU111 and 2x2 Radio Frequency System on Chips (RFSoCs). This analysis, as well as the work done developing firmware and software for this purpose is also outlined.

MKIDs were designed and fabricated for this project which were measured, using the setups described above, to internal quality factors of the order of $100,000$. Moreover, they also displayed energy resolutions ranging from 3.14 for 400 nm light, to 2.50 for 900 nm light.

Finally, a next generation MKID readout system based on a Xilinx 2x2 Radio Frequency System-on-Chip (RFSoC) is proposed, with a potential cost-per-pixel of $\sim$ €1.

List Of Publications

- **E. Baldwin**, M. De Lucia, C. Bracken, G. Ulbricht, O. Creaner, J. Piercy, and T. Ray "Frequency Domain Multiplexing for MKIDs: Comparing the Xilinx ZCU111 RFSoC with their new 2x2 RFSoC board", (*accepted*)
- Ulbricht, G.; De Lucia, M.; **Baldwin, E.** Applications for Microwave Kinetic Induction Detectors in Advanced Instrumentation. Appl. Sci. 2021, 11, 2671 https://doi.org/10.3390/app11062671
- M. De Lucia, **E. Baldwin**, G. Ulbricht, C. Bracken, P. Stamenov, and T. P. Ray "Multiplexable frequency retuning of MKID arrays using their non-linear kinetic inductance", Proc. SPIE 11454, X-Ray, Optical, and Infrared Detectors for Astronomy IX, 114542Z (13 December 2020); https://doi.org/10.1117/12.2560384
- C. Bracken, **E. Baldwin**, G. Ulbricht, M. De Lucia, T. Ray "Modeling Results and Baseline Design for an RF-SoC-Based Readout System for Microwave Kinetic Inductance Detectors" (*under review*)
- M. De Lucia, **E. Baldwin**, G. Ulbricht, and T. P. Ray "Modelling the figures of merit of an MKIDs array: understanding fabrication yield and energy resolution", (*in prep.*)
- M. De Lucia, **E. Baldwin**, G. Ulbricht, J.D. Piercy, O. Creaner, C. Bracken and T. P. Ray " Characterisation of a Microwave Kinetic Inductance Detector produced from an annealed TiN/Ti/TiN mulitlayer film", (*in prep.*)
- Thurareithinam V., **Baldwin E.**, Coffey D., De Lucia M., Hawkins G., Piercy J. D., Ray T. P., Savini G., Ulbricht G. "Monte Carlo transmission line modelling of multilayer optical coatings for performance sensitivity of a dichroic filter for the ARIEL space telescope" (*in prep.*)

Acknowledgements

I would first of all like to thank Professor Tom Ray for giving me the opportunity to pursue this PhD in such a wonderful place as DIAS, and for all of the help over the past four and a half years. I would like to thank the post-docs in the DIAS MKIDs group, namely Colm, Gerhard, Oisín, Jack and Ivan, from whom I have learned a wealth of information about kinetic inductance detectors but also about pretty much everything else. You all managed to make DIAS a fun, and inspiring place to work. It was an absolute pleasure to have worked with you all. In particular I would like to thank Colm and Gerhard, who were there from the very beginning to provide me with help and guidance whenever I needed it. I would also like to thank my supervisor in TCD, Professor Plamen Stamenov, and everybody else in Trinity who have helped me throughout the course of this project. I would also like to thank the Science Foundation Ireland, for making this project possible, under grant 15/IA/2880, and Xilinx for supplying us with the RFSoC boards as part of their Xilinx University Programme.

I would like to thank all of the other PhD students in DIAS, with whom I have shared this experience; to Rubén and Maria K, the senior PhD students who were there to lead the way; to Mario, Anton, Camille, Maria M, Pearse, Aoife, Ciara, Brendan and Sam who have all been completing this journey at the same time as myself; and to Johnny and Shilpi who are following soon behind. Thank you to you all.

To Mario, the sole other PhD student in the MKIDs group, I could not have asked for a better person to have shared a laboratory with for four and a half years. It was great to have someone with whom I could always talk about work, and more importantly with whom I could always talk about anything other than work. I know that I have made a friend for life.

To everybody else in DIAS, it was great to have worked with you all, and to have

spent countless lunch and tea breaks having some of the most interesting, thought provoking conversations that I have ever had. You have all made DIAS the amazing place that it is. Thanks to Eileen for all of the help, and for keeping DIAS running in one piece.

I would like to thank Alex, Andrew, Conor and Rudy, with whom I lived over the past four and a half years, and with whom I have shared an abundance of great memories. Four sounder men I do not know, and I could not have picked a better group of people to have survived lockdown with.

To my parents, grandparents, brother and sister, and all of my family, thank you for everything, for supporting me for the past four and a half years, but more importantly for the past twenty seven and a half years, and for all of the years to come. Thank you all. To my parents, Marion and Fred, thank you for making me the person that I am today, for giving me a love of learning, for supporting me in all of my endeavours, and for being the greatest influences in my life. To my brother and sister, Dara and Ciara, thank you for being the best friends that anybody could ever have.

Finally, and most importantly, I would like to thank Edel, the love of my life. Thank you for all of the patience, understanding, support, kindness and love, and for changing my life for the better. You have been a constant source of strength and wisdom, and I could not have done any of this without you. Thank you from the depths of my heart.

Contents

List of Figures

List of Tables

List of abbreviations

ADC	Analogue to Digital Converter
ADR	Adiabtic Demagnetization Refrigerator
CASPER	Collaboration for Astronomy and Signal Processing and Electronics Research
CCD	Charge Coupled Device
CORDIC	Coordinate Rotation Digital Computer
CRANN	Centre for Research on Adaptive Nanostructures and Nanodevices
DAC	Digital to Analogue Converter
DIAS	Dublin Institute for Advanced Studies
DSP	Digital Signal Processing
FDM	Frequency Domain Multiplexing
FFT	Fast Fourier Transform
FIR	Finite Impulse Response
FWHM	Full Width At Half Maximum
FPGA	Field Programmable Gate Array
GSPS	Giga Samples Per Second
HEMT	High Electron Mobility Transistor
IF	Intermediate Frequency
KID	Kinetic Inductance Detector
LEKID	Lumped Element Kinetic Inductance Detector
LO	Local Oscillator
LPF	Low Pass Filter
LTD	Low Temperature Detector
MKID	Microwave Kinetic Inductance Detector
MMC	Metallic Magnetic Calorimeter
MSPS	Mega Samples Per Second
PFB	Polyphase Filter Bank

QCD	Quantum Capacitance Detector
ROACH	Reconfigurable Open Access Computer Hardware
STJ	Superconducting Tunnel Junction
VNA	Vector Network Analyser
T_c	Critical temperature
TCD	Trinity College Dublin
TES	Transition Edge Sensor
TLS	Two Level Systems
UVOIR	Ultraviolet/Optical/Infrared

1 Introduction

This thesis describes the development of microwave kinetic inductance detectors (MKIDs) and the readout electronics system which is needed to be able to analyse them.

It opens with a brief introduction with relevant background information, covering superconductivity, low temperature detectors, the kinetic inductance effect, microwave resonators, and finally, microwave kinetic inductance detectors, including their readout systems and fabrication process. Chapter 2 details some of the applications of MKIDs, including observational astronomy, particle physics, material science and security applications. Chapter 3 outlines the work done to build up the experimental setup needed to characterise the MKIDs which were fabricated as part of this project. Chapter 4 details the work done to develop code for analysing these MKIDs while Chapter 5 covers the work done developing firmware and software for the ROACH board which was used to measure measure photon pulses in the MKIDs. Chapter 6 outlines the process of selecting an FPGA board to develop as a next generation MKID system, while Chapter 7 covers the work done developing firmware and software for this board. Finally, Chapter 9 concludes and details plans for continuing this work in the future.

1.1 Superconductivity

Superconductivity, first discovered by Kamerlingh Onnes in 1911, is the phenomenon where some materials, known as superconductors, demonstrate zero

electrical resistance, and also expel any magnetic fields, when they are cooled below a certain temperature known as the critical temperature, denoted T_c (22). While ordinary conductors will display a decrease in resistance with decreasing temperature, for a superconductor the resistance abruptly drops to zero at the critical temperature.

In an ordinary conductor, the amount of phonons will decrease with temperature. This decrease in vibrations in the lattice causes a corresponding decrease in collisions between the lattice and the electrons, causing the resistance of the material to decrease. However, for a normal conductor, impurities in the lattice mean that even at 0 K, there will still be interactions between the lattice and the charge carriers. These interactions results in ordinary conductors showing a finite resistance, even at 0 K.

Bardeen–Cooper–Schrieffer (BCS) theory was the first theory to explain superconductivity. Its basic premise is that at temperatures below the critical temperature electrons become bound together forming Cooper pairs, which act as superconducting charge carriers, allowing current to flow through the superconductor undisturbed by interactions with atoms in the conductor (23) (22). This has the effect of the causing the material to show zero resistance. For temperatures significantly below T_C these Cooper pairs will be bound together with an energy, 2Δ, given by:

$$2\Delta = 3.528 k T_C \tag{1.1}$$

The operation of microwave kinetic inductance detectors, as is described in Sections 1.3 and 1.5 is based upon the breaking of these Cooper pairs in superconductors, forming unpaired electrons which are called quasi-particles.

1.2 Low Temperature Detectors

Low temperature detectors (LTDs) have, in recent years, become an area of interest in astronomy due to their ability to achieve low noise, broadband photon measurements. LTDs are photon detectors which operate at extremely low temperatures, usually below 1 Kelvin. These are in contrast to charge-coupled devices (CCDs) which are room temperature or liquid nitrogen cooled semiconductor based photon detectors that are the standard photon detector currently used in astronomy. One of the primary advantages of low temperature detectors (including Microwave Kinetic Inductance Detectors (MKIDs)) over CCDs is that they offer inherent energy resolution. This energy resolution is given by:

$$R = \frac{E}{\Delta E} \tag{1.2}$$

In Equation 1.2, E is the energy of the photons being detected, while ΔE is the smallest difference in energy between two photons which the detector can differentiate.

Due to the extremely low band gap of superconductors, for example on the order of $10^{-4} eV$ for some, a single optical photon can generate on the order of 10,000 quasi-particles by breaking the Cooper pairs of the superconductor. This large ratio of charge-carriers per photon allows the energy of optical, and even near/mid-infrared photons to be resolved. In contrast, semiconductors have a much larger band gap, for example 1.1 eV for Silicon, meaning that the number of electrons excited from an incident optical photon is roughly 2 or 3. This low, almost unity ratio means that it is not feasible to differentiate photons of differing energies.

Of course, with the use of dispersive optics such as gratings or prisms, or selective

chromatic filtering, the photon energy spectrum of any signal can be determined. However, chromatic filtering reduces the efficiency of any broadband measurements being carried out, and dispersive techniques typically result in one dimension of the detector array being required for the spectroscopy, making it difficult to carry out spatio-spectral imaging in any efficient manner. Furthermore, the relatively large band gap of semiconductors like silicon result in them having a fundamental cut-off in terms of the lowest energy photons they can detect, typically in the near-infrared. However, it must be noted that there exists semiconductors such as mercury cadmium telluride (MCT) whose bandgaps can be tuned down to 0 eV. For MCT this is achieved by varying the amount of cadmium present (24).

The remainder of this section gives a brief explanation of some other low temperature detector technologies, as opposed to MKIDs, which are the focus of the remainder of this thesis. Note that these descriptions are not meant to be exhaustive, and only to provide some background information on low temperature detectors.

Low temperature detectors use one of two main modes of operation: thermal detection or athermal detection. Thermal detectors, such as transition edge sensors (TESs) and metalic magnetic calorimeters (MMCs), work on the principle that incident photons on the detector's absorber will cause an increase in its temperature. The increase in temperature is proportional to the energy of the incident photon, allowing the photon energy to be resolved.

Thermal detectors can be further divided into the categories of calorimeters and bolometers. Calorimeters measure single, high energy photons which cause a large change in temperatures, while bolometers measure the power of the incident flux of low energy photons. A photon flux of a certain power will cause the temperature of the absorber to stabilize at a certain value, from which the power of this incident flux can be resolved (5).

TESs are based on superconducting films which operate in the transition region

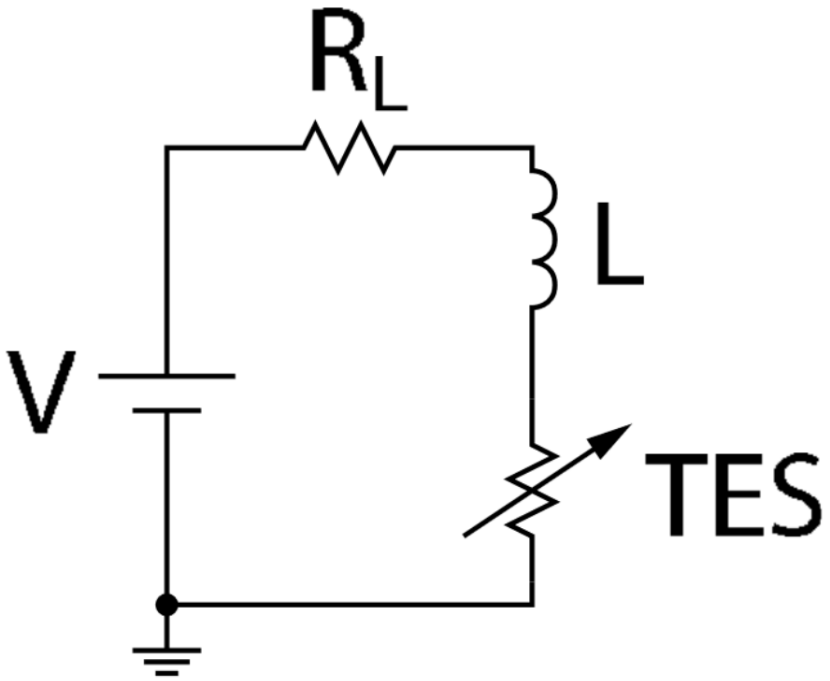

Figure 1.1: Model of a TES circuit, given as a bias voltage in series with a resistance, an inductance and the variable resistance of the TES. The resistance of the TES will be somewhere between its normal value and zero, depending on its temperature, which itself is dependent on the incident photons. (1)

between their superconducting and normal states, giving them a resistance between zero and its normal resistance which is temperature dependent. Thus, photons incident on the absorber will raise the temperature of the film, causing a measurable increase in the resistance (1). The equivalent circuit of a TES is shown in Figure 1.1 and an example of the temperature dependence of a superconducting film used as a TES is shown in Figure 1.2.

MMCs are based on a paramagnetic material in a weak magnetic field which is coupled to an absorber in order to act as a temperature sensor. Photons striking the absorber cause an increase in its temperature, decreasing the magnetization of the paramagnetic material. Photon energy is resolved by monitoring the change in the magnetic field (2). A diagram showing the operating principle of an MMC is shown in Figure 1.3.

Conversely, athermal detectors, instead of measuring the temperature change due to incident photons, measure the change in the number of quasi-particles that are

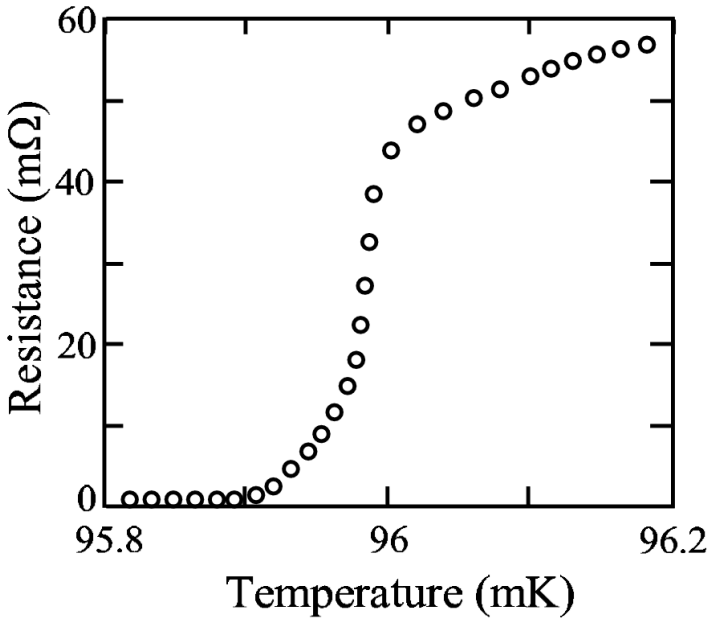

Figure 1.2: Transition profile of a superconducting film in a TES, showing the resistance of the film increasing from zero with increases in temperature. This change in resistance with respect to temperature, which is itself dependent on the energy of the incident photons is used to resolve the energy of these photons. (1)

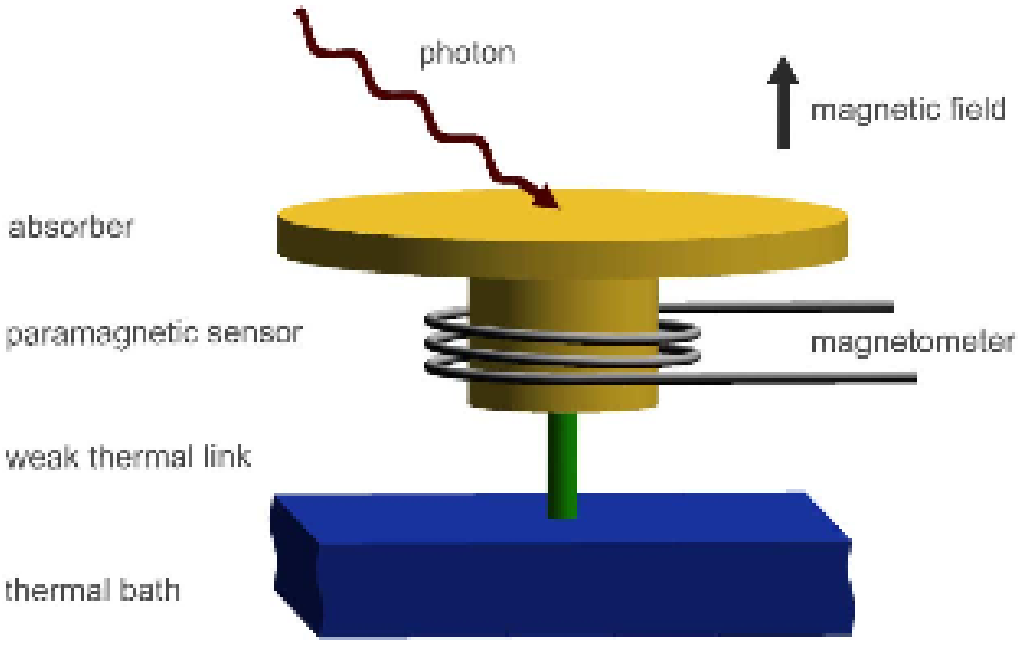

Figure 1.3: Drawing of an MMC showing their operating principle. Photons which strike the absorber cause a change in the temperature of the paramagnetic sensor, which decreases its magnetization. This change in magnetization can be detected by the magnetometer, and the energy of the photon can be resolved from this change. (2)

generated by photons striking a superconductor. Photons striking the superconductor break Cooper pairs, forming quasiparticles. Cooper pairs (25) are pairs of electrons which become bound together when a superconductor is cooled below its critical temperature, or T_c. It is these compound Bosons, which experience no scattering, that give rise to the superconducting effect. Superconducting Tunnel Junctions (STJs), Quantum Capacitance Detectors (QCDs), and Microwave Kinetic Inductance Detectors (MKIDs) are all examples of athermal low temperature detector technologies. STJs are made up of two superconducting layers, separated by an insulating layer, forming a Josephson junction. When photons strike the superconducting layers, Cooper pairs are broken and quasiparticles are formed. These quasiparticles tunnel through the insulating layer of the Josephson junction, forming a measurable increase in current. This increase in current is proportional to the photon energy, allowing the photon energy to be determined by measuring the tunnel current (26) (27).

The basis of QCDs are superconducting devices called Single Cooper Pair Boxes (SCBs). This a superconducting island coupled to a superconducting absorber by a pair of Josephson junctions. Radiation striking the absorber breaks Cooper pairs, forming quasiparticles. When these quasiparticles tunnel through the Josephson junctions to the superconducting island, they change its capacitance. This island forms part of a resonator circuit. The resonant frequency of an LC resonator is given by:

$$f_0 = \frac{1}{\sqrt{LC}} \tag{1.3}$$

By Equation 1.3, a change in the island's capacitance will cause a change in the frequency of the resonator. This frequency is monitored continuously, and from this, the photon energy is resolved. (3) Figure 1.4 displays a schematic of a QCD (3).

Finally, Microwave Kinetic Inductance Detectors (MKIDs) are low temperature

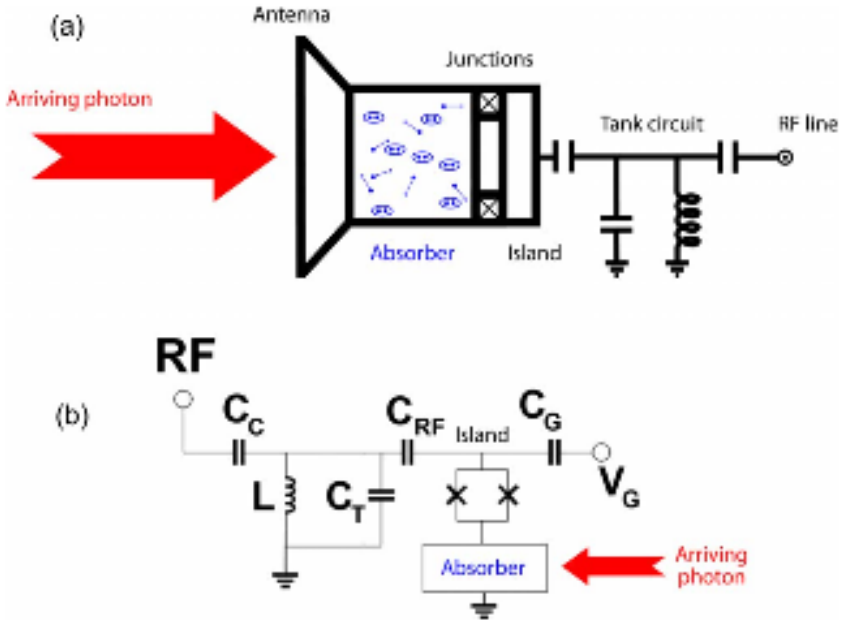

Figure 1.4: Cartoon schematic (a) and circuit diagram (b) of a QCD. Photons striking the absorber break Cooper pairs forming quasi-particles which tunnel through the Josephson junctions. This causes a measurable change in the capacitance of the superconducting island from which the photon energy can be resolved (3).

detectors based on superconducting LC resonators and the kinetic inductance effect. For each of the above described LTDs, unfortunately their inherent energy resolving capability, and their ability to detect low-energy photons (down to sub-mm) often comes at the cost of difficulties when trying to multiplex to large-format arrays. However, as will be described in this introduction, MKIDs offer a path to combining the sensitivity of LTDs with a relatively straight forward multiplexing strategy. As such, MKIDs are the most promising novel detector technology for achieving very large-format arrays of photon-counting, energy-resolving detectors. For these reasons, they were selected for this research, and are described in the remainder of this thesis. First though, their basis of operation is explained in more detail.

1.3 The Kinetic Inductance Effect

By definition, a superconductor below its critical temperature, T_c, has zero resistance at DC frequencies, $\sigma_{dc} \rightarrow \infty$ as $f \rightarrow 0$. This is because at cryogenic

temperatures the electrons in the superconductor form Cooper pairs, which are not effected by scattering as they move through the superconductor as a current. However, at non zero frequencies, the finite inertia of the charge carriers manifests as an inductance, which opposes an alternating electric field. This is the kinetic inductance effect, and it is described by the Drude model (17) (28).

The Drude model describes the complex conductivity of a conductor with real part σ_1 and imaginary part σ_2 as:

$$\sigma = \sigma_1 + j\sigma_2 = \frac{\sigma_0}{1+\omega^2\tau^2} - j\omega\tau\frac{\sigma_0}{1+\omega^2\tau^2} \tag{1.4}$$

where, τ is the collision time, $\omega = 2\pi f$, $j = \sqrt{-1}$, and σ_0 is the DC conductivity and is given by,

$$\sigma_0 = \frac{ne^2\tau}{m} \tag{1.5}$$

where, n is the number of charge-carriers, e is the elementary charge, and m is the electron mass. σ_1 and σ_2 are the real and imaginary parts of the conductivity.

As a perfect inductor has an impedance $Z_L = j\omega L$, it will have a conductance $\sigma_L = \frac{1}{j\omega L}$ or $\frac{-j}{\omega L}$. As this conductance has no real part, this means that changes in the kinetic inductance will manifest as a change in the imaginary part of the conductors conductance, σ_2. An increase in kinetic inductance will cause σ_2 to become more negative.

Typically, the collision time for a metallic conductor, τ, is of the order of $10^{-14}s$ meaning that $\omega^2\tau^2 << 1$, and $\sigma_2 \to 0$. Therefore, it is apparent that for a normal conductor, the kinetic inductance value is negligible as the imaginary part of Equation 1.4 tends to zero. It is also clear that as $f \to 0$, σ reduces to σ_0.

However, in a superconductor, there are no collisions meaning that $\tau \to \infty$. This gives:

$$\sigma_1 = \frac{ne^2}{\frac{m}{\tau} + m\omega^2\tau} = 0 \tag{1.6}$$

and,

$$\sigma_2 = -\frac{ne^2\omega}{\frac{m}{\tau^2} + m\omega^2} = -\frac{ne^2}{m\omega} \tag{1.7}$$

Thus, for a superconductor, the real part of the complex impedance disappears while the imaginary part, in which an inductance will appear, dominates.

Cooper pairs will be broken, and quasiparticles formed when the superconductor is struck by a photon with an energy greater than 2Δ, where Δ is the bandgap of the superconductor.

The number of quasiparticles generated, N_{qp} can be given by:

$$N_{qp} = \frac{P_{opt}\eta\tau_{qp}}{\Delta} \tag{1.8}$$

Here, P_{opt} is the optical power, η is the efficiency of converting photons to quasiparticles, and τ_{qp} is the quasiparticle lifetime. The corresponding change in the quasiparticle carrier density, n_{qp}, can be calculated using N_{qp} and the geometry of the absorber. This results in an increase in the total number of quasiparticles, n, which by Equation 1.7 causes σ_2 to become more negative, meaning that this gives an increase in kinetic inductance. As the quasiparticles recombine into Cooper pairs, the kinetic inductance and, thus, impedance return to their original state. This is later used in Section 1.4 to illustrate how this change in kinetic inductance will cause a change in the frequency of an MKID.

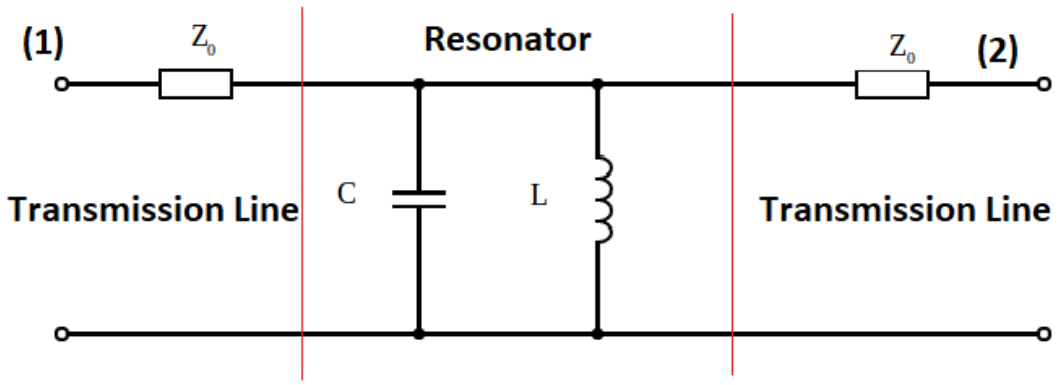

Figure 1.5: LC resonant circuit consisting of an inductor and capacitor in parallel, connected to a pair of feedlines, each with impedance Z_0.

1.4 Microwave Resonators

Having already discussed the kinetic inductance effect, the second topic which needs to be discussed in order to understand MKIDs is the physics of resonant circuits.

An MKID can be thought of as a parallel LC tank circuit connected to two feedlines of impedance Z_0 (29). Note that this model presumes that the resistance due to unpaired electrons, created by broken Cooper pairs, is negligible. A diagram of such a circuit is shown in Figure 1.5.

To clarify, here L denotes inductance, C denotes capacitance, Z denotes impedance, ω denotes frequency in $rads^{-1}$ and $j = \sqrt{-1}$. The total impedance through a parallel LC tank circuit can be described by adding impedances in parallel reciprocally to give:

$$\frac{1}{Z} = \frac{1}{Z_L} + \frac{1}{Z_C} \tag{1.9}$$

Where the impedance of the inductor is:

$$Z_L = j\omega L \tag{1.10}$$

and the impedance of the capacitance is

$$Z_C = \frac{1}{j\omega C} \tag{1.11}$$

This gives:

$$\frac{1}{Z} = j\omega C + \frac{1}{j\omega L} \tag{1.12}$$

$$\implies Z = \frac{j\omega L}{1 - \omega^2 LC} \tag{1.13}$$

To simplify the algebra, this is then rewritten in terms of s, where $s = j\omega$,

$$\implies Z = \frac{sL}{1 + s^2 LC} \tag{1.14}$$

Resonance occurs at the impedance's minimum point, meaning that the circuit will resonate when $dZ/ds = 0$, giving,

$$\frac{dZ}{ds} = \frac{L(1 + s^2 LC) - sL(2sLC)}{(1 + s^2 LC)^2} = 0 \tag{1.15}$$

$$\implies (1 + s^2 LC)L = sL(2sLC) \tag{1.16}$$

$$\implies s^2 LC = 1 \tag{1.17}$$

$$\implies s = \pm\frac{1}{\sqrt{LC}} \tag{1.18}$$

$$\implies \omega = \frac{\pm j}{\sqrt{LC}} \tag{1.19}$$

The square root term is taken to be the resonant frequency ω_0. This gives a value for the resonant frequency of a parallel LC tank circuit:

$$\omega_0 = \frac{1}{\sqrt{LC}} \tag{1.20}$$

It is shown in Section 1.3 that a photon striking a superconductor will cause an increase in its inductance by the kinetic inductance effect. Thus, by Equation 1.20, a photon striking the inductor of an MKID will cause an increase in its inductance, and thus a decrease in its frequency. As the quasi-particles recombine the inductance, and thus the resonant frequency will return to their original states. This is operating principal of an MKID.

The energy stored in the parallel LC tank circuit is given by:

$$E = C < V^2 > \tag{1.21}$$

Here, <> refers to averaging over the period of a full oscillation. This is the total energy stored in both elements of the circuit, the inductor and the capacitor.

The power dissipated in the circuit, P, across a full cycle is:

$$P = \frac{< V^2 >}{R} \tag{1.22}$$

Here, R is the resistance of the circuit, which comes from the transmission lines. E can be related to P by:

$$\frac{dE}{dt} = -P = -\frac{E}{\tau} \tag{1.23}$$

τ is the time constant of the circuit, which is the time taken for the energy in the circuit to decrease to $1/e$ of the initial value.

This gives:

$$\tau = -P = \frac{E}{P} \tag{1.24}$$

$$\implies \tau = \frac{C < V^2 >}{\frac{< V^2 >}{R}} \tag{1.25}$$

$$\implies \tau = RC \tag{1.26}$$

The total quality factor (Q) of a resonator describes how much energy it loses per oscillation. The quality factor of the circuit can be written in many forms, including as its resonant frequency multiplied by its time constant, $Q = \omega_0 \tau$. The total resistance of the circuit being $R = \frac{Z_0}{2}$ gives(29):

$$Q = \omega_0 RC = \frac{\omega_0 Z_0 C}{2} \tag{1.27}$$

Thus, Equations for the resonant frequency, ω_0 and quality factor, Q, of a parallel LC tank circuit have been derived. These are later used in Section 4.3 to derive an equation for the forward transmission coefficient, S_{21}, of an LC tank circuit. Measurment data is then fitted to this equation and from this fit ω_0 and Q are obtained.

1.5 Microwave Kinetic Inductance Detectors

Microwave kinetic inductance detectors are photon detectors based on superconducting LC resonators, capable of detecting individual photons with inherent energy resolution.

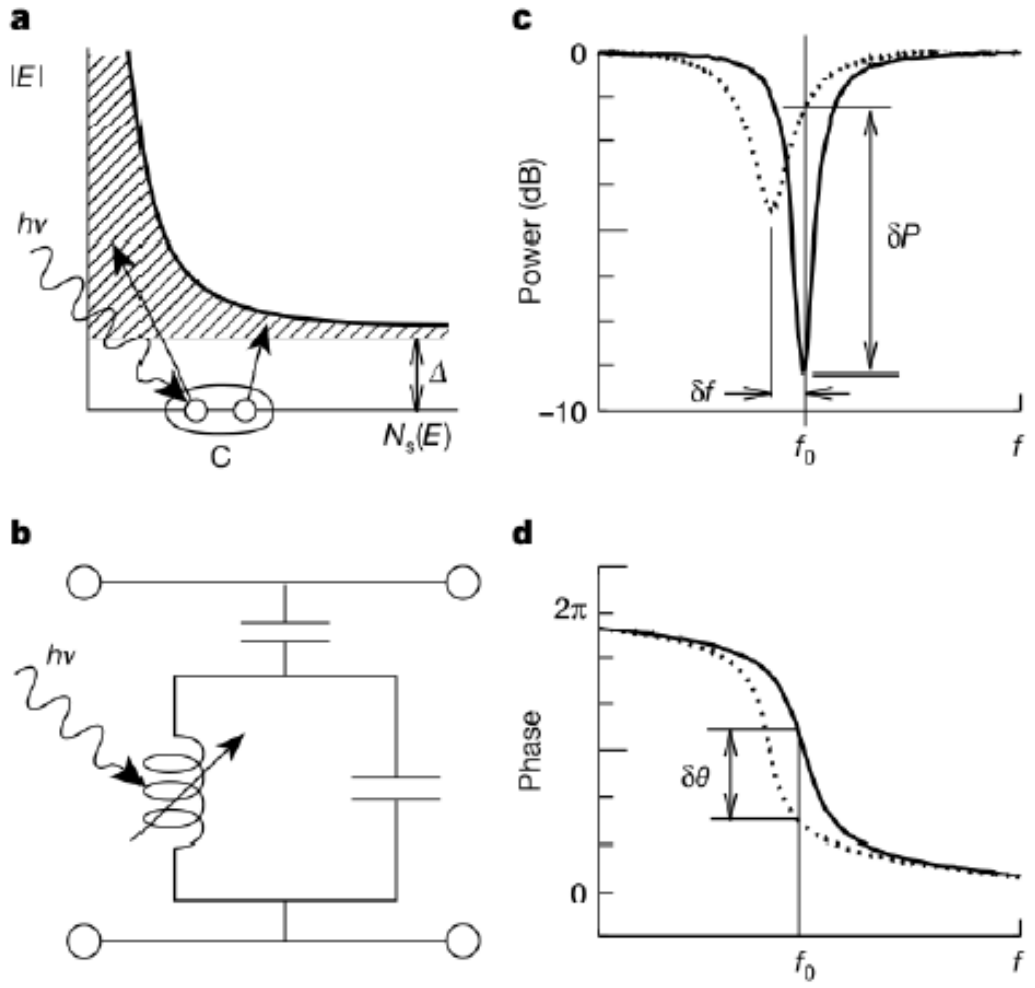

Figure 1.6: MKID detection principle from Day et al. (4). a) shows a photon with energy $h\nu$ striking a superconducting film breaking Cooper pairs forming quasi-particles. b) is the lumped element model of an MKID, showing the inductor as the absorbing element, whose kinetic inductance is dependent on the incident photons with energy $h\nu$. c) shows the transmission ($|S_{21}|$) of a single MKID, showing how the the resonant frequency and amplitude shift when a photon strikes the MKID. It must be noted that this effect is greatly exaggerated in this illustration. d) shows the phase response of an MKID, also showing the shift in phase response when a photon strikes the MKID. Similarly to in c), this effect is exaggerated in this illustration.

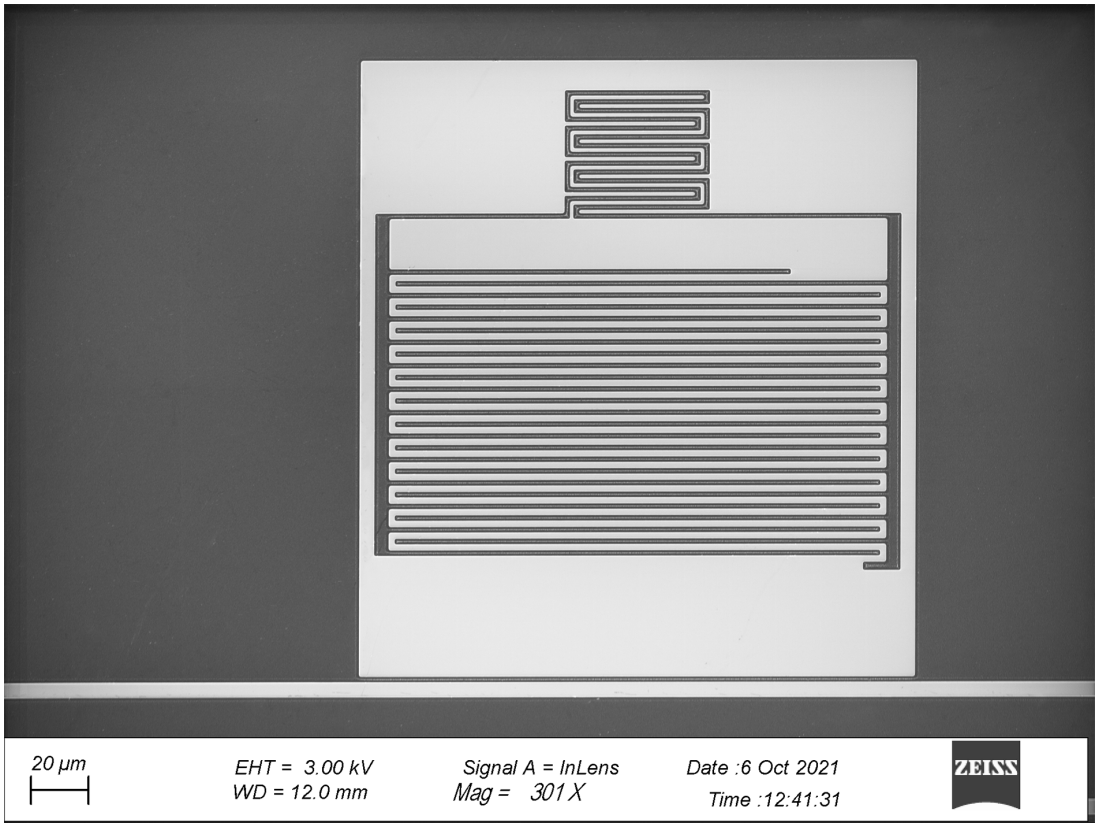

Figure 1.7: Sample MKID fabricated at CRANN for this project showing meandered inductor at top and interdigitated capacitor at bottom. To read out such an MKID a bond wire needs to be added to couple the MKID to the feedline. This photograph was taken using a scanning electron microscope.

Figure 1.6 illustrates the detection principle of microwave kinetic inductance detectors (4). The MKID's inductor acts as the detector's sensitive area, absorbing incident photons. When a photon of energy greater than 2Δ, where Δ is the superconducting bandgap, strikes the inductor, Cooper pairs are broken and form quasiparticles as was shown in 1.3. Since the kinetic inductance L_k is inversely proportional to the number of charge-carriers, the sudden decrease in the number of Cooper pairs results in an increase in L_k, and a related decrease in the resonant frequency (ω_0) of the resonator, as per Equation 1.20.

By driving the resonator with a single tone of frequency f_0 (matching the resonant frequency of the resonator), and monitoring the tone closely, any shift in the MKID's resonance will be measurable. Namely, when an incident photon causes the resonant frequency of the resonator to shift away from that of the probe tone driving it, the tone can no longer drive it efficiently and the signal line-throughput increases rapidly. The probe tone's amplitude and phase are both measurably affected, and the changes in both are proportional to the energy of the incident photon, $h\nu$.

While in principle one or both of amplitude and phase can be monitored to resolve the photon energy, in practice the phase measurement provides a stronger signal-to-noise ratio (SNR). Additionally, the phase measurement is only feasible if using complex I/Q signals, so almost all MKID arrays employ this I/Q readout scheme. (20) (30) (31) (32)

A sample MKID is displayed in Figure 1.7. By designing an array of MKIDs, each with a slightly different planar geometry and corresponding varying values for L and/or C, one can create an array of resonators with a unique resonant frequency for each pixel. This allows multiple MKIDs to be driven and monitored by a single feedline, with minimal crosstalk between pixels.

The total quality factor of an MKID, Q, can be described in physical terms as a measure of the resonator's full width at half maximum (FWHM), here written as

$\Delta\omega$ relative to its central frequency:

$$Q = \frac{\Delta\omega}{\omega_0} \tag{1.28}$$

This total Q can be described in terms of the internal quality factor, Q_i, and the coupling quality factor Q_c:

$$\frac{1}{Q} = \frac{1}{Q_i} + \frac{1}{Q_c} \tag{1.29}$$

While the total quality factor of a resonator describes how much energy it loses per oscillation, Q_c accounts for the loss through coupling to the feedline, while Q_i is responsible for all other loss.

S_{21}, the forward voltage gain scattering parameter, for a single MKID resonator, measured through the whole system, including cabling and amplifiers, can be shown to be given by the following (17):

$$S_{21}(\omega) = ae^{-2\pi if\tau}[1 - \frac{Q/Q_c e^{i\phi_0}}{1 + 2iQ(\frac{\omega-\omega_0}{\omega)}}] \tag{1.30}$$

Here, a is a coefficient depending on the transmission properties of the transmission line, and describes the gain and phase shift which it introduces, while τ describes the path length of the cables. ϕ_0 is the phase angle between the IQ loops centre point and the x-axis of the IQ plane. S-parameters are further explained in Section 4.1.

The transmission of an MKID, given by Equation 1.30, describes a dip in amplitude, and a shift in phase of π relative to the resonant frequency, as in Figure 1.6. Moreover, when plotted instead on the complex plane as IQ data, this describes a loop, as shown in Figure 1.8, where the distance to the origin denotes the amplitude of the signal and the angle relative to the positive horizontal axis denotes

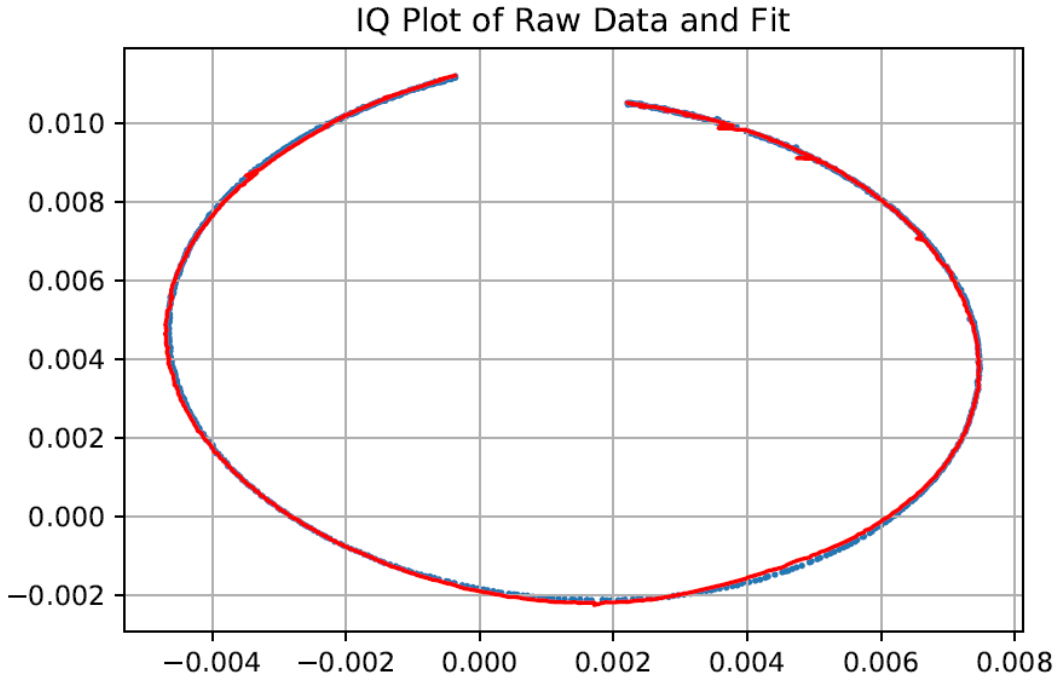

Figure 1.8: Sample IQ loop of an MKID measured as part of this project. Raw data is shown in blue and a fit is shown in red. This process is covered in Chapter 4.

the phase of the signal.

If monitoring the IQ data at a single frequency, just below the resonant frequency of the MKID, a photon striking the detector will cause the signal to move along this track in the IQ loop, before settling back at its original position once the Cooper pairs recombine. If the phase value is calculated with respect to the centre of this IQ loop, and the MKID is monitored at its resonant frequency, then the signal will be able to move through $\pi radians$, or 180°.

1.5.1 Important Parameters of KID Resonators

There are a range of important parameters that are used to quantify and qualify the performance of singular MKID devices, as well as complete MKID array instruments. These measurable parameters include quantum efficiency, pixel yield, time resolution $\Delta\tau$, energy resolution ΔE and cost per pixel. Some of these are interrelated, and may depend strongly on a single controllable parameter, such as resonator Q-factor. However, some are more weakly-coupled to others and may

even stand-alone on a single condition such as material choice.

The state-of-the-art ultraviolet/optical/infrared (UVOIR) MKIDs are already outperforming CCDs on some of these parameters. However, MKIDs are lagging behind semiconductor detectors on others. As such, there is a large parameter space open for the improvement of MKIDs for UVOIR astronomy and astrophysics applications.

Pixel Yield

The pixel yield of any detector array is defined as the fraction of usable pixels in a fabricated array, relative to the number of detectors in the designed array.

One factor which determines the total pixel count of an MKID array is the operating frequencies of the readout electronics used to read out the array. If the room temperature electronics are restricted to a certain frequency band, then the detectors must also be restricted to the same band. The frequencies which can be used are limited by the maximum operating frequency of the electronics, as this determines which frequency octave can be used. A frequency octave is a frequency band such that the maximum frequency is double that of the minimum frequency e.g. 4 - 8 GHz. An array must be limited to a single frequency octave in order to prevent crosstalk between resonators with resonant frequencies which are multiples of each other. Otherwise, there will be interference between signals which are at harmonics of each other. Similarly, the frequency octave which can be used is also determined by the operating frequencies of the amplifiers which are used, meaning that the frequencies of the MKIDs in the array must correspond to the operating frequency of the room temperature and low temperature electronics.

Within this band, the total pixel count is further confined by the frequency spacing between each pixel. When resonators are manufactured too close to each other in the frequency domain they become unusable due to overlapping and cannot be distinguished from each other by the electronics. While resonators are designed to

have ample frequency spacing between adjacent pixels, imperfections in the fabrication process cause the actual resonant frequency of MKIDs to stray from the design value. The minimum possible spacing between pixels in an array is governed by the Q factor of the resonators, as well as by the number of frequency bins used in the FFT which is applied by the readout electronics. This number of FFT bins is limited by the FPGA logic of the readout system, as well as by the desired sampling rate. Based on the current state-of-the-art, the minimum allowable frequency spacing between detectors is typically on the order of 500 kHz, though pixels are usually designed with a spacing of > 1 MHz (5).

Because the operating frequencies cannot be increased for a given readout system, the only way to increase the pixel count is by reducing the number of overlapping pixels by optimizing the fabrication process. This can be done by experimenting with more suitable superconductors, such as PtSi, WSi2, Os, PdSi, NbSi, or TiN,/Ti/TiN. Furthermore, using better simulations of the resonators may allow for a better understanding of the superconductor's kinetic inductance, and thus, precisely where its resonance will lie.

Energy Resolution

Another key parameter which is used to describe the performance of MKIDs is their energy resolution. Already described in Section 1.2, the energy resolution of an MKID is given by $R = E/\Delta E$, and describes the ability of MKIDs, or indeed any optical detector, to differentiate between different wavelengths of light.

Current MKIDs show energy resolutions of $R = E/\Delta E = 8 - 12$ for optical light, thought energy resolutions of upto 52 have been shown (33). The energy resolution of an MKID is determined by calibrating the instrument with a laser of known wavelength, λ. The phase pulse heights in the transmission of the MKID as a result of these photons are then plotted as a histogram. This histogram can be fitted to a Gaussian, as in Figure 1.9, and the full width at half maximum (FWHM) is taken to be ΔE. Thus, the energy resolution can be calculated.

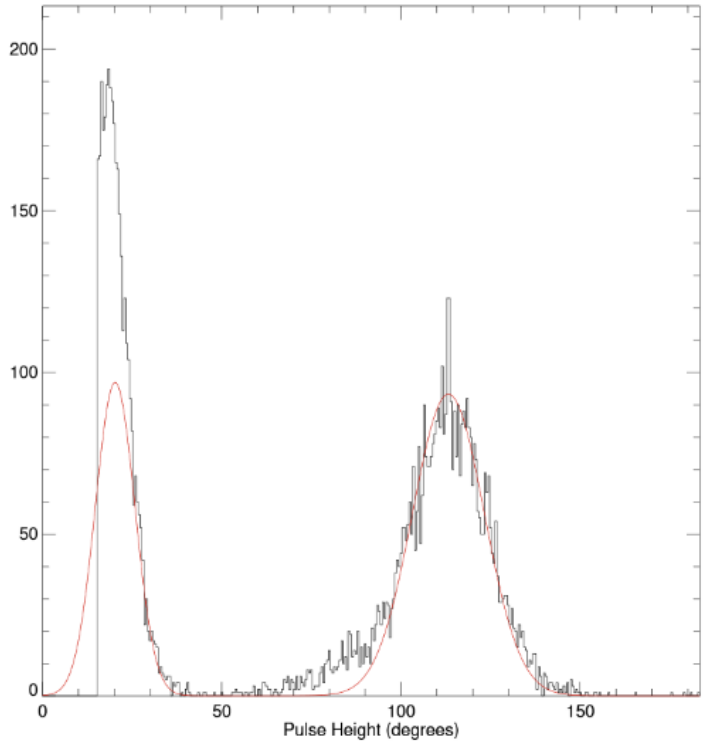

Figure 1.9: Pulse height histogram from Szypryt (5). The pulse heights of a range of photon pulses generated by photon source with known wavelength are plotted as a histogram. The energy resolution of these MKIDs can then be calculated by taking the full width at half maximum (FWHM) of the peaks in the histogram. The peak at 110°is the pulses caused by a 980 nm source, while the lower pulses is caused by false counts caused by excess thermal radiation.

Time Resolution

Another important parameter when discussing MKIDs, and one of their chief advantages, is their fast time resolution. Typically, we implement a time resolution of roughly $1\mu s$, but this can be further reduced at the cost of more FPGA resources, or by having less pixels per feedline.

This allows for the arrival time of single photons to be accurately tracked and is of interest in high time resolution astronomy, such as in the observation of millisecond optical pulsars and real-time tracking and removal of speckles, which is highly valuable for direct imaging of exoplanets (6).

Quantum Efficiency

Quantum efficiency is the percentage of light, at a given wavelength, that an optical detector absorbs. This is important when detecting extremely faint objects, such as in astronomy, where it is important to maximise the number of photons detected.

In an MKID, the inductor acts as the photon detection element. Thus, any photons which strike elsewhere in the detector will cause a decrease in its quantum efficiency. Thus, the quantum efficiency of an MKID array can be improved by coupling the array to a microlens array, increasing its fill factor. The fill factor is the fraction of the chip's area which can be used to collect light. Without using a microlens array, the only part of the chip collecting light would be each individual detectors' inductor. This array of lenses focuses incident light to the detector's inductor, thus reducing the amount of light striking elsewhere on the detector, thus increasing the quantum efficiency.

However, whilst this may increase the detectors fill factor, not all of the photons which strike the inductor will be absorbed. Because of this, it is important to fabricate the detector out of a material which is not reflective at the wavelength of interest. For example, aluminium is reflective at optical wavelengths and is

therefore not ideal for optical astronomy.

1.6 MKID Readout

A primary advantage which MKIDs have when compared to other low temperature detectors, such as TESs, is that they require relatively simple cryogenic electronics, needing only a high electron mobility transistor (HEMT) amplifier and a feedline. However, this simplicity at low temperatures comes at the cost of requiring complex room temperature electronic systems in order to readout arrays of MKIDs.

In order to read out large arrays of MKIDs, a readout system needs to be developed that can separate the entire frequency span into unique, non-uniform channels for each resonator, and subsequently monitor these channels for photon events. Multiple readout systems for MKIDs have previously been developed elsewhere, but each has been limited by several factors, such as the speed of available data converters at the time, high power consumption, high mass and volume, and have been very costly (per pixel). As such, if MKIDs are to be progressed toward array formats of 100 K pixels or more, a more compact, lower power, affordable readout solution will be essential. Furthermore, if large-format arrays of MKIDs are ever to be used for space-based applications, power consumption and mass/volume minimisation will be paramount. As such, the focus of this research will be the development a more affordable, low-power, compact readout system for the next generation of MKID camera. (30) (34) (32) (31)

Due to the intense signal processing needed to readout a large array of MKIDs, digital signal processing tools used for radio astronomy applications have been adapted to also be used for MKIDs. Because of this, technology developed by the Collaboration for Astronomy Signal Processing and Electronics Research (CASPER), which develop open source hardware and firmware for radio astronomy instruments, has been adapted to read out large arrays of MKIDs. (35) (6)

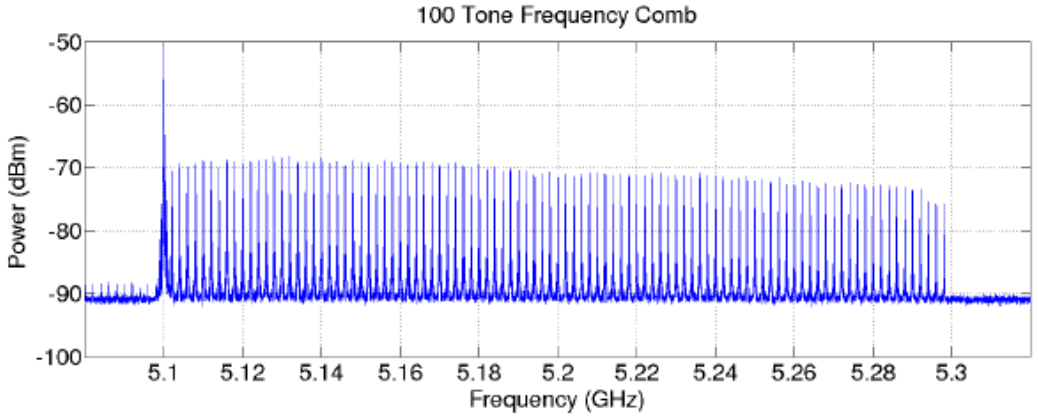

Figure 1.10: 100 tone frequency comb generated by the ROACH setup used in this project. A 100 tone frequency comb generated at frequencies from 2 MHz to 200 MHz is upmixed with the local oscillator frequenucy at 5.1 GHz, giving the waveform shown. This process is covered in Chapter 5.

1.6.1 Operation

MKID readout systems use frequency domain multiplexing (FDM) to differentiate between each of the pixels in the array. In FDM the total frequency span of a signal is divided in to a series of sub-bands which can be monitored independently. Here, this frequency span is equivalent to the frequency octave for which the the MKIDs are designed.

The first step in an MKID readout system is to generate a frequency comb of tones at low frequencies ($f_{baseband}$), typically MHz frequencies, using I/Q data by a two-channel digital to analogue converter (DAC). This frequency comb is then upmixed with a local oscillator (f_{LO}) to create a frequency comb at higher frequencies, the frequencies of the resonators in the MKID array (f_{tone}).

This up-mixing can be carried out in such a manner as to either add the baseband frequencies to the local oscillator frequency, or subtract them them from it (see Equation 1.32). In this way, both the upper and lower-sidebands can be utilised for readout bandwidth. In other words, this I/Q mixing allows both positive and negative frequency values within the Nyquist band to be employed, thus doubling the available bandwidth of a given DAC/ADC pair.

$$f_{tone} = f_{LO} \pm f_{baseband} \tag{1.31}$$

In order to monitor this data, the tones coming out of the ADR must be downmixed back to baseband frequencies:

$$f_{baseband} = f_{tone} - f_{LO} \tag{1.32}$$

These baseband frequencies must then be digitized by a pair of analogue to digital converters (ADCs). This digitized data can then be read in by a field programmable gate array (FPGA), which can perform the necessary digital signal processing (DSP). FPGAs are programmable integrated circuits (ICs) consisting of an array of logic blocks and interconnects.

Channelization

The first step in this DSP is for the digitized data to be channelized. This is the process of dividing the full frequency band into a series of sub-bands, with one for each resonator in the array. Each of these channels are then individually monitored for photons. This process typically takes place in two stages; coarse channelization and fine channelization. This is done because the pixels are not equally spaced in frequency, and also to improve the frequency response of the channels.

The coarse channelization divides the band into equally spaced channels, each containing one, zero or multiple tones. Fine channelization then further divides these bands into finer frequency bands, with only one tone, occupying the centre of the band, as in Figure 1.11. (6)

The coarse channelization stage is achieved using a polyphase filter bank (PFB). A PFB is a computationally efficient way of separating an input signal into individual frequency bands (7). A PFB is also used to ensure that these frequency bands maintain a flat frequency response (see Figure 1.13). In a PFB the input signal is

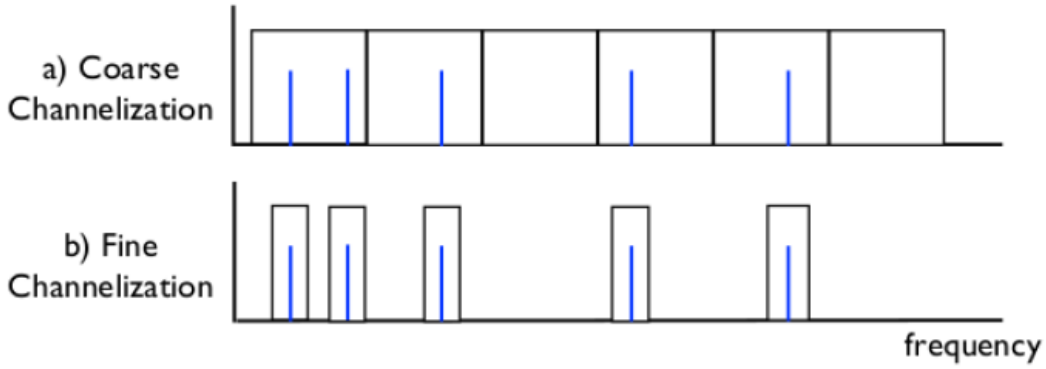

Figure 1.11: Coarse and fine channelization process described by Strader (6). The first step of channelization divides the bandwidth in a series of equally spaced channels, while the second stage takes any channel with a tone in it, and generates a unique fine channel for these tones.

divided into m blocks of identical length, P. These m blocks are then multiplied with the intended window function (7). These m time chunks are then summed up and fed into an FFT resulting in the coarse channelization. An FFT is an algorithm which achieves a digital Fourier transform (36). Thus, this PFB process divides the input signal into a series of equally spaced channels such that each channel will contain one, none or multiple tones (6).

Without the filtering step in the PFB an FFT bin would not have a flat frequency response, and would have significant side lobes. The PFB used in this project has the effect of flattening the frequency response and suppressing these side lobes. This prevents signals which are not at the centre of an FFT bin from being attenuated and also prevents leakage from signals in adjacent bins via the side lobes. The effect of this is shown in Figure 1.13. This could be quantified by calculating the sidelobe level (SLL) of one of these FFT bins, with and without using the filtering step. SLL is the ratio of the power of the main lobe to that of the side lobes.

The window functions being used in the PFB are bandpass finite impulse response (FIR) filters. A bandpass filter will pass a certain span of frequencies, defined by its cutoff frequency, and will block all frequencies outside of this span. An FIR filter is

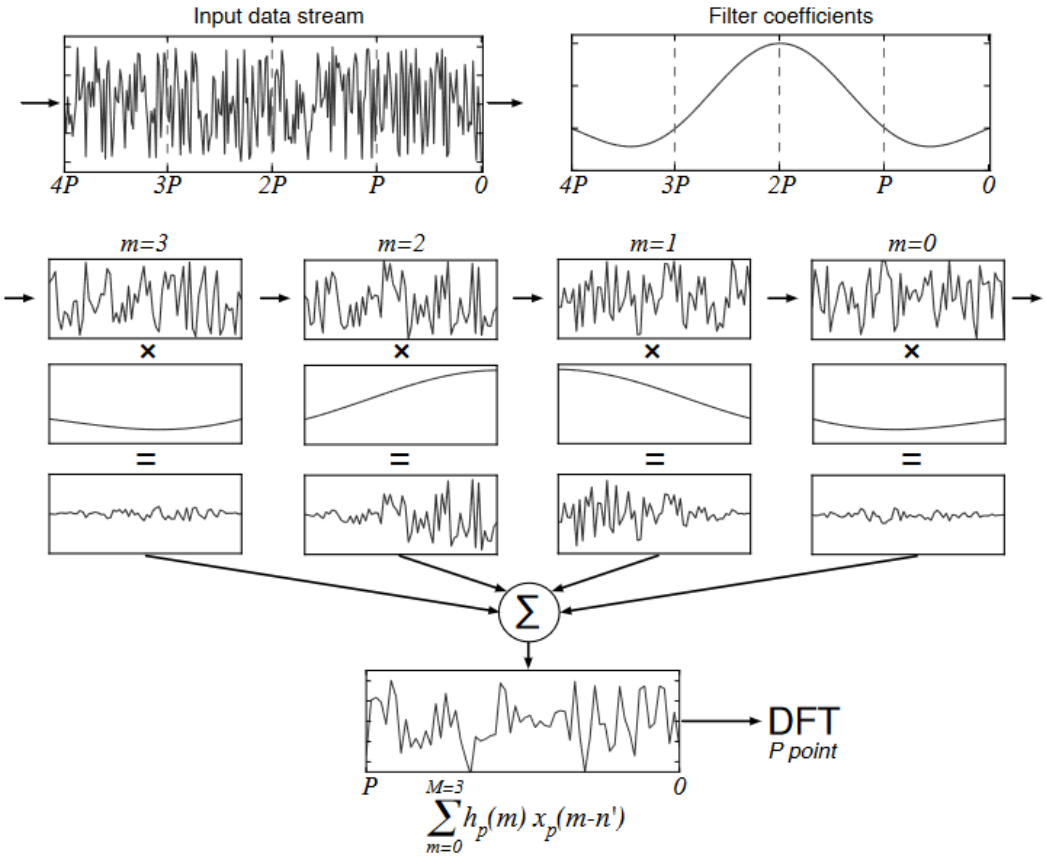

Figure 1.12: Diagram showing the operation of a polyphase filter bank (PFB) taken from Price (7), consisting of dividing the input signal into m chunks of size P which are each individually multiplied by the window function, summed up, and passed to an FFT.

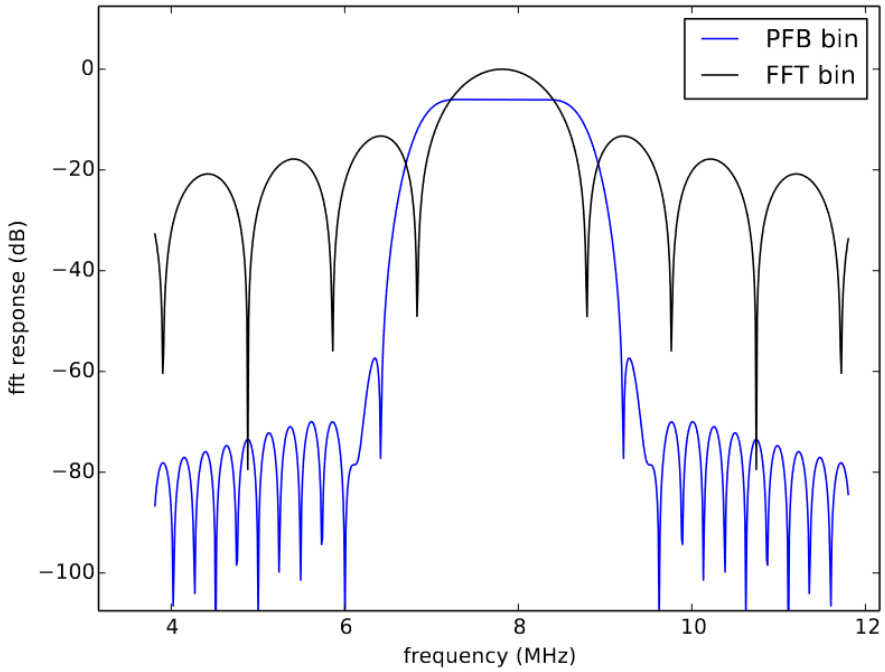

Figure 1.13: The frequency response of a typical FFT and PFB, taken from Strader (6). The frequency response of the FFT is flattened and the side lobes are suppressed by using the FIR filter bank.

one whose response to an impulse input will settle in a finite amount of time, meaning it is inherently stable (37).

The fine channelization step consists of taking one of the coarse channels and shifting the frequency of the tone so that it is now in the centre of the channel, before applying a low low pass filter (LPF).

Applying a LPF to this narrows the channel, attenuating any other tones which are nearby in the frequency space, such that there is now a narrow bin with a single tone in it. For channels which contain more than one tone after the coarse channelization, the above step is repeated for each individual tone. Any coarse channels with zero tones are ignored. Thus, the fine channelization leaves a series of unique fine channels of width $2f_c$, where f_c is the cutoff frequency of the LPF. Each of these channels will contain a single tone at the centre of the channel (6) (30). There are also other possible channelisation techniques, such as instead of using coarse and fine channelisation stages, using a very large FFT to divide the band into a large number of narrow frequency bins. Using a large enough FFT will ensure

that any tone will be close enough to the centre of a frequency bin. However, having a larger number of bins means a larger time stream must be fed into the FFT. This causes a decrease in the time resolution of the MKIDs. (31)

Pulse Detection

Finally, after the data has been sufficiently channelised, the phase, ϕ, can then be calculated from the IQ data using Equation 1.33:

$$\phi = tan^{-1}(\frac{Q - Q_0}{I - I_0}) \tag{1.33}$$

Here, I and Q are the in-phase and quadrature components respectively, while (I_0, Q_0) is the centre point of the resonator loop in the IQ plane. Calculating the phase relative to the centre point of the resonator loops allows for a pulse to give phase values from 0° to 180°. The phase calculation principal is illustrated in Figure 1.14.

In practice, this phase is calculated using a Coordinate Rotation Digital Computer (CORDIC) algorithm. These are algorithms which efficiently calculate trigonometric and hyperbolic functions without using hardware multipliers (38). This is important as it conserves the FPGA's hardware resources, in particular its DSP slices. A photon event is said to have occurred if a phase pulse relative to the phase baseline exceeds a predefined threshold, and if the pulse is in the negative direction. The relevant data is then stored to memory. As the CORDIC algorithm introduces some quantisation errors (39) when it calculates the inverse tangent shown in Equation 1.33, it is important to save both the calculated phase data, but also the raw I and Q data as sampled by the ADCs. This is covered in greater detail in Chapter 5.

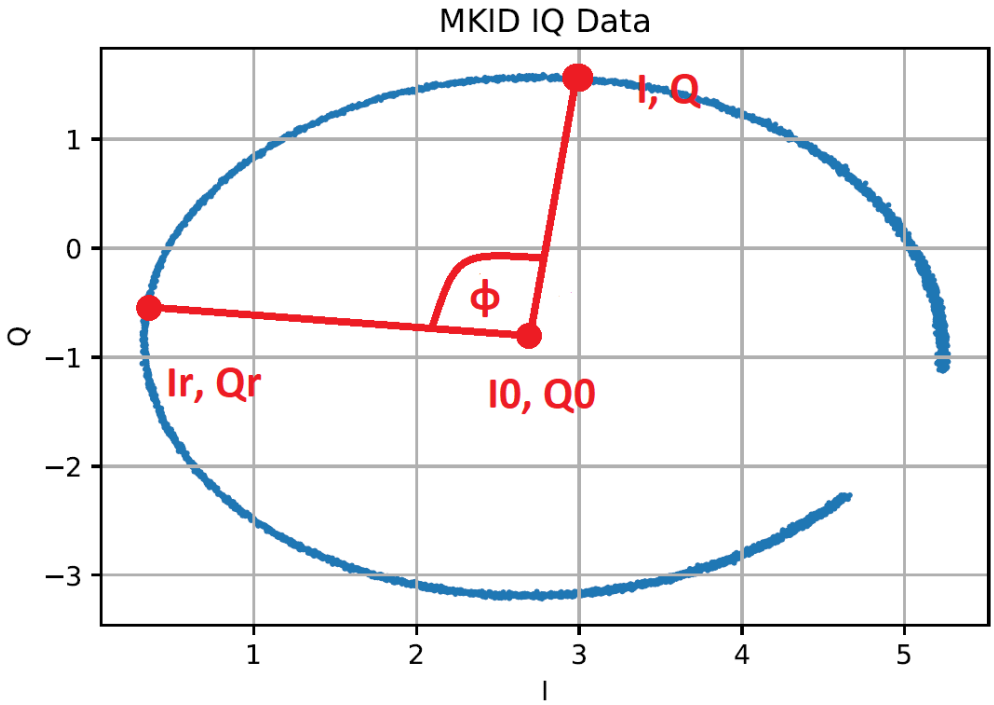

Figure 1.14: Diagram explaining the pulse detection principal. Here, (I0, Q0) is the centre point of the MKID's IQ loop, and (Ir, Qr) is the resonant point of the MKID. (I, Q) represents the instantaneous position on the IQ loop during a photon pulse with the phase, ϕ, being given by Equation 1.33. The pulse height is given by the phase at (Ir, Qr) subtracted from the phase at (I, Q), and a photon pulse is said to have occured when this value exceeds a threshold.

1.6.2 Existing Readout Systems

Previously developed MKID readout systems have used technology developed by the Collaboration for Astronomy Signal Processing and Electronics Research (CASPER). CASPER develops open source, general purpose hardware, software and firmware with the aim of reducing the cost and difficulty of developing radio astronomy instruments (35). Due to the similarity in the FDM readout needed for radio astronomy and MKIDs, this technology has been adapted for use in MKID readouts.

The Reconfigurable Open Access Computer Hardware (ROACH) board (see Figure 1.15 (8) (35)) is a standalone field programmable gate array (FPGA) processing board, the core of which is a Xilinx Virtex 5 SX95T FPGA (40). While this was initially devloped for radio astronomy applications, firmware was developed for it to readout MKIDs for the ARCONS instruments, using 8 ROACH boards, along with a pair of DACs, a pair of ADCs, and an intermediate frequency (IF) board for each ROACH board, to read out 2024 MKIDs. (20)

Following this, the ROACH 2 board, also developed by CASPER, was used as the readout system for the DARKNESS instrument. The ROACH 2 board has a Xilinx Virtex 6 FPGA and improved processing capabilites when compared to the ROACH 1. Similarly to the ARCONS ROACH 1 readout, 10 ROACH 2 boards were each combined with an ADC/DAC board and an IF mixer board to read out a total of 10,000 pixels. (21) (35) This system was later also used by the MEC instrument to read out 20,440 pixels with 20 ROACH2 boards. (41)

Table 1.1 compares the ROACH and ROACH2 boards in terms of their data converter and FPGA resources, as well as their costs and cost per pixel. Logic cells consist of a 4-input look-up table followed by a flip-flop, and act as reconfigurable, programmable logic gates. DSP slices are FPGA resources used for the resource intensive multiply-accumulate operations needed for DSP operations. (42) (43)

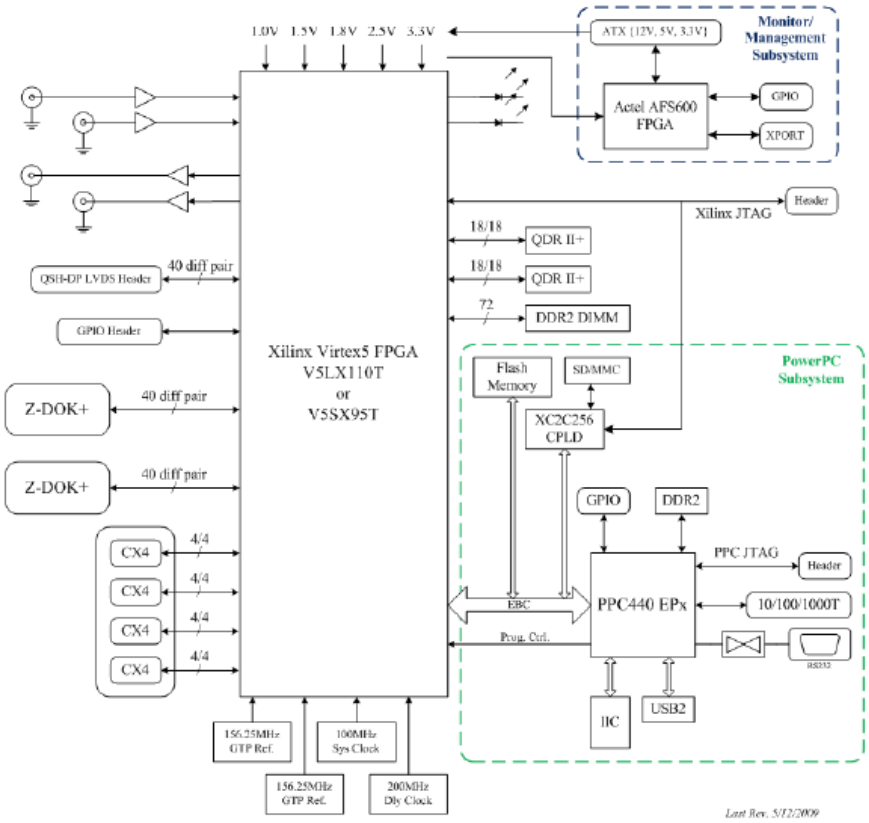

Figure 1.15: ROACH 1 board schematic (8)

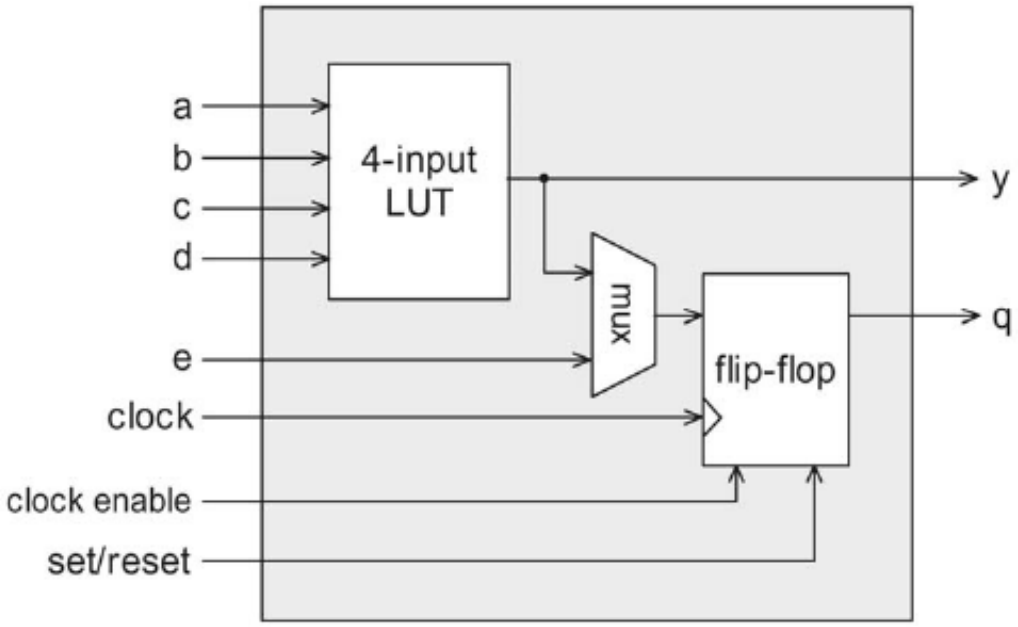

Figure 1.16: Block diagram of a Xilinx logic block which act as programmable, reconfigurable logic blocks in the FPGA.

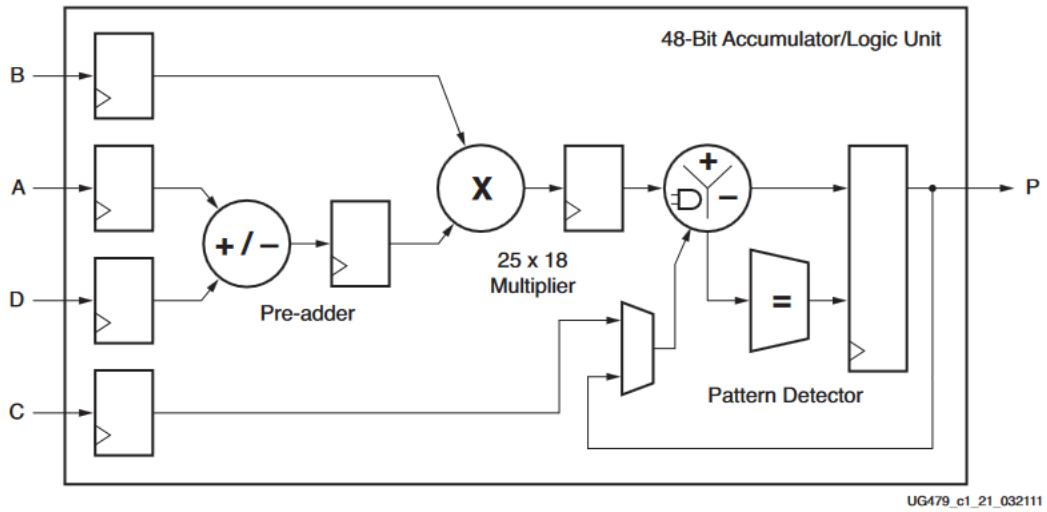

Figure 1.17: Xilinx DSP48E1 slice used to carry out resource intensive multiplication operations on the FPGA.

Table 1.1: ROACH and ROACH 2 board comparison, comparing their ADC and DAC capabilities, as well as the FPGA resources, made up of the DSP slices and logic blocks. Also given is the number of pixels which has been read out using these boards, and their costs and cost per pixel values. Note: MSPS means mega-samples-per-second and GSPS means giga-samples-per-second.

Board	ADCs	DACs	DSP Slices	Logic Cells	Pixel Count	Total Cost (€)	Cost per Pixel (€/ pixel)
ROACH	2x12bit, 550MSPS	2x16bit, 1GSPS	640	7,360	256	3,770	14.73
ROACH2	2x12bit, 2GSPS	2x16bit, 2GSPS	1,120	326,400	1,000	13,200	13.20

1.7 MKID Fabrication

While this project is mainly focussed on the readout of MKIDs, it is also important to mention the fabrication process which was used to develop these MKIDs. This work was done by others in this project, and was carried out in the the Centre for Research on Adaptive Nanostructures and Nanodevices (CRANN) in Trinity College Dublin, and in the Tyndall National Institute in University College Cork. The general recipe used to fabricate MKIDs which was used both in CRANN and Tyndall for this project, is listed below:

- Silicon Oxide Removal
- Metal Depostion
- Photolithography
- Inductively Coupled Plasma Etch
- Dicing
- Bonding

These are briefly described in more detail below.

1.7.1 Silicon Oxide Removal

The standard material which is used a substrate on which to fabricate MKIDs is undoped, high-resistivity silicon. Whilst some groups use sapphire as a substrate, for this project silicon was used. Because silicon forms silicon dioxide (SiO_2), these silicon wafers usually come with a SiO_2 coating layer of $\sim 100nm$. SiO_2 can cause high frequency losses to two level systems (TLSs) which can decrease the quality factor of resonators. Because of this the silicon oxide needs to be removed from the silicon wafers before they can be used for fabricating MKIDs. This is done using a hydrofluoric acid (HF) etch where the wafer is submerged in HF. This removes the SiO_2 without attacking the silicon.

1.7.2 Metal Deposition

The second step of the fabrication process is to deposit a thin superconducting film on the freshly etched Si substrate. This is done on a freshly etched wafer to ensure that the SiO_2 does not reform on the wafer. To do this for this project a high vacuum sputter system was used. This involves generating a gaseous plasma in an area which contains a target, made of the metal which is to be deposited. The surface of the target is eroded by the plasma these atoms are diffused towards the Si substrate, forming a thin film. In order to do this without contaminating the sample, the sputtering chamber must first be evacuated to a high vacuum of typically below $10^{-9}mbar$, and a high purity gas, such as argon, is fed into the chamber to achieve the desired operating pressure. Then a deposition technique called magnetron sputtering is used to produce a high density plasma and sputter the target metal on the substrate.

1.7.3 Photolithography

The third step in this fabrication process is photolithography. In the photolithography stage the film is covered in a thin layer of photoresist, which either hardens or softens when it is illuminated. This can be used to create a pattern on the photoresist. The photoresist consists of photsensitive polymers in a solution. Whether the photoresist hardens or softens depends on the kind of photoresist used. Here, "positive" photoresist" was mainly used, meaning it is removed upon being illuminated. The pattern which is created on the photoresists is achieved by illuminating through a mask, which has been designed with this pattern.

1.7.4 Inductively Coupled Plasma Etch

The next step in the fabrication recipe is to remove any excess metal from the film using an inductively coupled plasma (ICP) etch. This uses a reactive plasma to etch away the surface of the metal layer. This is different to in the deposition step where

an inert plasma is used. While this process will also begin to etch away the photoresist, this is not an issue as the photoresist is typically $3\mu m$ thick, while the metal layer has a thickness of tens of nm. Thus, the ICP etch will etch away the areas of the metal layer which are not coated by the photoresist, leaving the desired pattern of superconducting film on the substrate. Of course, the remaining superconducting layers are covered in the now hardened photoresist. Thus, this photoresist needs to be removed. This is removed using a two bath removal process. First the sample is ultrasonicated in a bath of 1165 photoresist remover, an organic solvent mixture, at 80°C for 60 minutes, before being further ultrasonicated in a fresh batch of 1165, also, at 80°C for a further 15 minutes. The wafer is then further cleaned using isopropanol, acetone and de-ionized water.

1.7.5 Dicing

After the ICP etching and photoresist removal steps, the fabrication process is complete and an array of MKIDs has been fabricated on the substrate. Next the wafer needs to diced into individual chips. A dicer uses a special blade for cutting silicon to dice the wafer according to the mask's pattern. To prevent silicon dust produced by the dicing from contaminating the sample, the samples are coated in photoresist before dicing. After this the photoresist is further cleaned from the individual chips using the same method as described in Section 1.7.4.

1.7.6 Bonding

Once the wafer has been diced and the individual chips have been cleaned of any photoresist, these chips now must be glued into and bonded to a sample box. These sample boxes are specially designed to be mounted in the cryostat system which is being used. Bonds then have to be made between the chip and the boxes SMA connectors, such that the array can be read out. In this project bonds are made between the chips and custom made printed circuit boards (PCBs). These PCBs are then connected to the SMA connectors on the outside of the box. Aluminium

bonds are made using a wedge bonder, which feeds a thin aluminium bond wire onto the wafer, and ultrasonicates it, welding the wire onto the wafer, ensuring an electrical connection. This is then repeated at the bond pad of the PCB, ensuring a connection between the MKID array's feedline and the SMA connector.

At this point one of these sample boxes can be mounted in a cryostat and cooled down.

2 Applications

Due to the advantages of MKIDs hitherto described, MKIDS have, in recent years, found use in a range of applications, including observational astronomy (for which they were originally developed(4)), particle physics, material science and THz imagery. The topics covered in this chapter are explored in greater detail by Ulbricht et al. (44) which was written as part of this project.

2.1 MKIDS for Observational Astronomy

To date, astronomy is the application for which MKIDs have become best established. MKIDs have been used extensively for detecting and characterizing photons for wavelengths ranging from infrared to ultraviolet. Here it must be noted that the detection principal used for low energy and high energy photons is slightly different. For high energy photons MKIDs are capable of detecting individual photons with energy resolution, whereby each photon incident on the MKID gives a single pulse, whose height will be proportional to the photon energy. Meanwhile, for lower energy photons (typically from about $1.5\mu m$), MKIDs cannot detect single photons, but are instead used to measure a photon flux, meaning that photon energy and photon flux become indistinguishable.

2.1.1 Infrared to mm-Wave Astronomy

For the infrared to mm-wave range of observational astronomy, MKIDs can be used as both on-chip spectrometers and as imagers.

MKID Spectrometers for Infrared to mm-Wave Astronomy

MKID on-chip spectrometers which have been developed include the Deep Spectroscopic High Red Shift Mapper (DESHIMA)(45), SuperSpec(46), the Cambridge Emission Line Surveyor (CAMELS)(47), WSPEC(48), and Micro-Spec(49).

DESHIMA uses an on-chip antenna to couple incident 332 to 377 GHz radiation to an NbTiN feedline, which is then coupled to 49 individual MKIDs, via 49 corresponding passband filters. DESHIMA achieves a spectral resolution $R = \frac{f}{\Delta f}$ of 380. SuperSpec is also using MKIDs to achieve an on-chip filter bank spectrometer for the 195 to 310 GHz range. It is being designed for 500 channels with a spectral resolution of $R = \frac{f}{\Delta f} = 700$. Also an on-chip filter-bank MKID spectrometer, targeting a range of 103 to 114.7 GHz, CAMELS is planned to use 512 channels to achieve $R = \frac{f}{\Delta f} = 3000$, be operated at the 12m Greenland Telescope. WSPEC, which does not use an on-chip filter bank, but instead a normal-metal rectangular waveguide splitting into 54 branches, is intended to cover two bands, 135 to 175 GHz and 190 to 250 GHz, with $R = 200$. Micro-Spec uses a different design, focusing light from a telescope onto an antenna which couples photons to a Nb feedline. This feedline is then split into 256 arms, each with microstrip transmission lines of varying lengths, causing each arm to have a unique phase delay structure. These 256 feedlines then emit light into a 2-dimensional parallel-plate wave-guide region, forming an interference pattern. This interference pattern is then measured using 345 feed-horns coupled to MKIDs. It is planned to achieve a spectral resolution of 512 to 1200. Six of these Micro-Spec spectrometers are intended to be used in the balloon-borne EXCLAIM(50) experiment to map the night sky.

MKID Imagers for Infrared to mm-Wave Astronomy

As well as spectrometers, MKIDs have also been used for a range of imagers for infrared to mm-wave wavelengths. For this, MKIDs have to be arranged in an array,

at the focal plane of a telescope, with each MKID acting as a pixel. Incident photons break Cooper pairs in the MKIDs, changing the quasi-particle density, which can be measured to resolve the photon flux, and used to construct an image.

Some MKID imagers for these wavelengths include the Multiwavelength Sub-millimeter Inductance Camera (MUSIC)(51), the New IRAM KIDs Array (NIKA)(52) and NIKA2(53), the Mexico UK Sub-mm Camera for Astronomy (MUSCAT)(54), TolTec(55), the Apex MKID Camera (A-MKID)(56), the Multicolor Sub-THz KID-array Camera (MUSICAM)(57), SPACEKIDs(58), the Balloon-born Large Aperture Submillimeter Telescope's sucessor BLAST-TNG(59), the Osservatorio nel Lontano Infrarosso e le Microonde su Pallone Orientabile (OLIMPO)(60), and GroundBIRD(61).

MUSIC was one of the first scientific instruments to use MKIDs and was used at the Caltech Submillimeter Observatory (CSO) on Mauna Kea, Hawaii. It consisted of 16 pixels, detecting at two bands of 240 and 350 GHz. NIKA, which was used at the 30 m Institute for Millimetric Radio Astronomy (IRAM) telescope, had 400 pixels, 144 of which were for the 125-175 GHz band, with the remaining 256 pixels for the 200 to 280 GHz band. NIKA2 is also operating around two bands, one centered around 150 GHz, and the other around 260 GHz, with 1040 pixels for the 150 GHz band, and two 1200 pixel arrays for the 260 GHz band, giving a total of 3440 pixels. The two 150 GHz arrays are for the two polarization directions. MUSCAT is a 1600 pixel array, for the band centered around 270 GHz using aluminium MKIDs, and installed at the Large Millimeter Telescope (LMT) in Mexico. TolTEC is also an MKID camera designed for the LMT, consisting of 1900, 950, and 475 pixel arrays for the 280, 220 and 150 GHz bands respectively, giving a total of 6650 MKIDs. The A-MKID camera is planned to consist of a 353 GHz and 855 GHz camera for the 12m Atacama Pathfinder Experiment (APEX) telescope in Chile, while MUSICAM is a proposed MKID camera made up of four 25 pixel arrays for 150, 225, 288 and 350 GHz for the Eurasian Sub-Millimeter Telescope (ESMT).

There have also been proposals to use far-IR MKIDs on space based telescopes, where the radiation is not absorbed by the Earth's atmosphere. This includes the SPACEKIDs project, which has demonstrated a 961 pixel, 850 GHz, MKID array made from Al and NbTiN. BLAST-TNG is a balloon borne mission, using three arrays of TiN MKIDs, with pixel counts of 1836, 938, and 544 for the 1200, 857, and 600 GHz bands. OLIMPO is also a balloon borne mission, containing a 2.6m telescope coupled to a four-band MKID camera, with bands centered on 150, 250, 350 and 460 GHz,and between 19 and 41 pixels per band. Finally, GroundBIRD is a ground based camera, observing the cosmic microwave background (CMB) B-mode polarization, using a rotating 30 cm telescope and 161 pixels in bands around 145 GHz and 220 GHz, with 138 pixels at the former and 23 pixels at the latter.

2.1.2 Near Infrared, Optical and Ultraviolet Astronomy

From approximately $1.5\mu m$, individual photons incident on an MKID will have enough energy, to break enough Cooper pairs, to cause a sufficiently large change in the phase of the resonator's transmission, such that individual photons can be detected and counted, and not just photon flux. In contrast to the previous for lower energy detectors, for near-IR and above, MKID detectors are capable of differentiating between changes in photons flux compared to changes in photon energy. The wavelength limit below which photon counting can be carried out depends on the pixel size, the detector geometry, and the thickness of the superconducting layer, along with other factors. Work is being carried out elsewhere to reduce this limit. (62) For these near-IR to ultraviolet photons, the main advantages which MKIDs offer over their competitors are that they offer no dark counts (provided the triggering threshold is set sufficiently high), are energy resolving, have high time resolution which is mainly constrained by their readout electronics, and they are easily multiplexed (compared to other low temperature detectors), meaning that they can be scaled up to large arrays. (44)

One of the first MKID instruments used for these higher energy photons was the

Array Camera for Optical to Near-IR Spectrophotometry (ARCONS)(20). ARCONS consists of 2024 sub-stochiometric TiN_x MKID pixels sensitive to the 350nm to 1100nm band, operating with a spectral resolution of $\frac{\lambda}{\Delta\lambda} = \sim 10$ at 400nm. ARCONS was developed to showcase what MKIDs can offer for astronomy, and was used to study transiting binaries(63). ARCONS was later replaced by the DARK-speckle Near-infrared Energy-resolving Superconducting Spectrophotometer (DARKNESS), a 10,000 pixel array made from PtSi MKIDs, and sensitive at 800 to 1400nm with a spectral resolution of 5 to 7, and designed to be used with a coronagraph to block out the light from a host star, allowing the high contrast imaging of exoplanets (21). Two further MKID cameras being developed for high contrast imaging of exoplanets are Planetary Imaging Concept Testbed Using a Recoverable Experiments - Coronagraph (Picture-C) MKID Camera(64) and the MKID Exoplanet Camera (MEC)(41). The Picture-C MKID Camera is a 10,000 pixel MKID array for 540 to 600 nm, and is part of the Picture-C project, consisting of a balloon borne 0.6 m telescope with coronagraph. It is optimized for imaging debris discs, exozodiacal light and young hot Jupiters. MEC, which is the largest MKID array currently in use consists of 20,440 PtSi MKIDs sensitive from 800nm to 1400nm, with a spectral resolution, $\frac{\lambda}{\Delta\lambda}$, of 5 to 7. MEC is being used at the Subaru Coronagraphic Extreme Adaptive Optics (SCExAO) instrument at the 8m Subaru telescope in Hawaii, also doing high contrast exoplanet imaging.

Due to their inherent energy resolution MKIDs have been used for integral field spectographs (IFS). In short, this is a camera whereby each pixel provides a full spectrum. With CCD devices this can be achieved with the use of filters, which has the effect of reducing the speed and energy resolution of the device. While MKIDs are still only capable of medium energy resolution, they can improve the performance of IFSs in certain situations. For example, the Keck Radiometer Array using KID Energy Sensors (KRAKENS) is a proposed MKID IFS for the Keck-1 Telescope. It will have 30,660 MKID pixels, sensitive between 380nm and 1350nm, and a planned energy resolution of 20. A later update to 57,600 pixels is also

planned. (65)

2.2 MKIDS for Particle Physics

While astronomy was the initial, and to date most prevalent field in which MKIDs have been used, they have also been used as detectors in other applications. One of the other main fields in which MKIDs have been used is in particle physics. Within particle physics, there are groups studying the use of MKIDs for rare events experiments, such as in experiments evaluating the nuetrino mass, as well as in detecting dark matter particles such as Weakly Interacting Massive Particles (WIMPs).

2.2.1 Neutrino Physics Experiments

Superconducting detectors have been proposed for neutrino physics experiments since the 1980s (66). The first proposed use of MKIDs for neutrino physics was for MARE (the Microcalorimeter Arrays for a Rhenium Experiment), which unfortunately was later cancelled (67). Later, improvements in MKIDs performance have allowed for them to be used in the CUORE(68), CUPID(69), CALDER(70) and HOLMES(71) experiments.

CUORE (the Cryogenic Underground Laboratory for Rare Events), and its successor CUPID (CUORE Upgrade with Particle IDentification), is an experiment to detect neutrino-less double beta decay events in tellurium oxide (TeO_2) crystals. CUORE, is intended to use Neutron Transmutation Doped (NTD) thermistors to detect temperature changes caused by the radioactive decay of ^{130}Te nuclei. For these rare event experiments, it is crucial to have an optimal backgrounbd rejection. For example, CUORE is intended to have a background of $10^{-2} counts/kg/keV/year$, giving approximately 200 counts over the 5 year span of the experiment (72) (68). CUPID, which is the successor to CUORE, will instead use Li_2MoO_4 crystals, and will detect particles by coupling photodetectors to CUORE's bolometers. While it is

currently planned for CUPID's photodetectors to also be based on NTD Ge thermistors, other options, including MKIDs, are also being explored.

CALDER (the Cryogenic wide-Area Light Detectors with Excellent Resolution) is an experiment to develop MKIDs for rare event searches. The two fundamental questions which CALDER aims to answer are whether the neutrino is a standard particle or is it a Majorana particle, and what is the nature of dark matter in our universe? (73) CALDER aims to develop phonon mediated MKIDs to detect UV and Cherenkov radiation emitted from TeO_2 crystals. The detection of this UV and Cherenkov radiation would allow the background radiation of the experiment to be greatly improved. CALDER is investigating using Al/Ti/Al trilayer MKIDs for these detectors. Further materials have also been investigated, such as TiN_x and Ti/TiN multilayers. (74) (75)

HOLMES is an experiment to directly measure the electron nuetrino mass using the electron capture decay of ^{163}Ho (71). HOLMES currently uses TESs, coupled to SQUIDs. However, because TESs are not as easily scaled up to larger arrays as MKIDS, HOLMES MKIDs are currently being developed. Both Ta and Ti/TiN multilayers are under development. Along with their ability to be scaled up to mega-pixel arrays, other reasons why MKIDs are currently being developed for HOLMES are that they are easier to fabricate, and that they require simpler readout electronics and cryogenic setup. MKIDs are capable of achieving sub-eV energy resolution for the energy range of this project. (76)

2.2.2 Dark Matter Experiments

Another field in particle physics where MKIDs have been proposed as detectors is in the search for WIMPs, a possible dark matter candidate. Because of their low interaction rate of $< 0.1 event/kg/day$, and their energy deposited per interaction of 10s of keV, state of the art detectors are being developed with increased sensitivity. Detector improvements which are desirable for the detection of WIMPs

include increased sensitive area, energy collection and improved fabrication reliability. These are all areas where MKIDs could be a useful technology, due to their sensitivity, ability to be multiplexed and thus scaled up to large arrays, and their insensitivity to inhomogenities and thus their relative ease of fabrication. (44)

One proposed use of MKIDs in this field is BULLKID (BULKy and Low-Threshold Kinetic Inductance Detectors), a project developing MKIDS for the detection of rare, low energy procesess (77). BULLKID is proposed to use 108 $5x5x5mm^3$, 0.29g Si voxels, which act as the interacting medium for the detection of WIMPS. These voxels are fabricated from a Si wafer, on which an MKID array is structured. Dark matter WIMPS in the voxels will produce phonons in the Si voxels, which will then be detected by the MKID array. Al/Ti/Al MKIDs with a critical temperature of $T_C = 805mK$, and an energy resolution of 20 eV have been proposed for BULLKID. (77)

2.3 MKIDs for Material Science with Synchrotrons

Another field where kinetic inductance detectors are being used is in the use of synchrotron radiation for material science. Synchrotron radiation is emitted by electrons accelerated while travelling with speeds close to the speed of light in the vacuum of a particle accelerator. In the reference frame of the electron, this emission is at radio frequencies, while in the reference frame of the detectors, it is shifted into the X-ray range. A periodic series of magnets, called undulators, cause transverse undulations in the electron. The wavelength of the emitted radiation is a function of the period of these undulators. Synchrotrons have increased the brightness of X-ray sources by 26 orders of magnitude since the 1970s. Using MKIDs as detector element in synchrotron beam lines allows to exploit their major advantages of energy resolution and their ability to be multiplexed to large arrays, and only having to deal with the disadvantage of requiring advanced cryogenics to

cool them down to mK temperatures. (44, 78)

T. Cecil et al. (79) have developed MKIDs for synchrotron X-ray spectroscopy. In particular they cite MKIDs ability to be scaled up to larger arrays as one of their benefits. As well as synchrotron experiments, they also mention laboratory tools and astronomical satellites as uses for X-ray MKIDs. WSi_x is proposed as a material for these detectors due to its high Q_i, T_C of between 1 and 3 K, and the ability to easily sputter W and Si from separate targets. Initial results for these detectors give Q factors in excess of 10^6 (80). Moreover, they later suggest the use of TKIDs for X-ray detection. In order to explore the use of TKIDs for X-ray spectroscopy, these TKIDs were simulated, and based on the results of these simulations, optimized TKIDs were designed for 6 keV X-rays. This simulated TKID has a critical temperature of $T_C = 1K$ and a heat capacity of 1 pJ/K. They further suggest the use of parametric amplifiers instead of HEMT amplifiers to improve noise performance. (81) (82)

Ulbricht et al. (83) have also developed TKIDs for X-ray spectroscopy, also referencing sychrotron experiments, as well as X-ray astronomy as potential applications. They refer to how both diffractometers (84) and TESs have been used for 5.9 keV photons with energy resolutions of 0.5 eV and 2.4 eV respectiviely, but note that diffractometers have the disadvantage of to be scanned across the energy range, and that TESs run into difficulties scaling upto kilo-pixel arrays. They have fabricated sub-stoichiometric TiN_X TKIDs, with a Nb feedline and ground plane, and 500 nm thick Ta absorber. These TKIDs were excited with a Fe^{55} source and found to have an energy resolution of 75 eV at 5.9 keV. They conclude that further optimization should allow MKIDs to achieve the energy resolution of TESs.

Furthermore, Faverzani, Giachero et al. (85) (86) are also developing TKIDs for X-ray spectroscopy, fabricating their arrays from Ti/TiN multilayers. Different trilayers were produced with Ti/TiN thicknesses of 10/7 nm (total thickness of 100 nm), 10/10 nm (total thickness of 102 nm), and 10/12 nm (total thickness of 110

nm). These films produced critical temperatures of 0.6 K, 0.8 K, and 1.2 K respectively and kinetic inductances of $30pH/\square$, $20pH/\square$, and $12pH/\square$. Chips were produced from each of these films, each with four resonators, showing quality factors of $Q_c = 17,000$ and $Q_i = 82,000$ at a resonant frequency of $f_0 = 5598MHz$. (85) (86)

2.4 MKIDs for Security Applications

Another area where MKIDs are being explored is in security applications, specifically in the area of GHz and THz imaging. Groups in Cardiff, Glasgow, Rome, Helsinki and Groningen are developing MKIDs for security applications. They have been developed for, for example, airport screening, the detection of landmines, and the screening of trucks and vans. MKIDs are an appealing technology for these applications as they allow for large arrays of detectors with response times of the order of $10^{-4}s$, while also being sensitive to radiation with frequencies from 300 GHz to 1000 GHz, at which certain materials appear translucent, thus allowing for concealed items to be detected. (87, 88, 89, 90, 91)

Doyle et al. (87) have developed a 152 pixel lumped element kinetic inductance detector (LEKID) camera fabricated with aluminium on a high purity silicon substrate, sensitive to 350 GHz radiation. It has a frame rate of 2 Hz a noise temperature of approximately 0.1 K per frame. This array has successfully shown the spatial resolution, frame rate, and sensitivity to detect objects such as a wallet, air pistol or coins concealed inside a person's clothes. (87)

Hassel et al. (90) have developed a 8208 pixel imager, CONSORTIS, for passive, "walk-by", airport security screening. This array consists of 8208 kinetic inductance bolometers (KIBs), one third of which are sensitive to the band centered at 250 GHz, and the remaining two thirds of which are sensitive to the band centered at 500 GHz. This system has been shown to detect aluminium, paper and plastic objects concealed under a person's clothing, demonstrating its basic operation. It is

now being scaled up to larger arrays. (90)

Messina et al. (89) have designed and fabricated $YBa_2Cu_3O_7$ (YBCO) MKIDs for use in security applications. YBCO has been used to achieve high T_C MKIDs, with critical temperatures of upto 89 K, with the aim of allowing cheaper, more reliable cryogenic systems. They propose using high critical temperature superconductors (HCTS) to achieve the high sensitivity of typical MKIDs, while allowing relatively cheap Stirling coolers to be used to cool the MKIDs to between 20 K and 40 K. (89)

Morosov et el. (88) have investigated using TiN thin films for MKIDs in passive THz imaging systems. They use TiN thin films due to their critical temperatures of above 300 mK, allowing for compact cryogenic systems. They state that desirable characteristics of such a system would be a noise effective temperature difference (NETD) of $\leq 0.1K$, frame rate of 25 Hz, a time constant of $\tau \leq 100\mu s$, and a noise effective power (NEP) of 100s of pW. Their test array of 12 pixels showed results of $NEP \approx 2.3 * 10^{-15} W/\sqrt{Hz}$ and $\tau \approx 31\mu s$. While this time constant is sufficient, optimization of the pixel design and improvements in the readout noise need to be implement to reduce this NEP. (88)

Fianlly, De Jonge et al. (91) are also developing MKIDs to be used as a passive THz imager for security and biomedical applications. As an initial proof of concept of MKIDs for these applications, they developed a 4 x 4 pixel MKID array which could be scanned to create 70 x 70 pixel images. These MKIDs are for the 350 GHz band. This system was used to take an image of the hand of the author, with spatial resolution of 3.2 mm. (91)

3 Experimental Setup

As part of this project, significant work was put into developing the laboratory setup needed for reading out and characterizing arrays of MKIDs.

3.1 General Setup

The first step in the general experimental setup for detecting photons with an MKID array is the generation of a 'comb' of probe tones (see Figure 1.10) using a DAC (Digital to Analogue Converter) - the first component of the room temperature electronics signal chain. A tone is generated at the resonance frequency of each pixel in the array. This process is explained in more detail in Section 1.6. This frequency comb, which is a single source defined as the sum of all tones, is passed into an adiabatic demagnetization refrigerator (ADR) by co-axial cables. The ADR, which ultimately cools the MKID array to mK temperatures, is mechanically and thermally separated into three stages: the 70 K, 4 K, and finally the mK stage, where the array is mounted. Stainless steel co-axial cables carry the input signal from room temperature to 4 K, with baseplate coaxial connectors linking the coaxial lines between the stages. From the 4 K stage, the signal passes through superconducting coaxial cables to the array at the 100 mK stage via on-chip microstrip or co-planar waveguides. The frequency comb then passes through the MKID array, and the detectors will imprint phase and amplitude changes on the probe tones when photons strike the detectors. The output of the array travels back to 4 K through two smaller lengths of superconducting coax line,

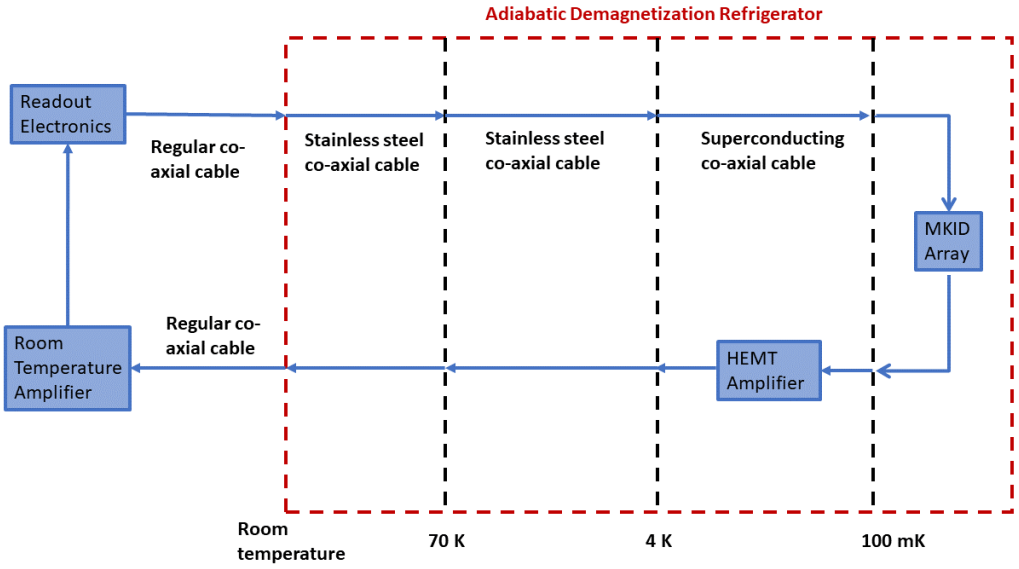

Figure 3.1: Schematic showing the microwave lines used in the experimental setup, from room temperature to 100 mK, and back to room temperature.

which are connected in series via a pre-amplifier stage consisting of a HEMT (High Electron Mobility Transistor) cryogenic amplifier. The amplified signal then travels through the stainless steel coax to room temperature, and back out of the cryostat, through another set of SMA cables. Next, the signal is further amplified by low noise, room temperature amplifiers and the signal is input to the readout electronics. The analogue signal is digitised with ADCs (Analogue to Digital Converters), before being processed on a field programmable gate array (FPGA) using digital signal processing (DSP) techniques based on SDR (Software Defined Radio). These signal processing techniques are further explored in Section 1.6. A schematic showing the type of microwave feedlines used at each stage in the ADR is including in Figure 3.1. The resonator array can also be analysed using a Vector Network Analyser (VNA). Connecting the VNA's output to input to the cryostat, and the VNA's input to the output of the room temperature amplifier, the resonator's transmission, S_{21}, can be measured and from this its quality factors can be calculated. This process is further covered in Chapter 4.

Furthermore, the readout systems developed as part of this work are covered in Chapter 5, Chapter 6 and Chapter 7.

Figure 3.2: Entropy adiabatic demagnetization refrigerator (ADR) which is used to cool the MKID arrays down to below 100 mK using the magnetocaloric effect (MCE)

3.2 Adiabatic Demagnetization Refrigerator

The centrepiece of this setup is the adiabatic demagnetization refrigerator (ADR) (see Figure 3.2) which was used to achieve the mK temperatures needed to operating superconducting detectors. This ADR was constructed by Entropy Cryogenics (92).

The operation of ADRs is based on the magnetocaloric effect (MCE) (see Figure 3.3 (9)). Magnetic materials store energy in two forms; phonon excitations and magnetic excitations. Initially, When an external magnetic field is applied to a paramagnetic material, the magnetic moments of the material become aligned, heating up the magnetic material. This heat is then lost to its surroundings. When

the magnetic field is removed, the magnetic moments become randomized and the paramagnet cools to below the ambient temperature. Using a heat transfer medium, heat can then be removed from the system. Using this method an ADR can be used to achieve mK temperatures (9). It was decided to use an ADR as opposed to other cryostat technologies, such as a dilution fridge, as it does not need continuous helium circulation to be pumped. This is an advantage as it is planned that this fridge will ultimately be transported to an observatory, where it will be impossible to place pumps close to an instrument. This is due to size restrictions and also due to vibrations caused by the pumping. The Entropy Cryogenics ADR used in this experimental setup has achieved temperatures as low as 30 mK.

Figure 3.4 and Figure 3.5 show Solidworks computer aided design (CAD) drawings of the sample space of the Entropy ADR. Figure 3.4 shows the open ADR, with the room temperature stage at the bottom, followed by the 70 K stage above that, and the 4 K stage above that again. At the top of the drawing is the magnetic shielding within which the sample box containing the MKID arrays is mounted. Figure 3.5 shows a more detailed drawing of the magnetic shielding (shown in transparent), as well as the sample box mounted inside it.

In order to be able to operate this ADR to measure arrays of MKIDs, some adjustments had to be made to it. These adjustments include the addition of low temperature high electron mobility transistor (HEMT) amplifiers, low temperature co-axial cabling, a setup for measuring the critical temperature of superconducting samples, and two stages of infrared filtering. These adjustments are covered in Sections 3.3, 3.5, 3.7 and 3.8. While these additions decreased the hold time of the setup, and slightly increased the time taken to reach 3 K when cooling down from room temperatures, the ADR is still capable of reaching 3 K within approximately 24 hours, and able to maintain 100 mK temperatures for approximately 12 hours, more than enough time for a full night of measurements. The ADR cools down in two stages, cooling down from room temperature to 3 K using a pulse tuber cooler, and from 3 K to 100 mK using the magnetocaloric effect described above. Figure

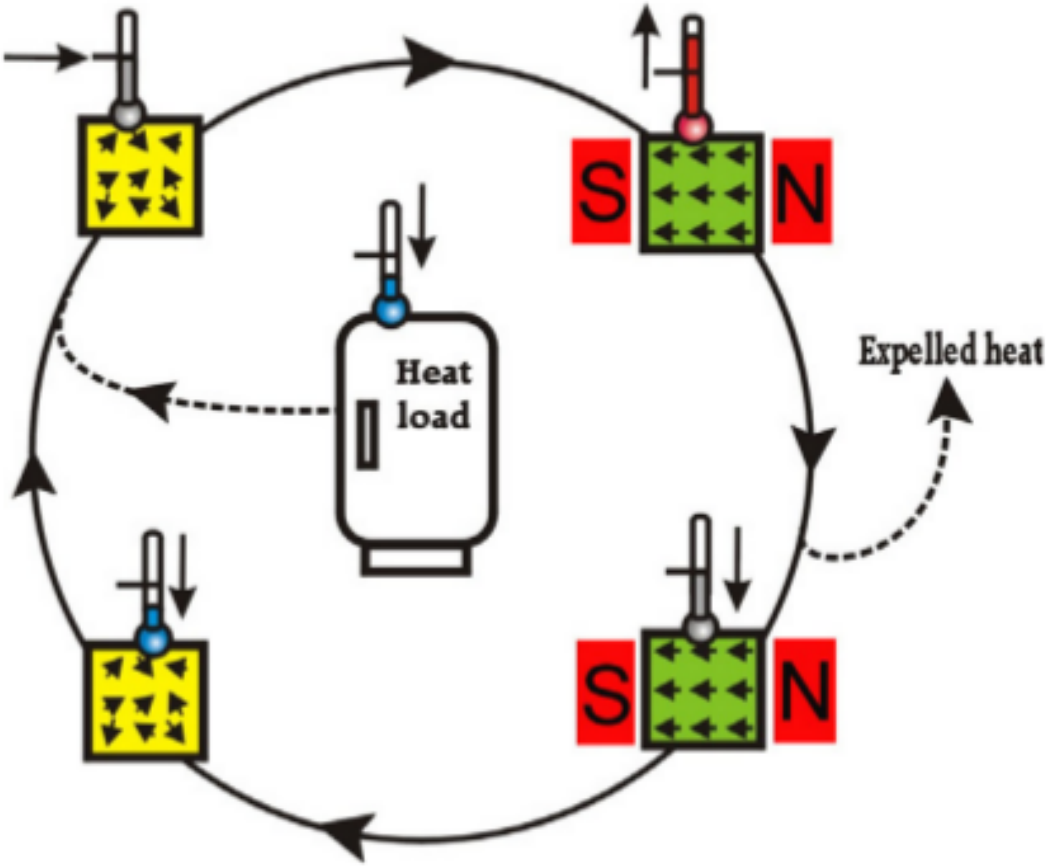

Figure 3.3: Schematic showing the magnetocaloric effect (MCE) which is the operating principle of an adiabatic demagnetization refrigerator (ADR). Applying an external magnetic field to a magnetic materials causes the magnetic moments to become aligned, causing the material to heat up. When this magnetic field is then removed the magnetic moments become randomized again, causing the magnetic material to cool down again. By using a movable heat switch to transfer heat to the surroundings the temperature can decrease below the ambient temperature upon decreasing the magnetic field. This is the process which cools the sample down from 3 K to below 100 mK. (9)

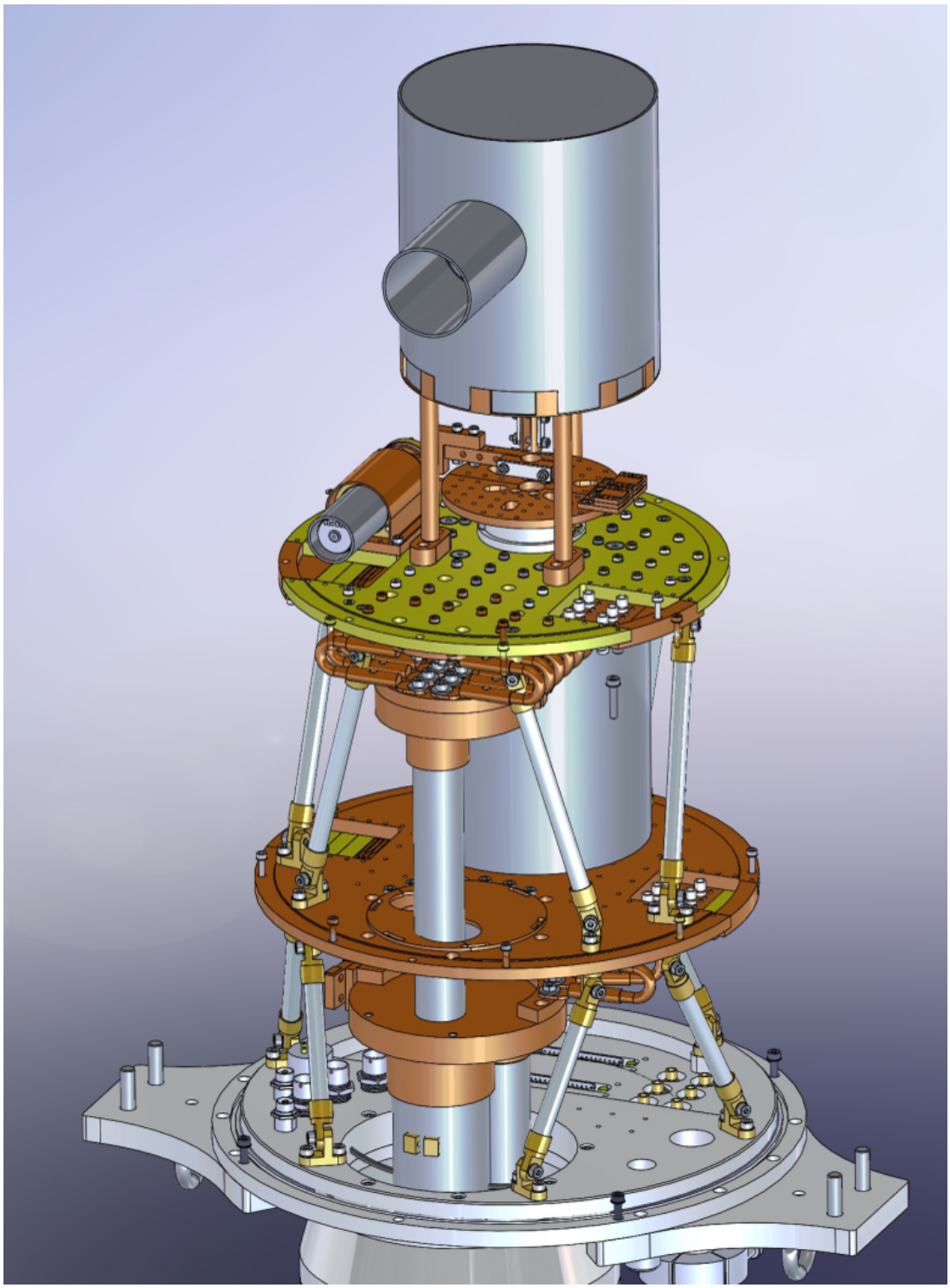

Figure 3.4: ADR Solidworks CAD model showing the room temperature, 70 K and 4 K stages, as well as the magnetic shielding within which the MKIDs are mounted

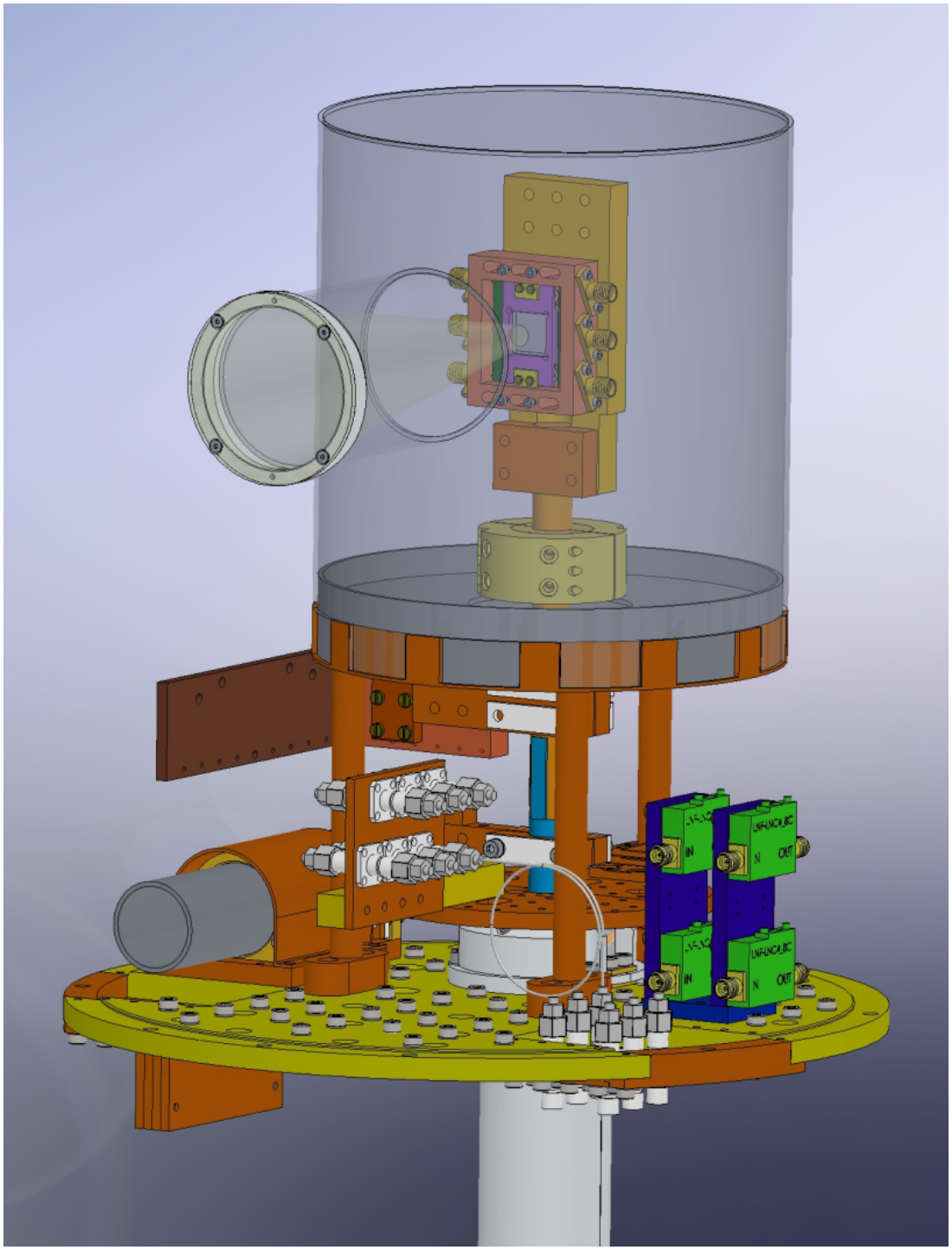

Figure 3.5: ADR Solidworks CAD model showing a close-up of the magnetic shielding (shown in transparent) and the sample box on which the MKID arrays are mounted within

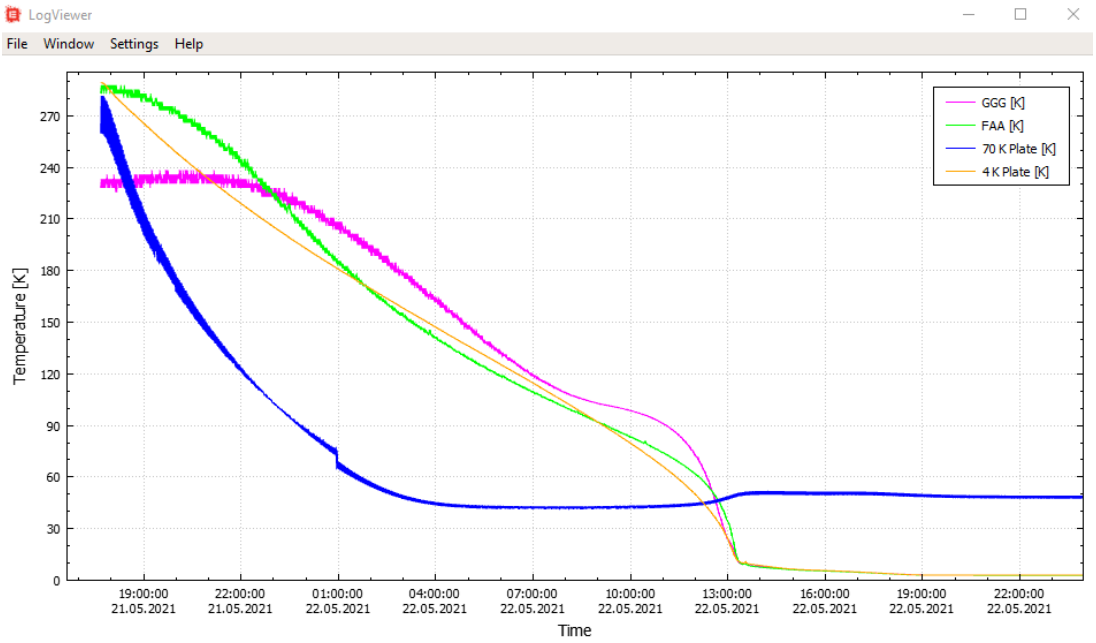

Figure 3.6: ADR cooldown from room temperature to 3 K. This part of the cooldown is achieved using a two stage pulse tube cooler. This process takes approximately 24 hours. Once the ADR has stabilised at 3 K it is let to soak for approximately another 4 hours to ensure that the magnet is fully cooled down. This is to prevent a quench from occurring.

3.6 shows a typical cooling curve when cooling down to 3 K, and Figure 3.7 shows the cooling curve when cycling the magnet to reach 100 mK.

3.3 High Electron Mobility Transistor Amplifiers

One of the primary benefits of MKIDs is that large numbers of the detectors can be readout using only a pair of co-axial cables and a cryogenic amplifier, without any other low temperature electronics, such as SQUIDs. The low temperature amplifier of choice is the high electron mobility transistor (HEMT) amplifier. HEMT amplifiers are used at the 4 K stage of the cryostat to provide amplification to the output from the array. Amplification is performed at cryogenic temperatures as placing the amplification as close to the detectors as possible maximizes the signal-to-noise ratio (SNR), and also because these HEMT amplifiers achieve better noise characteristics at cryogenic temperatures. It was decided to use Low Noise Factory LNF-LNC4-8C S/N 3957 Cryogenic HEMT amplifiers, and later Low Noise

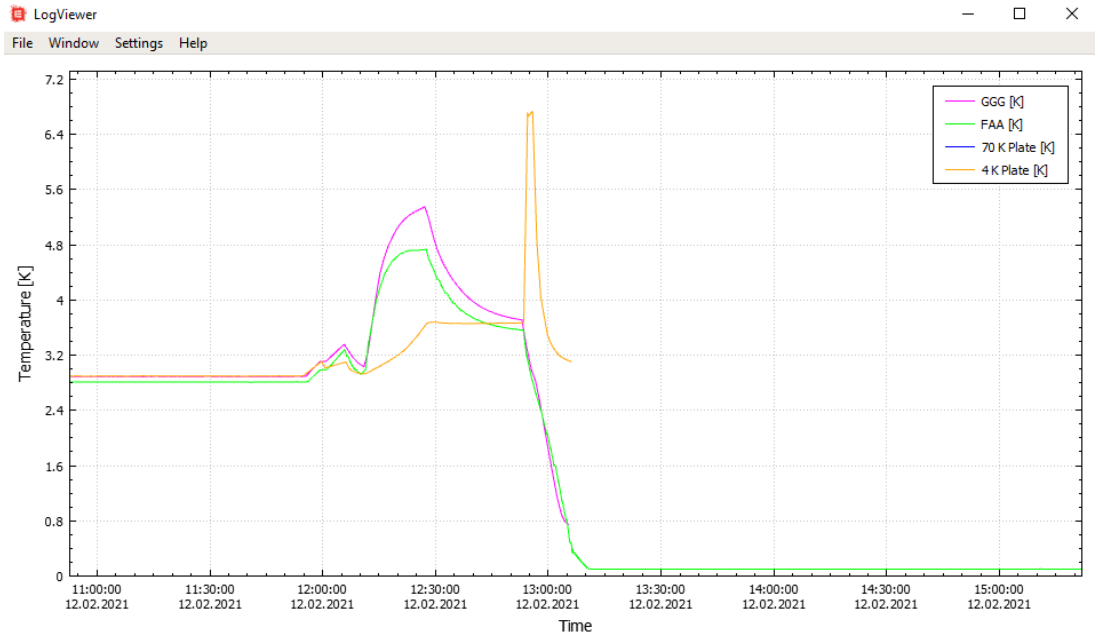

Figure 3.7: ADR cooldown From 3 K to 100 mK. This part of the cooldown is achieved by cycling the superconducting magnet from 0 A to 40 A and back to 0 A, using the magnetocaloric effect. Cooling from 3 K to 100 mK takes approximately 1 hour and once achieved this temperature can be maintained for approximately 12 hours.

Factory LNF-LNC4-8C S/N 2335 Cryogenic HEMT amplifiers. These provide approximately 40 dB of gain across 4 GHz of bandwidth, from 4 GHz to 8 GHz with a noise temperature of just above 2 K (see Figure: 3.8 and Figure 3.9) (10) (11). This constrains the frequencies for which the MKIDs can be designed for to this octave of bandwidth. However, this wide bandwidth also means that a single amplifier can be used to pre-amplify the signal from each of upto 2,000 MKIDs (assuming an approximate 2 MHz spacing between resonators).

As the HEMT amplifier is the first amplification stage in the process, the noise from this dominates when compared to the room temperature electronics (93). Moreover, the amplifier noise of the system limits the energy resolution of any measurements. It is suggested that using new cryogenic amplifier technologies, such as parametric amplifiers (paramps) may drive down this noise (5). HEMTs are a type of field effect transistor (FET) that contain a heterojunction. This is a junction between two material with different bandgaps. Commonly used materials include n-AlGaAs/GaAs and n-InAlAs/InGaAs. HEMTs are commonly used in

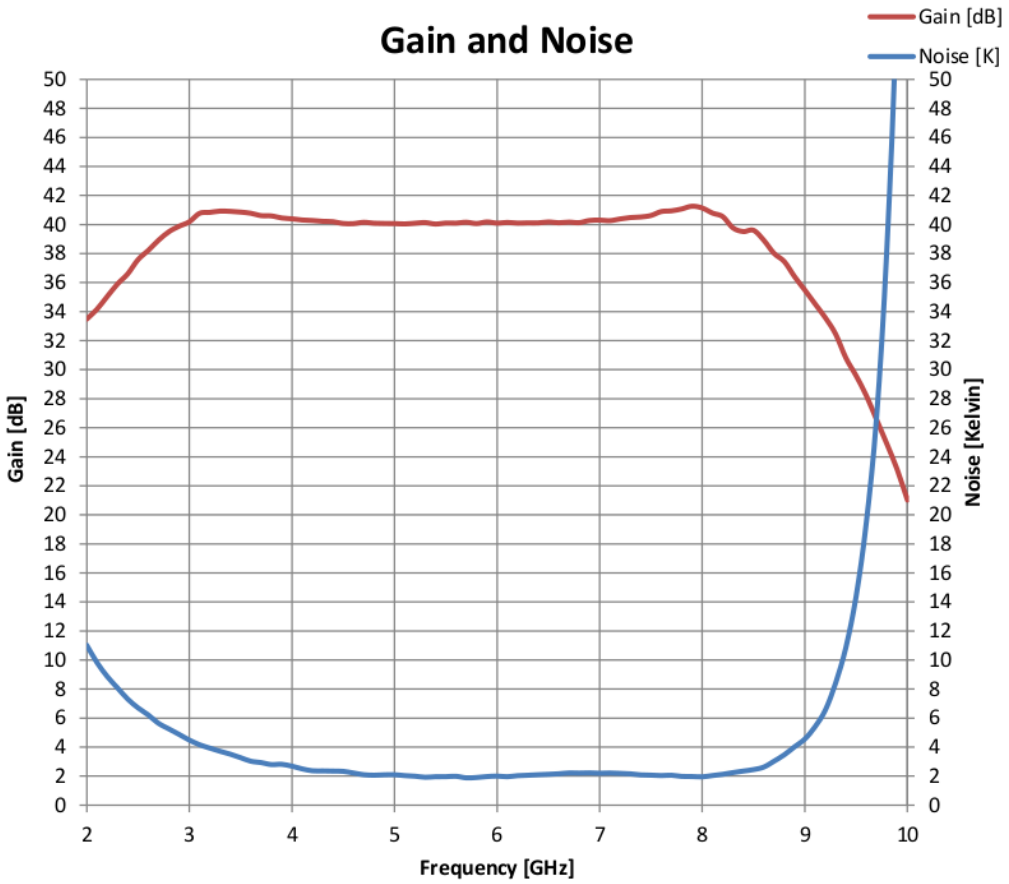

Figure 3.8: LNF-LNC-8C S/N 3957 HEMT gain and noise characteristics showing gains of approximately 40 dB and noise temperatures of approximately 2 K for the 4 to 8 GHz octave (10). The increase in noise and decrease in gain for frequencies below 4 GHz and above 8 GHz constrains the MKIDs' design frequencies to this 4 to 8 GHz octave.

applications that require high frequencies and low noise, such as radio astronomy, telecommunications and radar, and more recently in quantum computing technologies and research. (94) (95) (96)

3.4 Room Temperature Amplifier

The second stage of amplification used in this setup is the room temperature amplification. The output from the cryostat is amplified, at room temperature, before it is input to the readout electronics system. To date, two different room temperature amplifiers have been investigated for this purpose. These are the MiniCircuits ZVA-183-S+ and ZX60-83LN+. The ZVA-183-S+ provides 26 dB of

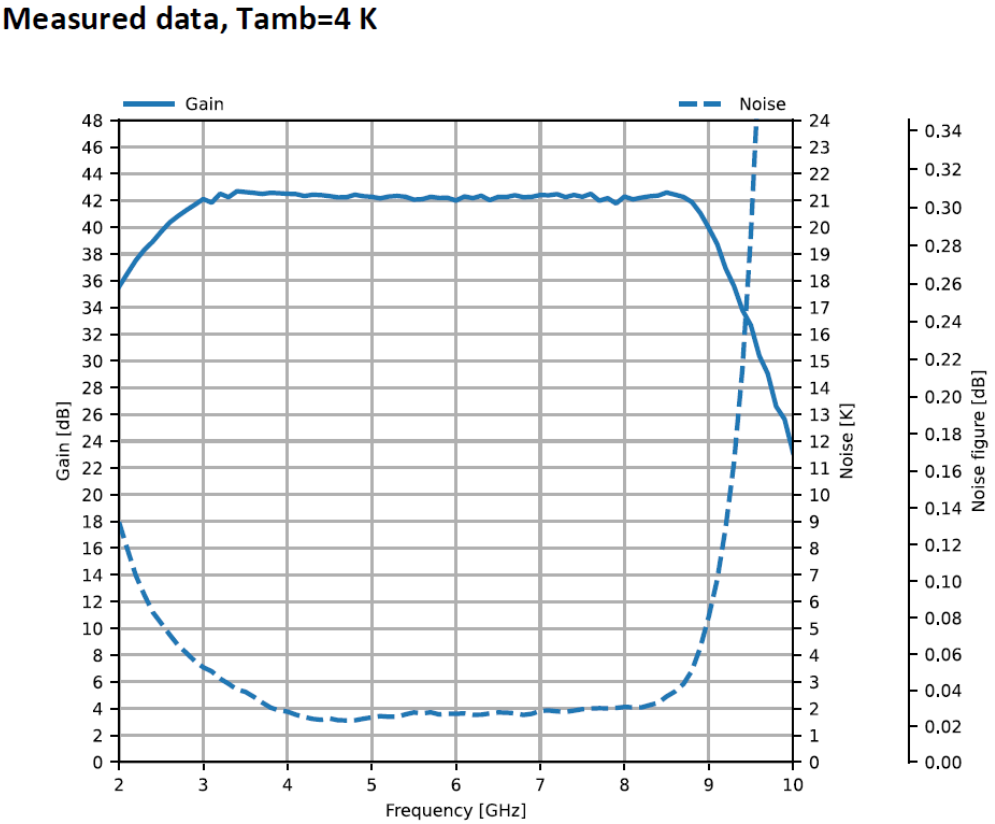

Figure 3.9: LNF-LNC-8C S/N 2355 HEMT gain and noise characteristics (11). This shows the improved gain performance compared to the HEMT shown in Figure 3.8, reaching a gains of approximately 42 dB and noise temperatures of approximately 1.8 K for the 4 to 8 GHz octave of interest.

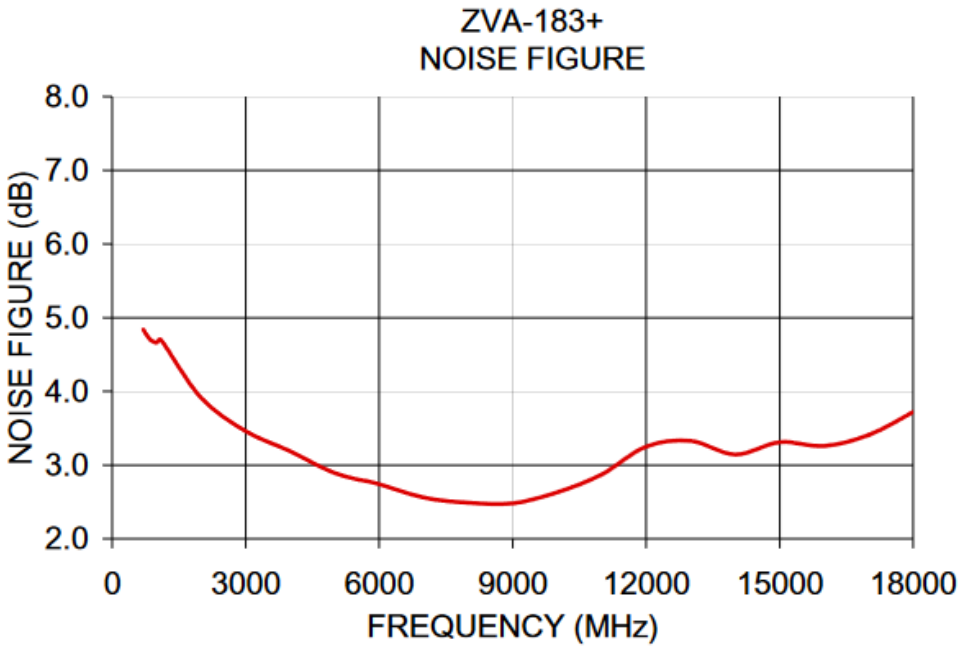

Figure 3.10: ZVA-183+ room temperature amplifier noise figure data giving noise figures of below 3 dB for the 4 to 8 GHz octave (12)

gain across a bandwidth of 0.7 GHz to 18 GHz with a noise figure of 3.2 dB to 2.5 dB, and a 1 dB compression point power of approximately 25 dBm. Meanwhile, the ZX60-83LN+ provides 21 dB of gain from 0.5 GHz to 8 GHz with a noise figure of 1.5 dB to 2.2 dB, and a 1 dB compression point power of approximately 20 dBm (see Figure 3.10 and Figure 3.11) (12) (13). Initially, the ZVA-183-S+ was used, but then it was noted that the ZX60-83LN+ provided a superior noise figure, while only costing a sixth of the price (€150 versus €900). While the cheaper option only supplies a bandwidth of 0.5 GHz to 8 GHZ, the HEMT amplifier already confines the frequency of operation to 4 GHz to 8 GHz. Thus, this cheaper amplifier was used to reduce the total cost-per-pixel figure of the system. However, it must also be noted that these cheaper amplifiers proved to be sensitive to overvoltage, causing them to malfunction, so slightly extra care must be used when using them. The main purpose of these room temperature amplifiers is to ensure that the full available dynamic range of the ADCs can be utilized.

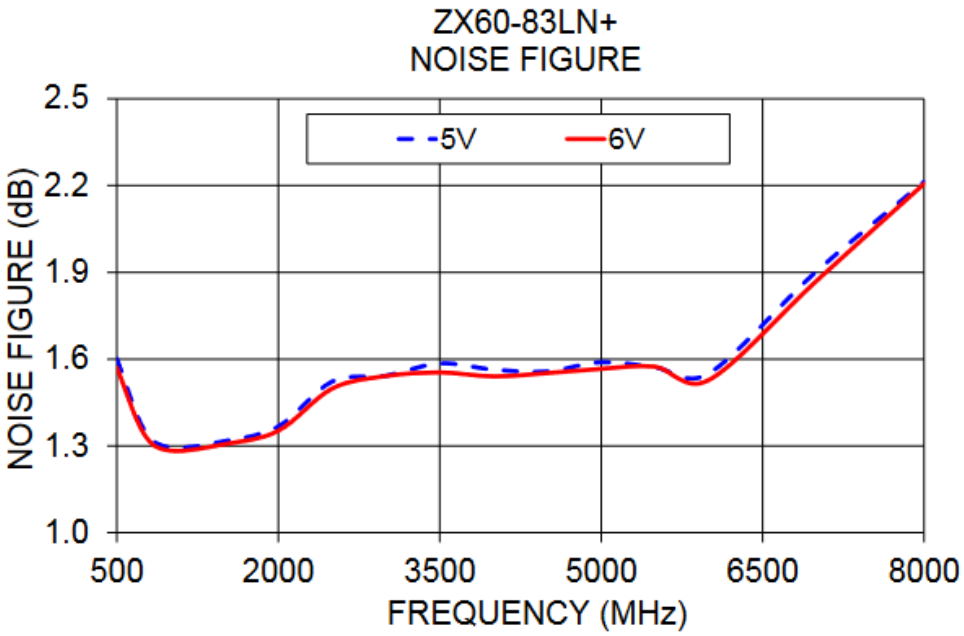

Figure 3.11: ZVX60-83LN+ room temperature amplifier noise figure data giving noise figures of below 1.6 dB for the 4 to 8 GHz octave (13)

3.5 Low Temperature Cabling

It is necessary to use special, superconducting cabling in the low temperature sections of the cryostat. This is to minimize the heat load on the mK stage of the ADR. Minimizing the heat load maximizes the hold time of the ADR. The hold time is the time for which the ADR can maintain its mK temperatures. Moreover, superconducting co-axial cables reduce the impedance, and thus the power loss, of the transmission line. The main source of heat load in the system is through thermal transport. Resistive heating in the system is almost insignificant due to the low currents involved. Thus, it is important to use low thermal conductivity cables, to reduce the thermal transport, as opposed to low resistance cables, to reduce the resistive heating. Superconducting co-axial cables need to be used for the GHz signals in and out of the MKID array, while low thermal conductivity wiring must be used for the DC signals which are used for the critical temperature measurement setup which is described in Section 3.7. For the GHz signals, Niobium Titanium

co-axial cables from Coax Japan are used at both the input and the output of the MKID array, reducing the transmission loss for the signals coming out of the array, while also minimizing the heat load. Meanwhile, for the DC signals, manganin low thermal conductivity loom is used. The only source of resistive heating in the system is in the DC power signals to the HEMT amplifier, where the source current is 100 mA. Thus, copper lines are used here, as copper's low electrical resistivity minimizes resistive heating, by $P = I^2R$.

Typically, materials with a high electrical conductivity also have a high thermal conductivity and vice versa. At 4 K, manganin has a thermal conductivity, $k_{manganin} = 5 * 10^{-1} Wm^{-1}K^{-1}$ and an electrical resistivity, $\rho_{manganin} = 4 * 10^{-7}\Omega m$, while copper has a thermal conductivity, $k_{Cu} = 200 Wm^{-1}K^{-1}$ and an electrical resistivity, $\rho_{Cu} = 5 * 10^{-10}\Omega m$. (97) Using these materials allowed the ADR to maintain a hold time of approximately 16 hours.

As the ADR has six SMA ports at each stage, it is capable of having three feedlines. With an input and an output co-axial cable for each feedline at each stage, it is important to ensure that none of these cables touch off of the cans of the ADR. This was because a touch could create a thermal short in the system, potentially preventing it from reaching mK temperatures, and reducing its hold time. In order to avoid this, care was taken to plan out the cabling with Solidworks, coming up with a cabling plan that allowed these superconducting co-axial cables to navigate from room temperature to mK stages without any touches. This is displayed in Figure 3.12.

3.6 Sample Boxes

The co-axial cables described in Section 3.5 carry the frequency comb waveform from the readout system to the MKID array, and also carry the output from the MKID array back to the readout system. Thus, it is necessary to a sample box on which the MKID array can be mounted and which can connect the co-axial cables

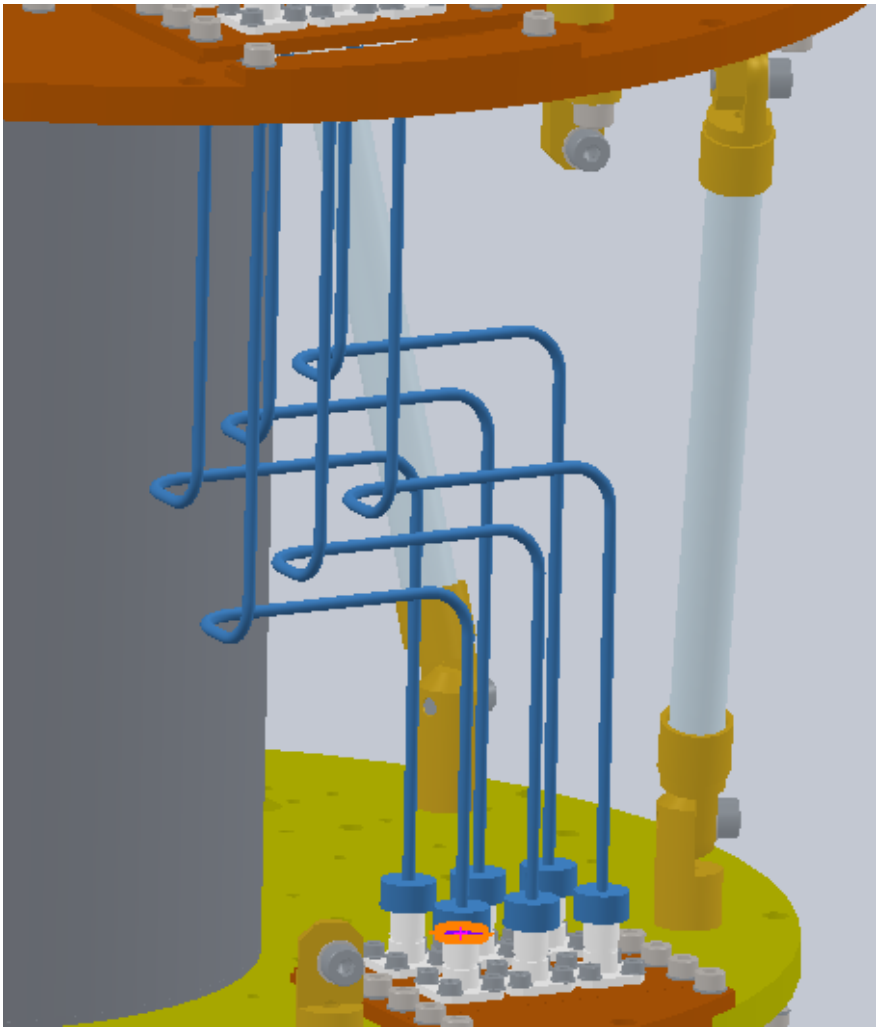

Figure 3.12: Superconducting semi-flexible co-axial cables Solidworks CAD plan. Six cables are needed to allow for three feedlines, with one cable for the input and one for the output. As space inside the ADR is limited, and each these six cables are all close together, it was neccessary to plan out the positioning of the bends in these cables such that they could all be mounted alongside each other in the ADR without any causing any thermal shorts. This figure shows the cable plan between the room temperature and 70 K stages. The same had to be done for the cabling between the 70 K and 4 K stages.

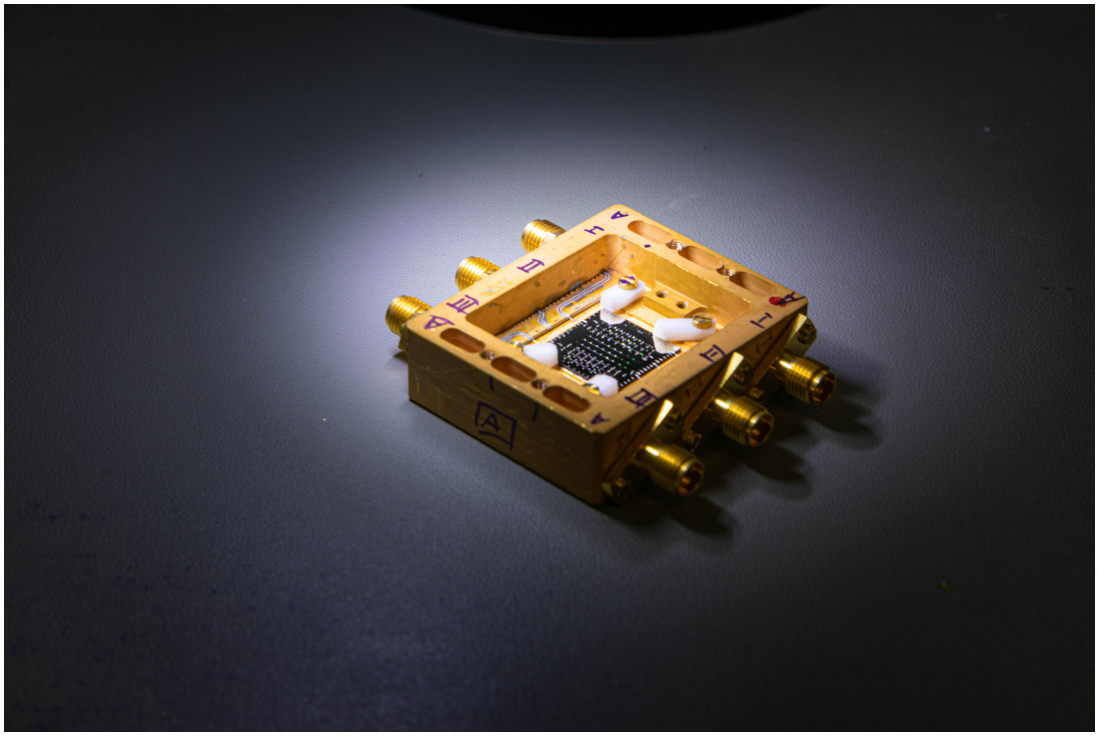

Figure 3.13: Gold plated oxygen free high conductivity Copper MKID sample box. Six SMA connectors allow for three feedlines to be connected. This sample box is mounted on the FAA plate, inside the magnetic shielding as shown in Figure 3.5.

to the arrays' feedlines. One of these sample boxes is shown in Figure 3.13. These boxes are made from oxygen free high conductivity (OFHC) copper, and are gold plated. Six cryogenic SMA connectors allow for three feedlines to be connected at once. Bonds are made between the feedlines on the chip and two printed circuit boards (PCBs) which are themselves soldered to the SMA connectors. These sample boxes are mounted onto the FAA (ferric ammonium alum) plate of the ADR. FAA is one of the paramagnetic salts used to achieve the magnetocaloric effect, and the FAA stage is the part of the ADR which achieves the coldest temperatures. The sample boxes are mounted facing out through the hole in the magnetic shielding, allowing them to be illuminated using a laser box. A Solidworks drawing showing a sample box mounted inside of the magnetic shielding can be seen in Figure 3.5.

3.7 Critical Temperature Measurement Setup

A critical temperature (T_C) setup has been constructed to allow the critical temperature of superconducting samples to be accurately measured. As such, a critical temperature setup was constructed to give better understanding of the behaviour of the MKIDs. To measure T_C, the resistance of the superconductor is monitored while the temperature in the cryostat decreases. At one instance, the resistance will rapidly drop to zero. The temperature at which this happens is the critical temperature. The resistance is measured using a 4-wire resistance measurement setup, where the current through, and voltage across a sample are measured simultaneously (by an ammeter and a voltmeter) and the resistance of the sample is determined in the usual manner using an I/V curve (based on Ohm's Law). This reduces inaccuracies caused by the resistance of the leads connecting the subject to the Ohmmeter. The resistance of the leads to the ammeter can be ignored as there is constant current through a closed loop, and the resistance of the leads to the voltmeter can be ignored as there is no current through an open circuit.

It is important to measure the resistance of the samples using an extremely low power resistance bridge. Otherwise, the excitation current from the resistance bridge will heat up the sample, causing inaccuracies in the measurements. As such, a Stanford Research Systems SIM921 AC Resistance Bridge is used to measure the critical temperature of the samples. This provides excitation powers of below 100 aW (98).

This resistance bridge connects to the ADR at room temperature using a D-sub connector and manganin loom runs from this connector to the mK stage. This loom is then soldered onto a pair of printed circuits boards (PCBs). A chip carrier containing the superconducting samples sits on top of these PCBs, thus connecting the low power resistance bridge to the samples which are to be measured.

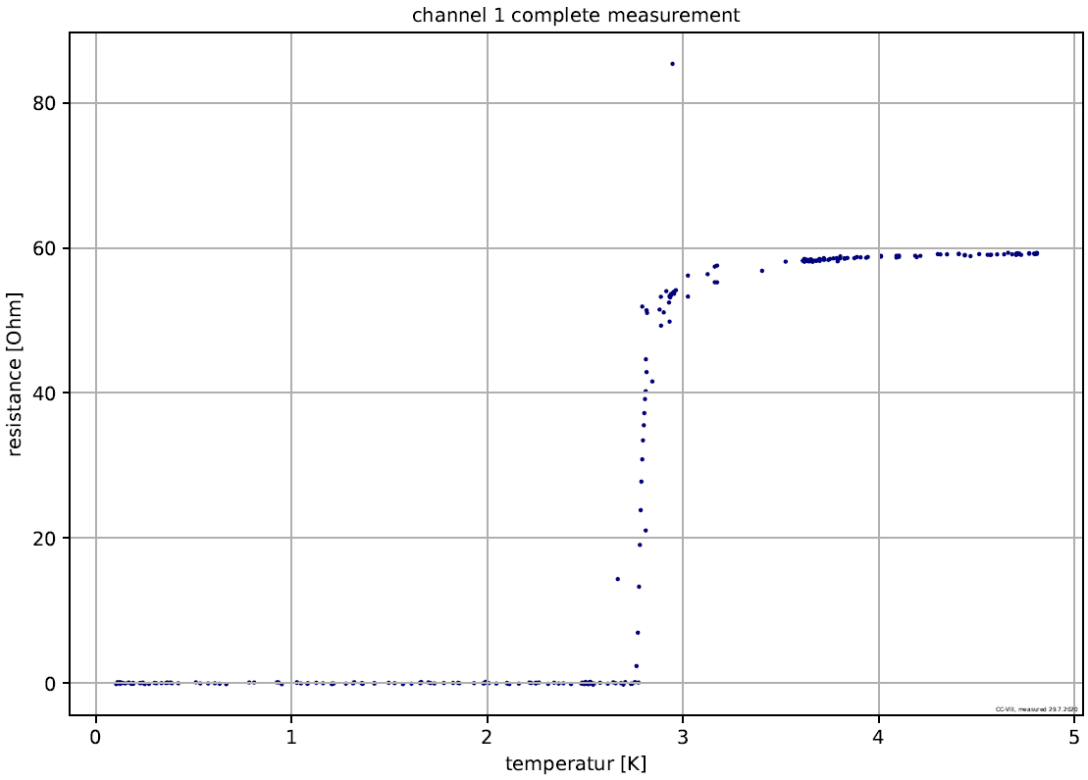

Figure 3.14: Critical Temperature Measurement for TiN_x on Silicon Showing a Critical Temperature of 2780 mK

This setup was used to optimize the recipe of the superconducting films which were then used to fabricate arrays. Before MKID arrays could be fabricated, it was important to optimize these recipes such that they had critical temperatures of $T_c \approx 1K$. T_c values of 1 K were desired as MKIDs are usually operated at a temperature of between $T_c/10$ and $T_c/8$ (5) (99), meaning that for the ADR's operating temperature of 100 mK, critical temperatures of between 800 mK and 1 K are desired.

Four such critical temperatures measurements, taken using the setup described above are shown in Figure 3.14, Figure 3.15, Figure 3.16 and Figure 3.17, with critical temperatures of 2780 mK, 1370 mK, 1160 mK and 1040 mK respectively. Various designs were tried, in order to achieve critical temperatures of $\approx 1K$ like which can be seen in Figure 3.17. Figure 3.14 and Figure 3.15 display TiN_x samples on silicon, fabricated in CRANN, differing in the ratio of Nitrogen to Argon used. Figure 3.16 and Figure 3.17 are Ti/TiN/Ti trilayers, differing by the thicknesses of

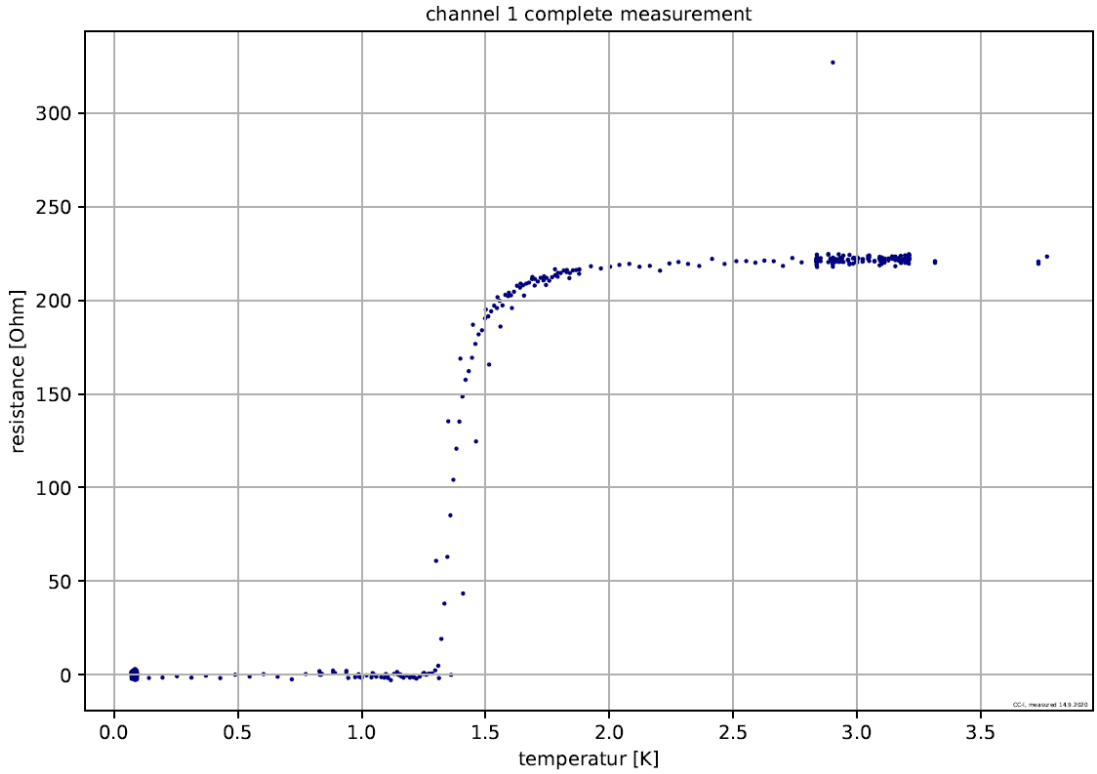

Figure 3.15: Critical Temperature Measurement for TiN_x on Silicon Showing a Critical Temperature of 1370 mK

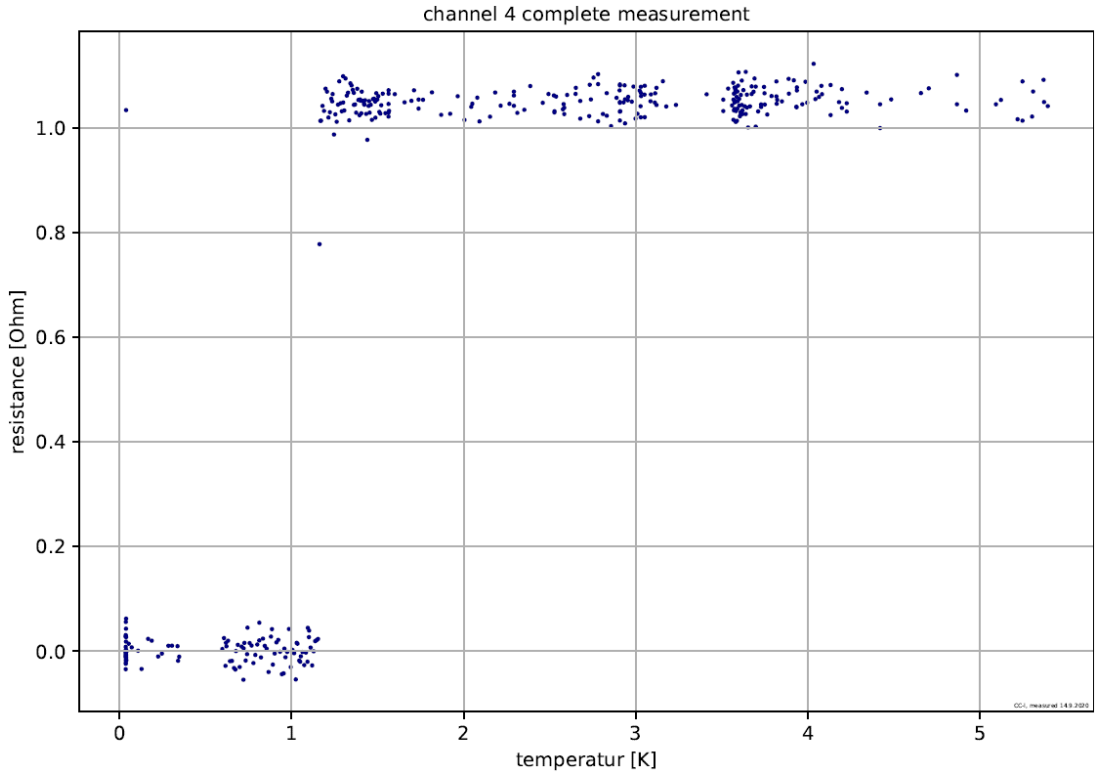

Figure 3.16: Critical Temperature Measurement for $Ti/TiN/Ti$ Tri-Layer Showing a Critical Temperature of 1160 mK

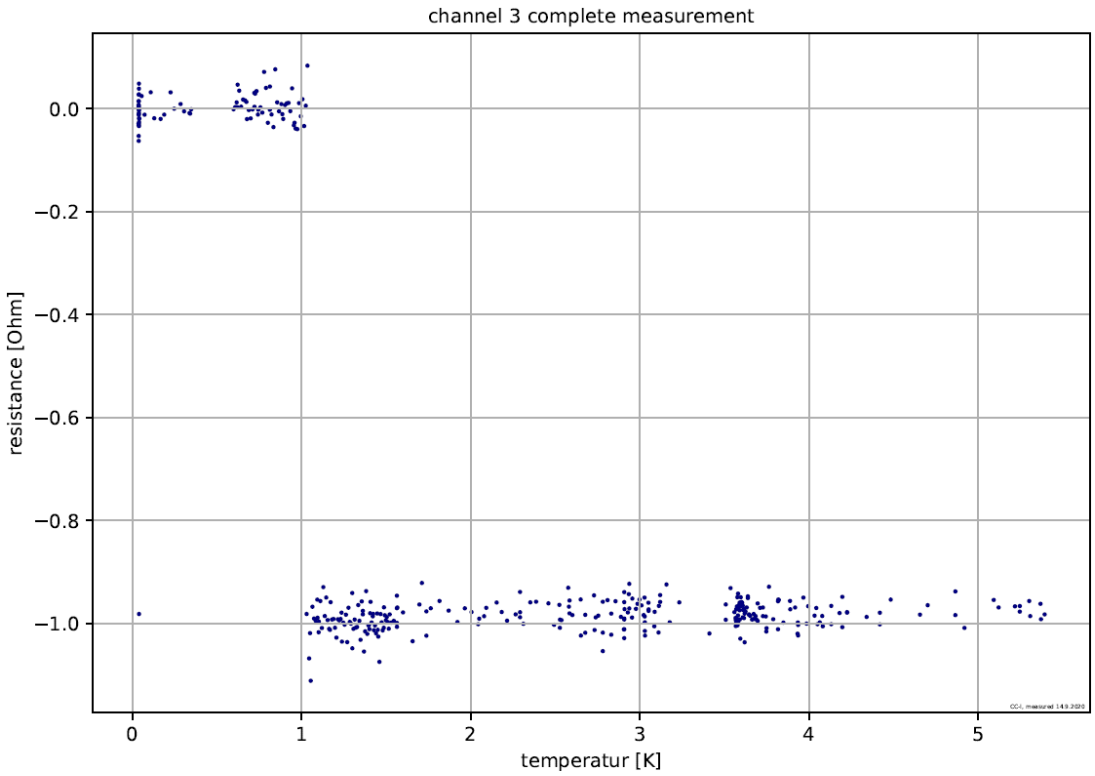

Figure 3.17: Critical Temperature Measurement for $Ti/TiN/Ti$ Tri-Layer Showing a Critical Temperature of 1040 mK. In this measurement the non superconducting resistance was measured as a negative value due to the sample being bonded in the wrong orientation.

the layers. Note that for Figure 3.17 the resistance begins as a negative value, due to it being bonded to its chip carrier in the wrong orientation.

3.8 Optical Setup and Infrared Filters

To properly characterize the MKID arrays made in this project, one of the key characteristics which need to be characterised is their energy resolution, $R = E/\Delta E$. To determine the energy resolution for an MKID, it has to be illuminated by a laser of known wavelength, and the MKID is then monitored for photon pulses. After a sufficient number of photon pulses are measured, they can be plotted as a histogram, from which the energy resolution can be calculated. This is explained in Section 1.5.1.

To do this, a laser box was constructed, capable of exciting MKID arrays with lasers with wavelengths of 450 nm, 635 nm, 808 nm, 980 nm, 1310 nm and 1550 nm. Light from these 6 lasers are coupled to a single fibre optic cable which is then connected to the entrance window of the cryostat, via a variable attenuator. As the 6 lasers are coupled to a single fibre, the MKIDs in the cryostat can be simultaneously excited by photons of 6 different wavelengths. Due to their inherent energy resolution an MKID will be able to distinguish between the photons from each of these six lasers, which each wavelength resulting in a different phase pulse height in the MKID's transmission.

The light from the fibre optic cable is then fed into the ADR's viewport. At this stage the light from the laser box enters the ADR through BK7 glass of the viewport. Between this point and the MKID array there are two stages of filtering, one at the ADR's 70 K can, and one at the ADR's 4 K can. It was important to ensure sufficient infrared filtering at this stages to ensure that the MKIDs were not swamped by infrared photons from both the room temperature and 70 K backgrounds. It is also important to note that the maximum filter dimensions was heavily constrained by the geometry of the ADR, and thus much work had to be

done to ensure that a filter was used which provided sufficient blocking to IR photons, while also fitting in the ADR's 70 K and 4 K cans without causing any thermal shorts. Based on the above, the design requirements for these filters was:

- Two filter stages, one at 70 K and one at 4 K.
- Total filter thickness of approximately 20 mm per stage.
- Transmission greater than 50% from wavelengths below 1400 nm.
- Transmission less than 0.5% for wavelengths above 1500 nm.

Here, the total thickness per stage is constrained by the available space in the ADR. The 50% transmission below 1400 nm is so that the MKIDs can be illuminated by optical and near-IR photons. It must be noted that UV photons are not a concern and thus the transmission below 400 nm is irrelevant. Also, while 50 % transmission will mean half of the incident radiation is blocked, is still more than sufficient photons to successfully characterize the MKIDs in the cryostat. Finally, the $< 0.5\%$ transmission above 1500 nm is to filter out these background IR photons. Of course, this optical setup is for characterizing MKIDs, and not for on-sky measurements. An optical setup for on-sky measurements would require stricter filter design requirements. Based on these requirements, the following filter setup was selected:

- **70 K stage:** 1 x 5 mm Asahi YSC1100 Super Cold Filter + 1 x 5 mm BK7 Filter
- **4 K stage:** 1 x 5 mm Asahi YSC1100 Super Cold Filter + 1 x 25 mm BK7 Filter

Figure 3.18, Figure 3.19 and Figure 3.20 show the transmission data of the 5 mm Asahi YSC1100 Super Cold Filter, 5 mm of BK7 and 25 mm of BK7 respectively. Note that the data for 25 mm of BK7 (Figure 3.20) is calculated from the data for 5 mm of BK7 (Figure 3.19). (14) (15)

As the main purpose of these filters is to filter out any infrared photons which may swamp the MKID arrays, and because these filters clearly provide enough transmission below 1450 nm to allow sufficient photons to excite the MKIDs such that they can be characterized for energy resolution, the next important thing to do was to look at the transmission data above 1450 nm and find the total possible transmission through these two stages of filtering. Figure 3.21 shows the combined transmission data for the to filter stages, calculated from the data displayed in Figure 3.18, Figure 3.19 and Figure 3.20. This gives a maximum transmission above 1450 nm of 0.028%, sufficiently below the design requirement of 0.5% maximum transmission. It should be noted that initially it was planned to use the same filtering at both 70 K and 4 K stages, i.e. 1 x 5 mm Asahi YSC1100 Super Cold Filter (made of fused silica) and 1 x 5 mm BK7 Filter at both stages. However, this was found to result in the quality factor of the MKIDs to be greatly reduced, implying that the 100 mk stage was indeed being swamped by infrared photons. It was then decided to increase the BK7 thickness at 4 K to 25 mm. While the transmission of the Asahi filters shown in Figure 3.18 shows good blocking for wavelengths above 1500 nm, the BK7 is important for ensuring good blocking for wavelengths even above 4000 nm. While there was no data available for the blocking characteristics of BK7 at extremely high wavelengths, it was found experimentally that there were no issues with long wavelength IR radiation from the ADR, provided that the filters were mounted.

Finally, it was important to verify that there was no issue with 4 K radiation striking the detectors, requiring another set of filters at the 100 mK stage. This was done by measuring the quality factor of MKIDs with the lid of the sample box both mounted and removed. With the lid on, no radiation from the 4 K stage would be able to strike the detectors. As there was no significant difference in the quality factors measured with and without the lid, it was determined experimentally that a further 100 mK filtering stage was not required.

With the laser box designed and built, and the correct infrared filters selected, the

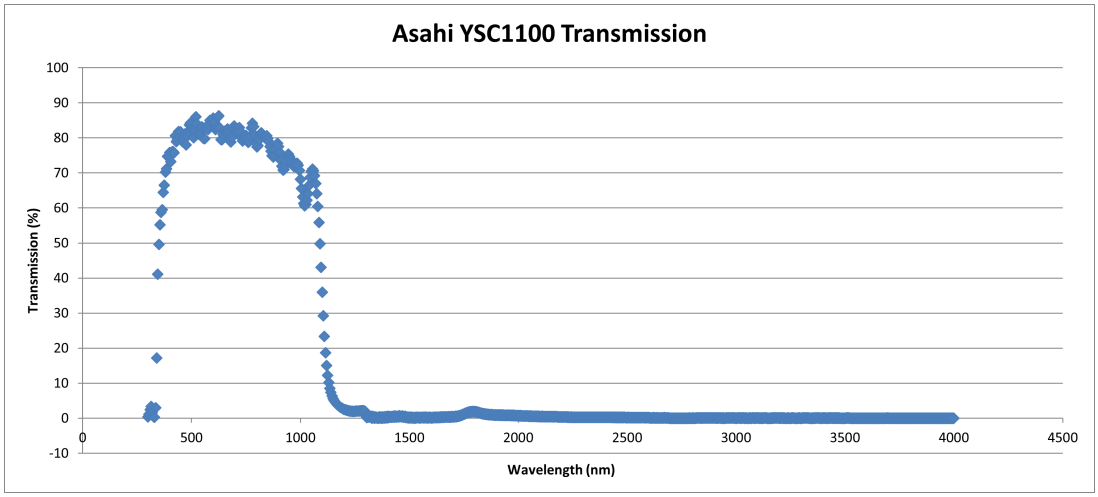

Figure 3.18: Asahi YSC1100 5mm Supercold Filter transmission data giving good transmission for wavelengths below 1100 nm (14). One of these is mounted at each of the 70 K and 4 K stages.

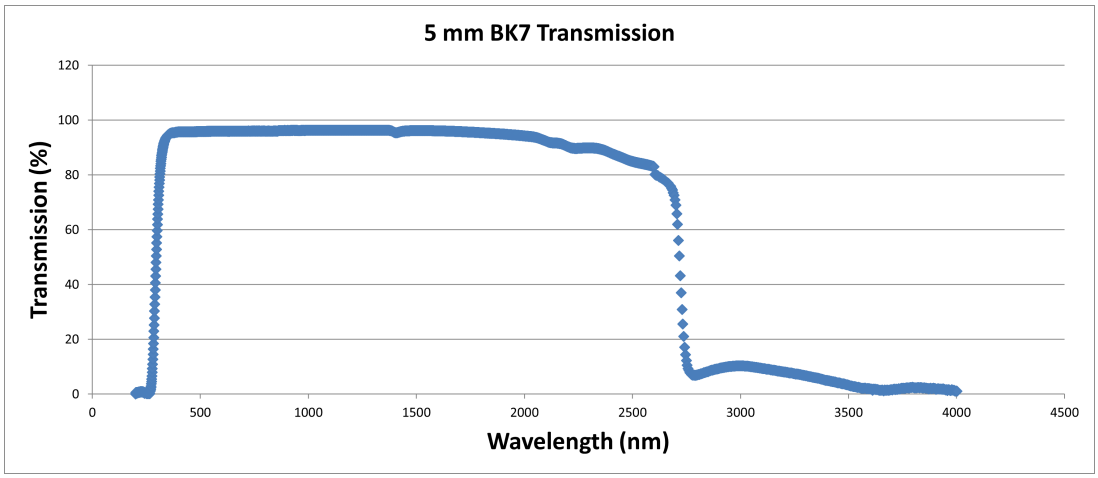

Figure 3.19: Transmission data for 5 mm of BK7 glass, showing good transmission for wavelengths below approximately 2500 nm (15). 5 mm of BK7 glass is mounted at the 70 K stages alongside one of the Asahi Supercold filters.

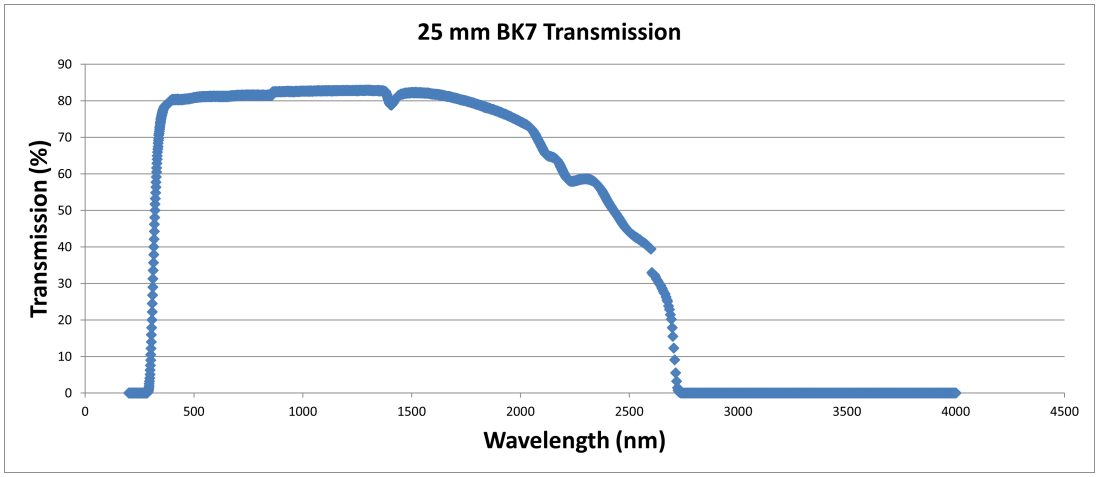

Figure 3.20: Transmission data for 25 mm of BK7 glass, calculated from the data given in Figure 3.19 (15). 25 mm of BK7 glass is mounted at the 4 K stages alongside one of the Asahi Supercold filters.

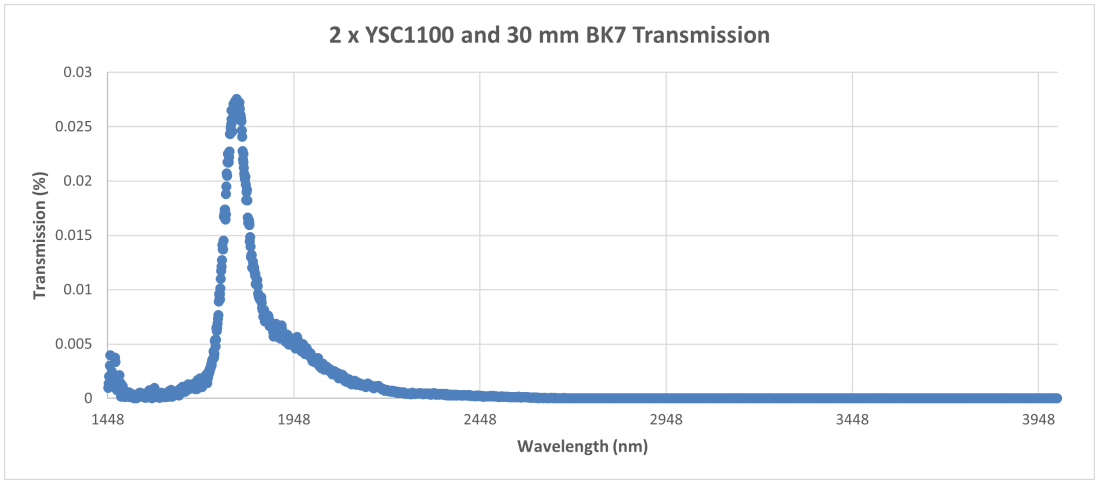

Figure 3.21: Transmission data for 2 Asahi YSC1100 Supercold filters and 30 mm of BK7 glass for wavelengths from 1448 nm to 4000 nm (14) (15). As good transmission is desired for wavelengths below 1400 nm, to allow for optical photons to strike the MKID array, it was only accessory to ensure good blocking for wavelengths above this wavelength. As this data shows the maximum optical transmission for wavelengths above 1450 nm to be 0.028 %, sufficiently below the design requirement of 0.5 %, two YSC1100 filters and a total of 30 mm of BK7 was deemed to be a suitable optical filtering setup for preventing the MKIDs from being swamped by room temperature infrared photons.

last necessary part of the optical setup was to design and build filter holders to mount the filters to the 70 K and 4 K cans of the ADR, without causing any thermal shorts which could reduce the hold time of the system . Two aluminium filter holders were designed with Solidworks, one at the 70 K stage to hold the 5 mm YSC1100 and 5 mm BK7, and one at 4 K to hold the 25 mm YSC1100 and 5 mm BK7. The 70 K and 4 K stage cans both have a removable view port upon which these filters were able to be mounted. These holder were manufactured by Trinity College Dublin, and Maynooth University workshops. The design for the 4 K filter is shown in Figure 3.22. The 70 K filter used the same design, albeit adjusted for 5 mm of BK7, as opposed to 25 mm.

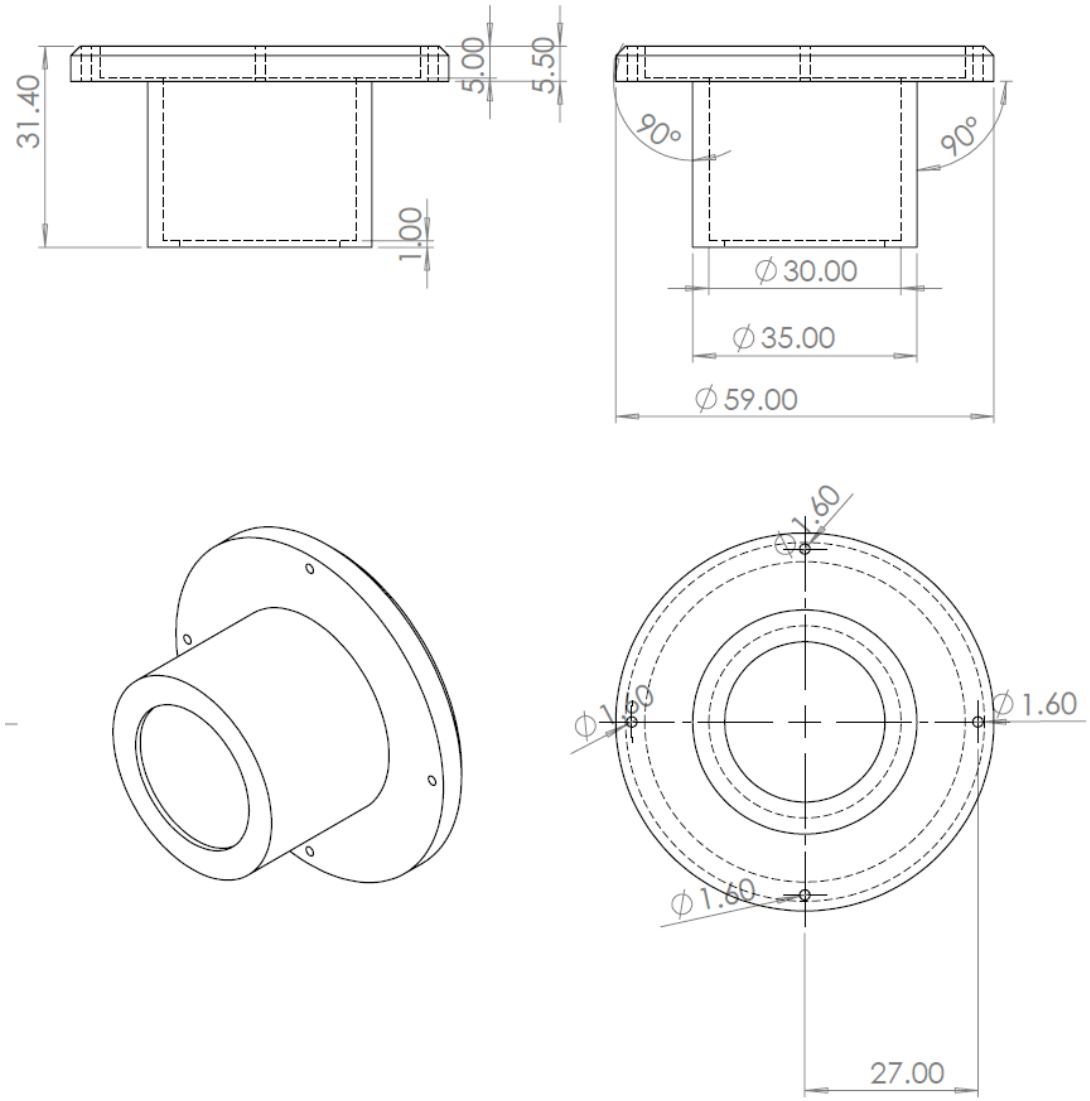

Figure 3.22: Solidowrks CAD design for the 4 K stage filter mount for the 5 mm Asahi YSC1100 Supercold filter and 25 mm of BK7 glass. A similar design was made for the 70 K stage filter mount for the 5 mm Asahi YSC1100 Supercold filter and 5 mm of BK7 glass. The filter holder is mounted to the ADR using copper screws, providing good thermalization between the filter holders and the ADR. All units are given in mm.

4 Resonator Analysis Code

In Chapter 3 the general experimental setup used in this project was described. It was briefly explained how a vector network analyser (VNA) is used to perform frequency sweep measurements on the MKID resonators in an array and how the MKID's quality factors, the total quality factor (Q), the coupling quality factor (Q_c) and the internal quality factor (Q_i), are calculated from this data. Much work was done writing control software to automate the VNA to perform frequency sweeps for each of the resonators in an array and to save this transmission data. Further code was written to take this data and fit it to the relevant equations from the literature and from these fits to obtain the quality factors. This chapter covers this work.

4.1 S-Parameters

Using a VNA, a frequency sweep can be performed across a defined frequency span, sourcing a signal from the VNA's port 1 with a defined power, and changing this frequency across the bandwidth of the sweep span with a defined step size, while maintaining a constant power. The output from port 1 is inputted the ADR, passing through the resonator array, before being amplified by the HEMT amplifier, passing back out of the ADR before being further amplified by the room temperature amplifier. This amplified signal is then inputted to the VNA's port 2. Thus, the VNA can measure the resonators forward transmission parameter, S_{21}.

S_{21} is an example of a scattering parameter or S-parameter. In a two-port network,

with ports 1 and 2, the S-parameter matrix can be written as:

$$b = S * a \tag{4.1}$$

Or:

$$\begin{bmatrix} b_1 \\ b_2 \end{bmatrix} = \begin{bmatrix} S_{11} & S_{12} \\ S_{21} & S_{22} \end{bmatrix} * \begin{bmatrix} a_1 \\ a_2 \end{bmatrix} \tag{4.2}$$

As linear equations this gives:

$$b_1 = S_{11}a_1 + S_{12}a_2 \tag{4.3}$$

And:

$$b_2 = S_{21}a_1 + S_{22}a_2 \tag{4.4}$$

In Equations 4.3 and 4.4 a_1 and a_2 are the waves travelling towards ports 1 and 2 respectively while b_1 and b_2 are the waves travelling away from ports 1 and 2 respectively. Thus, S_{21} is the ratio of the signal present at port 2 as a results of the signal sourced from port 1 and can be given by Equation 4.5 (16):

$$S_{21} = \frac{b_2}{a_1} \quad \text{where } a_2 = 0 \tag{4.5}$$

4.2 Vector Network Analyser Frequency Sweep Code

Thus, code was written for the VNA to automate the process of obtaining this S_{21} data. VBScript code was written which uses the SCPI (Standard Commands for

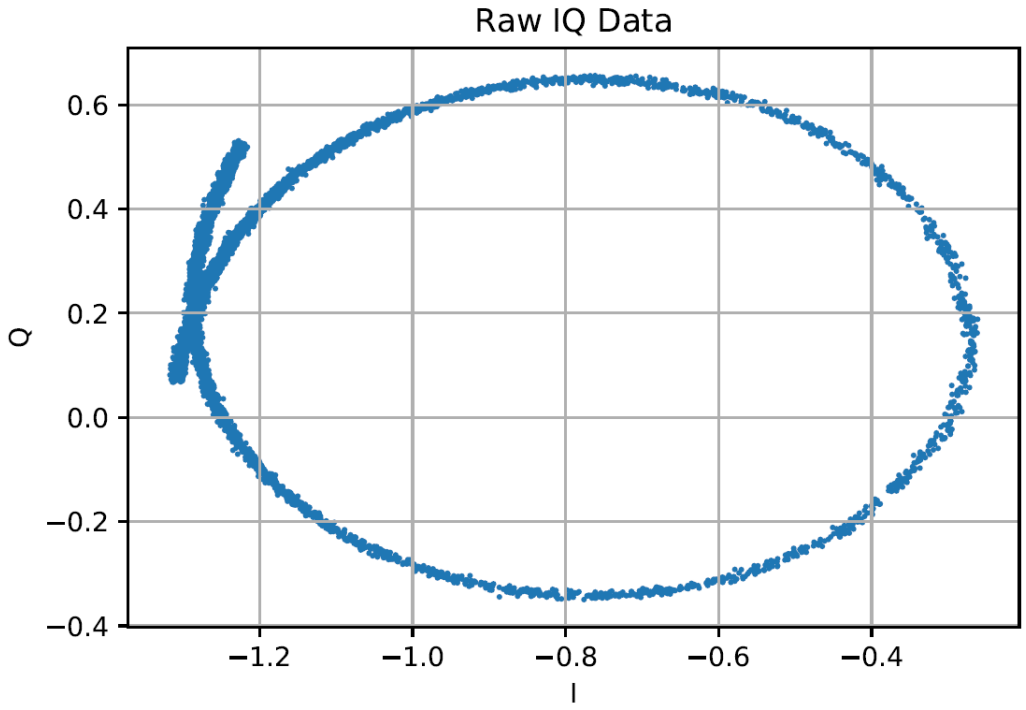

Figure 4.1: Sample IQ Frequency Sweep for a Ti/TiN/Ti MKID generated using a Keysight E5080A vector network analyser running the frequency sweep VBScript code included in Appendix A1.1. This code takes a list of frequencies and powers and performs a frequency sweep measurement for each of these frequencies, at the corresponding power, with a defined sweep bandwidth and number of steps in the sweep, and measures S_{21}, saving off the data in terms of I and Q.

Programmable Instruments) protocol (100) to control the VNA. SCPI is a standard set of commands for programming instrumentation. The VNA which was used was a Keysight E5080A ENA (101). This code takes an input of the frequency of the resonators which the user wants to analyze, the power at which they want to perform the frequency sweeps, and the bandwidth across which they want to sweep, and it saves off the S_{21} data for the resonators in question. This data is saved as raw, I/Q data. The VBSCript for code for performing these frequency sweeps is included in Section A1.1:

A sample IQ sweep, generated by this code for a Ti/TiN/Ti MKID with a resonant frequency of $f_0 = 5255.03 MHz$ is shown in Figure 4.1.

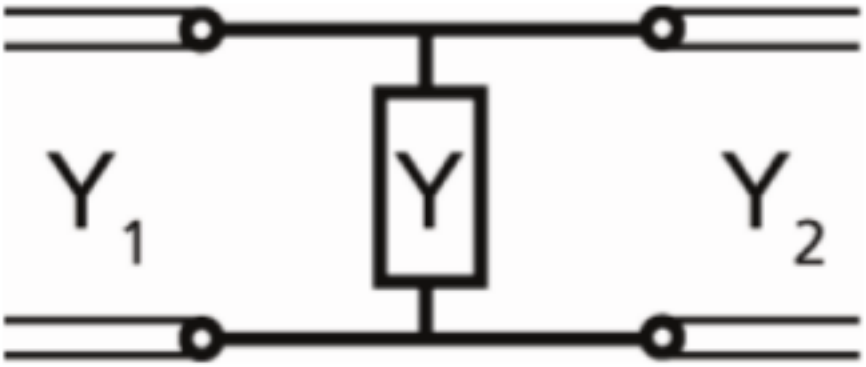

Figure 4.2: Shunt admittance circuit showing two feedlines with admittances Y_1 and Y_2, coupled to an admittance Y. This is equivalent to LC resonator circuit shown in Figure 1.5. (16).

4.3 Fitting Code

Now that code was written to reliably perform frequency sweeps across each resonator in an array, and to save off the I/Q data for each of these frequency sweeps, code was needed to take this data and fit it to some equation from which the total quality factor, Q could be obtained, and from this Q_i and Q_c could also be obtained.

The parallel LC tank circuit in Figure 1.5 can be simplified to a shunt admittance Y, coupled to two transmission lines with admittances, Y_1 and Y_2, as in Figure 4.2. Admittance is the reciprocal of impedance and here admittances are used as opposed to impedances as they allow for the maths to be simplified. RF circuit theory describes the S-paramaters for such a circuit (16). Scattering parameters, or S-parameters describe the scattering behaviour of high frequency signals in an electrical network. The S-parameters for the network shown in Figure 4.2 are given by the following matrix in Equation 4.6 (16):

$$\begin{bmatrix} S_{11} & S_{12} \\ S_{21} & S_{22} \end{bmatrix} = \frac{1}{D_S} \begin{bmatrix} Y_1 - Y_2 - Y & \sqrt{2Y_1Y_2} \\ \sqrt{2Y_1Y_2} & Y_1 - Y_2 - Y \end{bmatrix} \tag{4.6}$$

Here, $D_S = Y + Y_1 + Y_2$.

Thus, this gives:

$$S_{21} = \frac{2\sqrt{Y_1 Y_2}}{Y + Y_1 + Y_2} \tag{4.7}$$

From Figure 1.5, as the impedance of the transmission lines are Z_0, the admittance of the transmission lines can be given by:

$$Y_1 = Y_2 = \frac{1}{Z_0} = Y_0 \tag{4.8}$$

Moreover, with the admittance of an inductor given by $Y_L = \frac{1}{j\omega L}$, and the admittance of a capacitor as $Y_C = j\omega C$. The total admittance of two admittances in parallel can be found by simply adding them together. This gives:

$$Y = \frac{1}{j\omega L} + j\omega C \tag{4.9}$$

Thus, S_{21} can be written as:

$$S_{21} = \frac{2\sqrt{Y_0 Y_0}}{Y + Y_0 + Y_0} \tag{4.10}$$

$$\implies S_{21} = \frac{2Y_0}{Y + 2Y_0} \tag{4.11}$$

$$\implies S_{21} = \frac{2}{2 + \frac{Y}{Y_0}} \tag{4.12}$$

$$\implies S_{21} = \frac{2}{2 + YZ_0} \tag{4.13}$$

Substituting in the equation for Y gives:

$$\implies S_{21} = \frac{2}{2 + Z_0(\frac{1}{j\omega L} + j\omega C)} \tag{4.14}$$

$$\implies S_{21} = \frac{2}{2 + Z_0(j\omega C - \frac{j}{\omega L})} \tag{4.15}$$

$$\implies S_{21} = \frac{2}{2 + j(Z_0\omega C - \frac{Z_0}{\omega L})} \tag{4.16}$$

$$\implies S_{21} = \frac{2}{2 + 2j(\frac{Z_0\omega C}{2} - \frac{Z_0}{2\omega L})} \tag{4.17}$$

$$\implies S_{21} = \frac{1}{1 + j(\frac{Z_0\omega C}{2} - \frac{Z_0}{2\omega L})} \tag{4.18}$$

$$\implies S_{21} = \frac{1}{1 + j(\frac{Z_0\omega C}{2} - \frac{Z_0\omega C}{2}\frac{1}{\omega L}\frac{1}{\omega C})} \tag{4.19}$$

$$\implies S_{21} = \frac{1}{1 + j\frac{Z_0\omega C}{2}(1 - \frac{1}{\omega^2 LC})} \tag{4.20}$$

It has already been shown in Equation 1.20 that for an LC resonator circuit the resonant frequency of the circuit is $\omega_0 = \frac{1}{\sqrt{LC}}$, and in Equation 1.27 that its quality factor is $Q = \frac{\omega_0 Z_0 C}{2}$.

Thus, S_{21} can be further simplified to:

$$S_{21} = \frac{1}{1 + jQ(1 - \frac{{\omega_0}^2}{\omega^2})} \tag{4.21}$$

For the sake of simplicity, this is then rewritten in terms of x, where $x = \frac{\omega - \omega_0}{\omega_0}$.

For small perturbations from the resonant frequency $|\delta x| = |\frac{\delta\omega}{\omega_0}| \ll 1$ and $\omega = \omega_0 + \delta\omega$.

This allows the equation for S_{21} to be rewritten as:

$$S_{21} = \frac{1}{1 + jQ(1 - \frac{{\omega_0}^2}{(\omega_0+\delta\omega)^2})} \tag{4.22}$$

$$\implies S_{21} = \frac{1}{1 + jQ(1 - (\frac{\omega_0}{\omega_0+\omega_0\delta x})^2)} \tag{4.23}$$

$$\implies S_{21} = \frac{1}{1 + jQ(1 - (\frac{1}{1+\delta x})^2)} \tag{4.24}$$

$$\implies S_{21} = \frac{1}{1 + jQ(\frac{(1+\delta x)^2-1}{(1+\delta x)^2})} \tag{4.25}$$

$$\implies S_{21} = \frac{1}{1 + jQ(\frac{1+2\delta x+(\delta x)^2-1}{1+2\delta x+(\delta x)^2})} \tag{4.26}$$

Since, $\delta x \ll 1$, $(\delta x)^2 \approx 0$.

$$\implies S_{21} = \frac{1}{1 + jQ(\frac{2\delta x}{1+2\delta x})} \tag{4.27}$$

And, since $\delta x \ll 1$

$$S_{21} = \frac{1}{1 + jQ(2\delta x)} \tag{4.28}$$

$$\implies S_{21} = \frac{1}{1 + 2jQ\delta x} \tag{4.29}$$

Thus, Equation 4.29 describes the complex forward transmission of a single, ideal

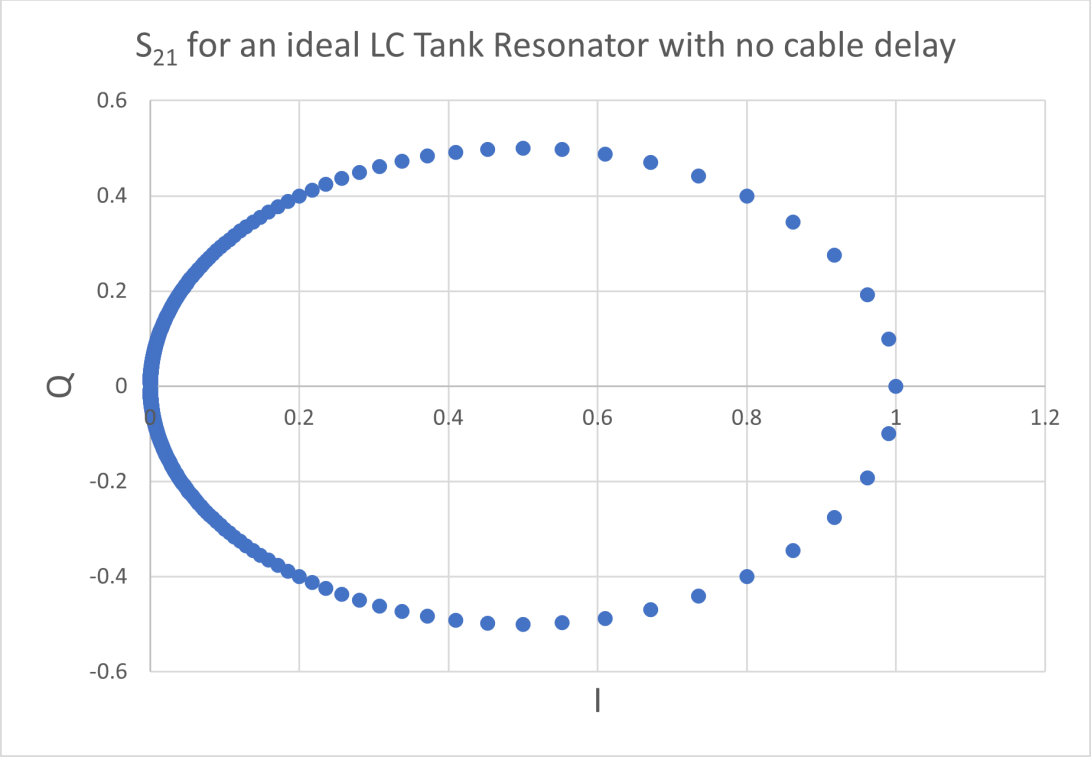

Figure 4.3: S_{21} for an ideal resonator with no cable delay, given by Equation 4.29.

LC resonator circuit, with no cable delay. This is plotted in Figure 4.3. Figure 4.3 differs from the data shown in Figure 4.1 as Equation 4.29 does not account for the cable delay of a resonator. Thus, the cable delay loop needs to be subtracted from the frequency sweep data before it can be fitted. After this it would seem like the data generated by the frequency sweep code could just simply be fitted to Equation 4.29. It was intended to use Python for this piece of code. Unfortunately, it was found that Python's curve fitting algorithm did not behave well when trying to fit to complex functions. Because of this, and based on the work by Gao (17), it was found that the best way to get around this problem was to separate Equation 4.29 into its magnitude ($|S_{21}|$) and phase (ϕ) components, which themselves could be fitted without running into any issues with complex numbers. Thus, S_{21} can be rationalized to $|S_{21}|$, giving:

$$|S_{21}| = \frac{|1|}{|1 + 2jQ\delta x|} \tag{4.30}$$

$$\implies |S_{21}| = \frac{1}{\sqrt{1 + 4Q^2\delta x^2}} \tag{4.31}$$

Furthermore, for simplicity, this was squared giving $|S_{21}|^2$:

$$|S_{21}|^2 = \frac{1}{1 + 4Q^2\delta x^2} \tag{4.32}$$

Substituting back in for δx gives:

$$|S_{21}|^2 = \frac{1}{1 + 4Q^2(\frac{\omega - \omega_0}{\omega_0})^2} \tag{4.33}$$

Finally, this is then used to fit the data to a skewed Lorentzian model, with constant background A_1, background slope A_2, maximum A_3 and skew A_4, as described by Gao (17) and Petersan and Anlage (102):

$$|S_{21}(\omega)|^2 = A_1 + A_2(\omega - \omega_0) + \frac{A_3 + A_4(\omega - \omega_0)}{1 + 4Q^2(\frac{\omega - \omega_0}{\omega_0})^2} \tag{4.34}$$

Thus, the data in Figure 4.1 had to be manipulated to give $|S_{21}|^2$ instead of S_{21}, and a model of the cable delay circle also had to be subtracted. At this point the data could be fitted to Equation 4.34.

Similarly to how Equation 4.29 could be manipulated to instead be in terms of $|S_{21}|^2$, it could also be manipulated to give the argument of S_{21}, written as $\phi(\omega)$. Starting with Equation 4.5, and taking its argument (denoted "arg()") (17):

$$\phi = arg(S_{21}) = arg(\frac{1}{1 + 2jQ\delta x}) \tag{4.35}$$

The argument of a complex number is given by taking the arctangent of the imaginary part divided by the complex part. To get the argument of Equation 4.29 it is easiest to use phasor algebra. Phasor algebra shows that the argument of a

fraction can be found by subtracting the argument of the denominator part from the argument of the numerator part. Thus:

$$\phi = arg(1) - arg(1 + 2jQ\delta x) \tag{4.36}$$

$$\implies \phi = \arctan(\frac{0}{1}) - \arctan(\frac{2jQ\delta x}{1}) \tag{4.37}$$

$$\implies \phi = -\arctan(2Q\delta x) \tag{4.38}$$

Substituting for δx gives:

$$\phi = -\arctan(2Q\frac{\omega - \omega_0}{\omega_0}) \tag{4.39}$$

$$\implies \phi = \arctan(2Q(1 - \frac{\omega}{\omega_0})) \tag{4.40}$$

Finally, including a term $-\theta_0$ denoting the starting phase angle of the IQ sweep data gives Equation 4.41.

$$\implies \phi = -\theta_0 + \arctan(2Q(1 - \frac{\omega}{\omega_0})) \tag{4.41}$$

Similarly, to how the raw data had to be manipulated to allow it to be fitted to Equation 4.34, the raw data can also be manipulated to allow it to be fitted for phase with Equation 4.41. First the cable delay needs to be fitted to a circle which is subtracted from the data in Figure 4.1. Next the resulting loop is translated to be centered around the origin, $(0, 0)$, and rotated such that the resonant point lies along the x-axis. Finally, this data can then be fitted to Equation 4.41.

Thus, there are now two equations to which the data generated by the frequency sweep code can now be fitted. Both of these equations, Equation 4.34 and Equation 4.41, contain a term for the total quality factor, Q, meaning this can now be easily obtained for any resonator in an array. Next, this must be used to obtain Q_i and Q_c. Zmuidzinas describes how Q_i and Q_c can be obtained from Q and $|S_{21}|$ by (103):

$$Q_i = \frac{Q}{min(|S_{21}|)} \tag{4.42}$$

And,

$$Q_c = \frac{Q}{1 - min(|S_{21}|)} \tag{4.43}$$

Thus, now Q, Q_i and Q_c can be obtained from the frequency sweeps generated by the VNA. A python script was written to read in the I/Q frequency sweep data for all of the resonators in the array and to fit it to Equation 4.34 and Equation 4.41. It was found that the most reliable way to operate this code was to first fit for $|S_{21}|$ and then to use the results of this fit as initial guesses in the fit for ϕ. Once the manipulated data is fitted to Equation 4.34 and Equation 4.41, the result of the fits can then be manipulated in the same way as described above, and combined to give an overall fit for the raw I/Q data in Figure 4.1. Thus, it is possible to generate a fit for the raw I/Q, in the complex plane, using Python despite the Python curve fitting algorithm's issues with plotting to complex functions. Figure 4.4 and Figure 4.5 are the results of fitting the frequency sweep data to Equation 4.34 and Equation 4.41 respectively. These plots also include the Q, Q_i and Q_c values calculated by the fits, as well as the resonant frequency value, f_0, calculated by the fits. Thus, for the Ti/TiN/TiN resonator shown in Figure 4.1, the calculated resonant frequency was $f_r = 5255.0324MHz$, and the calculated quality factors were $Q = 18717$, $Q_c = 23616$ and $Q_i = 90217$.

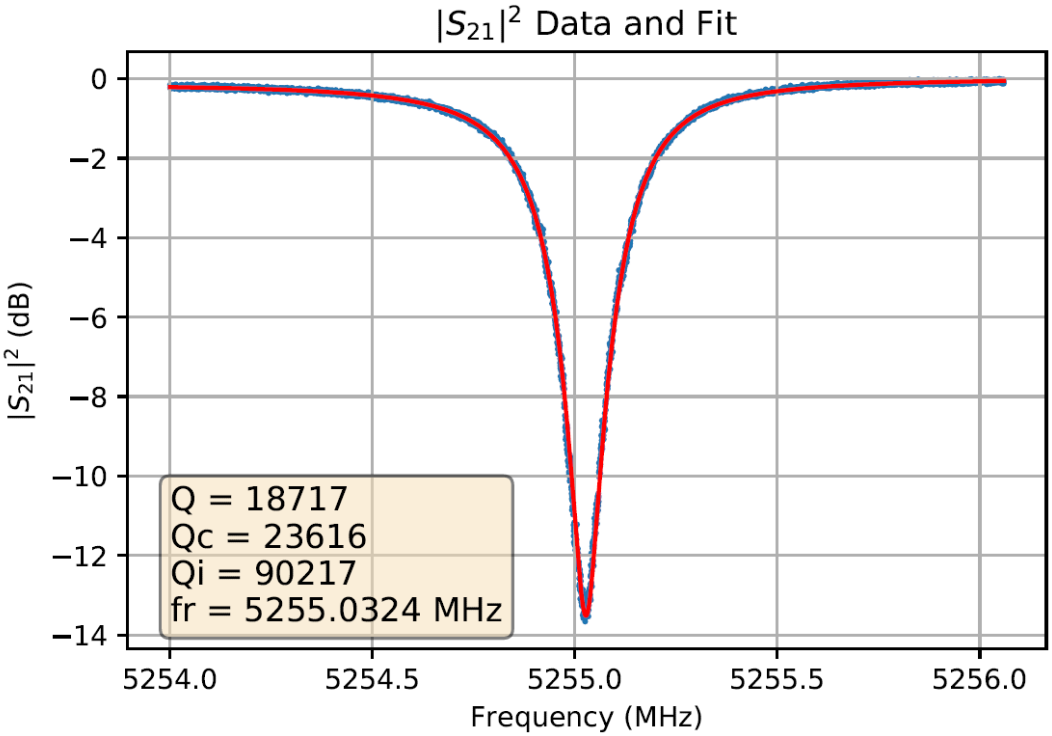

Figure 4.4: Sample $|S_{21}|^2$ frequency sweep (blue) and fit (red) for the same Ti/TiN/Ti MKID as shown in the sample frequency sweep in Figure 4.1 and fitted using the fitting code included in Appendix A1.2, giving $Q = 18717$, $Q_c = 23616$ and $Q_i = 90217$, with a resonant frequency of $f_r = 5255.0324 MHz$.

Once completed, this code was used to characterize the MKID arrays which were fabricated in Tyndall National Institute and CRANN (in Trinity College Dublin), and the information gained from this analysis was then used to inform future, always aiming to improve the internal quality factors of the resonators. Figures 4.7 to 4.12 show frequency sweeps and fits in terms of S_{21} and I/Q for three successive MKID designs, showing successive improvements in quality factors.

The code described in this chapter, and used to generate Figures 4.7 to 4.12 is included in Section A1.2.

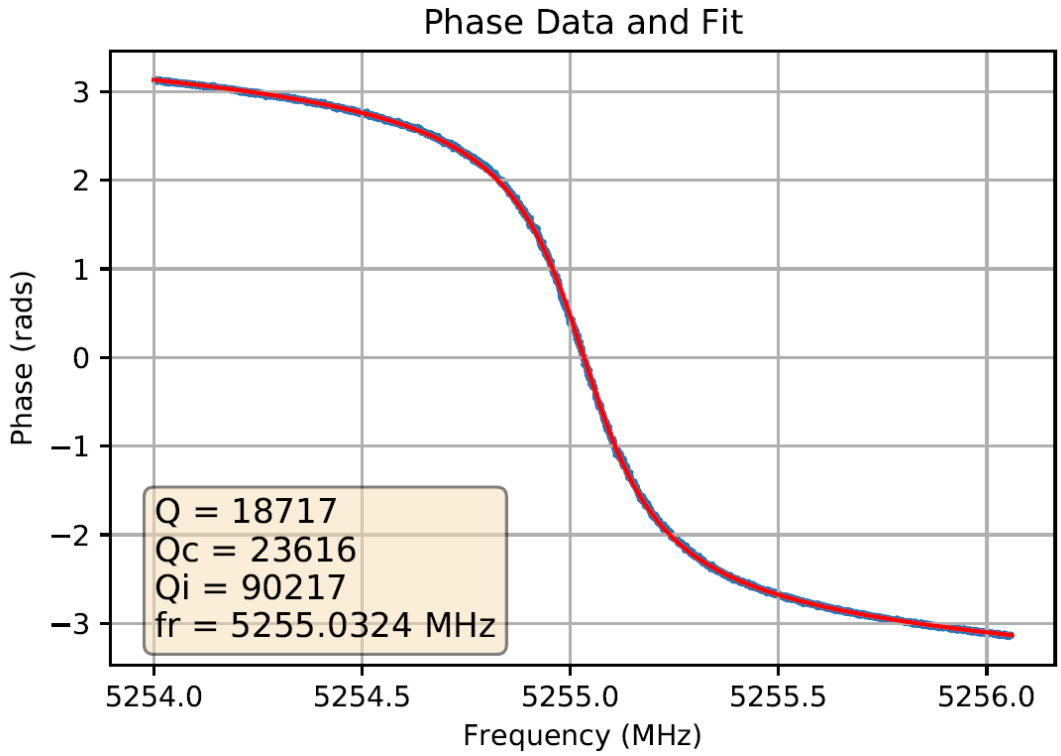

Figure 4.5: Sample frequency sweep (blue) and fit (red) in phase for the same Ti/TiN/Ti MKID as shown in the sample frequency sweep in Figure 4.1 and fitted using the fitting code included in Appendix A1.2, giving $Q = 18717$, $Q_c = 23616$ and $Q_i = 90217$, with a resonant frequency of $f_r = 5255.0324 MHz$.

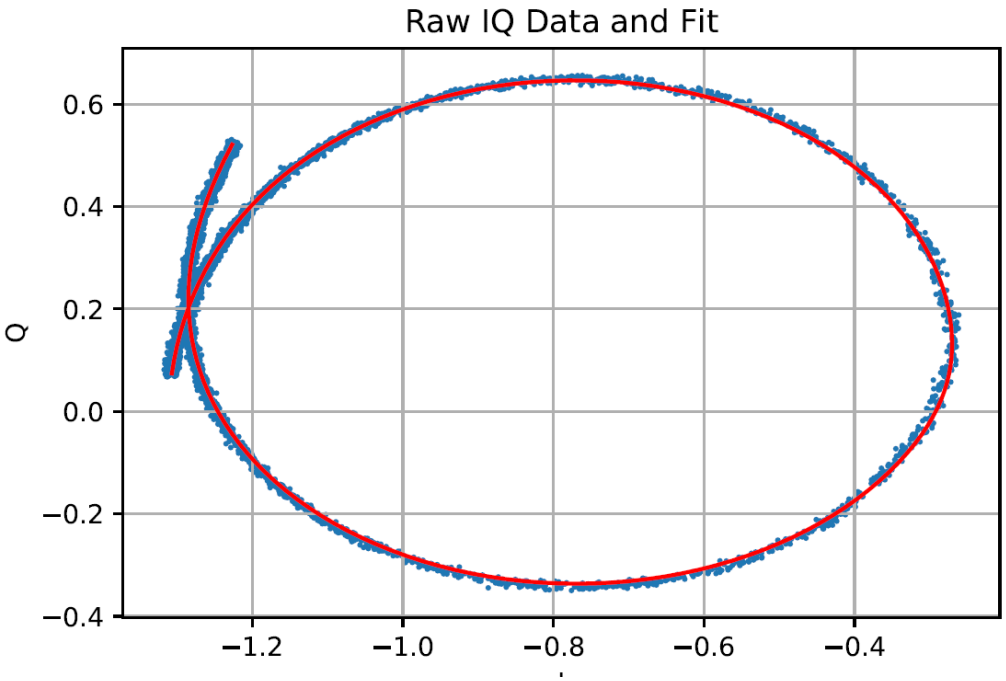

Figure 4.6: Sample frequency sweep (blue) and fit (red) in the IQ plane for the same Ti/TiN/Ti MKID as shown in the sample frequency sweep in Figure 4.1 and fitted using the fitting code included in Appendix A1.2, giving $Q = 18717$, $Q_c = 23616$ and $Q_i = 90217$, with a resonant frequency of $f_r = 5255.0324 MHz$.

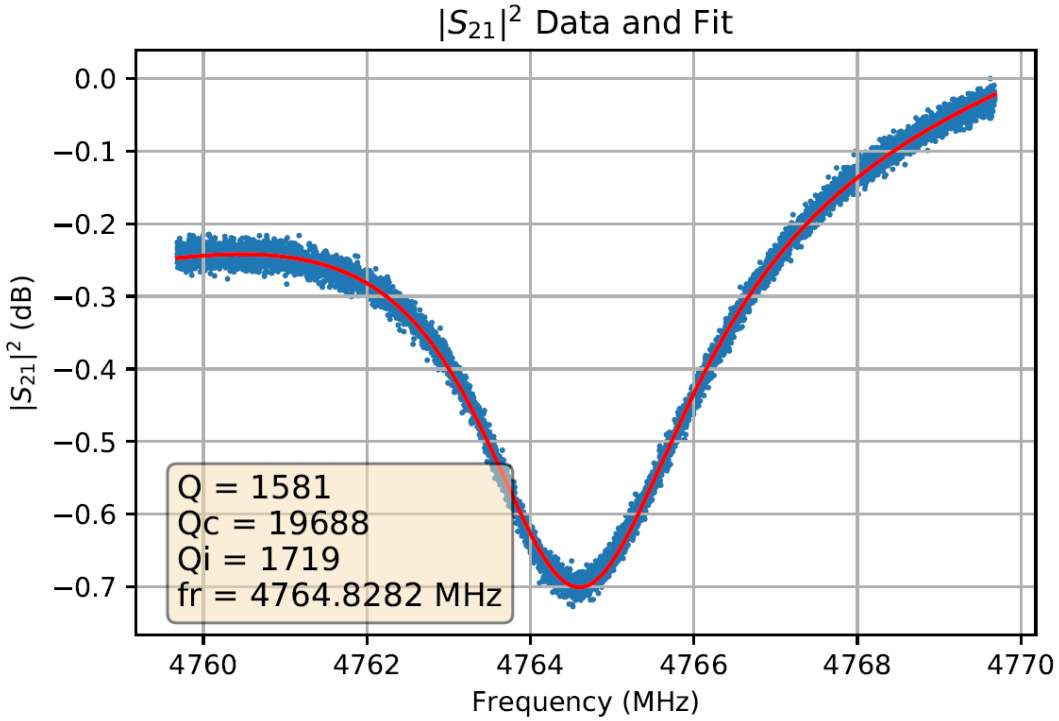

Figure 4.7: MKID design 1 $|S_{21}|^2$ frequency sweep (blue) and fit (red), giving $Q = 1781$, $Q_c = 22170$ and $Q_i = 1936$, with a resonant frequency of $f_r = 4764.811MHz$.

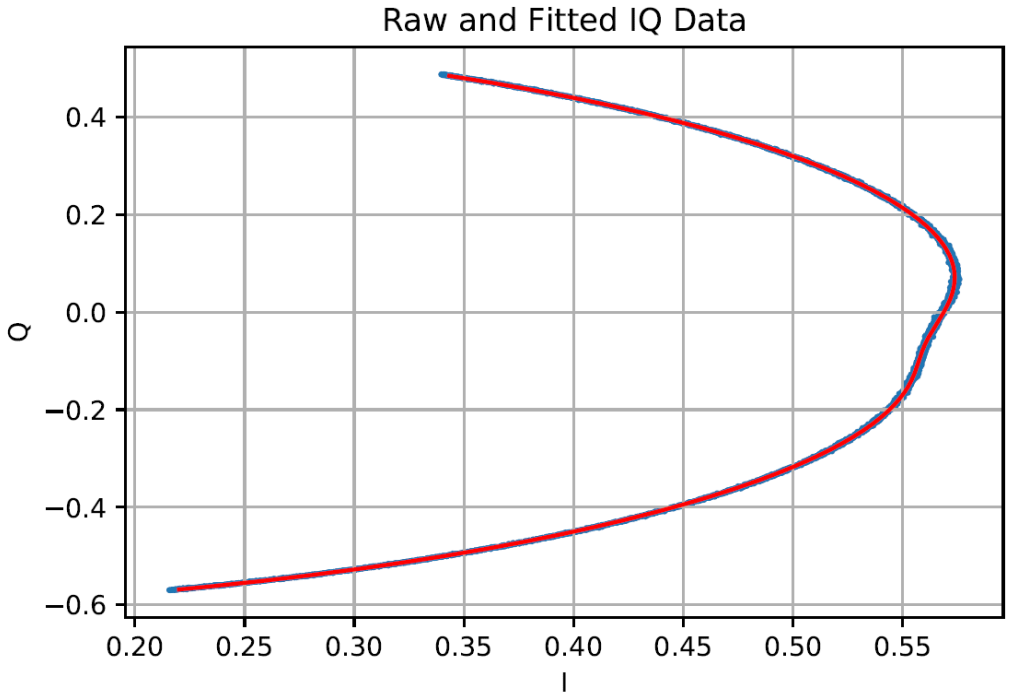

Figure 4.8: MKID Design 1 IQ frequency sweep (blue) and fit (red), giving $Q = 1781$, $Q_c = 22170$ and $Q_i = 1936$, with a resonant frequency of $f_r = 4764.811MHz$

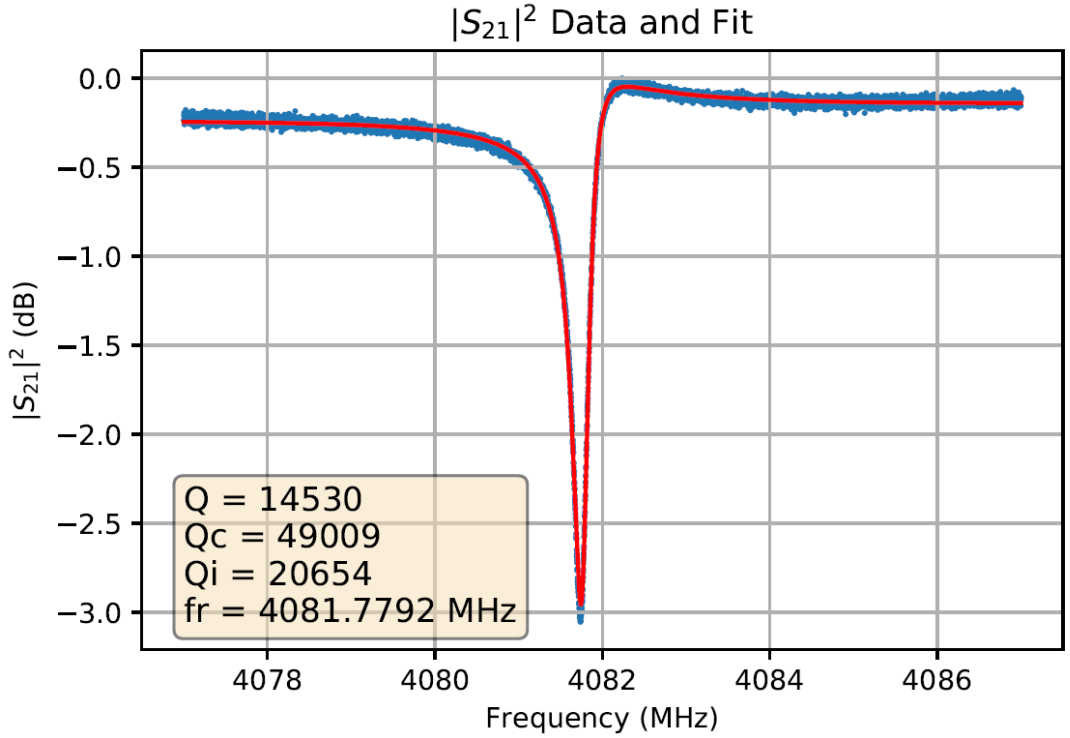

Figure 4.9: MKID Design 2 $|S_{21}|^2$ frequency sweep (blue) and fit (red), giving $Q = 13977$, $Q_c = 47144$ and $Q_i = 19868$, with a resonant frequency of $f_r = 4081.7789MHz$

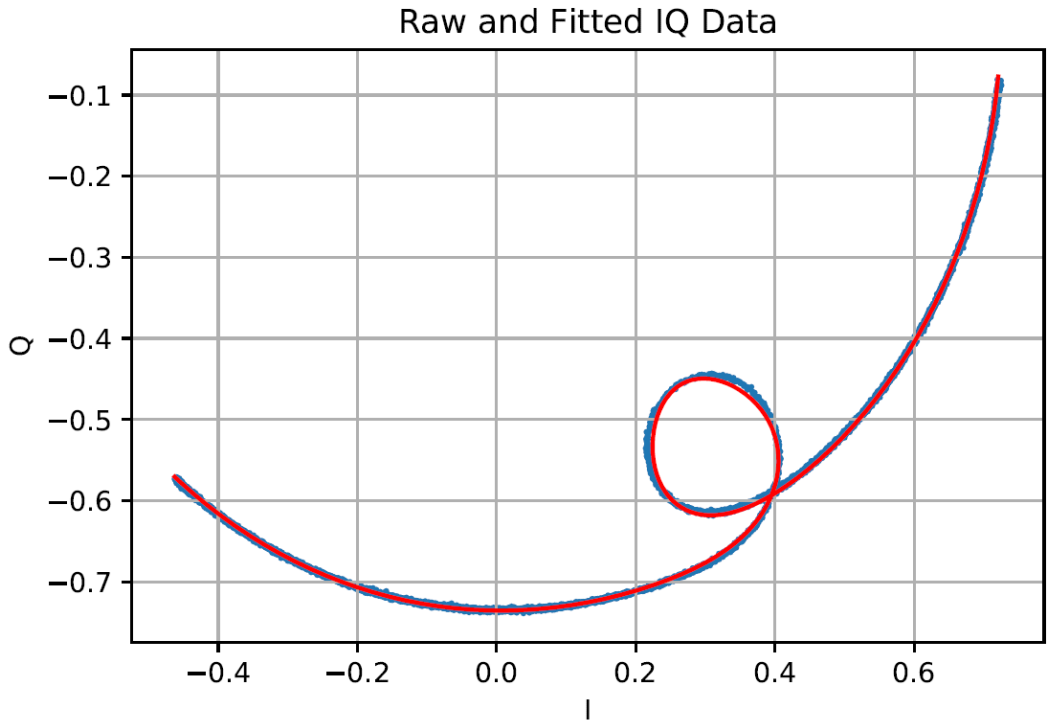

Figure 4.10: MKID Design 2 IQ frequency sweep (blue) and fit (red), giving $Q = 13977$, $Q_c = 47144$ and $Q_i = 19868$, with a resonant frequency of $f_r = 4081.7789MHz$

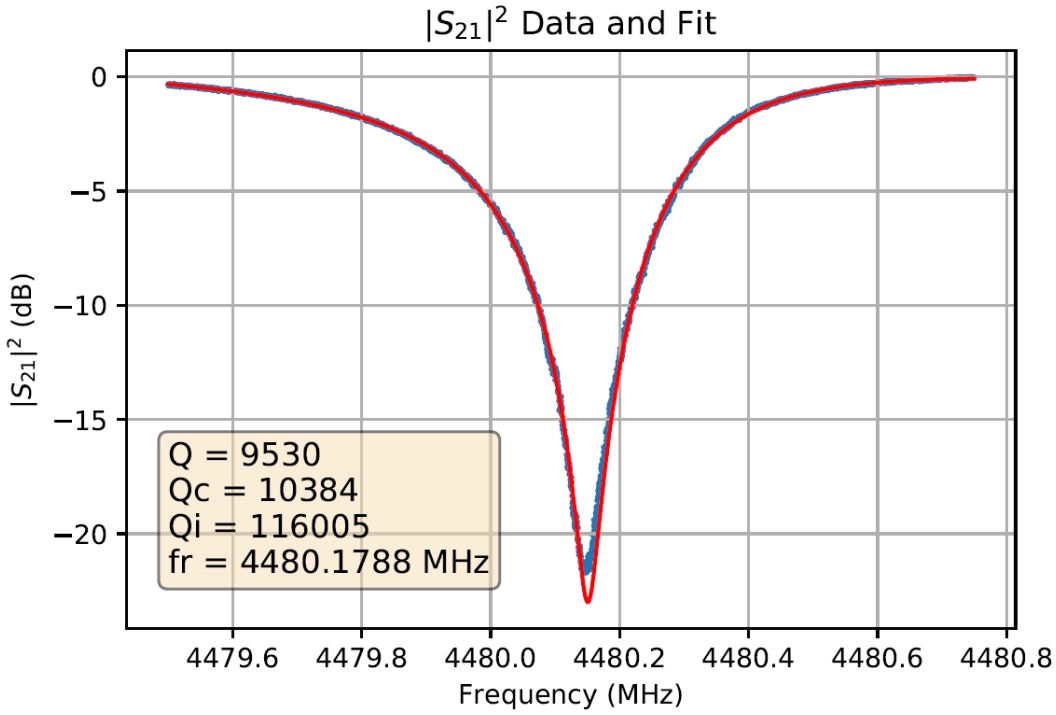

Figure 4.11: MKID Design 3 $|S_{21}|^2$ frequency sweep (blue) and fit (red), giving $Q = 9530$, $Q_c = 10384$ and $Q_i = 116005$, with a resonant frequency of $f_r = 4480.1788 MHz$

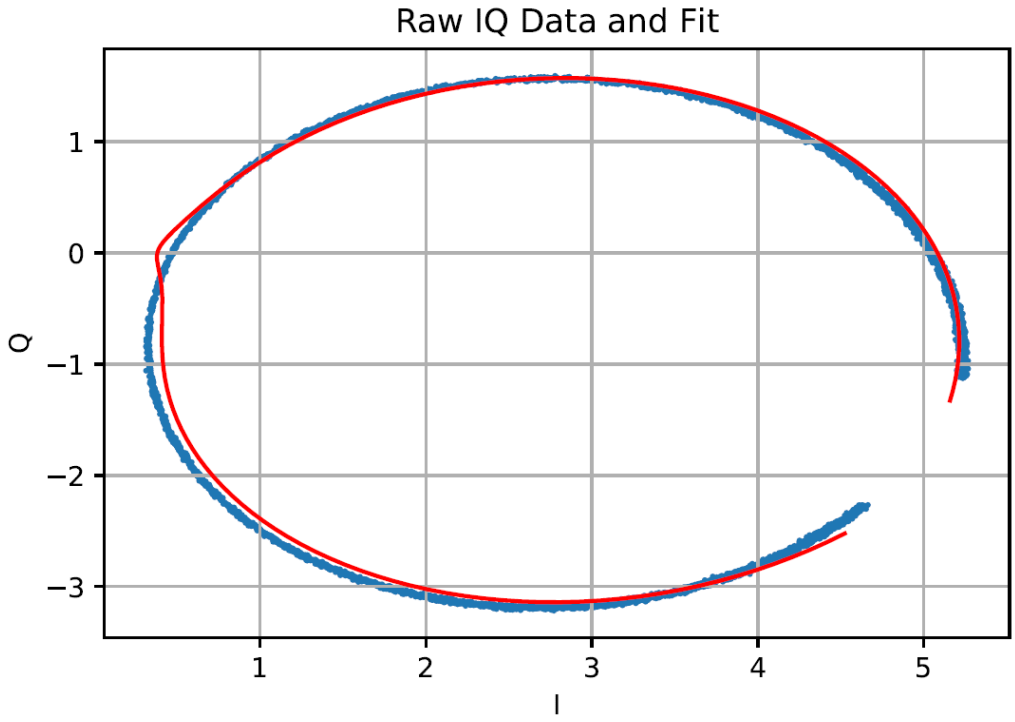

Figure 4.12: MKID Design 3 IQ frequency sweep (blue) and fit (red), giving $Q = 9530$, $Q_c = 10384$ and $Q_i = 116005$, with a resonant frequency of $f_r = 4480.1788 MHz$

5 ROACH Based Readout System

Section 1.6.2 mentions the Reconfigurable Open Access Computer Hardware (ROACH) 1 (8) board as an existing readout system, originally developed by the Collaboration for Astronomy, Signal Processing and Electronics Research (CASPER) (35) for radio astronomy applications, but later used for the ARCONS project (20) as an MKID readout. This board is manufactured by Digicom Electronics (104). Based on this, the initial readout system used in this project was a ROACH 1 based system, initially based on the firmware developed for ARCONS. This firmware was then modified to meet the demands of this project. This chapter will describe the work done with the ROACH 1 system and the results obtained using this system. Figure 5.1 displays one of these ROACH boards, while Figure 5.2 shows a Techne Instruments intermediate frequency mixer board (105) which is used to upmix the signals from the ROACH board, which are typically at MHz frequency, up to the frequency of the MKIDs, typically between 4 and 8 GHz.

5.1 CASPER Programming Approach

The work done programming the ROACH board was based on the philosophy of the CASPER collaboration, the group which developed the board (35). The CASPER philosophy is based on minimizing "time to science" in the development of astronomical instrumentation. This is done by developing open source hardware

Figure 5.1: Photograph of the ROACH board used in this project including the FPGA board board (blue) and the Techne Instruments ADC/DAC board (green).

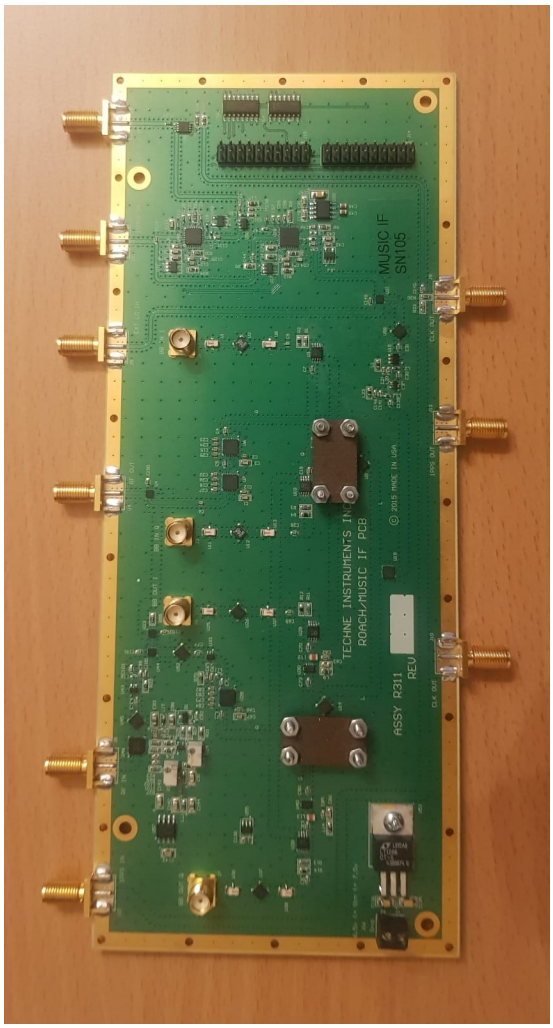

Figure 5.2: Photograph of the Techne Instruments intermediate frequency mixer board used in this project to upmix the baseband signals generated by the ROACH board from MHz to GHz frequencies, and also downmix the GHz frequency which come out of the ADR back to baseband frequencies.

platforms, such as the ROACH board, as well as re-usable, modular firmware libraries for programming this hardware. Typically, FPGAs are programmed using a hardware description language such as Verilog or VHDL. This is a low level, programming language that is used to program electronic devices, such as FPGAs or application specific integrated circuits (ASICs). The CASPER approach to programming FPGAs allows for a higher level of abstraction, being able to program the FPGA using pre-programmed blocks.

The CASPER approach for radio astronomy is based on digitization and channelization. Analogue signals received by a radio telescope are digitized by analogue-to-digital converters (ADCs), before being separated into a series of channels in frequency space by a fast fourier transform (FFT) and filter bank. This approach is also needed for reading out arrays of MKIDs, as MKID readouts also need to digitize the data signals coming out of the resonators, and then channelize this data to separate into a unique data stream for each resonator. This is why the CASPER open source hardware and firmware is also suitable for MKIDs. The main difference is that while for radio astronomy ADCs are needed to digitize the analogue data, for MKIDs digital-to-analogue converters (DACs) are also needed to generate the frequency comb which is used to excite the MKIDs in the array. The ROACH board shown in Figure 5.1 includes a Techne Instruments ADC/DAC board (bottom left), meaning that this setup can be used for MKID readouts. This consists of two 12 bit 550 mega-samples-per-second (MSPS) ADS54RF63 ADCs, and two 16 bit 1000 mega-samples-per-second (MSPS) DAC5681 DACs.
(106)

Using the CASPER approach, programming the ROACH board consists of two main steps:

- Writing firmware for the board using MATLAB Simulink and Xilinx ISE to do the digital signal processing (DSP).
- Writing Python code for the laboratory PC to interface with the ROACH

board's firmware.

The CASPER approach allows for Simulink blocks to be used to programme the firmware to perform complex signal processing tasks such as FFTs or filtering, without needing to write hardware description language (HDL) code such as VHDL or Verilog. This is because these Simulink blocks contain pre-written HDL code. Simulink can then connect each these individual blocks of HDL code together. These re-configurable CASPER blocks can be added to a Simulink model which can be compiled into a firmware file, typically a .bof or .bit file. This is an advantage as it allows for a higher level of abstraction, and simplifies the process of writing firmware for astronomical instruments. The ROACH board's FPGA can then be programmed with the firmware by loading these files onto it.

The Python scripts running on the laboratory PC can then be used to write to and read from registers in these firmware files. For example, the Python script can write a frequency value to a register in the firmware, which is then written to the DAC, telling it to output a signal at this frequency. Similarly, the data which is digitized by the ADC is also sent to a register by the firmware, and this can then be read by the Python code and saved on the PC.

5.2 Programming the ROACH Board

As explained in Section 1.6, the general approach for reading out arrays of MKIDs is to use frequency domain multiplexing (FDM) to divide the full bandwidth of interest (in this project this is 4 to 8 GHz) into a series of individual channels, such that each channel contains the signal from a single pixel, which is then monitored for photons pulses. Digital to Analogue Converters (DACs) generate a frequency comb at MHz frequencies, which are then upmixed to the frequencies of the MKIDs in the array using an intermediate frequency board (see Figure 1.10). Each signal in the upmixed comb consists of an I and Q component, with I referring to the in-phase and Q referring to the quadrature signals. This allows for both positive

and negative frequencies to be used.

These signals pass through co-axial cables, into the adiabatic demagnetization refrigerator (ADR), through the superconducting co-axial cables, and through the MKID array, with each MKID in the array being excited by the corresponding signal in the frequency comb. After exiting the MKID array the signals are amplified by the HEMT amplifier, and pass back through the superconducting co-axial cables, out of the ADR, through the regular co-axial cables, before being further amplified by the room temperature amplifier. Here the signals are downmixed back to MHz frequencies using the same local oscillator frequency as was used for upmixing, and divided into the separate I and Q components, and are re-digitized by the analogue-to-digital converter (ADC). Note that the ADR, co-axial cables, and the two stages of amplification are covered in Chapter 3.

Following the digitization of the baseband signals the FPGA performs the digital signal processing used to achieve this FDM process. The FPGA applies a polyphase filter bank, consisting of a finite impulse response (FIR) filter and fast Fourier transform (FFT), to divide the full bandwidth into a series of channels. The signals in each of these channels are then all downconverted to 0 Hz, and a low pass filter is applied to remove any other signals from the channel. Finally, pulse detection code is then applied to these downmixed signals.

This general approach, which was implemented on the ROACH, using the CASPER programming approach described above, is shown in Figure 5.3. Here, using the CASPER approach to program the ROACH board was advantageous due to the pre-existing firmware Simulink blocks for controlling the ROACH's ADCs DACs, as well as signal processing blocks for performing the FIR filtering and FFT needed for the polyphase filter bank, as well as the digital down conversion and low pass filtering. An example of these CASPER blocks are shown in Figure 5.4, showing the Simulink blocks which were developed by the CASPER community, and used in this project, to control the Techne Instruments ADC/DAC board (106). These blocks,

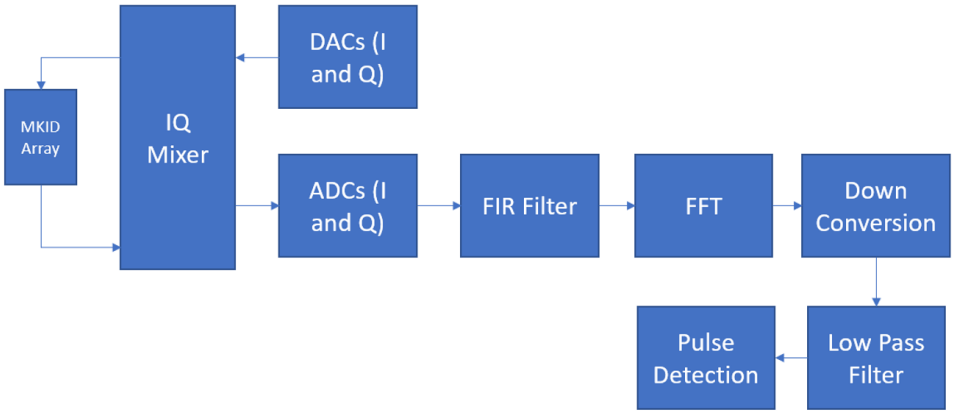

Figure 5.3: Flow diagram showing the approach used to read out arrays of optical MKIDs using frequency domain multiplexing (FDM) with the ROACH board in this project.

like the other CASPER blocks can be further modified by clicking them and defining the relevant properties, such as the clock speed.

5.3 Pulse Analysis Code

As already described, at the onset of this project the ROACH firmware and software developed for the ARCONS project (20) was used. However, it was soon realised that major changes would need to be made to this code for it to meet the needs of this project and to be capable of fully and accurately characterising prototype MKID resonators.

The first major requirement was to be able to use the ROACH board to monitor MKID pixels for photons, and save off a raw stream of both phase and a I/Q data for each pulse. The purpose of this was so that individual pulses could be looked at and analyzed, learning not only their pulse height (and thus being able to determine the energy resolution of the MKIDs), but also to be able to measure the pulses' rise and fall times. This is important data as the the fall time is related to the quasi-particle recombination time, and is needed to model these resonators.

This data is also used to create a model of a sample pulse which is used to design

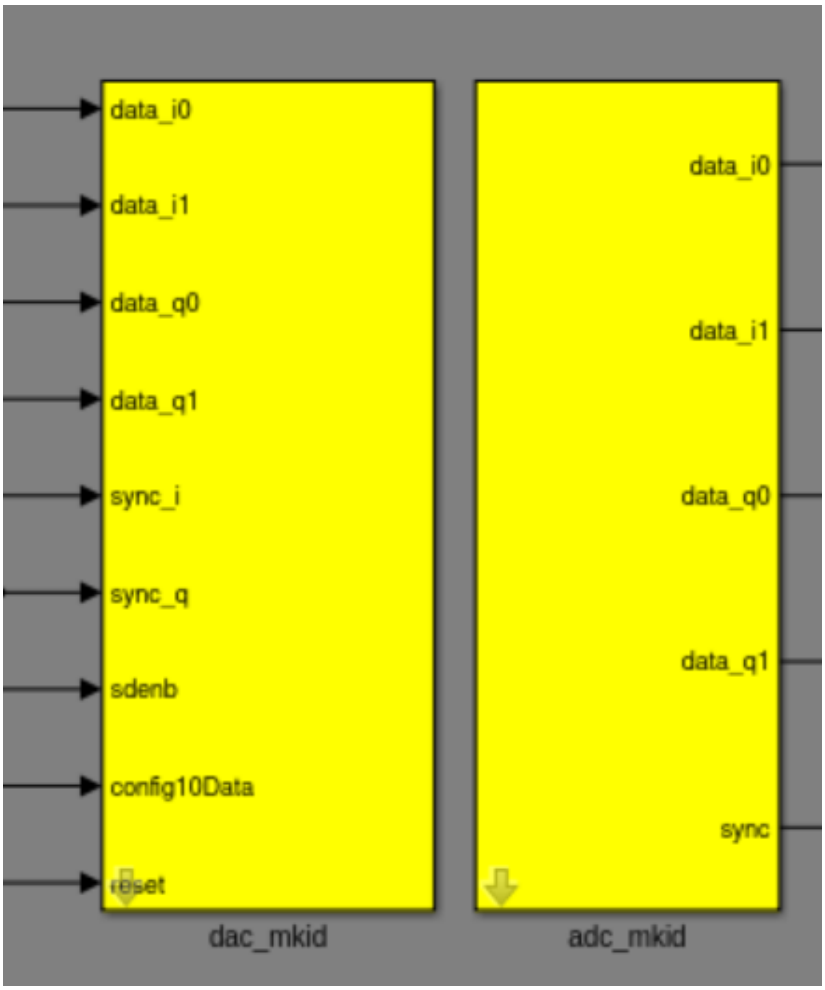

Figure 5.4: CASPER MATLAB Simulink blocks for controlling the Techne Instruments ADC/DAC Board used with the ROACH 1 readout system. These blocks allow for a higher level abstraction of programming the ROACH's FPGA. These blocks contain pre-written HDL code, meaning that the user can programme an FPGA by adding these blocks to a Simulink design, without having to write the HDL code from scratch, greatly speeding up the programming process. Blocks such as these are also available for performing an array of digital signal processing procedures, again without having to write the HDL code from scratch.

an optimal filter. When reading out an entire array of MKIDs, this optimal filter is used to calculate an accurate value for the pulse height. Thus, the raw pulse data needs to be saved off in order to properly characterize the MKIDs, before they can be used in a full kilo-pixel readout system (5).

While other groups have previously decided to use separate readout systems for reading out large arrays of pixels as for analysing pulses for single pixels, it was decided that it would be more economical to use a single system already capable of reading out large arrays, and to adapt this to also accurately characterise individual pulse data for prototype resonators. Thus, the pulse detection block shown in the flow diagram in Figure 5.3 had to be re-designed.

While the rise and fall times and the sample pulse model for the optimal filter can be calculated from the phase data, it is important to also save off the pulse data in terms of I and Q. This is because of the way in which FPGA's calculate the arctangent which gives the phase of the transmission by Equation 1.33. While other techniques can be used, such as using a look-up table, the main way in which FPGAs calculate certain mathematical functions, including trigonometric and inverse trigonometric functions such as arctangent, is to use the Coordinate Rotation Digital Computer (CORDIC) algorithm (38). CORDIC calculates these functions by replacing multiplications with a series of rotations, additions and substractions. This reduces the amount of hardware resources which need to be used to calculate the phase of the signal, especially the valuable DSP slices which are used for multiplications and which typically form the resource bottleneck.

While this CORDIC algorithm greatly reduces FPGA hardware resources needed to readout MKIDs, it was found to introduce some errors to our pulse analysis readout setup. It was noticed when saving off phase pulse data, that the phase signals often contained a noise element, consisting of distinct bands of noise. An example of this noise, introduced by the CORDIC algorithm is shown in Figure 5.5. Similarly, Figure 5.6 shows a cosmic ray measured with the ROACH system, with a pulse height of

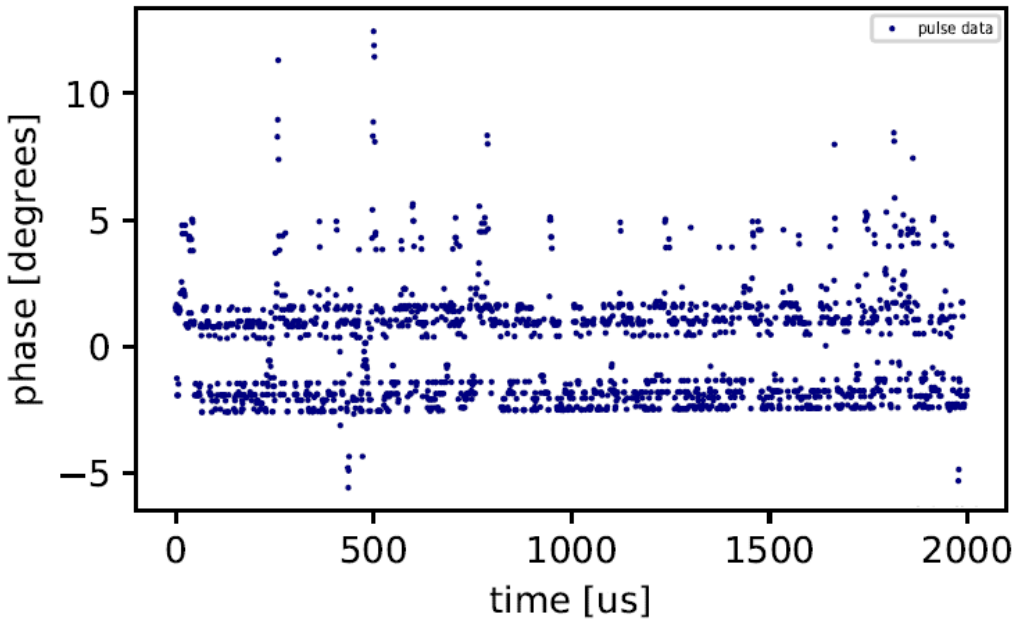

Figure 5.5: Example of the quantisation noise introduced by the CORDIC ARCTAN algorithm. This data was generated by monitoring a single pixel using the ROACH setup while it was in darkness. The phase value is calculated on the ROACH's FPGA using the CORDIC algorithm. This phase baseline clearly contains some un-physical element, manifesting as two distinct bands of noise. These are introduced by the CORDIC algorithm's quantisation error which is epsecially pronounced with small input signals.

approximately 125°, but also containing this quantisation noise in the phase baseline.

Hu (39) describes how the CORDIC algorithm introduces quantisation error into measurements, which is especially problematic when dealing with small signals. Thus, one way to minimize the effect of this was to ensure that the signal into the ROACH board's ADC was sufficiently amplified, ensuring that it uses the full range of the ADC. However, while this reduces the effect of the CORDIC algorithm's quantisation error, it could still introduce errors in these pulse measurements. In particular, as it would cause the readout to not give accurate pulse heights, this could effect any energy resolution measurements. Thus, in order to properly characterize the MKIDs in this project, the CORDIC algorithm would not be sufficient for arctangent calculations.

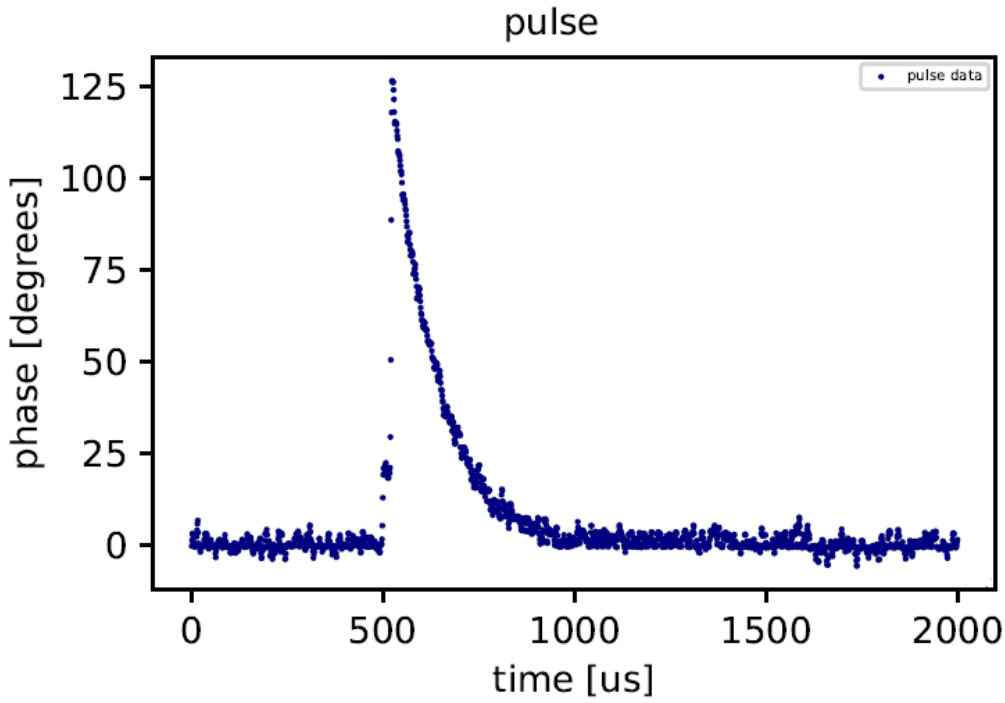

Figure 5.6: Example of a cosmic ray measured with the ROACH 1 setup, calculating the phase value using the CORDIC algorithm. While this signal clearly shows a pronounced phase pulse, the baseline contains the same quantisation noise element as in Figure 5.5. While this would not be an issue when using the system for reading out multiple pixels, only needing the maximum pulse height to resolve the photon energy, for pulse analysis of single pixels it is important that this pulse data is accurate.

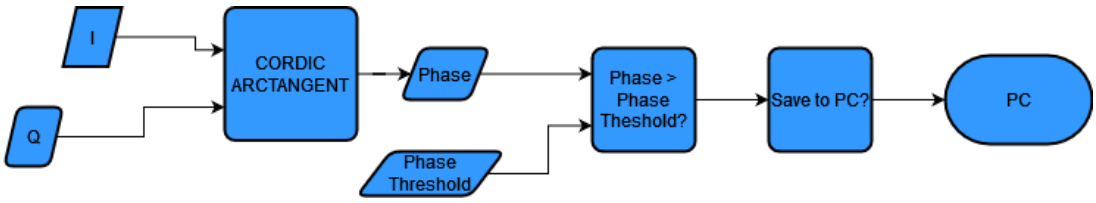

Figure 5.7: Flow diagram of process used to save phase data on FPGA. Phase is calculated on the FPGA using the CORDIC ARCTANGENT algorithm, and this phase value is compared to a defined phase threshold. If the phase value exceeds this threshold, it is deemed to be a pulse and a chunk of the phase data, consisting of 500 points before the pulse, and 1500 points after the pulse are saved to the PC. These pulses can then be plotted and analysed on the PC using Python.

As such, it was decided that for the single pixel readout, where individual pulses would be analysed, a different approach was needed. Instead, the stream of raw I and Q data on the FPGA would be sent to a buffer, and to the CORDIC block in parallel. The CORDIC block would calculate the arctangent, and this phase data would be compared to a threshold. However, when the phase value exceeded the threshold, instead of the phase data being saved, the raw I and Q data in the buffer would be saved to the PC. This data could then be plotted using Python, and the arctangent could be calculated from the raw I/Q data relative to the centre of the resonator IQ loop as per Equation 1.33 without any errors being introduced by the CORDIC algorithm. Figure 5.7 shows the original process used on the ROACH's FPGA, taking the I and Q data and using that to calculate phase, which is saved to the PC if it exceeds a pre-defined threshold, while Figure 5.8 shows the updated process which instead saves off the original I and Q data, when the phase exceeds the threshold.

The Simulink code used to achieve the process described in Figure 5.8 is shown in Figure 5.9. The block denoted "saveIQ" is a CASPER snapshot block which captures a chunk of data (inputted to "din"), whenever the trigger port ("trig") goes high. The "we" port of the snapshot block, when high, sends the chunk of data which is captured to the FPGA's block RAM (BRAM). The two yellow register blocks are inputs which can be written to by the user, in order to define the phase threshold and the channel to read out. The channel denotes for which MKID in the

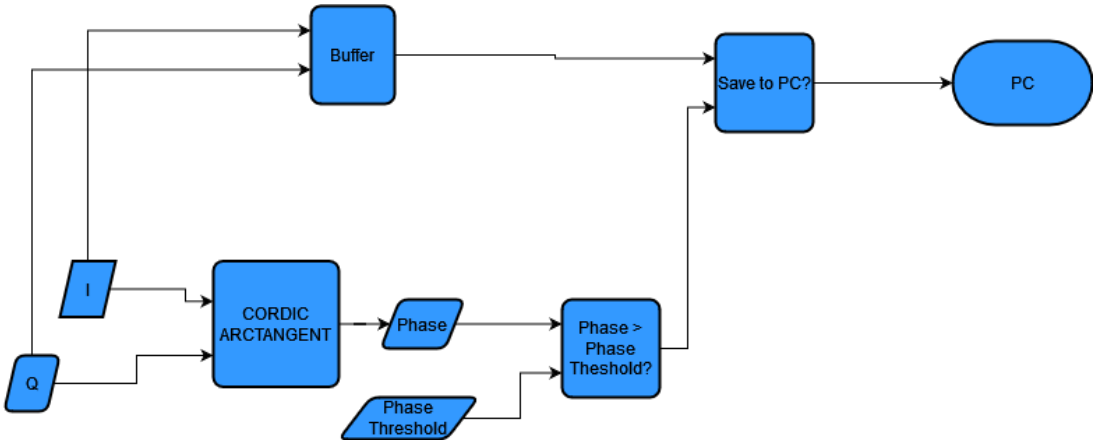

Figure 5.8: Flow Diagram of process used to save raw I/Q data on FPGA. The raw I and Q data is both sent to a buffer and also to the CORDIC ARCTANGENT block. In the same way as in Figure 5.7, the calculated phase value is compared to a defined phase threshold, and if it exceeds this threshold a pulse is said to have occurred. However, differing from Figure 5.7, when a pulse occurs instead the raw I and Q data is sent to the PC to be plotted and analysed with Python. Python can take this I/Q data and calculated the phase value, without having to use CORDIC, thus not resulting in additional quantisation noise.

array to collect pulse data. The "z" blocks are delays, delaying by a certain number of clock cycles, helping the design to meet timing requirements, helping to prevent errors when compiling the design.

Figure 5.10 and Figure 5.11 display the same pulse caused by a cosmic ray striking a Ti/TiN/Ti MKID in both the IQ and phase domains. Here, the IQ data is the data saved by the process described above, and shown in Figure 5.8, while the phase data is calculated on the PC, using Python, as opposed to using the FPGA's CORDIC block. Note that the pulse in Figure 5.10 is moving in the clockwise direction, while the pulse in Figure 5.11 is positive. This is because the phase data is simply multiplied by -1 to ensure that the phase pulses are positive. This is simply for ease of reading. The phase pulses are also re-centred, such that the phase baseline is at zero degrees.

As such, the ROACH 1 board was successfully used as a single pixel readout for characterizing pulses, negating the need for a second, separate system for reading out arrays as for pulse characterization. Obviously, as only a single readout system is needed, this reduces the cost of electronics needed for measuring and

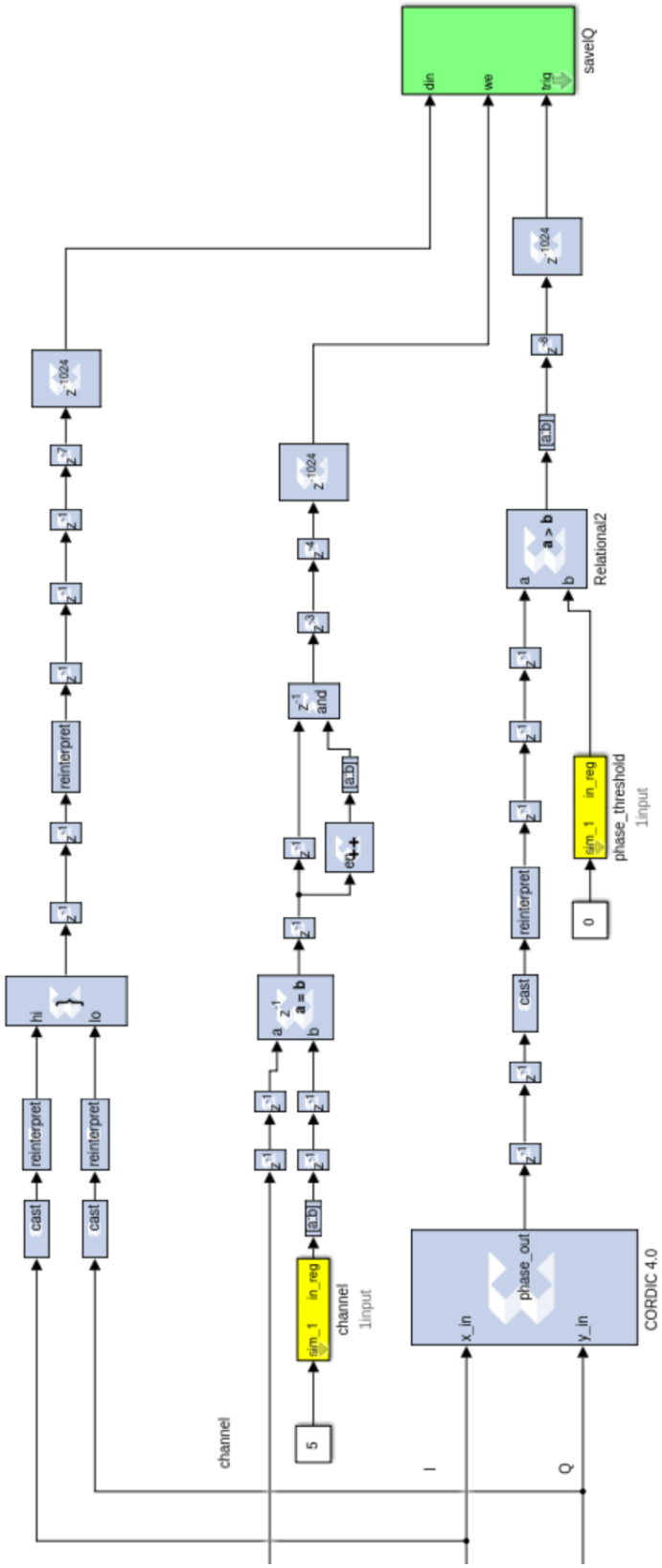

Figure 5.9: Simulink code used to save raw I/Q data on FPGA using the process illustrated in Figure 5.8.

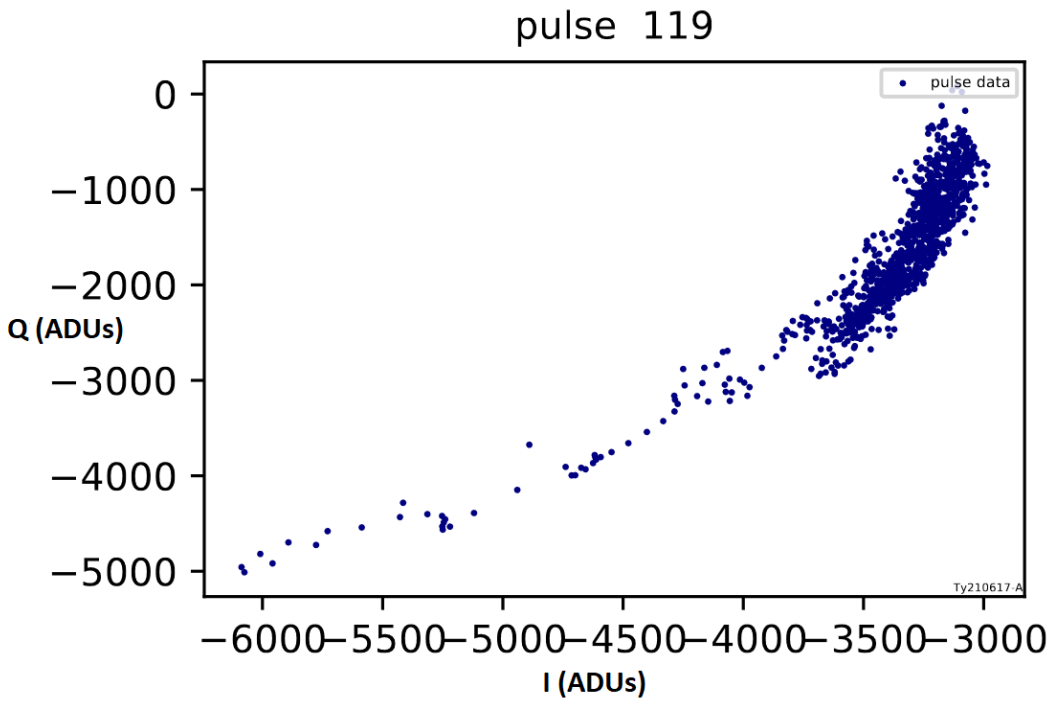

Figure 5.10: Cosmic ray pulse In IQ domain measured using the firmware illustrated in Figure 5.9. This is the raw IQ data which is sampled by the data converters, and is sent to the PC for plotting when a pulse is triggered in the way illustrated in Figure 5.8. The same pulse plotted as phase data is shown in Figure 5.11.

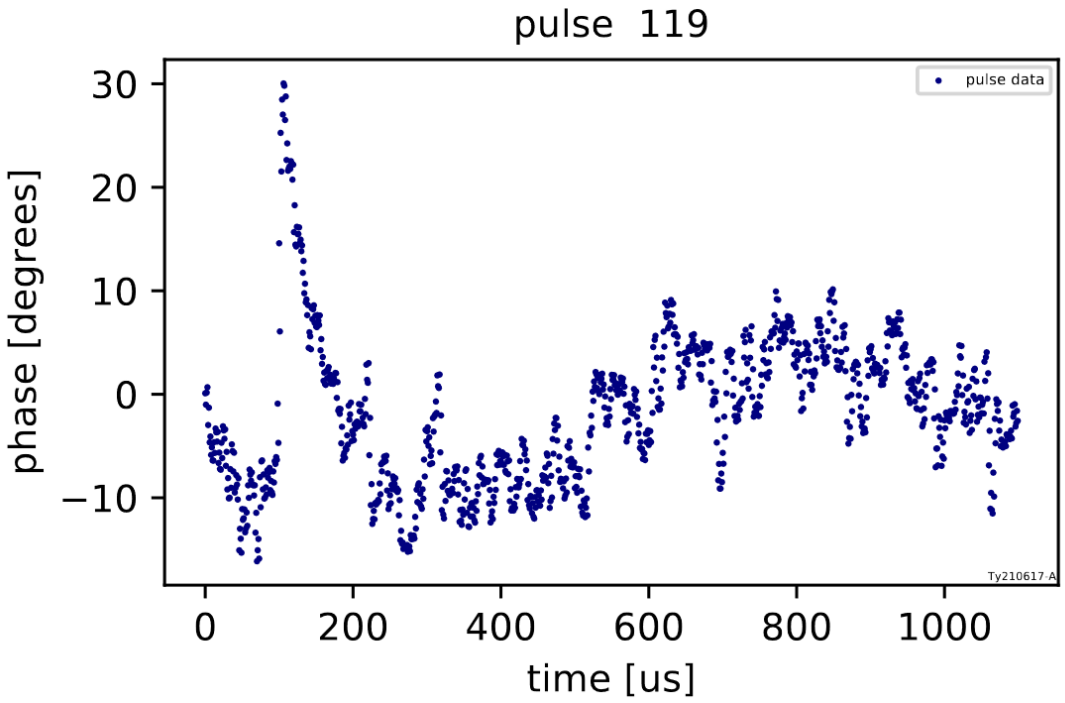

Figure 5.11: Cosmic ray pulse in phase domain, showing the same pulse as in Figure 5.10, but having used Python to calculate the phase numbers, without having to use the CORDIC algorithm. This pulse clearly contains an element of phase noise which is explored in Section 5.4.

characterising MKIDs.

5.4 Phase Noise Measurements

Using the pulse readout code which was developed, and described in Section 5.3, it was observed that the pulses observed in certain MKID arrays, caused either by photons from the laser box, or else by cosmic rays, featured a significant amount of noise, as can be seen in Figure 5.10 and Figure 5.11. This shows the importance of developing the ROACH readout system to not just measure photon heights and timestamps, but to also save the profiles, in terms of IQ and phase, for each individual pulse. For example, without saving all of this pulse data, the pulse shown in Figure 5.10 and Figure 5.11 would simply be logged as a pulse with height 30°, and the relevant timestamp. However, the new pulse analysis readout code allowed for the individual pulses to be analysed, and for this noise to be observed, motivating further improvements to the MKID design and fabrication process. Furthermore, it also highlighted the need to save not just the phase data, but also the IQ data. Noise in the IQ plane could appear as both amplitude and phase noise, with amplitude noise being in the direction of the centre of the resonator loop, and phase noise being tangential to this (17). Figure 5.12 taken from Gao (17), show a diagram of a "noise ellipse", with these two perpendicular components.

Monitoring a single MKID pixel with the ROACH readout, and saving off streams of IQ data, made it apparent that this noise was significantly more prevalent in the phase direction. These snapshots of IQ data were plotted on top of the MKID frequency sweep, showing the size of the phase noise relative to the MKIDs entire frequency sweep. Examples of these measurements are displayed in Figure 5.13, Figure 5.14 and Figure 5.15, showing the noise present in these Ti/TiN/Ti MKIDs. These measurements show 0.5 ms snapshots of IQ data for a single frequency, sampled at 1 MSPS. Note that these measurements are from the same array as shown in Figure 4.8. Also note that the frequency sweep data in these plots is

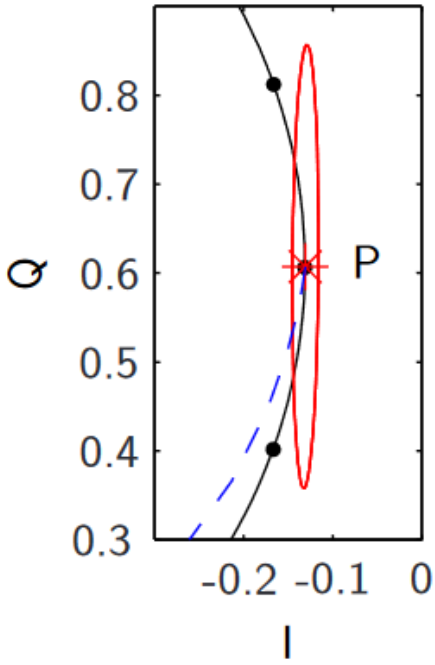

Figure 5.12: MKID noise ellipse showing amplitude and phase directions, with the amplitude noise corresponding to the minor axis and the phase noise corresponding to the major axis. This is taken from Gao (17).

measured using the ROACH setup, not with the VNA as in Chapter 4. This was to make sure that the phase noise data and frequency sweep data were both being measured with the same instruments. The VNA could not be used to measure the phase noise due to it not having as high a readout speed as the ROACH board, and thus only being able to measure "slow" shifts in the phase. Using the ROACH system with its high sampling rate allowed for high frequency noise to be analysed.

From these measurements, it is clear that the noise in these resonators is primarily in the phase direction. Note that in these plots, each step in the blue frequency sweep loops denotes a step of 10 kHz in the frequency sweep. The phase noise for these three resonators can be measured as approximately $\pm 15^{\circ}$. This figures are typical for the rest of the resonators in the array. This is problematic as it could lead to any photon pulses with height less than this 15° figure becoming lost within the noise. As such, these resonators clearly display problematic signal-to-noise ratios, causing smaller signals to be lost within the noise.

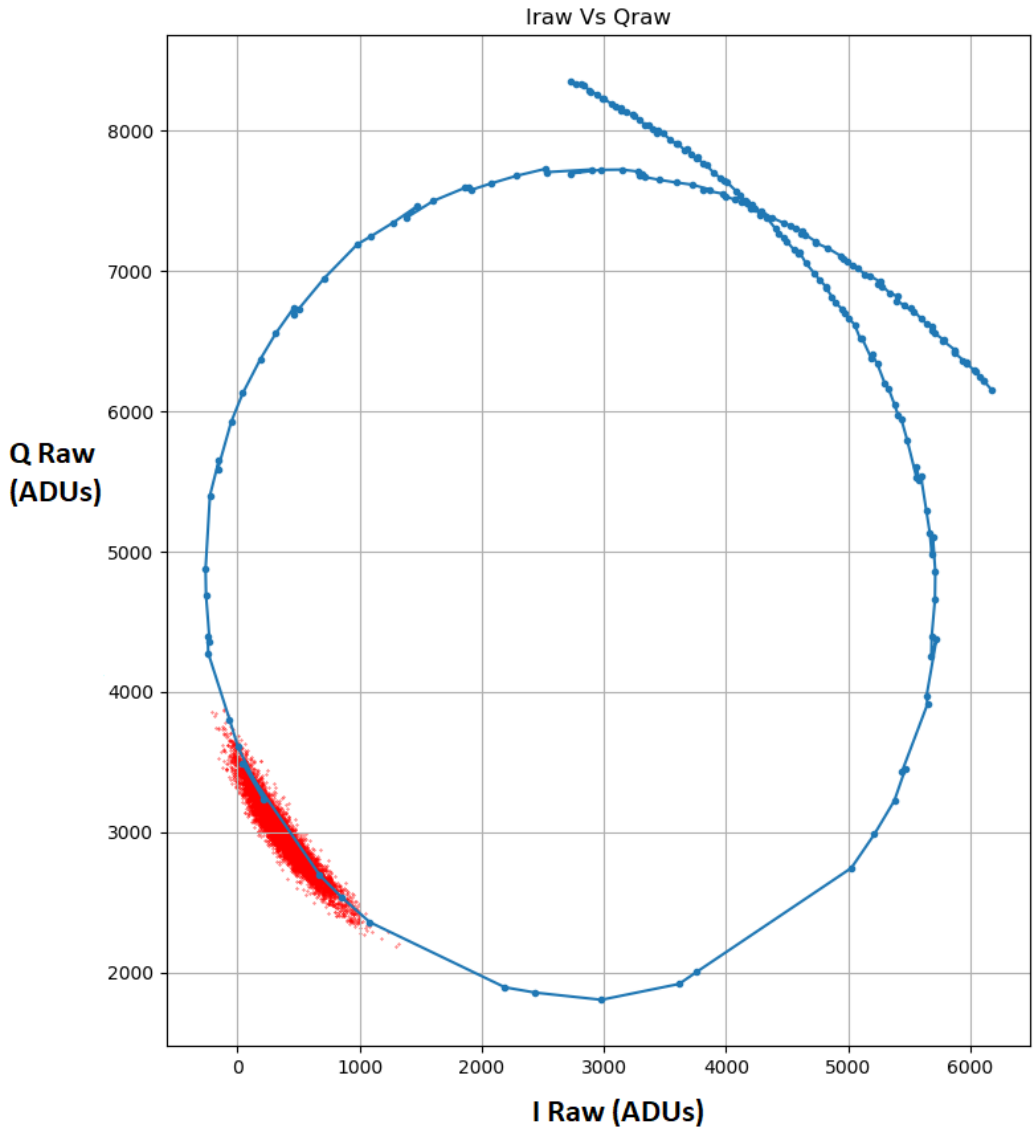

Figure 5.13: Phase noise measurement (red) frequency sweep (blue) for 5255 MHz MKID, showing phase noise of approximately $\pm 15^{\circ}$, corresponding to $\pm 30 kHz$. The spacing between each point in the frequency sweep is 10 kHz.

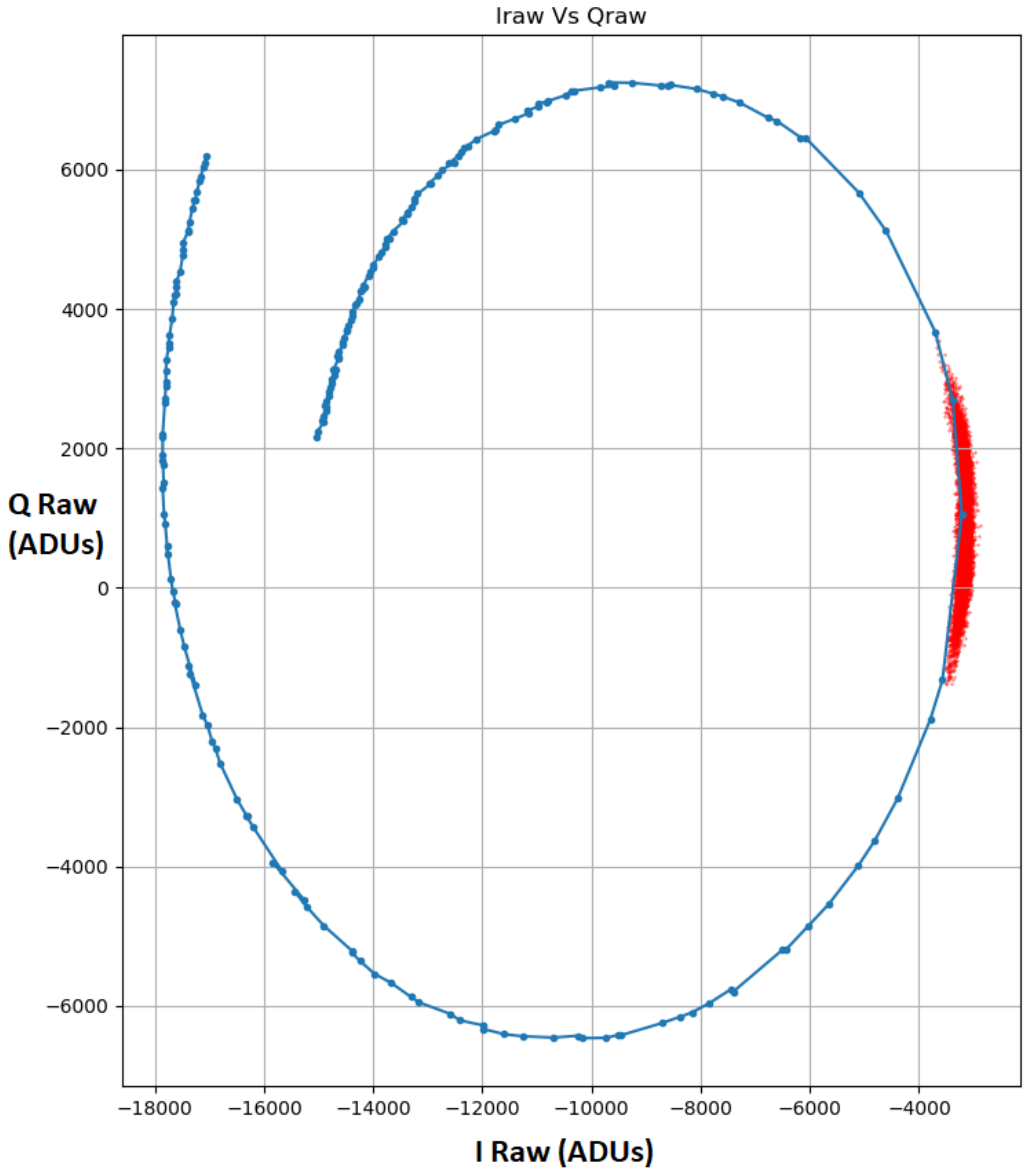

Figure 5.14: Phase noise measurement (red) and frequency sweep (blue)for 4512 MHz MKID, showing phase noise of approximately $\pm 15^{\circ}$, corresponding to $\pm 15 kHz$. The spacing between each point in the frequency sweep is 10 kHz.

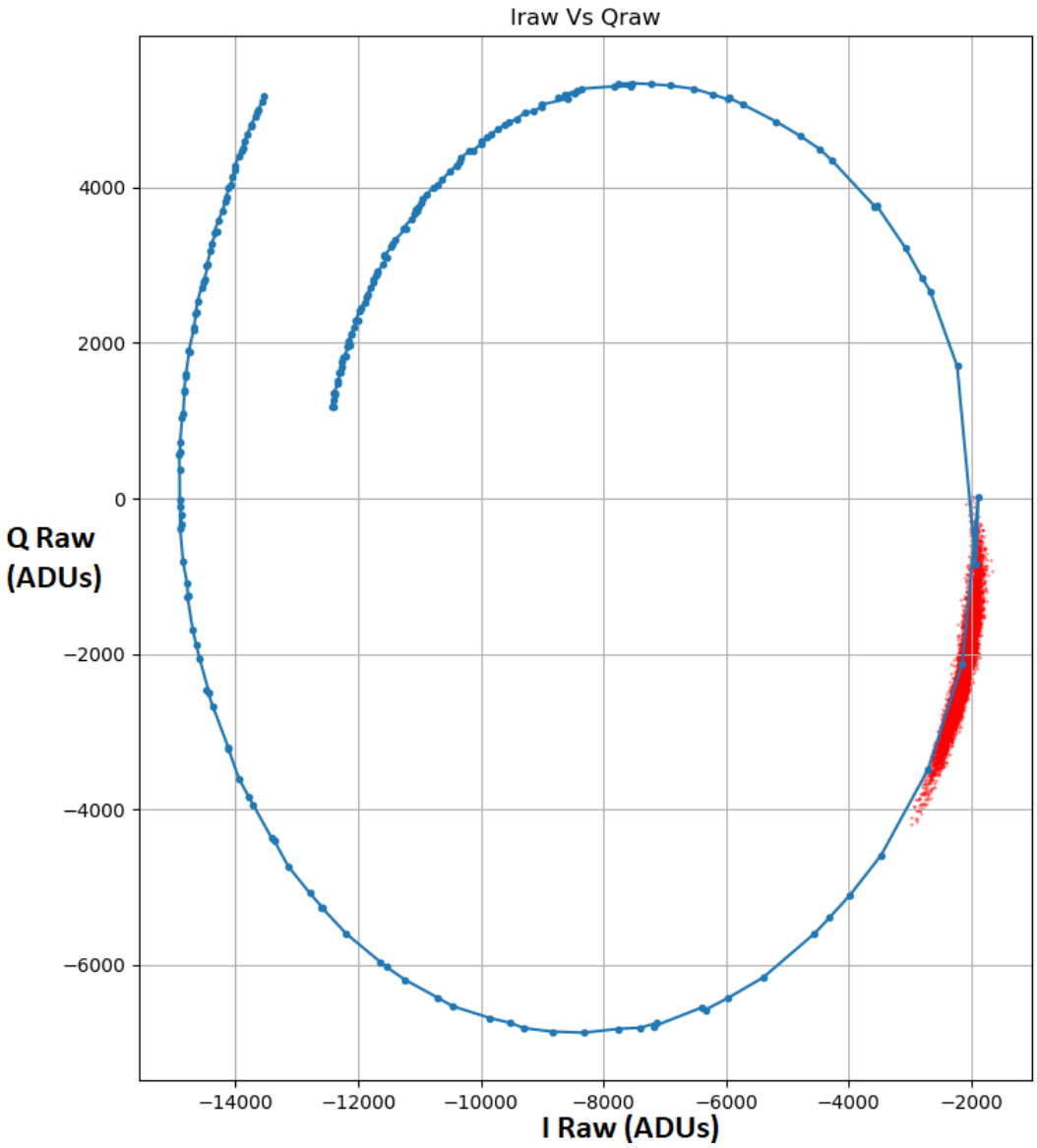

Figure 5.15: Phase noise measurement (red) and frequency sweep (blue) for 4666 MHz MKID, showing phase noise of approximately $\pm 15°$, corresponding to $\pm 15 kHz$. The spacing between each point in the frequency sweep is 10 kHz.

As a sanity check, these noise values were compared to the noise introduced by the readout electronics, to verify that this phase noise could not be attributed to the electronics. The readout electronics were re-configured to measure a loopback test, with the the DACs sourcing a frequency comb, that passed through a co-axial cable, before being re-digitized by the ADCs, without passing through the ADR and MKID array. Similarly, for this loopback test, a single frequency of 4512 MHz was measured, and a 0.5 s snapshot of IQ data was sampled at 1 MSPS, and plotted on top of a frequency sweep. For this measurement, as there is no resonator in the feedline, there is no loop visible in the frequency sweep. Here, the span of the frequency sweep is 2 MHz, while a span of approximately 50 MHz would be needed to see the cable delay loop given by the co-axial cable. The results of this are shown in Figure 5.16, showing how the readout introduces both amplitude and phase noise of approximately ± 20 analogue-to-digital units (ADUs).

This showed that the noise in the amplitude direction in Figure 5.13, Figure 5.14 and Figure 5.15 was slightly larger to that found in the loopback test, while the phase noise was significantly larger. For these resonators the noise in the amplitude direction was of the order of 100s of ADUs, while noise in the phase direction was an order of magnitude greater than this. Thus, it was apparent that the phase noise was inherent to the resonators.

Thus, the adapted ROACH readout developed for this project was used to diagnose noise in MKID resonators. This noise was later attributed to an issue in the fabrication process (see Section 1.7), caused by some sort of uncontrolled oxidization during fabrication. Thus, a modified fabrication process including an additional annealing step was developed, and results are presented in Section 5.5.

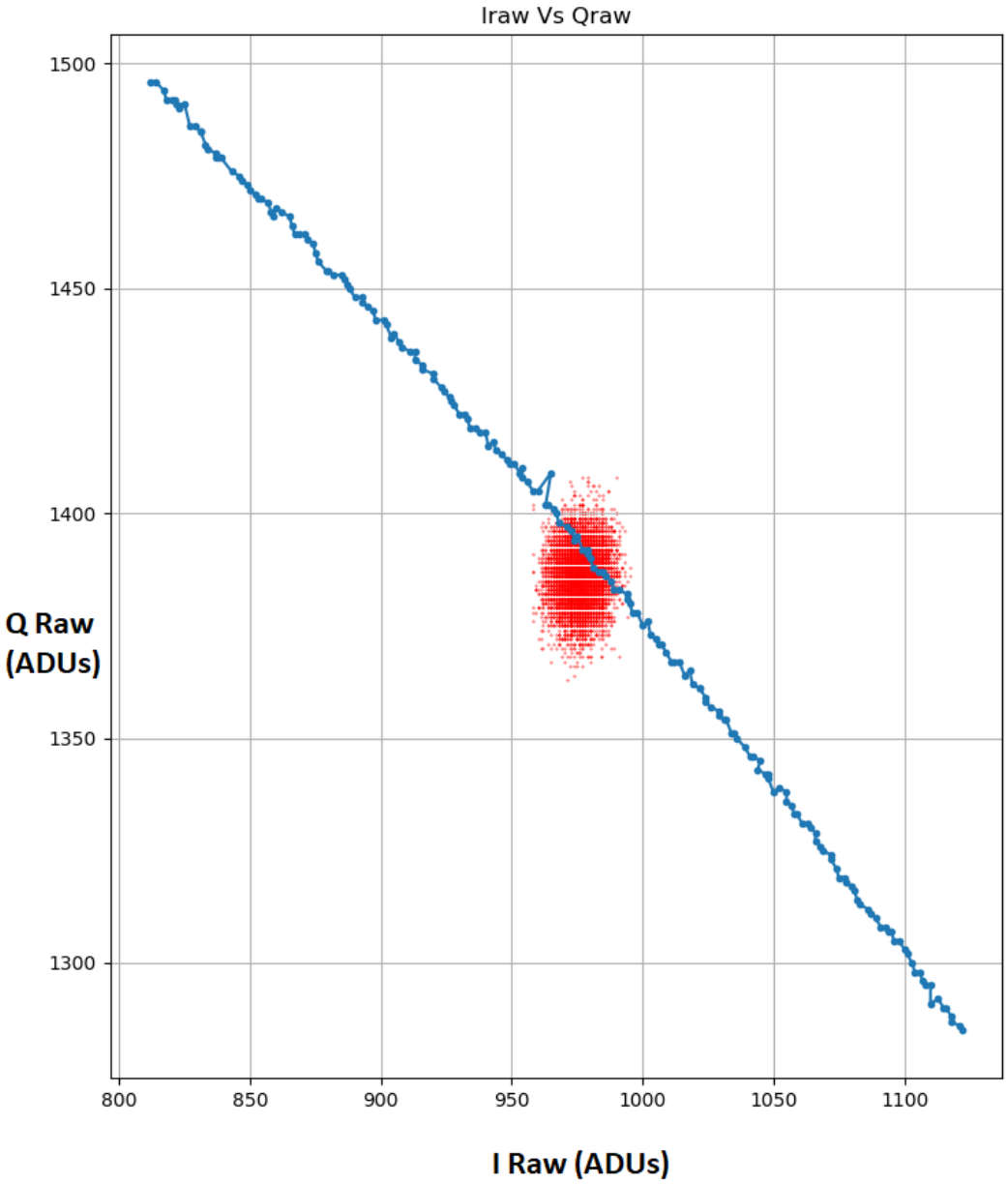

Figure 5.16: Phase noise measurement (red) and frequency sweep (blue) for loopback test. The spacing between each point in the frequency sweep is 10 kHz. Here the noise cycle is given by the noise of the ROACH board's data converters, with no additional phase noise introduced by the system. This was used to show that the phase noise seen in Figures 5.14, 5.15 and 5.13 was intrinsic to the MKIDs in the array, and not from the readout system.

5.5 Optimized Sample

After the problem with the excess phase noise was identified, it was suggested that after the fabrication process was complete, an additional step which may mitigate this problem would be to anneal the samples at 500°C for 50 minutes to remove this problem with excess oxidization, preventing the oxide from forming. The process was carried out on an array which was identical to the array shown in Figure 5.14, Figure 5.15 and Figure 5.13.

When these newly annealed samples were fabricated, the first test to characterize the phase noise of these samples in the same manner as was done in Section 5.4, and to verify whether or not the annealing process had any effect on the phase noise. The result of one of these phase noise measurement is shown in Figure 5.17. It is clear that the newly annealed samples are no longer showing the same noise shape was seen in Figure 5.14, Figure 5.15 and Figure 5.13. The phase noise profile shown in Figure 5.17 shows a more typical phase noise profile, similar to the noise ellipse which is described by Gao (17) and shown in Figure 5.12. One thing which needs to be noted here is that the MKID in Figure 5.17 had a Q_i value of approximately 60,000, while those in Figure 5.14, Figure 5.15 and Figure 5.13 had Q_i values of approximately 100,000 to 200,000. Thus, it the annealing process appeared to decrease the quality factor of the resonators, but also caused a reduction in the phase noise. This annealing also a change in the frequencies of the MKIDs in the array, shifting to below the 4 GHz. As this is below the optimal operating frequencies of the HEMT amplifier (see Figure 3.9), this may have affected the accuracy of the quality factor measurements.

Once it was apparent that the phase noise had been reduced, the next step was to verify if the resonators could be used to reliably measure pulses. The same resonator shown in Figure 5.17 was monitored using the ROACH readout system and while the resonator was illuminated with 400 nm light. With the reduced phase noise the readout was now reliably measuring photon pulses, typically measuring

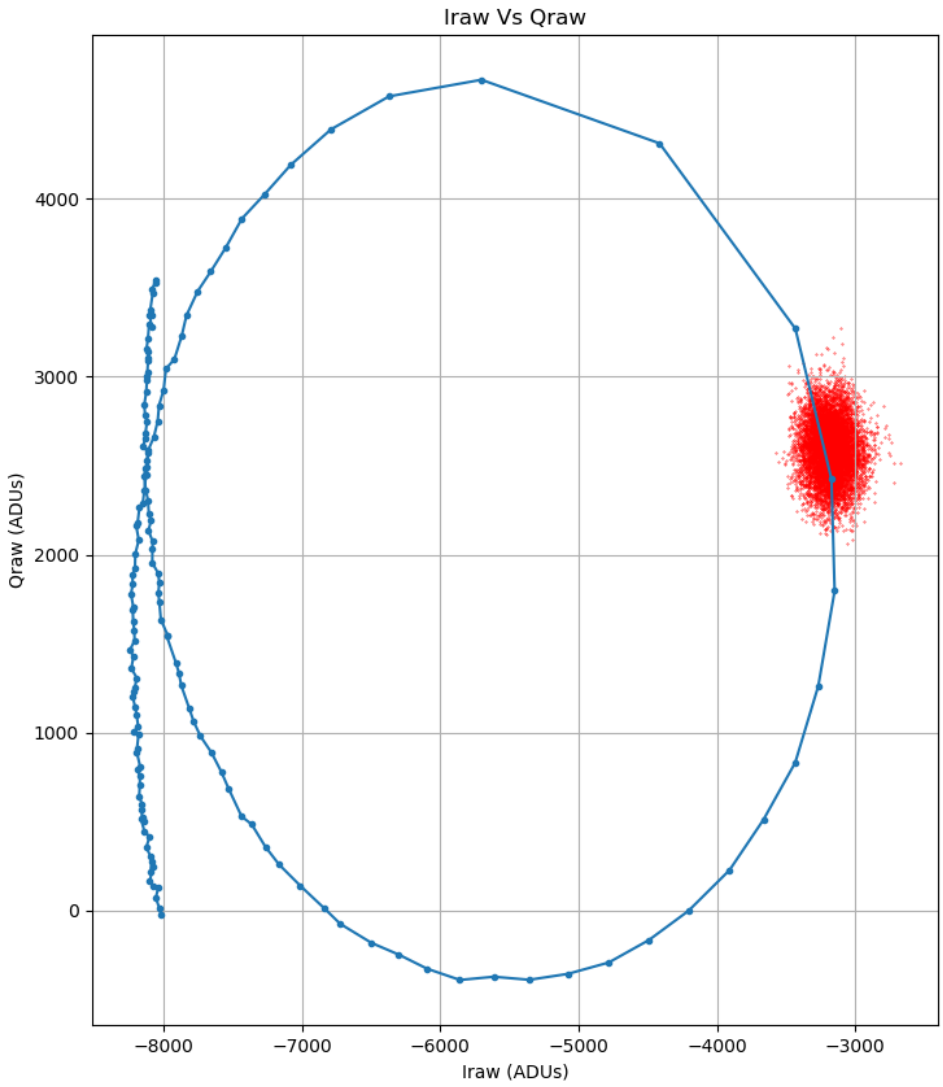

Figure 5.17: Phase noise measurement (red) and frequency sweep (blue) for 2893 MHz MKID which was fabricated with the additional annealing step, showing phase noise of approximately $\pm 7.5°$, corresponding to $\pm 5 kHz$. The spacing between each point in the frequency sweep is 10 kHz.

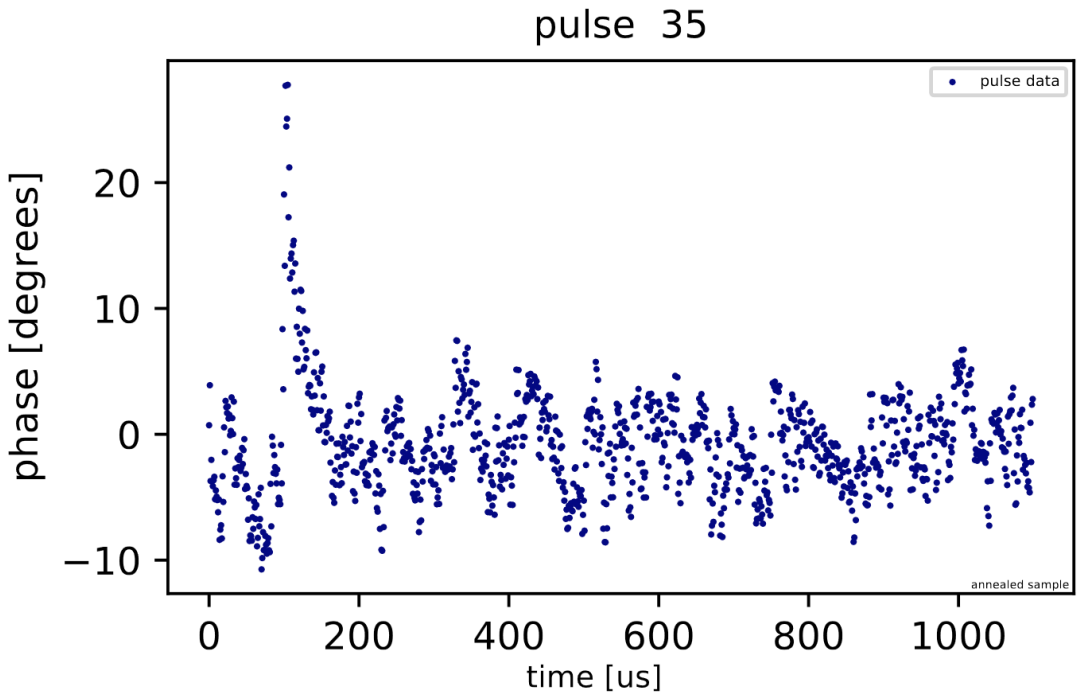

Figure 5.18: 400 nm photon pulse from an annealed MKID sample, measured using the ROACH readout system.

approximately 50 photon pulses per second. A sample photon pulse, caused by this 400 nm source is shown in Figure 5.18, showing a pulse height of approximately 30° with a baseline phase noise of approximately ±6°.

With the system now reliably measuring tens of photons per second, the next thing which needed to be done was to measure for a longer period of time and gather thousands of photon pulses which could be plotted to a histogram (as in Figure 1.9). Thus, integrating for 20 minutes allowed for tens of thousands of photon pulses to be saved for the 400 nm source. This was repeated for photon sources with wavelengths of 525 nm, 650 nm, 775 nm and 900 nm, thus measuring photons from violet up to the near infrared. While there is significant overlap between the 525 nm, 650 nm and 775 nm peaks, there is a clear distinction between these and the 400 nm and 900 nm peaks on either side, demonstrating the intrinsic energy resolution of MKIDs. Using Equation 1.2 the energy resolution was determined to be 3.14 at 400 nm, 3.01 at 525 nm, 2.60 at 650 nm, 2.57 at 775 nm and 2.50 at 900 nm. It should be noted again that these energy resolution values will be

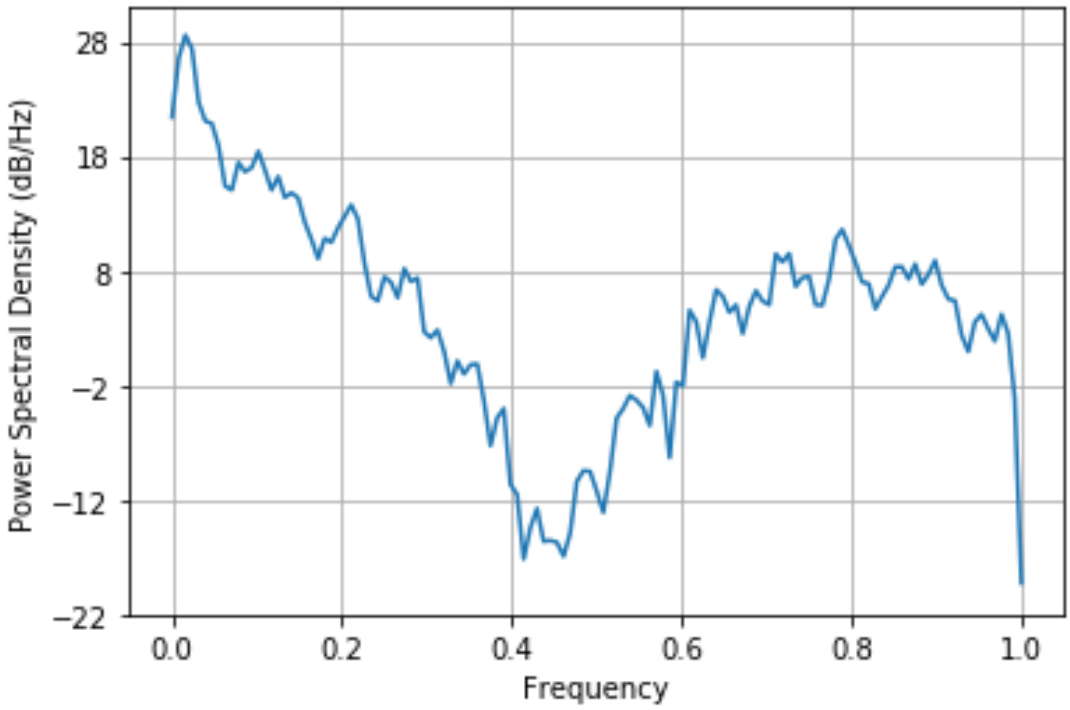

Figure 5.19: Power spectral density of 400 nm photon pulse shown in Figure 5.18

decreased to to the sub-optimum signal to noise.

To investigate the noise present in these pulses, the noise spectral density of the pulse shown in Figure 5.18 was calculated and plotted. This is shown in Figure 5.19. This shows significant noise power at low frequencies, degrading the signal to noise ratio of the measurements. Work is being continued by other members of this group to investigate this noise.

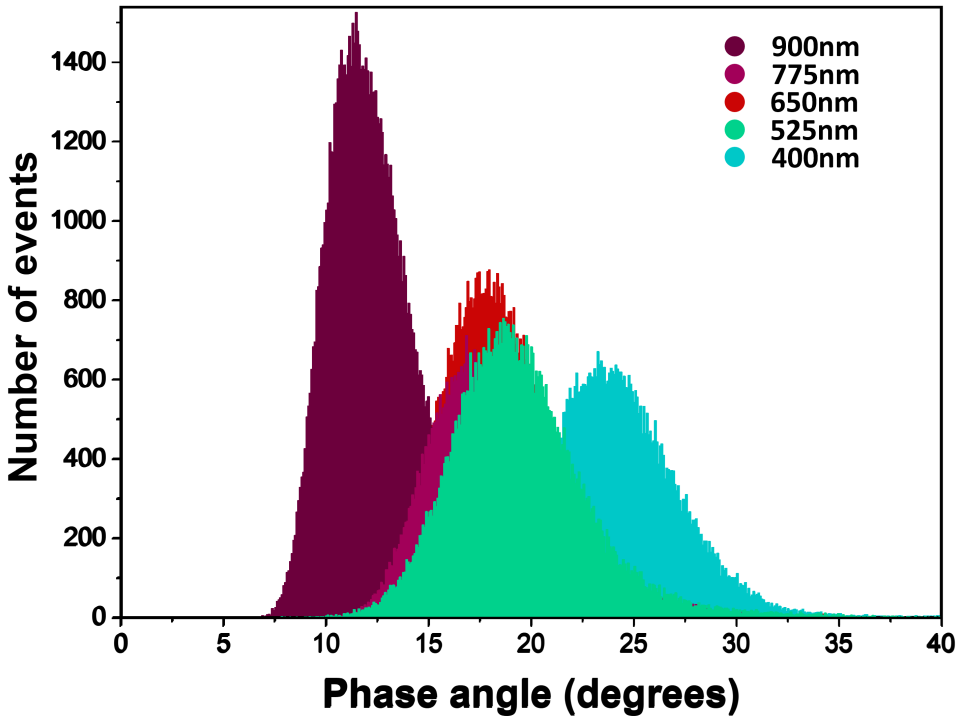

Figure 5.20: Pulse histogram showing tens of thousands of photon pulses for 400 nm, 525 nm, 650 nm, 775 nm and 900 nm photons. Note that the pulse heights used to plot these histograms were calculated by taking the maximum phase value of each pulse and subtracting it from the baseline. As such, no optimal filtering step has been carried out on this data.

6 Next Generation Readout Systems

While the ROACH 1 readout setup described in Chapter 5 has been adapted to perform single pixel analysis, characterizing photon and cosmic ray pulses for single pixels in an MKID array, it also capable of reading out upto 256 pixels simultaneously on a single feedline (20). However, this is far below the current state of the art. Thus, the next objective of this project was to develop a new readout system, capable of reading out a far higher number of pixels per feedline, at a lower cost per pixel.

While the MEC array (41), which is to date the largest array of optical MKIDs, has managed to use twenty ROACH 2 boards to read out over 20,000 MKID pixels, for larger arrays of MKIDs new readout systems are being developed. In order to meet the FPGA and data converter requirements for reading out tens of thousands of MKIDs, electronics boards containing on-chip FPGAs and data converters, used for industries such as telecommunications and defence, are also being adapted for MKIDs. While it would be possible to just increase the number of ROACH 2 boards used, scaling up like this introduces issues with increased costs, power consumption and size.

Thus, the first step in developing a new MKID readout system, capable of reading out arrays of 1000s of MKIDs on a single feedline, was to analyze the design requirements for this system, as well as the readout capabilities of any potential

future systems, and use this analysis to select a solution as to which FPGA board to develop. This chapter covers that process of selecting which board to use.

6.1 Requirements

With each resonator being designed with a spacing of 2 MHz, this gives 500 resonators per GHz per feedline. 2 MHz spacing is used to minimize crosstalk between adjacent resonators in frequency space and to optimize yield. As the operating frequencies are limited to a single octave, and the operating frequency of the HEMTs goes upto 8 GHz (see Figure 3.9), this means operation is limited to the 4 to 8 GHz octave, allowing for 2,000 pixels to be read out over 4 GHz of bandwidth per feedline. Thus, the future readout system needs DACs that are capable of producing 2,000 probe tones in 4 GHz of bandwidth. Thus, the ideal data converters for our purposes should be capable of handling 4 GHz of bandwidth spanning -2 GHz to + 2 GHz. This is because these baseband signals can then be upmixed with a 6 GHz local oscillator (LO). Tones can be generated at either side of the LO, allowing upmixing of these baseband signals to the desired 4-8 GHz band. This gives a Nyquist rate of twice of the maximum frequency to be outputted, giving $f_{Nyquist} = 2 * f_{Max} = 2 * 2GHz = 4GHz$, meaning that a 4 giga-samples-per-second (GSPS) DAC is necessary (107). Similarly, for the signals output from the ADR, the ADCs also need to be capable of sampling a 4 GHz bandwidth with GSPS sampling speed. Thus, it is clear that the DACs and ADCs are a major constraint on the design requirements of this next generation readout system, with sampling of $> 4GSPS$ needed for both the DACs and ADCs.

While the data converters are one aspect of the MKID readout system, the other aspect which needed to be considered when deciding upon a board is the FPGA resources, needed to perform the signal processing needed for large arrays of MKIDs, as shown in Figure 5.3. As explained in Section 1.6, the logic resources of the FPGA are characterized in terms of logic blocks and DSP slices, with logic

blocks acting as programmable logic gates, and DSP slices being used to perform more resource intensive operations such as multiplications.

The FPGA logic resources of potential future boards was compared to that of the ROACH 1 system, capable of analysing 256 pixels while using 313 out of 640 DSP slices, and 5,997 out of 7,360 logic blocks. Thus, a rough idea for the number pixels which another FPGA would be able to process was determined by scaling up the 256 ROACH 1 pixels with 313 DSP slices, and 5,997 logic blocks, relative to the number of DSP slices and logic blocks of the alternative systems. Thus, scaling up linearly, a rough estimate for the number of DSP slices and logic blocks needed to read out the 2,000 MKIDs per feedline would be ~ 2450 DSP slices and $\sim 47,000$ logic blocks per feedline. It should be noted that these are conservative estimates as it assumes a linear instead of logarithmic DSP usage increase with number of channels. Moreover, this also assumes that the ROACH system was ideal, and that no further improvements could be made to improve its resource usage. For example, ither, less resource intensive FFT algorithms could be used to save FPGA resources. In reality However, given the relative crudeness of the comparison, a conservative model was deemed sensible.

6.2 Potential Boards

With the basic requirements for a next generation readout system now defined, the next step was to gather a list of the currently available boards on the market, and to compare them in terms of those characteristics which were mentioned in Section 6.1, namely the data converter and FPGA resources, but also in terms of their total cost. Of course, ultimately these solutions must be compared in terms of their estimated cost per pixel.

The costs of some of these boards and their respective resources are summarised in Table 6.1. The Unit Price column only takes into account the price of the board in question, and does not consider the price of any additional electronics that would

be required to use it, such as ADC/DAC boards, or an additional, external FPGA board. This is because some of these boards contain a system-on-chip (SoC), which in this context means the entire system, of both data converters and FPGA resources are contained on a single chip, while others are like the ROACH 1 board, where external data converter boards need to be used. Furthermore, it was speculated that some boards, which do not have a significant amount of FPGA resources could be coupled to an external FPGA board, to increase the number of pixels which they could process.

The SKARAB board (108) has the advantage of being developed by CASPER, and being already in use, meaning that it has pre-existing firmware and software, as well as support from the CASPER community (35). This would mean that the CASPER Simulink blocks which were used for programming the ROACH board in Chapter 5 could again be used. However, it has the disadvantage of already starting to become outdated, having been released in 2017. Furthermore, while it is relatively cheap, costing only $\sim$ €11,000 the board does not containing any DACs, only ADCs. This is because, like the other CASPER boards, it has been developed for radio astronomy applications, where ADCs are required to digitize the analogue data from a radio telescope, but DACs are not needed. Thus, it would be necessary to purchase an external DAC board, further driving up the cost, and the workload.

Similarly, the Uniboard II, which is developed by ASTRON, does not have support from the CASPER community, and also does not contain any onboard data converters and thus would requires modifications to allow for compatibility with DAC and ADC boards, again increasing the cost and work needed to get it up and running (109) (110). It also has a relatively high cost to begin with, before considering external data converters.

The remaining boards are customized off the shelf solutions (COTS), based on readily available FPGA processing boards, developed for industrial applications such

Table 6.1: FPGA board resource and price comparison for a selection of potential MKID readout solutions. Note that the Uniboard II and Xilinx VCU118 boards do not give any figures for the ADC and DAC resources as these boards do not possess any data converters and thus would require an external data converter board. Similarly, the SKARAB board has ADCs, which are needed for the radio astronomy applications which it is designed for, but does not have any DACs. Prices are accurate for 2019 when this analysis was done.

Board	Logic Blocks	DSP Slices	ADCs	DACs	Unit Price (€)
SKARAB	693,120	3,600	2 x 14 x bit / 3 GSPS	N/A	10,693
UniBoard II	4,600,000	1,518	N/A	N/A	20,000
Xilinx VCU118	2,586,000	6,840	N/A	N/A	5,800
Xilinx ZCU111	930,000	4,272	8 x 12 bit / 4.096 GSPS	8 x 14 bit / 6.554 GSPS	8,995
Vadatech AMC599	1,451,000	5,520	2 x 12 bit / 6.4 GSPS	2 x 16 bit / 12 GSPS	20,000

as telecommunications and defence. These have the advantage of being, in general, affordable, having high performance, and having additional components, such as ADCs and DACs, available. These boards are the Xilinx VCU118 (111) (112), Xilinx ZCU111 (18), and Vadatech AMC599 (113). Of these, the Xilinx XCU118 would also need an external ADC/DAC board, as it does not have any on-chip data converters, unlike the ZCU111, which is classed as a radio frequency system-on-chip, having its data converters and FPGA on the same chip. While the Vadatech AMC599 is not an RFSoC, it does come with onboard data converters, meaning that it would not require an external ADC/DAC board.

Based on these characteristics, the estimated number of MKID pixels which each of these boards could process was calculated. For different systems, the maximum pixel count will be constrained by either the FPGA resources or the data converter resources. Obviously, as per Table 6.1 the UniBoard II and Xilinx VCU118 do not have any data converters, while the SKARAB board only has ADCs, meaning that for these boards only an estimate for the FPGA logic limited pixel count was calculated. For each of the FPGA constrained pixel count estimates, it was found that this was limited by the number of DSP slices, not by the logic blocks. These

Table 6.2: FPGA board pixel count estimates. These values are the estimated numbers of MKID pixels which these boards FPGA's and data converters could process. Similarly to in Table 6.1, no values are given for the ADC/DAC constrained estimated pixel counts for the SKARAB, UniBoard II and Xilinx VCU118 due them requiring external data converter boards.

Board	FPGA Constrained Estimated Pixel Count	ADC/DAC Constrained Estimated Pixel Count
SKARAB	$\sim 2,900$	N/A
UniBoard II	$\sim 1,200$	N/A
Xilinx VCU118	$\sim 5,600$	N/A
Xilinx ZCU111	$\sim 3,500$	8,000
Vadatech AMC599	$\sim 4,500$	3,200

estimates are summarised in Table 6.2

From the data presented in Table 6.1 and Table 6.2 the SKARAB and UniBoard II were immediately ruled out as a future MKID readout candidate due to their relatively high cost and low pixel counts. This was before even considering an ADC/DAC solution for these boards. Thus, the final cost would be even higher. The VCU118, though also requiring an external ADC/DAC board, has an abundance of FPGA resources, and was cheaper than the SKARAB and Uniboard II, meaning it was a more promising solution. However, ultimately this board was also eliminated from contention due to its lack of data converters. Finally, for the two remaining boards, the Xilinx ZCU111 and Vadatech AMC599 the ZCU111 was estimated to provide a higher pixel count, at a lower total cost.

Thus, of all of these boards, ultimately, the ZCU111 was seen as the best available system on the market to be developed to read out tens of thousands of MKID pixels, due to its FPGA and data converter capabilities, as well as its relatively low cost. Section 6.3 covers this board in more detail.

One aspect which has been not included in this analysis is the ease with which each of these systems can be integrated into a full MKID readout system. Instead it was the cost per pixel value which was the main metric which was considered. Moreover, it should be noted that Total Cost values which are given in this section only consider the total cost of the FPGA and data converter boards, and do not

include extra elements which would also be needed such as amplifiers and mixer boards. While it is acknowledged that including the cost of these additional elements is of interest, it was not included here as this would be the same for each of the boards analysed in this section, and thus would not have affected the ultimate decision of choosing the best system in terms of cost-per-pixel.

6.3 Xilinx ZCU111 RFSoC

The ZCU111 (see Figure 6.1) (18) is a radio frequency system-on-chip (RFSoC) developed by Xilinx. It boasts FPGA resources of 4,272 DSP slices and 930,000 logic blocks. What is particularly appealing about this board is that it does not require external data converters, having eight on-chip 12 bit / 4.096 GSPS ADCs and eight on-chip 14 bit / 6.554 GSPS DACs on the same system-on-chip (SoC) as the FPGA. The on-chip format of the data converters and FPGA greatly reduces the size of this MKID readout system. Each of the feedlines connected to the MKID array require two ADCs and two DACs in order to sample both the I and Q components of the resonators' transmission. With an ADC sampling rate of 4.096 GSPS and a pixel spacing of 2 MHz, this allows for 2,000 pixels to be read out on a single feedline, with the possibility for four feedlines. Thus, the ZCU111 has sufficient data converters resources to read out upto 8,000 MKIDs. However, while this is ample data converter resources to read out an array of 8,000 pixels (like which was described in Section 6.1), the FPGA resources are estimated to only be sufficient for processing less than 4,000 pixels (see Table 6.2). Thus, the ZCU111 has the FPGA resources to only use half of the eight ADC/DAC pairs. Thus, in order to fully utilize the RF bandwidth provided by the ZCU111's data converters, additional FPGA resources are required.

It was additionally proposed to simply use two ZCU111 boards to allow for enough FPGA resources to read out almost all of the 8,000 pixels which is desired. This would ultimately mean total data converter resources sufficient for reading out

Figure 6.1: Photograph of the Xilinx ZCU111 RFSoC Board (18)

16,000 pixels, with most of this bandwidth going to waste. Thus, using two ZCU111 boards, costing $\sim$ €9,000 each, to read out 8,000 pixels would give a final cost per pixel of $\sim$ €2.25. Another solution to this mismatch of data converter resources to FPGA logic resources, would be to couple a single ZCU111 board to an external FPGA board. Thus, the FPGA on the ZCU111 could be used to process the pixels on a pair of feedlines, while the secondary external FPGA could be used for the remaining two feedlines. This would also allow for the full, planned 8,000 MKID pixels to be processed. Thus, it was proposed to purchase a HiTech Global FPGA board to do this (114). This could be coupled to the ZCU111 using its FMC+ port, which allows for a data transfer rate of 524 Gbps, meaning that it has sufficient data transfer rate to get the data from the ZCU111 to the FPGA board to be processed. This would allow access to Xilinx Ultrascale+ VU9P FPGA's resources of 2,586,000 logic blocks and 6,840 DSP slices, allowing for a total pixel count of 8,000. With a cost of $\sim$ €10,000 this would give a total cost per pixel of $\sim$ €2.40. Eventually, another, more promising solution to this problem was found when Xilinx released their new 2x2 RFSoC for academic partners. This is covered in Section 6.4.

6.4 Xilinx 2x2 RFSoC

The 2x2 RFSoC (19) is a low cost alternative to the ZCU111 released by Xilinx and HiTech Global as part of their University Programme. While it contains the same FPGA resources as the ZCU111, it has only a quarter of the data converter resources, containing only two on-chip 12 bit / 4.096 GSPS ADCs and two on-chip 14 bit / 6.554 GSPS DACs. Significantly, the 2x2 board costs only one fifth of the price of the ZCU111, driving down the cost per pixel value of a potential MKID readout system. As it has an abundance of FPGA resources, relative to the data converter resources, all of the ADC/DAC pairs can be used, in contrast to with the ZCU111, meaning that each board can read out 2,000 pixels. A comparison

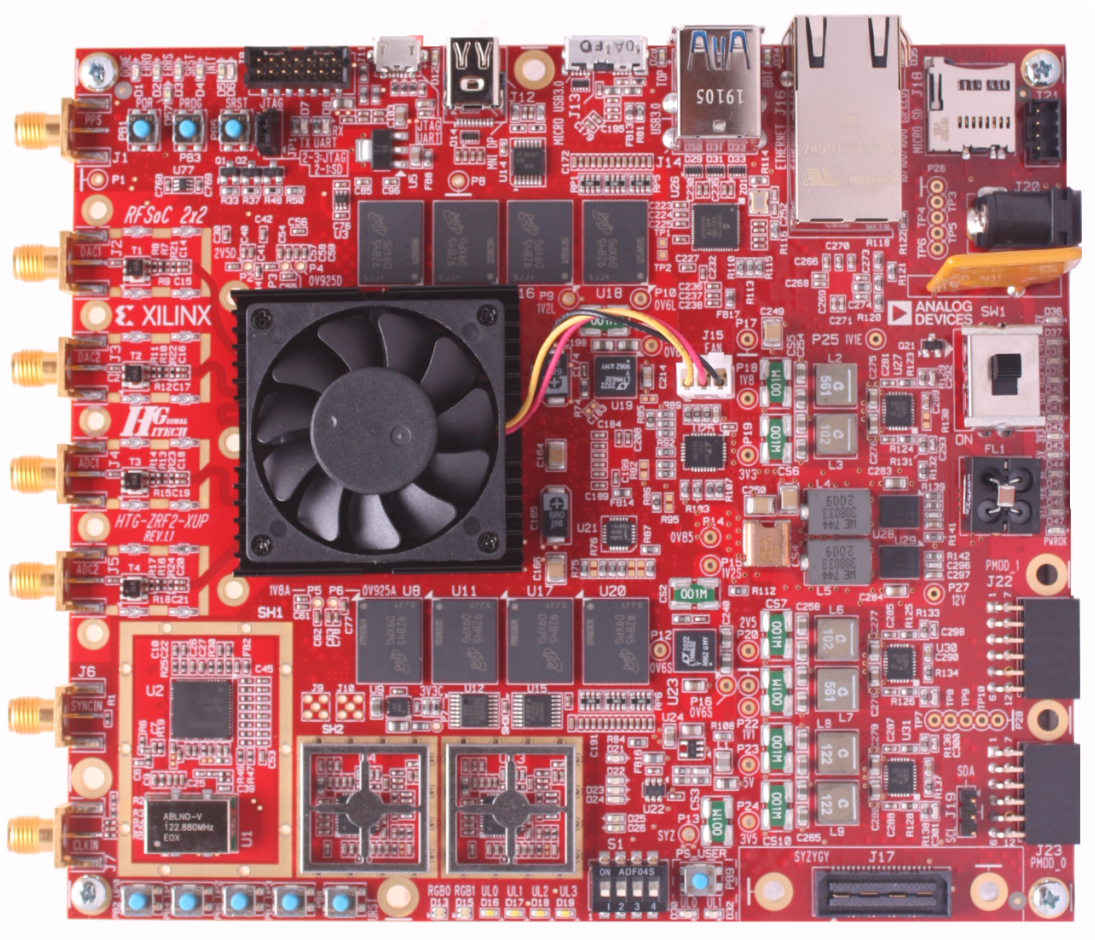

Figure 6.2: Photograph of the Xilinx 2x2 RFSoC board (19)

Table 6.3: Comparison of the estimated readout capabilities of the two Xilinx RFSoC boards, the ZCU111 and 2x2, with the ROACH 1 and ROACH 2 boards which were used for the ARCONS and DARKNESS optical MKID arrays, showing potential for reduced cost per pixel values for the RFSoC boards. (20) (21)

Board	**Total Cost (€)**	**Pixel Count**	**Approx. Cost/Pixel (€/pixel)**	**Logic Blocks**	**DSP Slices**
ROACH 1	4,000	256	16	7,360	640
ROACH 2	4,000	1,000	4	326,400	1,120
ZCU111 RFSoC	10,000	3,500	2.25	930,000	4,272
2x2 RF-SoC	2,000	2,000	1.00	930,000	4,272

between the important characteristics of the ROACH 1, ROACH 2, ZCU111 RFSoC and 2x2 RFSoC boards is shown in Table 6.3.

6.5 Cost Per Pixel Values of Xilinx RFSoCs

As described in Section 1.5.1 an important metric which is used to evaluate MKID readout systems is their cost per pixel value. For example, the ARCONS (20) and DARKNESS (21) arrays used ROACH 1 and ROACH 2 boards, respectively, to read out arrays of optical MKIDs, with cost per pixel values shown in Table 6.3.

As explained in Section 6.3, while the ZCU111 has ample data converter resources for reading out up to 8,000 pixels, the actual number of MKIDs which it is estimated to be capable of reading out is confined by the FPGA resources to ∼4,000 pixels. Thus, a single ZCU111, costing ∼ €10,000, has a cost per pixel of €2.50.

However, the 2x2 RFSoC, having four times the FPGA resources relative to data converter resources, when compared to the ZCU111, allows for the entire RF bandwidth of the data converters to be used. Thus, a single 2x2 RFSoC, capable of reading out 2,000 pixels and costing ∼€2,000, will have a cost per pixel of €1. This is summarised in Table 6.3.

Table 6.4: Possible Xilinx RFSoC solutions estimated costs per pixel. This shows the estimated costs per pixel of the RFSoC boards when including the additional electronics required for them to be able to read out a full array of $\approx 8,000$ pixels. The equivalent figure for a single ZCU111 board is included for reference.

Solution	**Total Cost (€)**	**Estimated Pixel Count**	**Estimated Cost Per Pixel (€)**
ZCU111 RFSoC	8,995	3,500	2.50
ZCU111 RFSoC x 2	17,990	7,000	2.50
ZCU111 RFSoC + HiTech Global FPGA Board	18,995	8,000	2.40
2x2 RFSoC x 4	8,000	8,000	1.00

Because of this, it was decided that the 2x2 RFSoC was a promising solution for an MKID readout, allowing for large arrays of MKIDs to be read out, without running into a bottleneck in terms of pixel count caused by the mismatch of FPGA resources to data converters. Thus, in order to meet the design requirements from Section 6.1, of being able to read out 8,000 MKIDs, four 2x2 RFSoCs would be needed. Table 6.4 summarises the different possible solutions to using a Xilinx RFSoC board to read out 8,000 pixels while overcoming this bottleneck issue.

As a result of the analysis in Chapter 6 both a Xilinx ZCU111 RFSoC and a pair of Xilinx 2x2 RFSoCs were purchased to be developed as a next generation MKID readout system. The progress in developing these systems is covered in Chapter 7.

7 Xilinx Based Readout Systems

Following on from the work in Chapter 5, developing firmware and software for the ROACH 1 readout system, and Chapter 6, selecting an FPGA board to develop as a future MKID readout system, readout firmware and software was also developed for these new Xilinx systems, namely the ZCU111 and 2x2 Radio Frequency System-on-Chips (RFSoCs). As the ZCU111 was released first, development began on this board. When the 2x2 was later released, development was continued on this. Thankfully, as both boards use the same FPGA, a ZYNQ UltraScale+ RFSoC XCZU28DR, adapting the firmware developed for the ZCU111 to the 2x2 was straightforward.

7.1 Programming Approach

Like with the ROACH 1 system, programming these RFSoCs consists of two steps, developing stable firmware for the hardware itself, namely the FPGAs and data converters, and then developing control software for real-time interfacing with the hardware via an external machine. For the ROACH 1 this was done using the CASPER approach (see Section 5.1) of developing the firmware using CASPER's re-configurable MATLAB Simulink blocks, and developing Python software scripts for interacting with this. While it was initially decided to use this same approach for the ZCU111 and 2x2 RFSoCs, at the beginning of this project these boards had not been sufficiently "CASPER-ised". To programme a board using CASPER firmware blocks, the board needs to have a board specific CASPER "yellow block", which is

used to compile the firmware design for that specific board. While a CASPER yellow block has now been developed for the Xilinx RFSoC platforms(115), at the beginning of this process there was no such CASPER support for the ZCU111 and thus it was deemed best to use a different approach.

While the ZCU111 and 2x2 RFSoCs did not initially have CASPER support, they could instead be programmed using Xilinx's Pynq development framework (116) (117). Pynq is an open source framework developed by Xilinx for programming Xilinx platforms. Similar to the CASPER approach, the Pynq approach intends to simplify the programming process by utilizing re-usable Python libraries. This Pynq approach which was employed for programming these boards also consisted of two steps:

- Writing firmware for the board using Xilinx Vivado for programming the data converters and performing the digital signal processing.

- Writing Python code via JupyterLab Notebooks to interact with the RFSoCs' firmware and output results.

Vivado (118) is a Xilinx package for developing HDL code for their packages and compiling this code into firmware files, namely .bit, .hwh and .tcl files. While it is at a lower level of abstraction than MATLAB Simulink, as was used for the ROACH, it still contains some pre-programmed, re-configurable firmware blocks which can be re-used for different boards and different firmware designs. While Vivado allows for the user to programme firmware using HDL code such as VHDL or Verilog, it also allows for higher level programming using these above-mentioned firmware blocks. This is what was used to programme the firmware for the RFSoCs. JupyterLab(119) is a web based notebook interface that is used to run interactive Python notebooks, that is used to generate visualisations of the data inputted and outputted from the RFSoC without the need for generating a bespoke graphical user interface for the project.

7.2 Design

The firmware design for this board follows the same basic approach as that used for ROACH 1 systems in Chapter 5 and shown in Figure 5.3. I and Q signals are generated for a comb of frequencies. These can be generated from -2 GHz to 2 GHz due to the RF data converters of the RFSoCs. This frequency comb then has to be upmixed to the the 4 GHz to 8 GHz octave. Obviously, this highlights the need for a mixer board for the RFSoCs. While the mixer board which was used for the ROACH system (105) could be re-purposed to be used with the RFSoCs, as it only has a bandwidth of 512 MHz, the remaining bandwidth of the RFSoCs' data converters would be wasted. Again, these upmixed signals are fed into the ADR and excite the MKID array, such that photon events are imprinted on the signals in the frequency comb. These output signals are then downmixed back to baseband frequency and are digitized by the RFSoCs' RF ADCs. The FPGA then performs frequency domain multiplexing, made up of an FIR filter and FFT followed by a digital down conversion stage and low pass filter. Finally, the same pulse detection approach as used in Section 5.3 is used to search for photons in each individual channel based on the phase, calculated using Equation 1.33 exceeding a certain threshold.

The main difference between this implementation for the RFSoCs and for the ROACH 1 is in the dimensions of the signal processing blocks. For example while both implementations are using a polyphase filter bank based on an FIR filter on FFT, due to the increased FPGA and data converter capacity of the RFSoCs, a much larger PFB can be implemented, which can channelize more MKIDs. Similarly, while both designs use the DACs to output a comb of frequencies, and the ADCs to re-digitize the output from the ADR, due to the significantly fast data converters on the RFSoC, it can operate with 2,000 signals per feedline, as opposed to 256 for the ROACH 1. For the convenience of the reader, this readout implementation plan is included again in Figure 7.1, updated to include the capabilities of the ZCU111 and 2x2 RFSoCs.

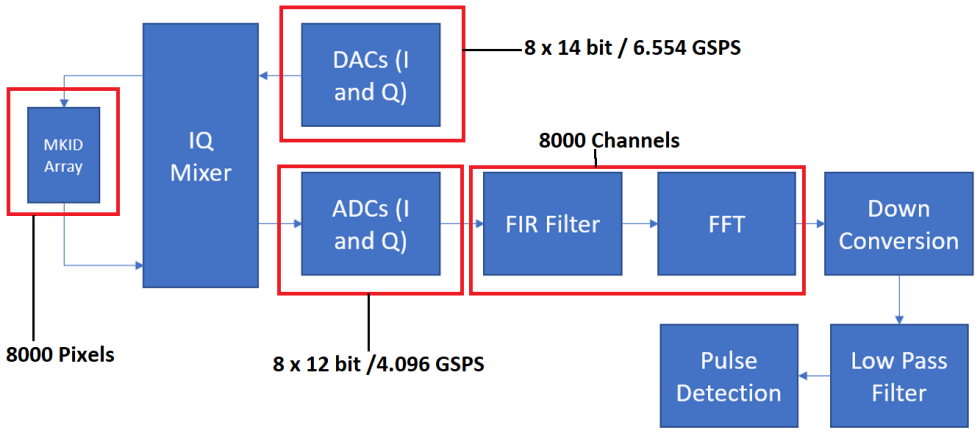

Figure 7.1: Flow Diagram showing the approach used to readout arrays of optical MKIDs using frequency domain multiplexing (FDM) for the ZCU111. This is adapted from Figure 5.3.

7.3 Progress

7.3.1 Data Converters

Following the design outline shown in Figure 5.3, the first step taken in programming the RFSoCs was to develop the control firmware for the ZCU111's RF data converters. Figure 7.2 and Figure 7.3 show the Vivado firmware design which was developed for controlling these data converters. Figure 7.3 in particular shows the contents of the 'dataconverters' block that can be seen in Figure 7.2. As described above, while Vivado does allow for pre-designed blocks of firmware to be used in a design, this is at a lower level than when using MATLAB Simulink and CASPER. However, the Zynq Ultrascale+ RF Data Converter block (120), which is shown in Figure 7.3 was able to be used as the basic control firmware for the data converters. This block can be modified to define characterisitcs such as the data converter's sampling and clock rates, and which of the ZCU111's SMA ports to connect the data converter. To allow for the data converters to interact with the chips processor, the Zynq Ultrascale+ RF Data Converter block is coupled with an AXI Direct Memory Access (DMA) Block (121) which provides high bandwidth access between firmware blocks, such as this data converter block, and the CPU,

and memory. These two firmware blocks are then lumped together into a single 'dataconverters' block which is coupled to the Zynq Ultrascale+ MPSoC block(122), which is used to connect between the processor and FPGA's programmable logic. The three remaining firmware blocks shown in Figure 7.2 manage and synchronize the clock and reset signals between the data converters, DMA block, processor and programmable FPGA logic. The design shown in Figure 7.2 was successfully compiled into .bit, .hwh, and .tcl firmware files that could then be loaded onto the ZCU111.

With these firmware designs compiled and loaded onto the ZCU111, the next step in controlling the board's data converters was to write Python control scripts. As stated above, using the Pynq approach to programming RFSoCs, instead of just using a regular Python script, this Python code was written as JupyterLab notebooks. Using this, a user can open JupyterLab in a browser window, and, provided their PC is connected to the ZCU111 board via Ethernet, connect to it by navigating to the board's IP address. From here the board can be programmed by calling the firmware files which have already been loaded onto the board. Then the data converters can be programmed by writing to their registers, similarly as was done for the ROACH board in Chapter 5.

Code was written to allow a user to input an array of frequencies, each with a corresponding amplitude relative to the full scale of the 14-bit DACs. A sine wave was then generated in software for each of these frequency/amplitude pairs, giving each individual signal in the desired frequency comb. All of these individual tones were summed together to get the entire waveform of the frequency comb. At this point it was important to verify that the maximum value of this combined waveform did not exceed the maximum 2^{14} range of the DACs. This was done in software simply by checking the maximum value of the integer array describing this combined waveform. If this happened the frequency comb waveform was multiplied by a constant make sure it didn't exceed the maximum and cause overflow issues. This final waveform could then be written to the data converters' registers via the DMA

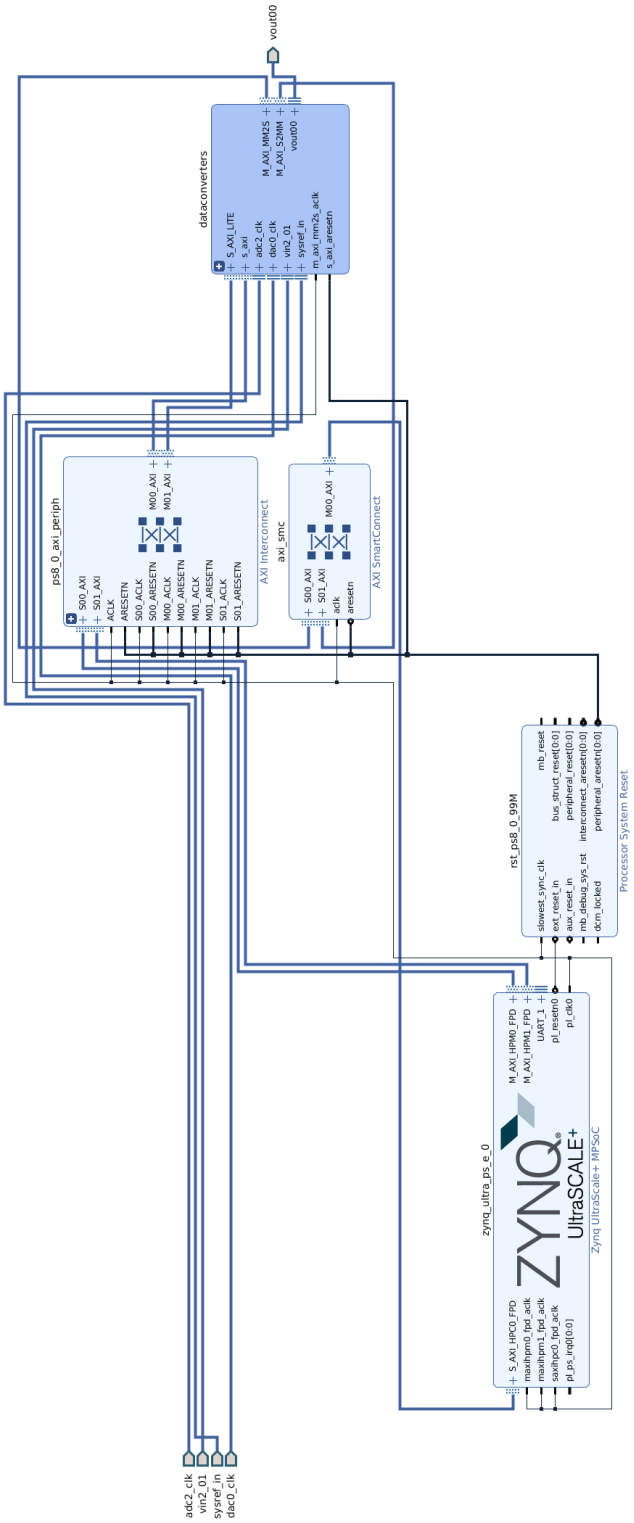

Figure 7.2: Vivado block diagram for data converter control firmware. The 'data-converters' block is connected to the ZCU111's Zynq Ultrascale+ MPSoC processing unit via the Xilinx AXI Interconnect and SmartConnect firmware blocks.

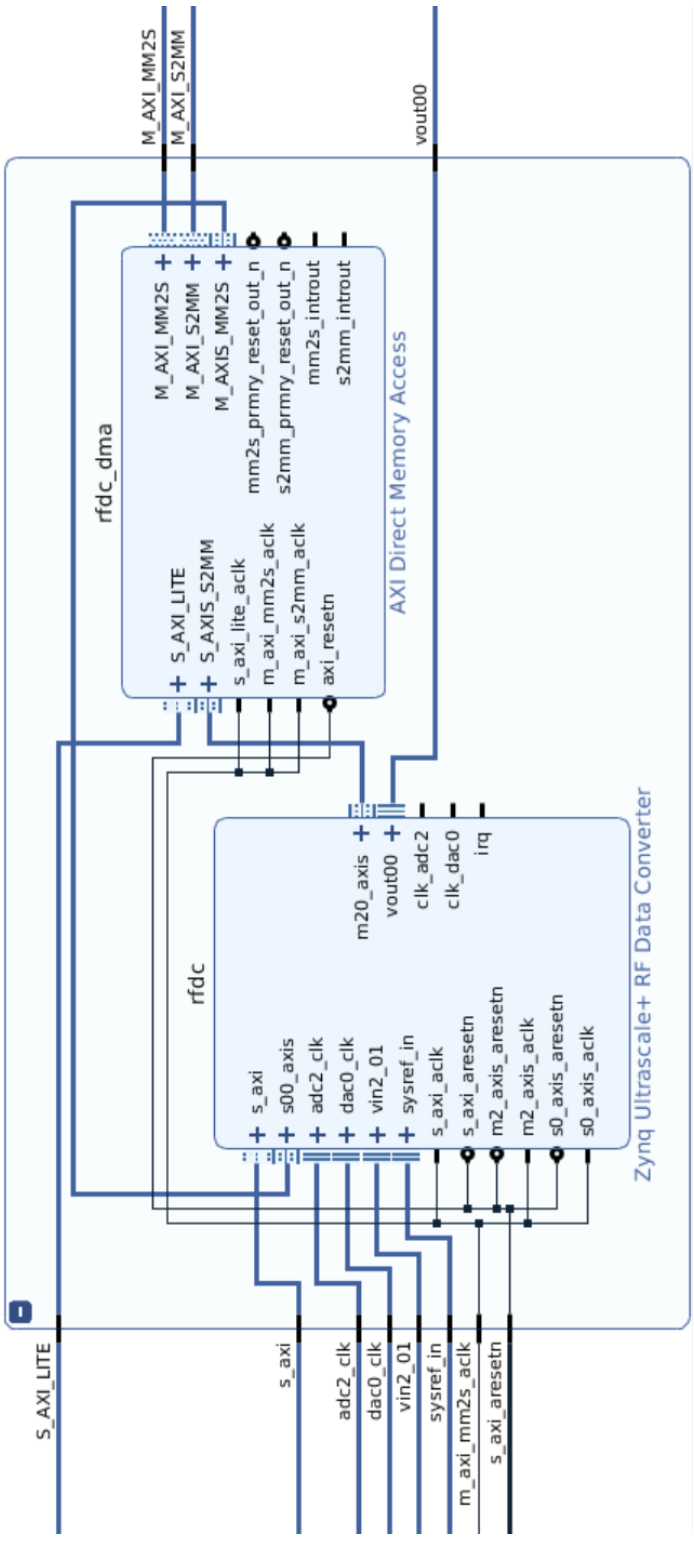

Figure 7.3: Vivado block diagram of the contents of the 'dataconverters' block which is shown in Figure 7.2. This consists of a Zynq Ultrascale+ RF Data Converter block which is coupled to an AXI Direct Memory Access block.

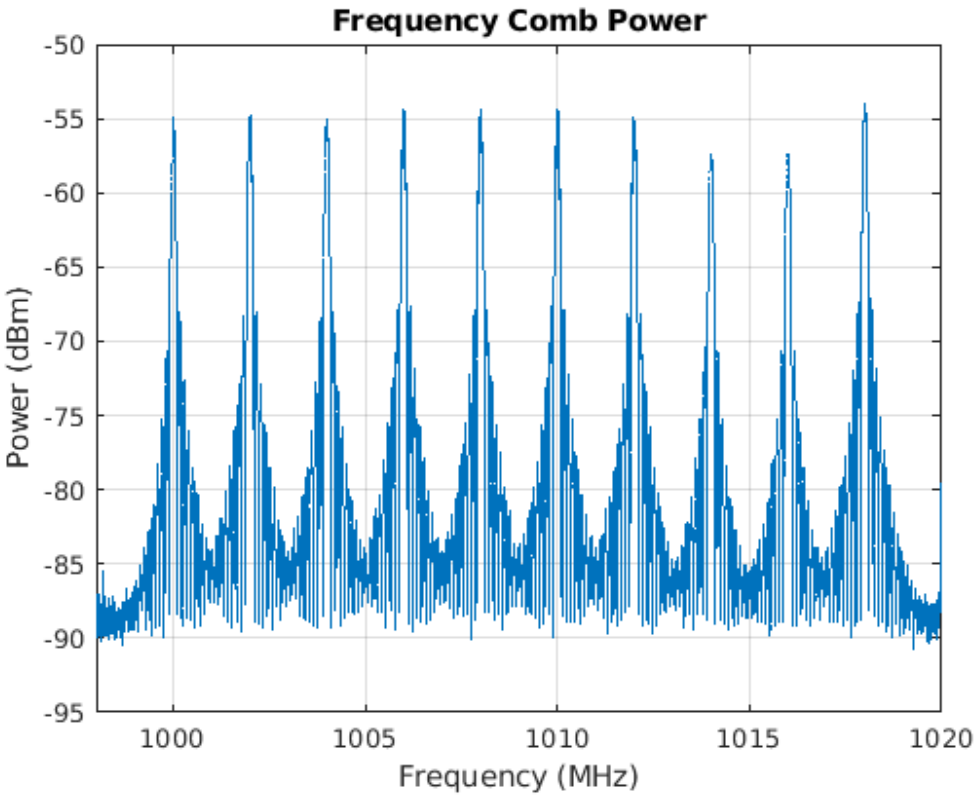

Figure 7.4: Frequency comb generated by ZCU111 at frequencies between 1000 MHz and 1018 MHz and measured using a vector network analyser

block in Figure 7.3. At this point the DAC outputs the desired array of frequencies, with their corresponding amplitude. Figure 7.4 displays a frequency comb generated with the ZCU111 using the firmware and software described in Section 7.3.1 and measured using the Vector Network Analyzer used in Chapter 4.

While Figure 7.4 shows a frequency comb generated by the ZCU111's DACs and measured using the VNA, shows the operation of these DACs, the ADCs also had to be programmed. In the same way as done for the DACs, the Python code was written for JupyterLab to read from the ADCs registers, via the direct memory access block in Figure 7.3. Thus, a frequency comb was generated with the DACs, but instead of reading it in with the VNA, a loop back test was carried out. This means that the output from the ADC was connected directly to the DAC via a co-axial cable. An FFT was then performed in software on both the data outputted by the DACs and the data digitized by the ADCs to confirm that both showed the same frequency comb, confirming that the ADCs were also programmed

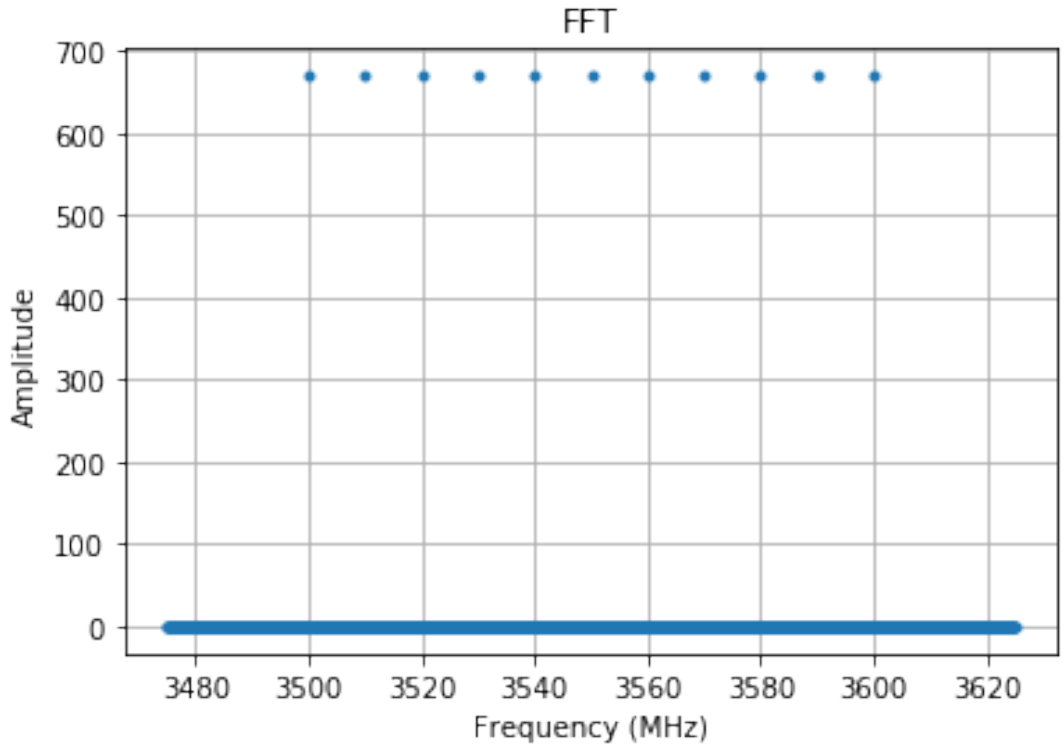

Figure 7.5: FFT applied using Python to frequency comb generated by ZCU111's DACs at frequencies from 3500 MHz to 3600 MHz.

correctly.

Figure 7.5 displays the result of applying a FFT using Python to the combined frequency comb waveform which is sent to the DACs. At this stage, this is a purely mathematical function, consisting of nine sine waves summed together. Because of this, the FFT gives eleven ideal signals, each with the same power and zero width. Figure 7.6 shows the result of applying the same Python FFT to the corresponding data when it is digitized by the ADCs. While it is clear that the same eleven tones in the frequency comb have been received by the ADCs, showing that both sets of data converters are operating correctly, unlike the data in Figure 7.5, the tones in Figure 7.6 are no longer ideal signals with uniform height and zero width.

Along with the code described above, the Python code was also modified to perform frequency sweeps with the RFSoCs, in the same way as was done using both the VNA in Chapter 4 and using the ROACH 1 in Chapter 5.4. This can be used to change the frequency in the signals in a frequency comb across a defined

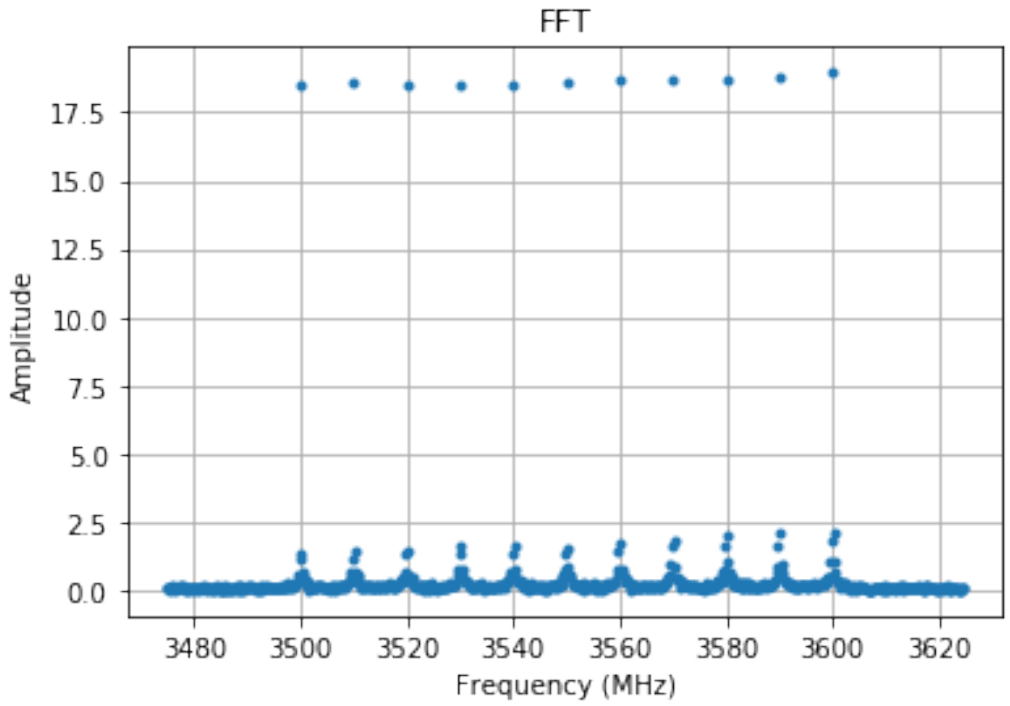

Figure 7.6: FFT applied using Python to frequency comb digitized by ZCU111's ADCs. This shows the same signals as displayed in Figure 7.5, but after they have been re-digitized by the ADCs.

span, with a defined number of steps, thus sweeping the frequencies being output by the DACs.

7.3.2 Mixer Board

While the firmware and software presented in Section 7.3.1 was able to successfully programme the ZCU111's data converters, it must be noted that frequency combs presented in Section 7.3.1 were all at lower frequencies lower than the 4 to 8 GHz octave for which the MKIDs in this project are designed. Thus, despite the far larger bandwidth of the RFSoCs' data converters compared to the ROACH 1, a mixer board board was still required to access this octave. Similarly, due to the expanded bandwidth of the RFSoC, the Techne Instruments mixer board used for the ROACH 1, with its bandwidth of 512 MHz, could not be used for the RFSoCs.

Thus, to solve this issue, an intermediate frequency mixer board was sourced from Dr. Deli Geng in Durham Univeristy who is also developing firmware for reading out

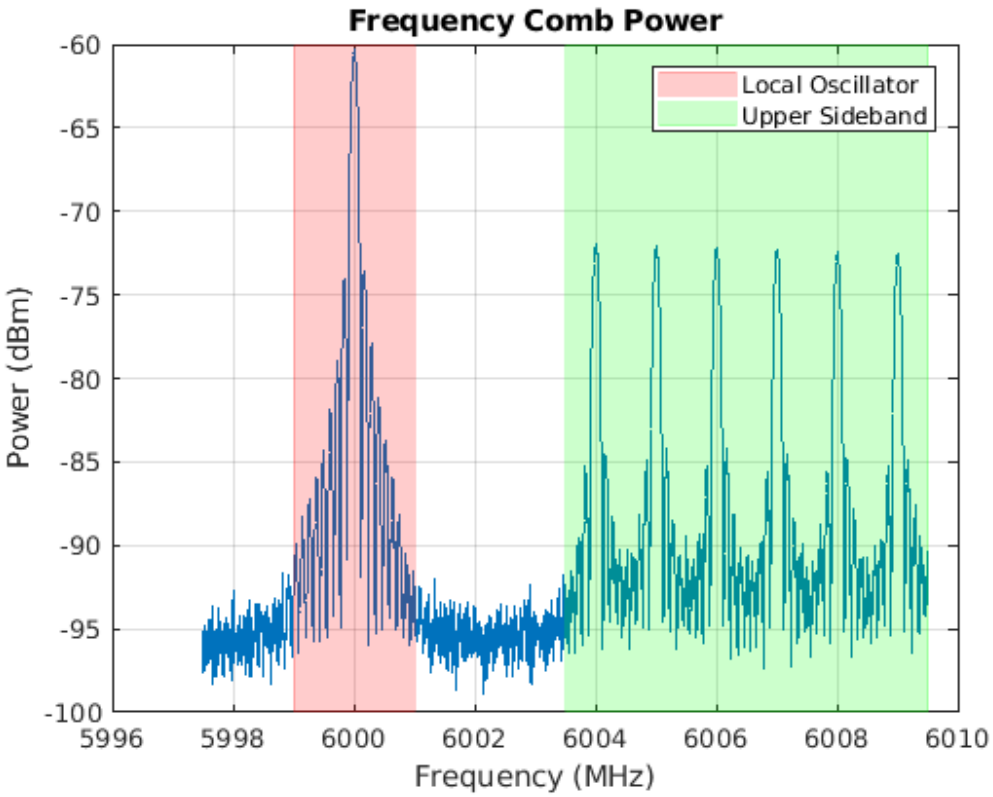

Figure 7.7: Frequency comb generated by ZCU111 from 4 MHz to 9 MHz and upmixed with 6 GHz local oscillator with mixer board and measured using vector network analyser.

MKIDs using the ZCU111 RFSoC. Figure 7.7 shows an example of a frequency comb, generated at baseband frequencies, and then upmixed with the 6 GHz local oscillator of this mixer board, to the upper sideband.

7.3.3 Fast Fourier Transform

For programming the FPGA to perform an FFT on the digitized data, the Xilinx Fast Fourier Transform firmware block(123) on Vivado was used. This block implements a programmable FFT which can be modified to perform different length FFTs, from size 2^3 to 2^{16}. This can be easily modified and re-compiled for different firmware designs. While this value can be easily changed, a default FFT length of $2^{11} = 2,048$ was selected. This was because the optimum solution for minimizing cost-per-pixel, as detailed in Chapter 6, was to use four 2x2 RFSoC boards, with each reading out 2,000 MKIDs. Thus, a 2048 tap FFT would be sufficient for

providing one frequency bin for each resonator in the array. For interacting with this FFT block, the same approach was used as for interacting the data converter blocks, coupling the FFT to an AXI direct memory access block, which is then connected to the processor with additional firmware to control the reset and clock signals. The Vivado firmware block design for this process is displayed in Figure 7.8.

To test this design, firstly an idealized frequency comb, like that shown in Figure 7.5, was applied to the FFT block. After this, the real frequency comb data, which was digitized by the ADCs, like that shown in Figure 7.6 was also applied to the FFT block. Thus the performance of the firmware implemented FFT could be compared to one performed using Python. Figure 7.9 shows the results of applying an ideal 14-tone frequency comb to this firmware block.

7.3.4 Finite Impulse Response Filter

With one component of the polyphase filter bank, which consists of an FFT and FIR filter (as is highlighted in Figure 7.1), now complete, the next piece of firmware needed was the FIR filter section. This could be done with the same design as was used for the FFT firmware and shown in Figure 7.8, but replacing the Vivado FFT block with a Vivado FIR compiler block(124). This firmware block can be modified to achieve the desired filtering with a choice of filter coefficients. Up to 1024 sets of filter coefficients can be implemented by this FIR compiler block, thus allowing 1024 individual filters to be applied. A MATLAB script was written to use MATLAB's "fir1" function to generate filter coefficients based on user defined characteristics, such as corner frequencies, number of filter taps, and filter type, such as rectangular, Blackman, Hamming or Hanning filters (37). This code is included in Appendix A1.3.

The results from testing this FIR filtering firmware is shown in Figure 7.10 and Figure 7.11. Figure 7.10 shows an FFT of a ten tone frequency comb outputted

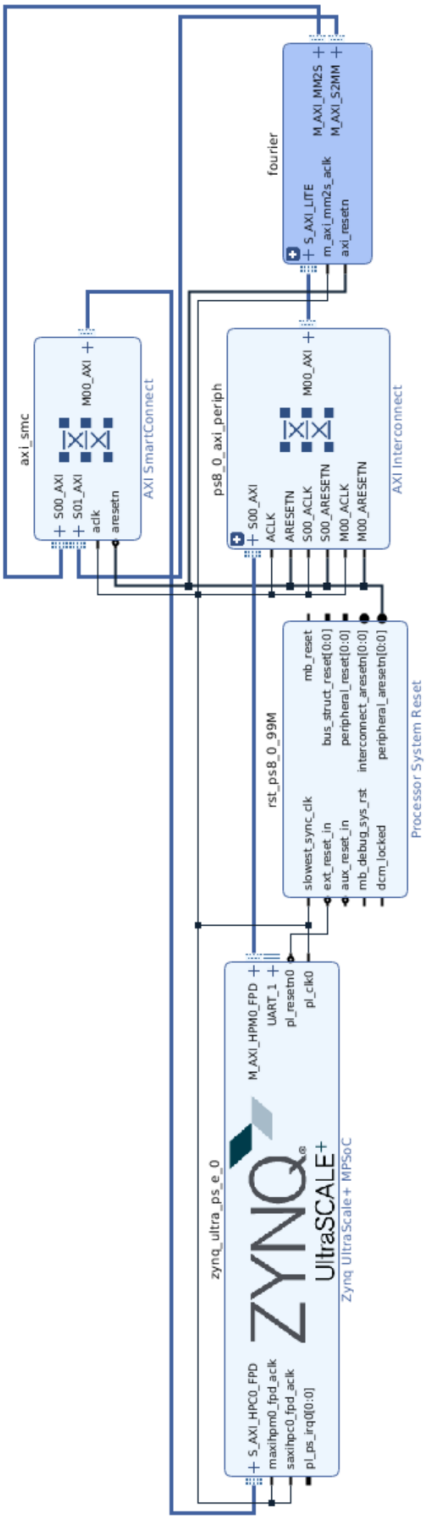

Figure 7.8: Vivado block diagram for fast Fourier fourier transform firmware. The 'fourier' block is connected to the ZCU111's Zynq Ultrascale+ MPSoC processing unit in the same way as was done for the data converters in Figure 7.2.

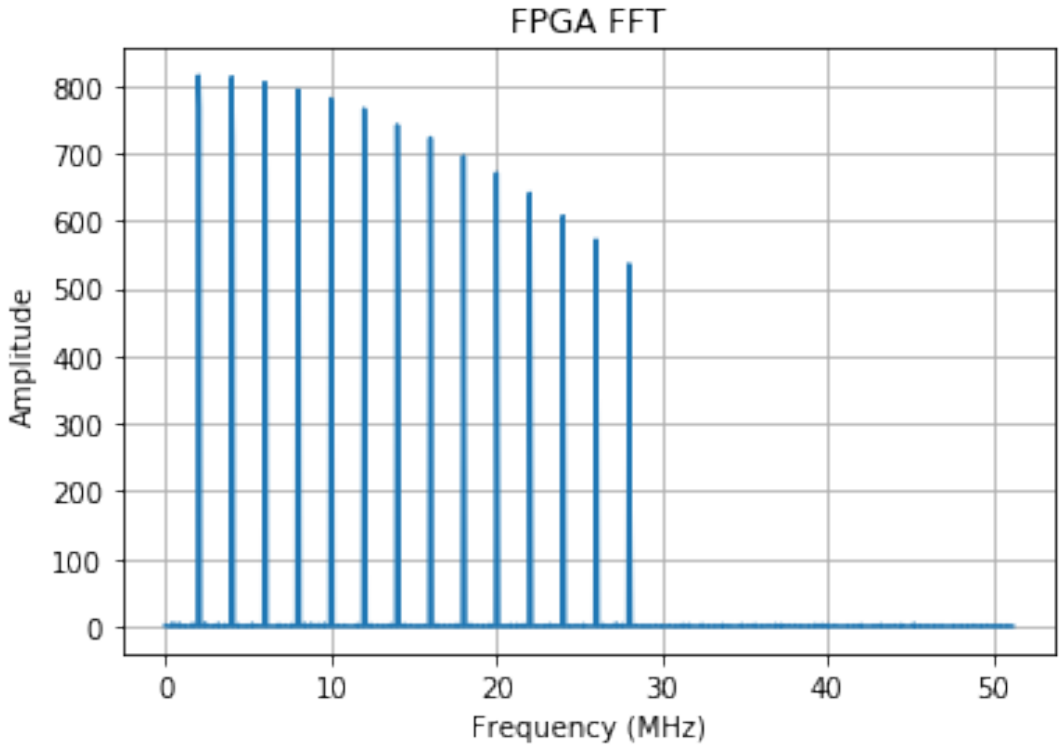

Figure 7.9: FFT of a 14 tone frequency comb applied to fast Fourier transform firmware which was developed for ZCU11, shown in Figure 7.8. The power of the tones drops off due to the non flat frequency response of the FFT.

which has been digitized by the ADCs. Figure 7.11 shows the results of digitizing this signal with the ADCs and sending it to the FIR filter block in the firmware. In this instance the filter block is configured to apply a low pass filter (with frequency response shown in Figure 7.12) with a cutoff frequency of 5 MHz, thus filtering out frequencies above this point. This shows the correct operation of a programmable FIR filter on the ZCU111 FPGA. It is important to note that while this shows a single filter (shown in Figure 7.12) being applied to a single frequency comb, this filter block can be programmed with a range of different sets of filter coefficients, thus achieving a filter bank.

7.3.5 Combined Firmware Design

With working firmware successfully developed for programming the DACs and ADCs, as well as for applying a programmable series of FIR filters and an FFT, the next step of the firmware design was to take each of these individual components

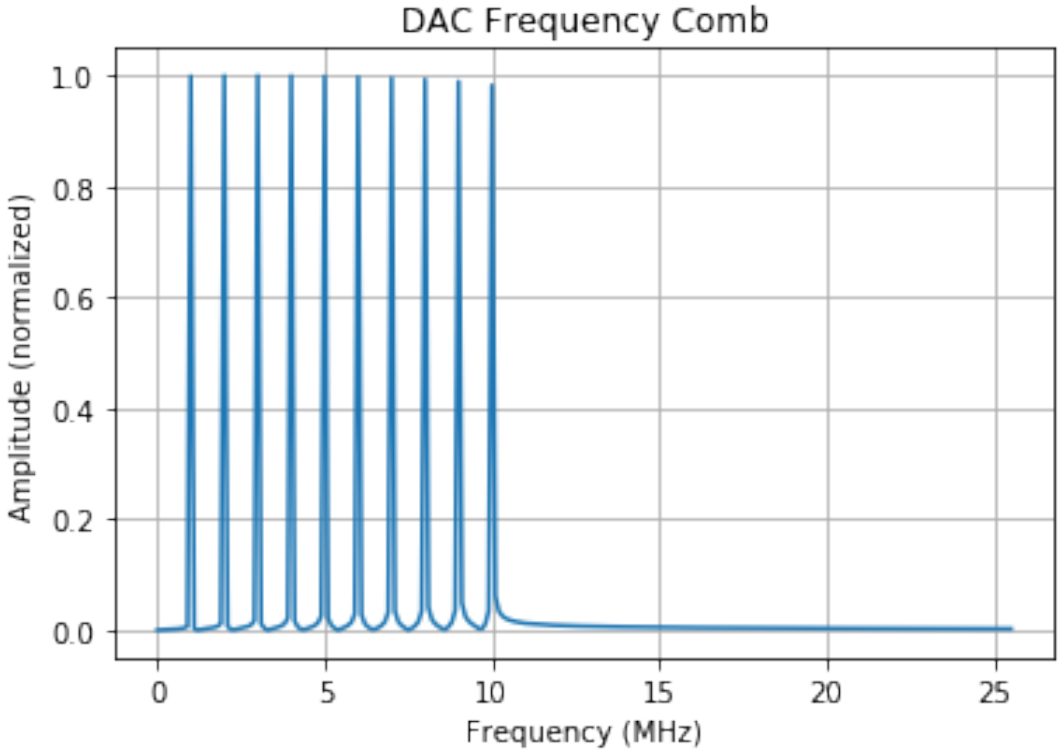

Figure 7.10: FFT of a 10 tone frequency comb sent to DACs before applying FIR filtering firmware.

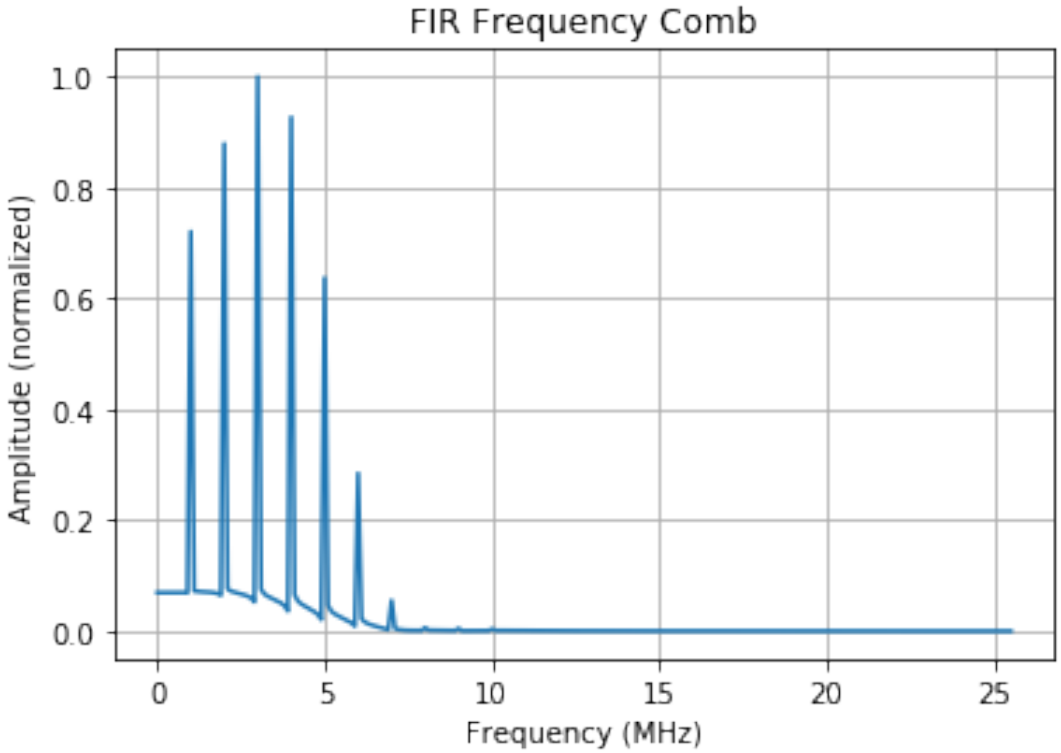

Figure 7.11: FFT of a 10 tone frequency comb sampled by ADCs and filtered using the FIR low pass filtering firmware which was developed.

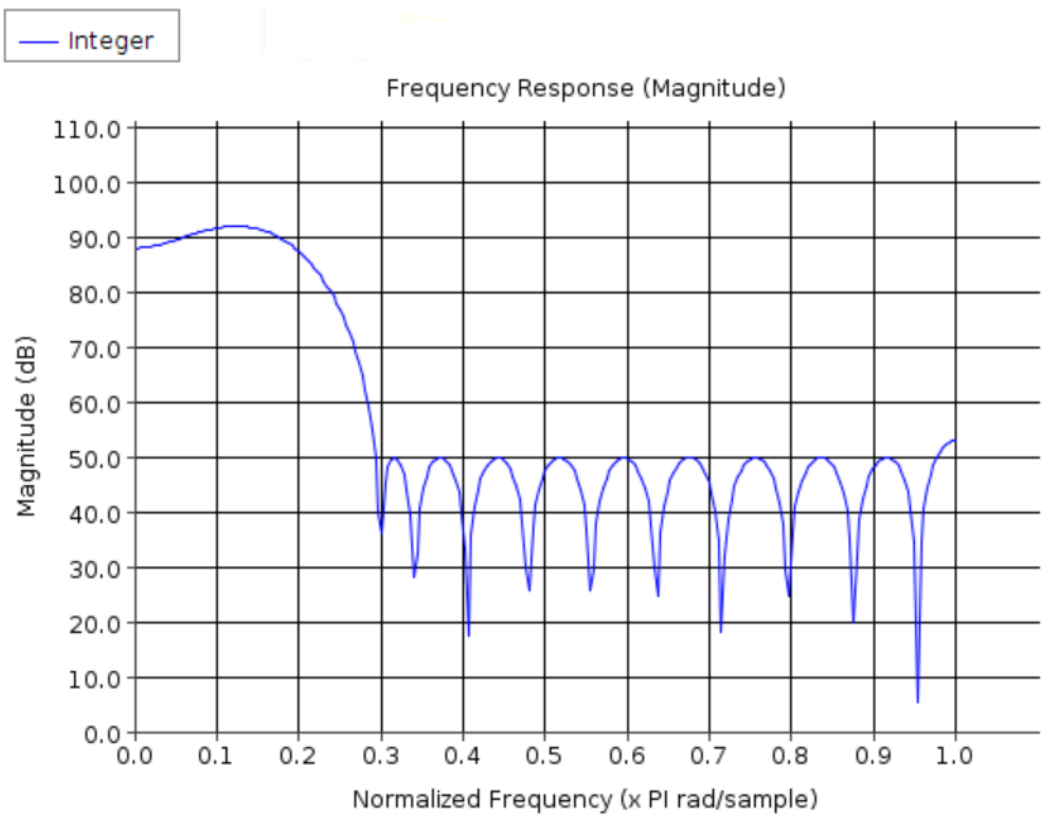

Figure 7.12: Frequency response of a sample low pass FIR filter with coefficients generated by the code in Appendix A1.3. These filter coefficients can be loaded onto the FIR filtering firmware.

and combine them together into a single firmware file which can be compiled and loaded onto the ZCU111's FPGA. To achieve this each of the firmware programmes described in Section 7.3.1, Section 7.3.3 and Section 7.3.4, were combined such that each element was coupled to a single direct memory access block, connecting each of them to the processor. Similarly, the corresponding JupyterLab Python notebooks for each of these firmware files were also combined giving a single file that allows a user to sequentially programme the DACs to output a frequency comb, the ADCs to digitize the output from the ADR, and then send this digitized waveform to the FIR filter bank and FFT block to channelize the digitized waveform into a series of frequency bins, with each bin corresponding to a single bandwidth, and thus a single tone in the frequency comb and a single pixel in the MKID array.

7.3.6 Adapting Firmware for 2x2 RFSoC

While the work described in Chapter 7 was initially carried out on the ZCU111, due to it being released first, once a 2x2 RFSoC was obtained the ZCU111 firmware was adapted to also be usable with the 2x2. As already described, as both boards use a ZYNQ UltraScale+ RFSoC XCZU28DR FPGA (18) (19) it is relatively straightforward to adapt the firmware which is developed for one of these boards to the other board. To use the ZCU111 firmware for the 2x2 the only thing which needed to be changed was to download the relevant 2x2 RFSoC board files for Vivado and to select the 2x2 instead of the ZCU111 when setting up the project. On top of this, as the 2x2 only has one pair of ADCs and one pair of DACs, it was important to make sure that the correct data converters were selected in the RF Data Converter firmware block. Once this was done the firmware designs were compiled and loaded onto the 2x2 boards and were also shown to work correctly, in the same way as they did for the ZCU111. Similarly, the same Python notebooks also worked for the 2x2 board with minor adjustments.

8 Conclusion

This thesis has detailed the work completed developing MKIDs and MKID readout systems at the Dublin Institute for Advanced Studies and Trinity College Dublin, as well as providing an introduction into the operation of MKIDs, and some background information into some of the fields in which they have been applied.

A complete laboratory setup was built up from scratch, including an adiabatic demagnetization refrigerator capable of cooling down to temperatures as low as 30 mK, as well maintaining temperatures of 100 mK for approximately 16 hours. While this ADR was purchased from Entropy Cryogenics, significant modifications had be made to ensure it was capable of cooling down MKID arrays and allowing then be analysed. Modifications had to be made to the sample space to add a plate on which a sample box containing an MKID array could be mounted. Low temperature co-axial cabling was installed from the room temperature stage of the ADR, down to the mK stage where the sample box is mounted, allowing GHz signals from either the readout system or the vector network analyser to excite the MKIDs, and also to allow the signals outputted from the MKID array to pass back out from the ADR. Furthermore, optical filters were characterised and installed in the fridge allowing light from a laser box to be shone on the samples. Other additions to the ADR which were made were the addition of HEMT amplifiers, to amplify the signals output from the MKID array at cryogenic temperatures, as well as the design and construction of a critical temperature measurement setup. This uses a

resistance bridge to measure the resistance of superconducting films as the temperature decreases below the critical temperature.

VBScript code was written to perform frequency sweeps for multiple resonators in an array, measuring S_{21} for a selected excitation power, and saving off the data in terms of I and Q. Python code was then also written to take this data and to fit it to equations from the literature and to extract Q, Q_i, Q_c and ω_0 from these fits. This allowed for the MKIDs which were fabricated to be characterized, and this characterization was used to tweak the design of these resonators until the quality factors of the MKIDs were optimized. This was used to increase in internal quality factor of the MKIDs from initial values of approximately 2,000 to optimized values of approximately 120,000.

As well as this, single pixel analysis firmware and software was developed for a ROACH board allowing for photon pulse data from an MKID array to be saved to an external PC for analysis. This code was used to diagnose an issue with excess undesirable phase noise in the resonators, which was later mitigated by annealing the resonators at the end of the fabrication process. After this change was made to the fabrication recipe, the ROACH readout system was used to measure tens of thousand of pulses from the resonators, caused by being excited by light with wavelengths ranging from 400 nm to 900 nm. From this data the energy resolution was determined to be 3.14 for 400 nm, 3.01 for 525 nm, 2.60 for 650 nm, 2.57 for 775 nm and 2.50 for 900 nm.

With an operational MKID readout system based on the ROACH board, it was decided to develop a new readout system capable of reading out thousands of MKID pixels, using a single electronics board. Thus, an analysis was carried out on some of the solutions which were available on the market. Comparing the prices of these boards and the number of pixels which they could potentially read out, as well as considering some other factors such as what additional parts would be required, it was ultimately decided that the Xilinx ZCU111 and 2x2 radio frequency

system-on-chips were the most promising solutions.

Finally, firmware and software was then written for these Xilinx boards, with the intention of using them to read out thousands of MKIDs. This code controls their data converters, outputting frequency combs at the desired frequencies from the DACs. These frequency combs can be fed into the ADR, exciting the MKIDs. The output signals from the MKIDs can then be digitized by the ADCs, and filters and FFTs can be applied to the digitized data, separating this data into equally spaced channels. Work is ongoing scaling up this code to allow for it to be used a kilo-pixel MKID readout.

9 Future Work

9.1 Optimizing Resonator Performance

As shown in Section 5.4, the first MKIDs which were measured using the ROACH readout system showed considerable amounts of undesirable phase noise. However, by annealing the MKID samples at the end of the fabrication process this phase noise was greatly reduced and the MKIDs were able to be reliably used to measure photon pulses with intrinsic energy resolution. However, these resonators still only showed an energy resolution of approximately 4, and thus the first suggested piece of future work is to improve upon this figure.

While the annealing process did succeed in causing a decreased phase noise, it also reduced the quality factor of the resonators, while also introducing a considerable shift away from their design frequency, and a decrease in the critical temperature. A shift in the resonant frequency of the MKIDs suggests a shift in the inductance of the samples, as per Equation 1.20. The resonator shown in Section 5.5 was for a $5pH/\square$ design. This means that the design presumed that the superconducting film had a sheet inductance of $5pH/\square$. The fact that the actual resonant frequency was lower than expected suggests that the actual sheet inductance of the superconducting film was greater than this. Thus, it is suggested to characterise another MKID array, with the fabrication process as in Section 5.5, but which has been designed for a lower sheet inductance.

This should result in a higher resonant frequency, which should shift the resonators

back into the ideal operating range of the HEMT amplifier. This should reduce the noise and thus cause an increase in the quality factor of the resonators. This noise reduction could also improve the energy resolution of the resonators.

Another thing which must be noted is that the annealing step decreased the critical temperature of the MKIDs from 1520 mK to below 1000 mK. This is an important factor to consider because it was found in earlier samples that TiN/Ti multilayer MKIDs display low quality factors if their T_c drops below 1.2 K. Also, in general the best MKID energy resolutions is achieved at temperatures below approximately $T_c/10$, because at this point there no more unpaired electrons. However, it must be noted that this is only a rule of thumb. Since the ADR is unable to maintain an operating temperature of 75 mK for considerable time, it was impossible to properly characterise these resonators at their optimal temperature. Instead the energy resolution measurements were done at the sub-optimum temperature of 100 mK. Thus, a second step in optimizing the performance of these MKIDs is to optimize the critical temperatures of the annealed samples. The effect of operating an MKID at above its ideal operating temperature is shown in Figure 9.1, demonstrating the need to properly optimize the critical temperature of the annealed samples.

9.2 Using RFSoCs to Read Out MKID Arrays

While firmware was developed for the ZCU111 and 2x2 RFSoCs to control the data converters and perform the fast Fourier transform and finite impulse response filtering (see Chapteer 7), the remaining firmware as shown in Figure 7.1 needs to be developed to allow it to read out arrays of thousands of MKIDs. The FIR filter and FFT blocks perform the first stage of channelization, while a further fine channelization stage, consisting of down conversion and low pass filtering needs to be added to create individual channels for each pixel in the array. Additionally, once this fine channelization firmware has been created, the final element of the readout which needs to be designed is the pulse detection firmware to monitor a single one

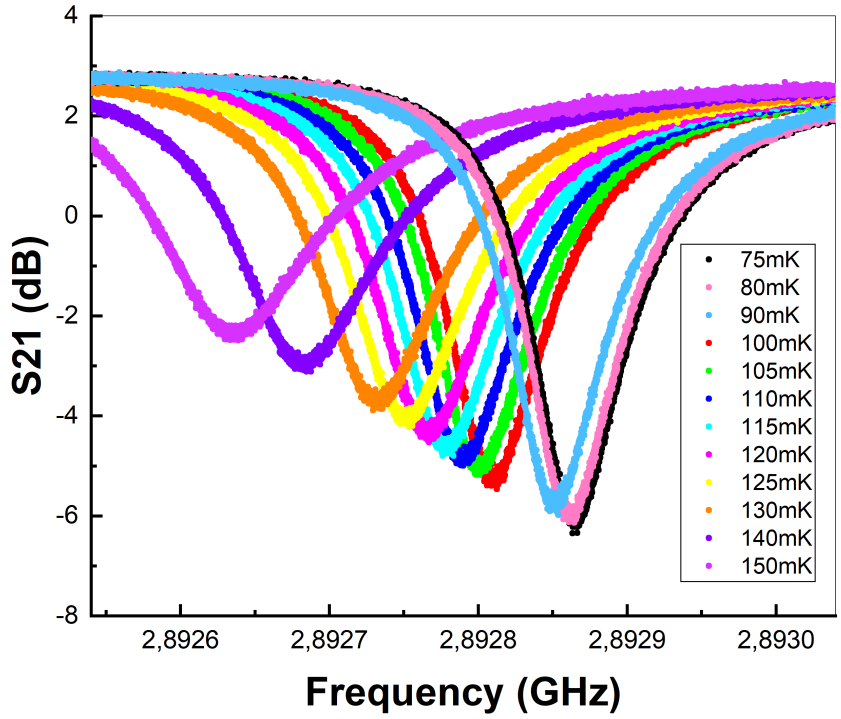

Figure 9.1: Plot showing the effect of temperature on the quality factor of an MKID at temperatures above approximately $T_c/10$.

of these fine channels for photons. Thus, the first future piece of work to be done for the RFSoCs is to write this firmware using Vivado, and similarly to write the corresponding Python notebooks for interacting with this firmware.

Following this, it is intended to use all of this firmware on a single 2x2 RFSoC to read out, potentially, 2,000 pixels. As was explained in Chapter 6, it is planned to eventually use four of these 2x2 RFSoCs to read out a total of 8,000 pixels. Thus, once a single 2x2 RFSoC is used to show the correct operation of the firmware, additional boards will need to be acquired. Previously, two RFSoC 2x2 boards have been purchased meaning that another two will be needed. One thing which must be noted is that while the first two boards were purchased at a cost of €2,000, this price may be now increased due to the current global chip shortage. Thus, this should cause an increase to the final cost per pixel value for the readout system.

9.3 Programming CASPER Boards with CASPER

A second recommended future piece of work for the RFSoC systems, both the ZCU111 and 2x2, is to examine the use of the CASPER approach for programming these boards. As was described in Chapter 7, the CASPER approach could not initially be used for the RFSoC boards due to them not yet being "CASPER-ised". This meant instead that the firmware had to be designed using the lower level abstraction of Vivado. However, other groups have since made progress with making the RFSoC board compatible with CASPER programming. Because of this it is hoped to employ this approach to compile an adapted version of the firmware used for the ROACH board in Chapter 5 for the ZCU111 and 2x2 RFSoCs and to use it to measure photon pulses. This should simplify the process of designing firmware for these boards.

9.4 Using MKIDs for Astronomy Applications

While this thesis was mainly focused on optimizing MKIDs and their readout, it must be remembered that these MKIDs are ultimately being developed in order to be used in some application, such as those detailed in Chapter 2. As the MKIDs which were developed for this project were for optical to near-infrared wavelengths, one interesting application which they could be used for is for the imaging of exoplanets. Once the energy resolution of the MKID arrays is improved (as mentioned in Section 9.1), and the ZCU111 and 2x2 readout systems are fully operational (as mentioned in Section 9.2) it is hoped to scale up the size of the MKID arrays in order to achieve a fully operational kilo-pixel MKID camera. Finally, eventually it is hoped to bring this camera to a telescope and to use it for astronomy.

A1 Appendix

A1.1 Frequency Sweep Code for Vector Network Analyser

Included below is the VBScript code used for the Keysight E5080A ENA Vector Network Analyzer to perform frequency sweep measurements for an array of MKIDs. The user defines the freuencies of the MKIDs that they want to measure, as well as the optimal power with which to excite the MKID, a well as the desired frequency sweep span. The user can define as many resonators as they desire. The code then performs frequency sweep measurements for each of these resonators, measuring S_{21} and saving off the output data in 3 columns, one for frequency, one for I and one for Q. This is described in Section 4.2.

Listing A1.1: Frequency Sweep Code

```
'This program creates a S21 measurement
'It is written in VBscript using SCPI commands

Dim app
Dim scpi
Dim oFSO

' required for creating a folder
```

```
'Create / Get the VNA application
Set app = CreateObject ("AgilentPNA835x.Application")
Set scpi = app.ScpiStringParser
Set oFSO = CreateObject("Scripting.FileSystemObject")

'Create / Get the VNA application
Set app = CreateObject ("AgilentPNA835x.Application")
Set scpi = app.ScpiStringParser

'Define frequency etc
freqs = Array(5254.1975)
powers = Array(-60)
spans = Array(3)
Name_Var = "Sample Sweep"
power_change = 0
Folder_Name = CSTR(Year(Now)) + "_" + CSTR(Month(Now)) + "
   _" + CSTR(Day(Now)) + "_" + Name_Var
oFSO.CreateFolder "C:\Users\Instrument\My Documents\
   Frequency_Sweeps\" + Folder_Name

For i = 0 to UBound(freqs) Step 1

    freq = freqs(i)*1000000
        power = powers(i) + power_change
        span = spans(i)*1000000
        freqstr = CSTR(freq)
        powerstr = CSTR(power)
        spanstr = CSTR(span)
```

```
'Preset the Analyzer.FPREset presets the setting
   and deletes all traces and windows
scpi.Execute ("SYST:FPReset")
'Create and turn on window 1
scpi.Execute ("DISPlay:WINDow1:STATE␣ON")

'Define a measurement name, parameter
scpi.Execute ("CALCulate:PARameter:DEFine:EXT␣'
   MyMeas',␣'s21'")

'Set power level
scpi.Execute("SOUR:POW1␣" + powerstr)

'Set centre frequency of sweep
scpi.Execute("SENS:FREQ:CENT␣" + freqstr)

'Set frequency span of sweep
scpi.Execute("SENS:FREQ:SPAN␣" + spanstr)

'Set number of points in sweep
scpi.Execute("SENS:SWE:POIN␣10001")

'Change format to Polar
scpi.Execute("CALC:MEAS:FORM␣POL")

'Associate ("FEED") the measurement name ('MyMeas
   ') to WINDow (1), and give the new TRACE a
   number (1).
```

```
scpi.Execute ("DISPlay:WINDow1:TRACe1:FEED␣'MyMeas
    '")

'Autoscales display
scpi.Execute ("DISP:MEAS:Y:AUTO")

'Starts averaging
scpi.Execute ("SENS:AVER␣ON")

'Set number of points to average over
scpi.Execute ("SENS:AVER:COUN␣64")

WScript.Sleep(10000) 'sleeps for 10 second to
    allow averaging to finish

'Dim measurementdate as String
filename = "C:\Users\Instrument\My␣Documents\
    Frequency_Sweeps\" + Folder_Name + "\" + "
    sweep_" + Name_Var + "_" + CSTR(Year(Now)) + "_
    " + CSTR(Month(Now)) + "_" + CSTR(Day(Now)) + "
    _" + powerstr + "_" + freqstr + ".csv"

savestring = "'" + filename + "','CSV␣Formatted␣
    Data','displayed','RI',-1"

'Save data to csv file
scpi.Execute ("MMEM:STOR:DATA␣" + savestring)
```

Next

A1.2 S_{21} Fitting Code

Included here is the Python fitting code, as described in Section 4.3, which takes the output files generated by the VNA code (see Section A1.1), and fits this data to the equations from the literature (17) (103) and extracts the resonant frequency, total quality factor, coupling quality factor and internal quality factor from these fits. Derived in Section 4.3, the final equations, for $|S_{21}|^2$ and phase, ϕ, are giving below:

$$|S_{21}(\omega)|^2 = A_1 + A_2(\omega - \omega_0) + \frac{A_3 + A_4(\omega - \omega_0)}{1 + 4Q^2(\frac{\omega - \omega_0}{\omega_0})^2} \tag{A1.1}$$

And,

$$\phi = -\theta_0 - \arctan(2Q(1 - \frac{\omega}{\omega_0})) \tag{A1.2}$$

Listing A1.2: S21 Fitting Code

```
#note, works for IQ files saved using fsweep macro saved
    on the VNA
#import usual packages
import numpy as np
from scipy.signal import argrelextrema
from scipy.signal import argrelmin
from scipy import optimize
from scipy.optimize import curve_fit
import pylab
import matplotlib.pyplot as plt
import array as arr
import csv
#from fpdf import FPDF
```

```
from matplotlib.backends.backend_pdf import PdfPages
from datetime import date
import os


#gets todays date.
#This is used in the name of the results files that are
    saved.
today = date.today()
todaystr = today.strftime("%Y_%m_%d")

#E.17 from Gao thesis - will be used later to  amplitude
    data fit curve
def amplitudeequation(f, A1, A2, A3, A4, Qr, fr):
    return A1 + A2*(f - fr) + ((A3 + A4*(f - fr)) / (1 + 4
        * Qr**2  * ((f - fr)/fr)**2 ))

#E.11 from Gao thesis - can be used to fit phase data
def phaseequation(f, theta0, theta1, Qr, fr):
    return -theta0 - theta1*(f - fr) + 2*np.arctan(2*Qr*(1
        - (f/fr)))


#ask user to enter filename.
#Uncomment these too lines if you want to prompt the user
#print('Please enter name of .csv file: ')
#filename = input()

#file name. Hard codes the filename.
```

```
#Comment this out if prompting user for name
foldername = 'Sweep_Files/2022_01_31/'
filename = 'sweep_2021_11_10_4480250000.csv'
fullname = foldername + filename

#start reader and calculate length of file
with open(fullname) as csv_file:
    csv_reader = csv.reader(csv_file, delimiter=',')
    row_count = sum(1 for row in csv_reader)
    # fileObject is your csv.reader

number_of_values = row_count - 8
#accounts for extra lines at start and end of file

#declare 3 arrays, for frequency and I and Q values
freqs = np.zeros(number_of_values)
Ivalues = np.zeros(number_of_values)
Qvalues = np.zeros(number_of_values)


#open reader again, this time to read in data
with open(fullname) as csv_file:
    csv_reader = csv.reader(csv_file, delimiter=',')

    line_count = 0
    for row in csv_reader:
        if line_count <= 6: #opening lines, before actual
            data
             #print(f'{", ".join(row)}')
```

```
            line_count += 1

        elif line_count < row_count - 1 : #this is the
            actual IQ data
            #print(f'f = \t{row[0]} Hz, I = {row[1]}, Q =
                {row[2]}') #prints data, for debugging

            freqs[line_count-7] = row[0]
            #saves data to array from csv file
            Ivalues[line_count-7] = row[1]
            #saves data to array from csv file
            Qvalues[line_count-7] = row[2]
            #saves data to array from csv file

            line_count += 1

    #print(f'Processed {line_count} lines.')
    #prints number of lines read out. Used for debugging.

freqsMHz = freqs / 10**6
#calculate amplitude of IQ data
amplitudes = np.sqrt((Ivalues)**2 + (Qvalues)**2)

#find phases of raw data relative to origin
#have to do this for 4 different quadrants
phases = np.arctan2(Qvalues, Ivalues)



#magnitudes = amplitudes**2
```

```
#normalizedmagnitudes = magnitudes / np.max(magnitudes)

normalizedamplitudes = amplitudes / np.max(amplitudes)
#normalizes magnitude data relative to max value
squaremagnitudes = normalizedamplitudes**2
#calculates square magnitude

p0 = np.array([1, 1, 1, 1, 10000, np.mean(freqsMHz)])
#initial guesses for fit


#need to define sigma array to weight certain points
    heavier
resonant_index = np.argmin(squaremagnitudes)
#index of resonant point in array

weight_amplitude = np.ones(number_of_values)
#set relative error everywhere to 1

#weight_amplitude[resonant_index - 100 : resonant_index +
    100] = 0.01
#set error around resonant to smaller


#fits square magnitude data to amplitude equation
#popt is the array of fitted parameters
#pcov is the covariance of popt
popt, pcov = curve_fit(amplitudeequation, freqsMHz,
    squaremagnitudes, p0, sigma = weight_amplitude,
```

```
    absolute_sigma=False, maxfev=10000)


Q = popt[4] #total Q is taken from the fit
Q = abs(Q)

fr = popt[5]  #resonant frequency is taken from the fit
#fr_MHz = fr / 10**3 #resonant frequency in MHz

Qi = Q / np.min(normalizedamplitudes)
#calulculates instrinsic Q using equation 28 from
    Zmuidzinas review
Qi = abs(Qi)

Qc = Q / (1 - np.min(normalizedamplitudes))
#calulculates coupling Q using equation 29 from Zmuidzinas
     review
Qc = abs(Qc)


squaremagnitudesdb = 10*np.log10(squaremagnitudes)
#converts square magnitude data to dbs


#next need to convert this to IQ data and plot versus raw
    data
squaremagnitudefit = amplitudeequation(freqsMHz, popt[0],
    popt[1], popt[2], popt[3], popt[4], popt[5])
#saves square magnitude fit data
```

```
fitamplitude = np.abs(np.sqrt(squaremagnitudefit))
#takes sqrt to get amplitude

fitamplitudescaled = fitamplitude * np.max(amplitudes)
#unnormalizes data relative to max value


#get centre of loop
#find centre of loop
raw_data_xc = (np.max(Ivalues) + np.min(Ivalues)) / 2
raw_data_yc = (np.max(Qvalues) + np.min(Qvalues)) / 2


#Next step, remove cable delay term from data.
#To do this, normalize by cable delay loop
#For now, using circle with radius 4, centered on origin
#Will have to use actual data, after next cooldown
cabledelayphase = np.zeros(number_of_values)

#first find total angle, between first and last point
#find initial phase

initial_phase = np.arctan2(Qvalues[0], Ivalues[0])
final_phase = np.arctan2(Qvalues[number_of_values-1],
    Ivalues[number_of_values-1])

total_phase = abs(final_phase - initial_phase)
```

```
phase_per_freq = total_phase / (number_of_values - 1)

i = 0
for x in cabledelayphase:
    cabledelayphase[i] = initial_phase - phase_per_freq*i
    i += 1



#need to find amplitude of cable delay loop - take average
    of start and end  of loop
#amplitudes = np.zeros(number_of_values)
amplitudes = np.sqrt(Ivalues**2 + Qvalues**2)

cableamplitude = np.max(amplitudes) #takes max value
cabledelayI = cableamplitude*np.cos(cabledelayphase)

#finds I component of cable
cabledelayQ = cableamplitude*np.sin(cabledelayphase)
#finds Q component of cable

#plt.plot(cabledelayI, cabledelayQ, 'r')

#substract cable delay from IQ data to normalize
Inormalized = Ivalues - cabledelayI
Qnormalized = Qvalues - cabledelayQ

#amplitudes_normalized = np.zeros(number_of_values)

amplitudes_normalized = np.sqrt(Inormalized**2 +
```

```
    Qnormalized**2)

#next have to move loop to be centred on (0, 0)

xc = (np.max(Inormalized) + np.min(Inormalized)) / 2
yc = (np.max(Qnormalized) + np.min(Qnormalized)) / 2

#find alpha - the argument of zc, the centre of the
    normalized circle
alpha = np.arctan2(yc, xc)

translatedcircleI = Inormalized - xc #finds I component of
    cable
translatedcircleQ = Qnormalized - yc #finds Q component of
    cable

amplitudes_translated = np.sqrt(translatedcircleI**2 +
    translatedcircleQ**2)

#plt.scatter(translatedcircleI, translatedcircleQ, s = 5,
    color = 'm')

theta = np.arctan2(translatedcircleQ, translatedcircleI)
r_translated = np.sqrt((translatedcircleI)**2 + (
    translatedcircleQ)**2)

#now rotate everything by alpha

#need to rotate every point in this circle by -alpha
```

```
theta_rotated = theta - alpha #rotates by alpha
I_rotated = r_translated*np.cos(theta_rotated)
#finds I component of cable
Q_rotated = r_translated*np.sin(theta_rotated)
#finds Q component of cable

#amplitudes_rotated = np.zeros(number_of_values)
amplitudes_rotated = np.sqrt(I_rotated**2 + Q_rotated**2)



#plt.scatter(I_rotated, Q_rotated, s = 5, color = 'y')
thetafinal = np.unwrap(theta_rotated)

#now, fit this to phase equation
p_phase = np.array([1, 1, Q, fr])

#weight_phase = 0.001*np.ones(number_of_values)
#set relative error everywhere to 1
#weight_phase[resonant_index - 1500: resonant_index +
    1500] = 0.01
#set error around resonant to smaller

#popt_phase, pcov_phase = curve_fit(phaseequation,
    freqsMHz, thetafinal, p_phase, sigma = weight_phase,
    absolute_sigma=True)
popt_phase, pcov_phase = curve_fit(phaseequation, freqsMHz
    , thetafinal, p_phase)

#print(f'theta0 = {popt[0]}, Qr = {popt[1]}, fr = {popt
```

```
    [2]}) ')

theta0_phase = popt_phase[0]
theta1_phase = popt_phase[1]
Qr_phase = popt_phase[2]
fr_phase = popt_phase[3]

#fr_MHz_phase = fr_phase / 10**3

#plt.plot(freqs, phaseequation(freqs, popt_phase[0],
    popt_phase[1], popt_phase[2]), 'r')

Q_phase = abs(Qr_phase)

Qi_phase = Q_phase / np.min(normalizedamplitudes)
#calulculates instrinsic Q using equation 28 from
    Zmuidzinas review
Qi_phase = abs(Qi_phase)

Qc_phase = Q_phase / (1 - np.min(normalizedamplitudes)) #
    calulculates instrinsic Q using equation 29 from
    Zmuidzinas review
Qc_phase = abs(Qc_phase)



#print(f'Amplitude fit: Q = {Q}, Qc = {Qc}, Qi = {Qi}, fr
    = {fr*10**9}')
#print(f'Phase fit: Q = {Q_phase}, Qc = {Qc_phase}, Qi = {
    Qi_phase}, fr = {fr_phase}')
```

```
#final step, convert phase and amplitude fit back to IQ
    data
#and replot fit
fitted_phase = phaseequation(freqsMHz, popt_phase[0],
    popt_phase[1], popt_phase[2], popt_phase[3])

#first step, get I and Q data and rotate and translate
    back to position



#fitted_phase_rotated = np.zeros(number_of_values)
fitted_phase_rotated = fitted_phase + alpha

fitI = np.mean(amplitudes_rotated)*np.cos(fitted_phase)
#finds I component of fit
fitQ = np.mean(amplitudes_rotated)*np.sin(fitted_phase)
#finds Q component of fit

fitIrotated = np.mean(amplitudes_rotated)*np.cos(
    fitted_phase_rotated)
#finds I component of fit
fitQrotated = np.mean(amplitudes_rotated)*np.sin(
    fitted_phase_rotated)
#finds Q component of fit

fitItranslated = fitIrotated + xc
fitQtranslated = fitQrotated + yc
```

```
fitIunnormalized = fitItranslated + cabledelayI
fitQunnormalized = fitQtranslated + cabledelayQ

#get phase of unnormalize data
fitphaseunnormalized = np.arctan2(fitQunnormalized,
    fitIunnormalized)

#last thing to do, combine fitted amplitude and phase data
Ifitfinal = fitamplitudescaled*np.cos(fitphaseunnormalized
    )
#finds I component of cable
Qfitfinal = fitamplitudescaled*np.sin(fitphaseunnormalized
    )
#finds Q component of cable


#make name of pdf file to save plots ot
savefilename = foldername + filename.replace('.csv', '') +
     '_Fit_' + todaystr + '.pdf'



#creates pdf to save plots
pp = PdfPages(savefilename)

#plots square magnitudes verus frequency in dbs
plt.figure()
plt.scatter(freqsMHz, squaremagnitudesdb, marker='.', s=5)
```

```
plt.title('$|S_{21}|^2$ Data and Fit')
plt.xlabel('Frequency (MHz)')
plt.ylabel('$|S_{21}|^2$ (dB)')
plt.grid()

#plots square magnitude fit in decibels over data
plt.plot(freqsMHz, 10*np.log10(amplitudeequation(freqsMHz,
    popt[0], popt[1], popt[2], popt[3], popt[4], popt[5]))
   , 'r')

#calculates midpt of y-axis in plot. Used for saving plot
   to file
midpt = (np.min(squaremagnitudesdb) + np.max(
   squaremagnitudesdb)) / 2

boxprops = dict(boxstyle='round', facecolor='wheat', alpha
   =0.5) #properties of text box on plot
boxstr = f'Q = {round(Q_phase)}\nQc = {round(Qc_phase)}\
   nQi = {round(Qi_phase)}\nfr = {round(fr_phase, 4)} MHz'
#contents of text box
plt.text(np.min(freqsMHz), np.min(squaremagnitudesdb),
   boxstr, fontsize=12, bbox=boxprops)
#adds textbox to plot

plt.savefig(pp, format='pdf')
#plt.savefig(pp, format='pdf')



#now plot unwrapped, rotated phase data
```

```
plt.figure()
plt.scatter(freqsMHz, thetafinal, marker='.', s=5)
plt.title('Phase Data and Fit')
plt.xlabel('Frequency (MHz)')
plt.ylabel('Phase (rads)')
plt.plot(freqsMHz, phaseequation(freqsMHz, popt_phase[0],
    popt_phase[1], popt_phase[2], popt_phase[3]), 'r')
plt.grid()
boxprops = dict(boxstyle='round', facecolor='wheat', alpha
    =0.5)
#properties of text box on plot
boxstr = f'Q = {round(Q_phase)}\nQc = {round(Qc_phase)}\
    nQi = {round(Qi_phase)}\nfr = {round(fr_phase, 4)} GHz'
#contents of text box
plt.text(np.min(freqsMHz), np.min(thetafinal), boxstr,
    fontsize=12, bbox=boxprops)
#adds textbox to plot

plt.savefig(pp, format='pdf')

#now plot just origianl IQ data and fitted data
plt.figure()
plt.scatter(Ivalues, Qvalues, marker='.', s=5)
plt.plot(Ifitfinal, Qfitfinal, 'r')
plt.xlabel('I')
plt.ylabel('Q')
plt.title('Raw IQ Data and Fit')
plt.grid()
#boxprops = dict(boxstyle='round', facecolor='wheat',
```

```
    alpha=0.5) #properties of text box on plot
#boxstr = f'Q = {round(Q_phase)}\nQc = {round(Qc_phase)}\
    nQi = {round(Qi_phase)}\nfr = {round(fr_MHz_phase, 4)}
    GHz'
#contents of text box
#plt.text(np.min(Ifitfinal), np.min(Qfitfinal), boxstr,
    fontsize=12, bbox=boxprops)
#adds textbox to plot

#creates pdf to save plots
plt.savefig(pp, format='pdf')
pp.close()
```

A1.3 Filter Coefficient Generator Code

The following MATLAB code was written to generate filter coeffieicents for a defined filter size, type, and corner frequency. These filter coefficients could be used in the FIR filter blocks in the RFSoC firmware.

Listing A1.3: Frequency Coefficient Generator Code

```
function[] = get_filter_coefficients(wc)

clear all
close all

%wc = 500000; %cutoff frequency
fs = 1000000; %normalizing frequency, sampling frequency
    of 1 MHz

N = 25; %Number of filter taps


bRectangular = fir1(N, 2*wc/fs, 'low', rectwin(N+1)); %
    Rectangular fir filter
figure
freqz(bRectangular)
title('Rectangular Filter - Normalized')
RectFile = fopen('RectFilter.txt','w');
fprintf(RectFile,'%f \n',bRectangular);
fclose(RectFile);
```

```
bHamming = fir1(N, 2*wc/fs, 'low', hamming(N+1)); %
   Hamming fir filter
figure
freqz(bHamming)
title('Hamming␣Filter␣-␣Normalized')
HammingFile = fopen('HammingFilter.txt','w');
fprintf(HammingFile,'%f␣\n',bHamming);
fclose(HammingFile);

bHanning = fir1(N, 2*wc/fs, 'low', hann(N+1)); %Hanning
   fir filter
figure
freqz(bHanning)
title('Hanning␣Filter␣-␣Normalized')
HanningFile = fopen('HanningFilter.txt','w');
fprintf(HanningFile,'%f␣\n',bHanning);
fclose(HanningFile);

bBlackman = fir1(N, 2*wc/fs, 'low', blackman(N+1)); %
   Blackman fir filter
figure
freqz(bBlackman)
title('Blackman␣Filter␣-␣Normalized')
BlackmanFile = fopen('BlackmanFilter.txt','w');
fprintf(BlackmanFile,'%f␣\n',bBlackman);
fclose(BlackmanFile);
```

```
fvtool(bRectangular, 'Fs', fs)    %plots unnormalized
    filter response with filter visualisation tool
title('Magnitude Response (dB) - Rectangular Filter')

fvtool(bHamming, 'Fs', fs)    %plots unnormalized filter
    response with filter visualisation tool
title('Magnitude Response (dB) - Hamming Filter')

fvtool(bHanning, 'Fs', fs)    %plots unnormalized filter
    response with filter visualisation tool
title('Magnitude Response (dB) - Hanning Filter')

fvtool(bBlackman, 'Fs', fs)    %plots unnormalized filter
    response with filter visualisation tool
title('Magnitude Response (dB) - Blackman Filter')

figure
stem(bRectangular); %Plots filter co-efficients of
    rectangular filter
grid on;
title('Filter Co-Efficients - Rectangular Filter');
xlabel('n');
ylabel('h(n)');

figure
stem(bHamming); %Plots filter co-efficients of hamming
    filter
grid on;
title('Filter Co-Efficients - Hamming Filter');
```

```
xlabel('n');
ylabel('h(n)');

figure
stem(bHanning);    %Plots filter co-efficients of hanning
    filter
grid on;
title('Filter Co-Efficients - Hanning Filter');
xlabel('n');
ylabel('h(n)');

figure
stem(bBlackman);   %Plots filter co-efficients of blackman
    filter
grid on;
title('Filter Co-Efficients - Blackman Filter');
xlabel('n');
ylabel('h(n)');


end
```

Bibliography

[1] K.D. Irwin and G.C. Hilton. *Transition-Edge Sensors*, volume 99, pages 81–97. 07 2005. doi: 10.1007/10933596_3.

[2] Loredana Fleischmann, Mara Linck, A Burck, C Domesle, Sina Kempf, A Pabinger, C Pies, Jp Porst, H Rotzinger, S Schafer, R Weldle, A Fleischmann, C Enss, and G.M. Seidel. Metallic magnetic calorimeters for x-ray spectroscopy. *Applied Superconductivity, IEEE Transactions on*, 19:63 – 68, 05 2009. doi: 10.1109/TASC.2009.2012724.

[3] M. D. Shaw, J. Bueno, P. Day, C. M. Bradford, and P. M. Echternach. Quantum capacitance detector: A pair-breaking radiation detector based on the single cooper-pair box. *Phys. Rev. B*, 79:144511, Apr 2009. doi: 10.1103/PhysRevB.79.144511. URL https://link.aps.org/doi/10.1103/PhysRevB.79.144511.

[4] Peter Day, Henry Leduc, Benjamin A Mazin, Anastasios Vayonakis, and Jonas Zmuidzinas. A broadband superconducting detector suitable for use in large arrays. *Nature*, 425:817–21, 10 2003. doi: 10.1038/nature02037.

[5] P. Szypryt. *Development of Microwave Kinetic Inductance Detectors for Applications in Optical to Near-IR Astronomy*. PhD thesis, University of California, Santa Barbara, 2017.

[6] Matthew James Strader. *Digital Readout for Microwave Kinetic Inductance*

Detectors and Applications in High Time Resolution Astronomy. PhD thesis, University of California, Santa Barbara, 2016.

[7] Danny C. Price. Spectrometers and polyphase filterbanks in radio astronomy, 2016. URL `https://arxiv.org/abs/1607.03579`.

[8] Collaboration for Astronomy Signal Processing and Electronics Research. Reconfigurable open architecture computing hardware, 2013. URL `https://casper.ssl.berkeley.edu/wiki/ROACH`.

[9] E Brück. Developments in magnetocaloric refrigeration. *Journal of Physics D: Applied Physics*, 38:R381, 11 2005. doi: 10.1088/0022-3727/38/23/R01.

[10] *LNF-LNC 8C S/N 3957 4-8GHz Cryogenic Low Noise Amplifier*. Low Noise Factory, 11 2014.

[11] *LNF-LNC 8C S/N 2355 4-8GHz Cryogenic Low Noise Amplifier*. Low Noise Factory, 12 2020.

[12] *ZVA-183+ Wideband Amplifier*. Low Noise Factory, .

[13] *ZX60-83LN+ Low Noise Amplifier*. Low Noise Factory, .

[14] Asahi spectra ysc1100 transmission data, Feb 2022. URL `https://www.asahi-spectra.com/opticalfilters/detail.asp?key=YSC1100`.

[15] Thorlabs bk7 transmission data, Feb 2022. URL `https://www.thorlabs.com/newgrouppage9.cfm?objectgroup_id=1117`.

[16] F. Caspers. Rf engineering basic concepts: S-parameters, 2012.

[17] Jiansong Gao. *The Physics of Superconducting Microwave Resonators*. PhD thesis, California Institute of Technology, 2008.

[18] *ZCU111 Evaluation Board User Guide*. Xilinx, 10 2018.

[19] HTG. *RFSoC 2x2 User Manual*. Hitech Global, 1 2021. URL `http://www.hitechglobal.com/Boards/RFSoC2x2.htm`.

[20] B A. Mazin, S R. Meeker, Matthew Strader, B abd Bumble, Kieran O'Brien, P Szypryt, D Marsden, J C. van Eyken, G E. Duggan, G Ulbricht, C Stoughton, and M Johnson. Arcons: A 2024 pixel optical through near-ir cryogenic imaging spectrophotometer. *Publications of the Astronomical Society of the Pacific*, 125, 06 2013. doi: 10.1086/674013.

[21] S. Meeker. *DARKNESS: The First Microwave Kinetic Inductance Detector Integral Field Spectrograph for Exoplanet Imaging*. PhD thesis, University of California, Santa Barbara, 2017.

[22] Michael Tinkham. *Introduction to Superconductivity*, volume 2. McGraw-Hill, 1996.

[23] J. Bardeen, L. N. Cooper, and J. R. Schrieffer. Theory of superconductivity. *Phys. Rev.*, 108:1175–1204, Dec 1957. doi: 10.1103/PhysRev.108.1175. URL https://link.aps.org/doi/10.1103/PhysRev.108.1175.

[24] A Rogalski. HgCdTe infrared detector material: history, status and outlook. *Reports on Progress in Physics*, 68(10):2267–2336, aug 2005. doi: 10.1088/0034-4885/68/10/r01. URL https://doi.org/10.1088/0034-4885/68/10/r01.

[25] Leon N. Cooper. Bound electron pairs in a degenerate fermi gas. *Phys. Rev.*, 104:1189–1190, Nov 1956. doi: 10.1103/PhysRev.104.1189. URL https://link.aps.org/doi/10.1103/PhysRev.104.1189.

[26] B.D. Josephson. Possible new effects in superconductive tunnelling. *Physics Letters*, 1:251–253, July 1962. doi: 10.1016/0031-9163(62)91369-0.

[27] A. Peacock, P. Verhoeve, N. Rando, A. van Dordrecht, B.G. Taylor, C. Erd, M.A.C. Perryman, R. Venn, J. Howlett, D.J. Goldie, J. Lumley, and M. Wallis. On the detection of single optical photons with superconducting tunnel junction. *Journal of Applied Physics*, 81:7641–7646, June 1997. doi: 10.1063/1.365342.

[28] P. Drude. Zur Elektronentheorie der Metalle. *Annalen der Physik*, 306: 566–613, 1900. doi: 10.1002/andp.19003060312.

[29] Benjamin A. Mazin. *Microwave Kinetic Inductance Detectors*. PhD thesis, California Institute of Technology, 2004.

[30] Sean McHugh, Benjamin A Mazin, Bruno Serfass, Seth Meeker, Kieran O'Brien, Ran Duan, Rick Raffanti, and Dan Werthimer. A readout for large arrays of microwave kinetic inductance detectors. *The Review of scientific instruments*, 83:044702, 04 2012. doi: 10.1063/1.3700812.

[31] O Bourrion, Aurélien Bideaud, Alain Benoit, Angelo Cruciani, J F. Macias-Perez, Alessandro Monfardini, Markus Roesch, Loren Swenson, and C Vescovi. Electronics and data acquisition demonstrator for a kinetic inductance camera. *Journal of Instrumentation - J INSTRUM*, 6, 02 2011. doi: 10.1088/1748-0221/6/06/P06012.

[32] S Yates, Andrey Baryshev, J.J.A. Baselmans, B Klein, and R Güsten. Ffts readout for large arrays of microwave kinetic inductance detectors. 04 2009.

[33] Pieter J. de Visser, Steven A.H. de Rooij, Vignesh Murugesan, David J. Thoen, and Jochem J.A. Baselmans. Phonon-trapping-enhanced energy resolution in superconducting single-photon detectors. *Physical Review Applied*, 16(3), Sep 2021. ISSN 2331-7019. doi: 10.1103/physrevapplied.16.034051. URL http://dx.doi.org/10.1103/PhysRevApplied.16.034051.

[34] Joris van Rantwijk, Martin Grim, Dennis van Loon, Sophia Yates, Andrey Baryshev, and J.J.A. Baselmans. Multiplexed readout for 1000-pixel arrays of microwave kinetic inductance detectors. *IEEE Transactions on Microwave Theory and Techniques*, 64, 07 2015. doi: 10.1109/TMTT.2016.2544303.

[35] Jack Hickish, Zuhra Abdurashidova, Zaki Ali, Kaushal Buch, Sandeep Chaudhari, Hong Chen, Matthew Dexter, Rachel Simone Domagalski, John

Ford, Griffin Foster, David George, Joe Greenberg, Lincoln Greenhill, Adam Isaacson, Homin Jiang, Glenn Jones, Francois Kapp, Henno Kriel, Rich Lacasse, and Dan Werthimer. A decade of developing radio-astronomy instrumentation using casper open-source technology. *Journal of Astronomical Instrumentation*, 05, 11 2016. doi: 10.1142/S2251171716410014.

[36] James W. Cooley and John W. Tukey. An algorithm for the machine calculation of complex fourier series. *Mathematics of Computation*, 19: 297–301, 1965.

[37] Simon. Haykin and Barry Van Veen. *Signals and Systems*, volume 2. Wiley, 10 2002.

[38] Jack E. Volder. The cordic computing technique. In *IRE-AIEE-ACM '59 (Western)*, 1959.

[39] Y.H. Hu. The quantization effects of the cordic algorithm. *IEEE Transactions on Signal Processing*, 40(4):834–844, 1992. doi: 10.1109/78.127956.

[40] *Virtex-5 Family Overview*. Xilinx, 8 2015.

[41] A. Walter. *MEC: The MKID Exoplanet Camera for High SpeedFocal Plane Control at the Subaru Telescope*. PhD thesis, University of California, Santa Barbara, 2019.

[42] Maria Teresa Pont, Gregorio de Miguel, Higinio Mora, and J. Chamizo. Table-based recursive method for function evaluation. *AIP Conference Proceedings*, 936, 09 2007. doi: 10.1063/1.2790193.

[43] *DSP48E1 Slice User Guide*. Xilinx, 3 2018.

[44] Gerhard Ulbricht, Mario De Lucia, and Eoin Baldwin. Applications for microwave kinetic induction detectors in advanced instrumentation. *Applied*

Sciences, 11(6):2671, Mar 2021. ISSN 2076-3417. doi: 10.3390/app11062671. URL http://dx.doi.org/10.3390/app11062671.

[45] Akira Endo, Kenichi Karatsu, Yoichi Tamura, Tai Oshima, Akio Taniguchi, Tatsuya Takekoshi, Shin'ichiro Asayama, Tom J. L. C. Bakx, Sjoerd Bosma, Juan Bueno, Kah Wuy Chin, Yasunori Fujii, Kazuyuki Fujita, Robert Huiting, Soh Ikarashi, Tsuyoshi Ishida, Shun Ishii, Ryohei Kawabe, Teun M. Klapwijk, Kotaro Kohno, Akira Kouchi, Nuria Llombart, Jun Maekawa, Vignesh Murugesan, Shunichi Nakatsubo, Masato Naruse, Kazushige Ohtawara, Alejandro Pascual Laguna, Junya Suzuki, Koyo Suzuki, David J. Thoen, Takashi Tsukagoshi, Tetsutaro Ueda, Pieter J. de Visser, Paul P. van der Werf, Stephen J. C. Yates, Yuki Yoshimura, Ozan Yurduseven, and Jochem J. A. Baselmans. First light demonstration of the integrated superconducting spectrometer. *Nature Astronomy*, 3(11):989–996, Aug 2019. ISSN 2397-3366. doi: 10.1038/s41550-019-0850-8. URL http://dx.doi.org/10.1038/s41550-019-0850-8.

[46] K. S. Karkare, P. S. Barry, C. M. Bradford, S. Chapman, S. Doyle, J. Glenn, S. Gordon, S. Hailey-Dunsheath, R. M. J. Janssen, A. Kovács, H. G. LeDuc, P. Mauskopf, R. McGeehan, J. Redford, E. Shirokoff, C. Tucker, J. Wheeler, and J. Zmuidzinas. Full-array noise performance of deployment-grade superspec mm-wave on-chip spectrometers. *Journal of Low Temperature Physics*, 199(3-4):849–857, Feb 2020. ISSN 1573-7357. doi: 10.1007/s10909-020-02407-4. URL http://dx.doi.org/10.1007/s10909-020-02407-4.

[47] C. N. Thomas, S. Withington, R. Maiolino, D. J. Goldie, E. de Lera Acedo, J. Wagg, R. Blundell, S. Paine, and L. Zeng. The cambridge emission line surveyor (camels), 2014.

[48] Sean Bryan, James Aguirre, George Che, Simon Doyle, Daniel Flanigan, Christopher Groppi, Bradley Johnson, Glenn Jones, Philip Mauskopf, Heather

McCarrick, Alessandro Monfardini, and Tony Mroczkowski. Wspec: A waveguide filter-bank focal plane array spectrometer for millimeter wave astronomy and cosmology. *Journal of Low Temperature Physics*, 184(1-2): 114–122, Dec 2015. ISSN 1573-7357. doi: 10.1007/s10909-015-1396-5. URL http://dx.doi.org/10.1007/s10909-015-1396-5.

[49] Giuseppe Cataldo, Wen-Ting Hsieh, Wei-Chung Huang, S. Harvey Moseley, Thomas R. Stevenson, and Edward J. Wollack. Micro-spec: an ultracompact, high-sensitivity spectrometer for far-infrared and submillimeter astronomy. *Appl. Opt.*, 53(6):1094–1102, Feb 2014. doi: 10.1364/AO.53.001094. URL http://opg.optica.org/ao/abstract.cfm?URI=ao-53-6-1094.

[50] P. A. R. Ade, C. J. Anderson, E. M. Barrentine, N. G. Bellis, A. D. Bolatto, P. C. Breysse, B. T. Bulcha, G. Cataldo, J. A. Connors, P. W. Cursey, N. Ehsan, H. C. Grant, T. M. Essinger-Hileman, L. A. Hess, M. O. Kimball, A. J. Kogut, A. D. Lamb, L. N. Lowe, P. D. Mauskopf, J. McMahon, M. Mirzaei, S. H. Moseley, J. W. Mugge-Durum, O. Noroozian, U. Pen, A. R. Pullen, S. Rodriguez, P. J. Shirron, R. S. Somerville, T. R. Stevenson, E. R. Switzer, C. Tucker, E. Visbal, C. G. Volpert, E. J. Wollack, and S. Yang. The experiment for cryogenic large-aperture intensity mapping (exclaim). *Journal of Low Temperature Physics*, 199(3-4):1027–1037, Jan 2020. ISSN 1573-7357. doi: 10.1007/s10909-019-02320-5. URL http://dx.doi.org/10.1007/s10909-019-02320-5.

[51] Jack Sayers, Clint Bockstiegel, Spencer Brugger, Nicole G. Czakon, Peter K. Day, Thomas P. Downes, Ran P. Duan, Jiansong Gao, Amandeep K. Gill, Jason Glenn, Sunil R. Golwala, Matthew I. Hollister, Albert Lam, Henry G. LeDuc, Philip R. Maloney, Benjamin A. Mazin, Sean G. McHugh, David A. Miller, Anthony K. Mroczkowski, Omid Noroozian, Hien Trong Nguyen, James A. Schlaerth, Seth R. Siegel, Anastasios Vayonakis, Philip R. Wilson, and Jonas Zmuidzinas. The status of MUSIC: the multiwavelength

sub-millimeter inductance camera. In Wayne S. Holland and Jonas Zmuidzinas, editors, *Millimeter, Submillimeter, and Far-Infrared Detectors and Instrumentation for Astronomy VII*, volume 9153, pages 57 – 74. International Society for Optics and Photonics, SPIE, 2014. doi: 10.1117/12.2055444. URL https://doi.org/10.1117/12.2055444.

[52] A. Monfardini, L. J. Swenson, A. Bideaud, F. X. Désert, S. J. C. Yates, A. Benoit, A. M. Baryshev, J. J. A. Baselmans, S. Doyle, B. Klein, M. Roesch, C. Tucker, P. Ade, M. Calvo, P. Camus, C. Giordano, R. Guesten, C. Hoffmann, S. Leclercq, P. Mauskopf, and K. F. Schuster. Nika: A millimeter-wave kinetic inductance camera. *Astronomy and Astrophysics*, 521:A29, Oct 2010. ISSN 1432-0746. doi: 10.1051/0004-6361/201014727. URL http://dx.doi.org/10.1051/0004-6361/201014727.

[53] M. Calvo, A. Benoît, A. Catalano, J. Goupy, A. Monfardini, N. Ponthieu, E. Barria, G. Bres, M. Grollier, G. Garde, J.-P. Leggeri, G. Pont, S. Triqueneaux, R. Adam, O. Bourrion, J.-F. Macías-Pérez, M. Rebolo, A. Ritacco, J.-P. Scordilis, D. Tourres, A. Adane, G. Coiffard, S. Leclercq, F.-X. Désert, S. Doyle, P. Mauskopf, C. Tucker, P. Ade, P. André, A. Beelen, B. Belier, A. Bideaud, N. Billot, B. Comis, A. D'Addabbo, C. Kramer, J. Martino, F. Mayet, F. Pajot, E. Pascale, L. Perotto, V. Revéret, A. Ritacco, L. Rodriguez, G. Savini, K. Schuster, A. Sievers, and R. Zylka. The nika2 instrument, a dual-band kilopixel kid array for millimetric astronomy. *Journal of Low Temperature Physics*, 184(3-4):816–823, Mar 2016. ISSN 1573-7357. doi: 10.1007/s10909-016-1582-0. URL http://dx.doi.org/10.1007/s10909-016-1582-0.

[54] Tom Brien, Simon M. Doyle, Edgar Castillo-Domínguez, Daniel Ferrusca, David H. Hughes, Enzo Pascale, Sam Rowe, Carole Tucker, Peter A. R. Ade, Amber L. Hornsby, Peter Barry, Thomas Gascard, Victor Gomez, Peter Hargrave, Josie Parrianen, Abel Perez, and Salvador Ventura González.

Muscat: the mexico-uk sub-millimetre camera for astronomy. *Millimeter, Submillimeter, and Far-Infrared Detectors and Instrumentation for Astronomy IX*, Jul 2018. doi: 10.1117/12.2313697. URL http://dx.doi.org/10.1117/12.2313697.

[55] J. E. Austermann, J. A. Beall, S. A. Bryan, B. Dober, J. Gao, G. Hilton, J. Hubmayr, P. Mauskopf, C. M. McKenney, S. M. Simon, J. N. Ullom, M. R. Vissers, and G. W. Wilson. Millimeter-wave polarimeters using kinetic inductance detectors for toltec and beyond. *Journal of Low Temperature Physics*, 193(3-4):120–127, May 2018. ISSN 1573-7357. doi: 10.1007/s10909-018-1949-5. URL http://dx.doi.org/10.1007/s10909-018-1949-5.

[56] Luis Esteras Otal. *The Optical System and the Astronomical Potential of A-MKID, a New Camera Using Microwave Kinetic Inductance Detector Technology*. PhD thesis, Rheinische Friedrich-Wilhelms-Universität Bonn, November 2015.

[57] R. Duan, V. Khaikin, M. Lebedev, V. Shmagin, G. Yakopov, V. Vdovin, G. Bubnov, X. Zhang, C. Niu, Di Li, and I. Zinchenko. Toward eurasian submillimeter telescopes: the concept of multicolor subthz mkid-array demo camera musicam and its instrumental testing, 2020.

[58] M. Griffin, J. Baselmans, A. Baryshev, S. Doyle, M. Grim, P. Hargrave, T. Klapwijk, J. Martin-Pintado, A. Monfardini, A. Neto, H. Steenbeek, I. Walker, K. Wood, A. D'Addabbo, P. Barry, A. Bideaud, B. Blázquez, J. Bueno, M. Calvo, J-L. Costa-Kramer, L. Ferrari, A. Gómez-Gutiérrez, J. Goupy, N. Llombart, and S. Yates. SPACEKIDS: kinetic inductance detectors for space applications. In Wayne S. Holland and Jonas Zmuidzinas, editors, *Millimeter, Submillimeter, and Far-Infrared Detectors and Instrumentation for Astronomy VIII*, volume 9914, pages 10 – 20.

International Society for Optics and Photonics, SPIE, 2016. doi: 10.1117/12.2231100. URL https://doi.org/10.1117/12.2231100.

[59] Nicholas Galitzki, Peter Ade, Francesco E. Angilè, Peter Ashton, Jason Austermann, Tashalee Billings, George Che, Hsiao-Mei Cho, Kristina Davis, Mark Devlin, Simon Dicker, Bradley J. Dober, Laura M. Fissel, Yasuo Fukui, Jiansong Gao, Samuel Gordon, Christopher E. Groppi, Seth Hillbrand, Gene C. Hilton, Johannes Hubmayr, Kent D. Irwin, Jeffrey Klein, Dale Li, Zhi-Yun Li, Nathan P. Lourie, Ian Lowe, Hamdi Mani, Peter G. Martin, Philip Mauskopf, Christopher McKenney, Federico Nati, Giles Novak, Enzo Pascale, Giampaolo Pisano, Fabio P. Santos, Douglas Scott, Adrian Sinclair, Juan D. Soler, Carole Tucker, Matthew Underhill, Michael Vissers, and Paul Williams. Instrumental performance and results from testing of the blast-tng receiver, submillimeter optics, and mkid detector arrays. *Millimeter, Submillimeter, and Far-Infrared Detectors and Instrumentation for Astronomy VIII*, Jul 2016. ISSN 0277-786X. doi: 10.1117/12.2231167. URL http://dx.doi.org/10.1117/12.2231167.

[60] A. Paiella, A. Coppolecchia, L. Lamagna, P.A.R. Ade, E.S. Battistelli, M. G. Castellano, I. Colantoni, F. Columbro, G. D'Alessandro, P. de Bernardis, S. Gordon, S. Masi, P. Mauskopf, G. Pettinari, F. Piacentini, G. Pisano, G. Presta, and C. Tucker. Kinetic inductance detectors for the olimpo experiment: design and pre-flight characterization. *Journal of Cosmology and Astroparticle Physics*, 2019(01):039–039, Jan 2019. ISSN 1475-7516. doi: 10.1088/1475-7516/2019/01/039. URL http://dx.doi.org/10.1088/1475-7516/2019/01/039.

[61] Shugo Oguri, Jihoon Choi, Thushara Damayanthi, Makoto Hattori, Masashi Hazumi, Hikaru Ishitsuka, Kenji Kiuchi, Ryo Koyano, Hiroki Kutsuma, Kyungmin Lee, Satoru Mima, Makoto Minowa, Makoto Nagai, Taketo Nagasaki, Chiko Otani, Yutaro Sekimoto, Munehisa Semoto, Jun'ya Suzuki,

Tohru Taino, Osamu Tajima, Nozomu Tomita, Eunil Won, Tomohisa Uchida, and Mitsuhiro Yoshida. GroundBIRD: observations of CMB polarization with fast scan modulation and MKIDs. In Helen J. Hall, Roberto Gilmozzi, and Heather K. Marshall, editors, *Ground-based and Airborne Telescopes VI*, volume 9906, pages 1288 – 1294. International Society for Optics and Photonics, SPIE, 2016. doi: 10.1117/12.2231672. URL https://doi.org/10.1117/12.2231672.

[62] Omid Noroozian, Emily M. Barrentine, Thomas R. Stevenson, Ari D. Brown, Samuel Harvey Moseley, Edward Wollack, Klaus Martin Pontoppidan, Konpop U-Yen, and Vilem Mikula. Photon-Counting Kinetic Inductance Detectors (KID) for Far/Mid-Infrared Space Spectroscopy with the Origins Space Telescope (OST). In *American Astronomical Society Meeting Abstracts #231*, volume 231 of *American Astronomical Society Meeting Abstracts*, page 447.01, January 2018.

[63] P. Szypryt, G. E. Duggan, B. A. Mazin, S. R. Meeker, M. J. Strader, J. C. van Eyken, D. Marsden, K. O'Brien, A. B. Walter, G. Ulbricht, T. A. Prince, C. Stoughton, and B. Bumble. Direct detection of sdss j0926+3624 orbital expansion with arcons. *Monthly Notices of the Royal Astronomical Society*, 439(3):2765–2770, Feb 2014. ISSN 0035-8711. doi: 10.1093/mnras/stu137. URL http://dx.doi.org/10.1093/mnras/stu137.

[64] C. Bockstiegel. *The MKID Camera for PICTURE-C and Photon Counting Stochastic Speckle Discrimination*. PhD thesis, University of California, Santa Barbara, 2019.

[65] Benjamin A. Mazin, George D. Becker, Gustavo Cancelo, Kevin France, Wesley C. Fraser, Tucker Jones, Seth R. Meeker, Kieran O'Brien, J. Xavier Prochaska, Shriharsh Tendulkar, and Gautam Vasisht. KRAKENS: a superconducting MKID integral field spectrograph concept for the Keck I telescope. In Christopher J. Evans, Luc Simard, and Hideki Takami, editors,

Ground-based and Airborne Instrumentation for Astronomy VII, volume 10702, pages 108 – 127. International Society for Optics and Photonics, SPIE, 2018. doi: 10.1117/12.2312221. URL https://doi.org/10.1117/12.2312221.

[66] A. De Rújula and M. Lusignoli. Calorimetric measurements of 163holmium decay as tools to determine the electron neutrino mass. *Physics Letters B*, 118(4):429–434, 1982. ISSN 0370-2693. doi: https://doi.org/10.1016/0370-2693(82)90218-0. URL https://www.sciencedirect.com/science/article/pii/0370269382902180.

[67] E. Ferri, D. Bagliani, M. Biasotti, G. Ceruti, D. Corsini, M. Faverzani, F. Gatti, A. Giachero, C. Gotti, C. Kilbourne, A. Kling, M. Maino, P. Manfrinetti, A. Nucciotti, G. Pessina, G. Pizzigoni, M. Ribeiro Gomes, and M. Sisti. The status of the mare experiment with 187re and 163ho isotopes. *Physics Procedia*, 61:227–231, 2015. ISSN 1875-3892. doi: https://doi.org/10.1016/j.phpro.2014.12.037. URL https://www.sciencedirect.com/science/article/pii/S1875389214006506. 13th International Conference on Topics in Astroparticle and Underground Physics, TAUP 2013.

[68] C. Arnaboldi, F. Avignone, M. Balata, M. Barucci, J. Beeman, C. Brofferio, C. Bucci, S. Capelli, L. Carbone, S. Cebrian, O. Cremonesi, R. J. Creswick, H. A. Farach, E. Fiorini, G. Frossati, A. Giuliani, E. E. Haller, I. G. Irastorza, R. J. McDonald, A. Morales, E. B. Norman, A. Nucciotti, V. Palmieri, M. Pavan, M. Pedretti, G. Pessina, S. Pirro, C. Pobes, E. Previtali, A. R. Smith, M. Vanzini, G. Ventura, A. de Waard, and L. Zanotti. The cuore experiment. *AIP Conference Proceedings*, 605(1):469–472, 2002. doi: 10.1063/1.1457688. URL https://aip.scitation.org/doi/abs/10.1063/1.1457688.

[69] O. Azzolini, J.W. Beeman, F. Bellini, M. Beretta, M. Biassoni, C. Brofferio,

C. Bucci, S. Capelli, L. Cardani, P. Carniti, N. Casali, D. Chiesa, M. Clemenza, O. Cremonesi, A. Cruciani, I. Dafinei, S. Di Domizio, F. Ferroni, L. Gironi, A. Giuliani, P. Gorla, C. Gotti, G. Keppel, M. Martinez, S. Nagorny, M. Nastasi, S. Nisi, C. Nones, D. Orlandi, L. Pagnanini, M. Pallavicini, L. Pattavina, M. Pavan, G. Pessina, V. Pettinacci, S. Pirro, S. Pozzi, E. Previtali, A. Puiu, C. Rusconi, K. Schäffner, C. Tomei, M. Vignati, and A.S. Zolotarova. Final result of cupid-0 phase-i in the search for the se82 neutrinoless double-beta decay. *Physical Review Letters*, 123(3), Jul 2019. ISSN 1079-7114. doi: 10.1103/physrevlett.123.032501. URL http://dx.doi.org/10.1103/PhysRevLett.123.032501.

[70] Nicola Casali, Fabio Bellini, L. Cardani, M. Castellano, Ivan Colantoni, C. Cosmelli, A. Cruciani, Antonio D'Addabbo, S. Domizio, M. Martinez, L. Minutolo, C. Tomei, and M. Vignati. *Cryogenic Light Detectors for Background Suppression: The CALDER Project: Volume 2*, pages 267–270. 08 2018. ISBN 978-981-13-1315-8. doi: 10.1007/978-981-13-1316-5_50.

[71] M. Faverzani, B. Alpert, D. Backer, D. Bennet, Michele Biasotti, C. Brofferio, Valentina Ceriale, G. Ceruti, Dario Corsini, Peter Day, Matteo De Gerone, R. Dressler, E. Ferri, Jie Fowler, Elisa Fumagalli, Johnathon Gard, Flavio Gatti, Andrea Giachero, J. Hays-Wehle, and Leila Vale. The holmes experiment. *Journal of Low Temperature Physics*, 184, 08 2016. doi: 10.1007/s10909-016-1540-x.

[72] C. Alduino, K. Alfonso, D. R. Artusa, F. T. Avignone, O. Azzolini, T. I. Banks, G. Bari, J. W. Beeman, F. Bellini, G. Benato, A. Bersani, M. Biassoni, A. Branca, C. Brofferio, C. Bucci, A. Camacho, A. Caminata, L. Canonica, X. G. Cao, S. Capelli, L. Cappelli, L. Carbone, L. Cardani, P. Carniti, N. Casali, L. Cassina, D. Chiesa, N. Chott, M. Clemenza, S. Copello, C. Cosmelli, O. Cremonesi, R. J. Creswick, J. S. Cushman, A. D'Addabbo, I. Dafinei, C. J. Davis, S. Dell'Oro, M. M. Deninno,

S. Di Domizio, M. L. Di Vacri, A. Drobizhev, D. Q. Fang, M. Faverzani, G. Fernandes, E. Ferri, F. Ferroni, E. Fiorini, M. A. Franceschi, S. J. Freedman, B. K. Fujikawa, A. Giachero, L. Gironi, A. Giuliani, L. Gladstone, P. Gorla, C. Gotti, T. D. Gutierrez, E. E. Haller, K. Han, E. Hansen, K. M. Heeger, R. Hennings-Yeomans, K. P. Hickerson, H. Z. Huang, R. Kadel, G. Keppel, Yu. G. Kolomensky, A. Leder, C. Ligi, K. E. Lim, Y. G. Ma, M. Maino, L. Marini, M. Martinez, R. H. Maruyama, Y. Mei, N. Moggi, S. Morganti, P. J. Mosteiro, T. Napolitano, M. Nastasi, C. Nones, E. B. Norman, V. Novati, A. Nucciotti, T. O'Donnell, J. L. Ouellet, C. E. Pagliarone, M. Pallavicini, V. Palmieri, L. Pattavina, M. Pavan, G. Pessina, V. Pettinacci, G. Piperno, C. Pira, S. Pirro, S. Pozzi, E. Previtali, C. Rosenfeld, C. Rusconi, M. Sakai, S. Sangiorgio, D. Santone, B. Schmidt, J. Schmidt, N. D. Scielzo, V. Singh, M. Sisti, A. R. Smith, L. Taffarello, M. Tenconi, F. Terranova, C. Tomei, S. Trentalange, M. Vignati, S. L. Wagaarachchi, B. S. Wang, H. W. Wang, B. Welliver, J. Wilson, L. A. Winslow, T. Wise, A. Woodcraft, L. Zanotti, G. Q. Zhang, B. X. Zhu, S. Zimmermann, S. Zucchelli, and M. Laubenstein. The projected background for the cuore experiment. *The European Physical Journal C*, 77 (8), Aug 2017. ISSN 1434-6052. doi: 10.1140/epjc/s10052-017-5080-6. URL http://dx.doi.org/10.1140/epjc/s10052-017-5080-6.

[73] L. Cardani, F. Bellini, N. Casali, M. G. Castellano, I. Colantoni, A. Coppolecchia, C. Cosmelli, A. Cruciani, S. Di Domizio, C. Tomei, and M. Vignati. Calder: Cryogenic light detectors for background-free searches. *AIP Conference Proceedings*, 1672(1):130001, 2015. doi: 10.1063/1.4928011. URL https://aip.scitation.org/doi/abs/10.1063/1.4928011.

[74] Ivan Colantoni, Laura Cardani, Nicola Casali, Angelo Cruciani, Fabio Bellini, Maria Gabriella Castellano, Carlo Cosmelli, Antonio D.' Addabbo, Sergio Di Domizio, Maria Martinez, Claudia Tomei, and Marco Vignati. Calder: The

second-generation light detectors. *IEEE Transactions on Applied Superconductivity*, 28(8):1–3, 2018. doi: 10.1109/TASC.2018.2841925.

[75] I. Colantoni, L. Cardani, N. Casali, A. Cruciani, F. Bellini, M.G. Castellano, C. Cosmelli, A. D'Addabbo, S. Di Domizio, M. Martinez, C. Tomei, and M. Vignati. Design and Fabrication of the Second-Generation KID-Based Light Detectors of CALDER. *Journal of Low Temperature Physics*, 193(5-6): 726–731, December 2018. doi: 10.1007/s10909-018-1905-4.

[76] A. Giachero, P. K. Day, P. Falferi, M. Faverzani, E. Ferri, C. Giordano, M. Maino, B. Margesin, R. Mezzena, R. Nizzolo, A. Nucciotti, A. Puiu, and L. Zanetti. Development of microwave superconducting microresonators for neutrino mass measurement in the holmes framework. *Journal of Low Temperature Physics*, 184(1–2):123–130, Jan 2016. ISSN 1573-7357. doi: 10.1007/s10909-015-1441-4. URL http://dx.doi.org/10.1007/s10909-015-1441-4.

[77] I. Colantoni, C. Bellenghi, M. Calvo, R. Camattari, L. Cardani, N. Casali, A. Cruciani, S. Di Domizio, J. Goupy, V. Guidi, H. Le Sueur, M. Martinez, A. Mazzolari, A. Monfardini, V. Pettinacci, G. Pettinari, M. Romagnoni, and M. Vignati. BULLKID: BULky and Low-Threshold Kinetic Inductance Detectors. *Journal of Low Temperature Physics*, 199(3-4):593–597, February 2020. doi: 10.1007/s10909-020-02408-3.

[78] Yeukuang Hwu and Giorgio Margaritondo. Synchrotron radiation and sensors: A history of synergies. *IEEE Sensors Journal*, 21(11):12764–12773, 2021. doi: 10.1109/JSEN.2020.3023292.

[79] Thomas Cecil, Antonino Miceli, Lisa Gades, Aaron Datesman, Orlando Quaranta, V. Yefremenko, Val Novosad, and B. Mazin. Kinetic inductance detectors for x-ray spectroscopy. *Physics Procedia*, 37:697–702, 12 2012. doi: 10.1016/j.phpro.2012.03.719.

[80] Thomas Cecil, Antonino Miceli, Orlando Quaranta, Chian Liu, Daniel Rosenmann, Sean McHugh, and Benjamin Mazin. Tungsten silicide films for microwave kinetic inductance detectors. *Applied Physics Letters*, 101(3): 032601, Jul 2012. ISSN 1077-3118. doi: 10.1063/1.4737408. URL http://dx.doi.org/10.1063/1.4737408.

[81] O Quaranta, T W Cecil, L Gades, B Mazin, and A Miceli. X-ray photon detection using superconducting resonators in thermal quasi-equilibrium. *Superconductor Science and Technology*, 26(10):105021, sep 2013. doi: 10.1088/0953-2048/26/10/105021. URL https://doi.org/10.1088/0953-2048/26/10/105021.

[82] Thomas W. Cecil, Lisa Gades, Timothy Madden, Daikang Yan, and Antonino Miceli. Optimization of thermal kinetic inductance detectors for x-ray spectroscopy. *IEEE Transactions on Applied Superconductivity*, 25(3): 2400805 (5 pp.)–, 2015. doi: 10.1109/TASC.2014.2384995.

[83] Gerhard Ulbricht, Benjamin A. Mazin, Paul Szypryt, Alex B. Walter, Clint Bockstiegel, and Bruce Bumble. Highly multiplexible thermal kinetic inductance detectors for x-ray imaging spectroscopy, 2015.

[84] F. Schaefers, M. Mertin, and M. Gorgoi. Kmc-1: A high resolution and high flux soft x-ray beamline at bessy. *Review of Scientific Instruments*, 78(12): 123102, 2007. doi: 10.1063/1.2808334. URL https://doi.org/10.1063/1.2808334.

[85] M. Faverzani, A. Cruciani, Antonio D'Addabbo, Peter Day, S. Domizio, E. Ferri, P. Fresch, Andrea Giachero, Benno Margesin, R. Mezzena, L. Minutolo, A. Nucciotti, A. Puiu, and M. Vignati. Thermal kinetic inductance detectors for soft x-ray spectroscopy. *Nuclear Instruments and Methods in Physics Research Section A: Accelerators, Spectrometers, Detectors and Associated Equipment*, 936, 09 2018. doi: 10.1016/j.nima.2018.09.004.

[86] A. Giachero, A. Cruciani, A. D'Addabbo, P. K. Day, S. Di Domizio, M. Faverzani, E. Ferri, B. Margesin, M. Martinez, R. Mezzena, L. Minutolo, A. Nucciotti, A. Puiu, and M. Vignati. Development of thermal kinetic inductance detectors suitable for x-ray spectroscopy. *Journal of Low Temperature Physics*, 193(3–4):163–169, Jul 2018. ISSN 1573-7357. doi: 10.1007/s10909-018-2043-8. URL http://dx.doi.org/10.1007/s10909-018-2043-8.

[87] Sam Rowe, Enzo Pascale, Simon Doyle, Chris Dunscombe, Peter Hargrave, Andreas Papageorgio, Ken Wood, Peter A. R. Ade, Peter Barry, Aurélien Bideaud, Tom Brien, Chris Dodd, William Grainger, Julian House, Philip Mauskopf, Paul Moseley, Locke Spencer, Rashmi Sudiwala, Carole Tucker, and Ian Walker. A passive terahertz video camera based on lumped element kinetic inductance detectors. *Review of Scientific Instruments*, 87(3):033105, Mar 2016. ISSN 1089-7623. doi: 10.1063/1.4941661. URL http://dx.doi.org/10.1063/1.4941661.

[88] D. Morozov, Simon Doyle, Archan Banerjee, Thomas Brien, Dilini Hemakumara, Iain Thayne, Ken Wood, and Robert Hadfield. Design and characterisation of titanium nitride subarrays of kinetic inductance detectors for passive terahertz imaging. *Journal of Low Temperature Physics*, 193, 11 2018. doi: 10.1007/s10909-018-2023-z.

[89] Gabriele C. Messina, Valentina Brosco, Angelo Cruciani, Lara Benfatto, Sara Cibella, Giorgio Pettinari, Maria Gabriella Castellano, Alfonso A. Tanga, Michele Ortolani, Leonetta Baldassarre, Marco Vignati, and José Lorenzana. High-tc superconducting kinetic inductance detectors for terahertz imaging. In *2019 44th International Conference on Infrared, Millimeter, and Terahertz Waves (IRMMW-THz)*, pages 1–2, 2019. doi: 10.1109/IRMMW-THz.2019.8874002.

[90] Juha Hassel, Shahab Oddin Dabironezare, Erio Gandini, Leif Grönberg,

Hannu Sipola, Anssi Rautiainen, Aleksi Tamminen, Mikko Leivo, Hannu Lindström, Hannu Vasama, Arttu Luukanen, and Nuria Llombart. Dual-band submillimeter-wave kinetic inductance bolometers and an imaging system for contraband object detection. In David A. Wikner and Duncan A. Robertson, editors, *Passive and Active Millimeter-Wave Imaging XXI*, volume 10634, pages 107 – 112. International Society for Optics and Photonics, SPIE, 2018. doi: 10.1117/12.2304722. URL `https://doi.org/10.1117/12.2304722`.

[91] C. de Jonge, A.M. Baryshev, L. Ferrari, S. J. C. Yates, J.J.A. Baselmans, and A. Endo. Development of a passive stand-off imager using mkid technology for security and biomedical applications. In *2012 37th International Conference on Infrared, Millimeter, and Terahertz Waves*, pages 1–2, 2012. doi: 10.1109/IRMMW-THz.2012.6380107.

[92] Entropy cryogenics, Jan 2017. URL `https://www.entropy-cryogenics.com/`.

[93] John D. Kraus. *Radio astronomy*. 1966.

[94] Takashi Mimura. Development of high electron mobility transistor. *Japanese Journal of Applied Physics*, 44:8263–8268, 12 2005. doi: 10.1143/JJAP.44.8263.

[95] J.M. Hornibrook, J.I. Colless, I.D. Conway Lamb, S.J. Pauka, H. Lu, A.C. Gossard, J.D. Watson, G.C. Gardner, S. Fallahi, M.J. Manfra, and D.J. Reilly. Cryogenic Control Architecture for Large-Scale Quantum Computing. *Physical Review Applied*, 3:024010, Feb 2015. doi: 10.1103/PhysRevApplied.3.024010.

[96] T. Mimura. The early history of the high electron mobility transistor (hemt). *IEEE Transactions on Microwave Theory and Techniques*, 50(3):780–782, 2002. doi: 10.1109/22.989961.

[97] P Duthil. Material properties at low temperature. 01 2015. doi: 10.5170/CERN-2014-005.77.

[98] *AC Resistance Bridge SIM921*. Stanford Research Systems, 9 2011.

[99] Jie Hu, Faouzi Boussaha, Jean-Marc Martin, Paul Nicaise, Christine Chaumont, Samir Beldi, Michel Piat, and Piercarlo Bonifacio. Large inverse transient phase response of titanium-nitride-based microwave kinetic inductance detectors. *Applied Physics Letters*, 119(21):212601, Nov 2021. ISSN 1077-3118. doi: 10.1063/5.0074103. URL http://dx.doi.org/10.1063/5.0074103.

[100] *Standard Commands for Programmable Instruments*. SCPI Consortium, 5 1999.

[101] *E5080A ENA Vector Network Analyzer*. Keysight, 6 2020.

[102] Paul Petersan and Steven Anlage. Measurement of resonant frequency and quality factor of microwave resonators: Comparison of methods. *Journal of Applied Physics*, 84, 05 1998. doi: 10.1063/1.368498.

[103] Jonas Zmuidzinas. Superconducting microresonators: Physics and applications. *Annual Review of Condensed Matter Physics*, 3:169–214, 02 2012. doi: 10.1146/annurev-conmatphys-020911-125022.

[104] Digicom electronics roach and roach2 systems, Mar 2022. URL https://www.digicom.org/roach-board.html.

[105] *MUSIC IF Board fro ROACH*. Techne Instruments, .

[106] *MKID DAC/ADC Board for ROACH*. Techne Instruments, .

[107] C.E. Shannon. Communication in the presence of noise. *Proceedings of the IRE*, 37(1):10–21, 1949. doi: 10.1109/JRPROC.1949.232969.

[108] Casper skarab board, Mar 2022. URL https://casper.astro.berkeley.edu/wiki/SKARAB.

[109] A. Szomoru. The UniBoard. In *10th European VLBI Network Symposium and EVN Users Meeting: VLBI and the New Generation of Radio Arrays*, page 98, 2010.

[110] Uniboard i and uniboard ii, Mar 2022. URL http://old.astron.nl/r-d-laboratory/uniboard/uniboard-i-and-ii.

[111] Xilinx vcu118, Mar 2022. URL https://www.xilinx.com/products/boards-and-kits/vcu118.html.

[112] *VCU118 Evaluation Board User Guide*. Xilinx, 10 2018.

[113] Vadatech amc599, Mar 2022. URL https://www.vadatech.com/product.php?product=473.

[114] Htg-940: Virtex ultrascale+ ™ quad fmc+ development platform, Mar 2022. URL http://www.hitechglobal.com/Boards/UltraScale+QuadFMC+.htm.

[115] Getting started with rfsoc, Mar 2022. URL https://casper-toolflow.readthedocs.io/projects/tutorials/en/latest/tutorials/rfsoc/tut_getting_started.html.

[116] Pynq - python productivity, Mar 2022. URL http://www.pynq.io/.

[117] Pynq read the docs, Mar 2022. URL https://pynq.readthedocs.io/en/latest/.

[118] Vivado overview, Mar 2022. URL https://www.xilinx.com/products/design-tools/vivado.html.

[119] Jupyterlab read the docs, Mar 2022. URL https://jupyterlab.readthedocs.io/en/stable/.

[120] *Zynq UltraScale+ RFSoC RF Data Converter v2.4 Gen 1/2/3 LogiCORE IP Product Guide*. Xilinx, 11 2020.

[121] *AXI DMA v7.1 LogiCORE IP Product Guide*. Xilinx, 6 2019.

[122] *Zynq UltraScale+ MPSoC Processing System v3.2 Product Guide*. Xilinx, 12 2018.

[123] *Fast Fourier Transform v9.1 LogiCORE IP Product Guide*. Xilinx, 8 2021.

[124] *FIR Compiler v7.2 LogiCORE IP Product Guide*. Xilinx, 1 2021.